

AD-A272 725 ON PAGE

Form Approved  
OMB No. 0704-0188Public  
gathering  
collection  
Davis Hig

1 hour per reference, including the time for reviewing instructions, searching existing data sources, collection of information. Send comments regarding this burden estimate or any other aspect of this collection of information, including suggestions for reducing the burden, to Washington Headquarters Services, Directorate for Information Operations and Reports, 1215 Jefferson Avenue, Washington, DC 20503.

1. AGE... 2. REPORT DATE  
October 12, 1993 3. REPORT TYPE AND DATES COVERED Final Report  
Oct. 1, 1989 to Sept. 30, 1993

4. TITLE AND SUBTITLE

Chemistry of the Burning Surface

5. FUNDING NUMBERS

PE - 61102F  
PR - 2308  
SA - AS  
G - AFOSR-89-0521

6. AUTHOR(S)

Thomas B. Brill

7. PERFORMING ORGANIZATION NAME(S) AND ADDRESS(ES)

Department of Chemistry  
University of Delaware  
Newark, DE 197168. PERFORMING ORGANIZATION  
REPORT NUMBER

AFOSR-R-89-0040

9. SPONSORING / MONITORING AGENCY NAME(S) AND ADDRESS(ES)

AFOSR/NA  
110 Duncan Avenue Suite B115  
Bolling AFB, DC 20332-000110. SPONSORING / MONITORING  
AGENCY REPORT NUMBER

11. SUPPLEMENTARY NOTES

DTIC  
ELECTE  
NOV 17 1993

12a. DISTRIBUTION / AVAILABILITY STATEMENT

Approved for public release; distribution is  
unlimited

12b. DISTRIBUTION CODE

A

13. ABSTRACT (Maximum 200 words)

The objective of this project was to identify the dominant thermal decomposition and secondary reaction pathways that exist in the surface zone of a burning propellant. T-jump/FTIR spectroscopy and SMATCH/FTIR spectroscopy are new diagnostic techniques that were designed for this project. They enable a film of material to be heated at a high rate in such a manner as to simulate a thin volume element of the surface during combustion. The semiglobal thermal decomposition reactions and the first strongly exothermic secondary reaction of important oxidizers and monopropellants were identified. The compounds studied were nitramine (CL-20, HMX, RDX, DNNC), ammonium salts (AP, AN, ADN), and azide polymers (GAP, BAMO).

14. SUBJECT TERMS -Thermal decomposition  
-Burning surface chemistry  
-IR spectroscopy  
-Thermal Techniques-CL-20 -AN  
-HMX -AP  
-RDX -AN  
-GAP15. NUMBER OF PAGES  
201

16. PRICE CODE

17. SECURITY CLASSIFICATION  
OF REPORT  
Unclassified18. SECURITY CLASSIFICATION  
OF THIS PAGE  
Unclassified19. SECURITY CLASSIFICATION  
OF ABSTRACT  
Unclassified20. LIMITATION OF ABSTRACT  
UL

## I. Objectives

The research summarized in this final report of AFOSR-89-0521 covers the period of October 1, 1989 to September 30, 1993. The objective in the first year was to characterize the rapid thermal decomposition of hexanitrohexaazaisowurtzitane (HNIW or Cl-20). The remaining three years of work were devoted to surmounting one of the major barriers that exists in describing the combustion of solid rocket propellants. This problem is the experimental characterization of the chemical reactions that exist in the surface zone (melt and/or foam layer) during combustion. Determination of these chemical reactions cannot be made with the flame present because the surface zone is too thin and too heterogeneous to study by spectroscopic techniques.

The major processes that need to be defined in the surface reaction zone are the initial decomposition reactions of the constituent molecules and the first strongly exothermic reaction. These two chemical processes play a major role in determining the flame structure and the burn rate.

The project has required unique and original experimental techniques to be developed that combine infrared spectroscopy and heat-flow measurements. The experiments are performed at high heating rates to high and constant temperature. The most powerful of our new methods is T-jump/FTIR spectroscopy. A second technique involves the simultaneous measurement of the mass change and temperature change of the condensed phase along with the IR spectrum of the gaseous products that leave the surface (SMATCH/FTIR spectroscopy).

93-28113



93 11 16 052

Accession For	
NTIS CRASH	
DTIC TAB	
Unannounced	
Justification	
By	
Dist (Optional)	
Availability Codes	
Dist	Avail and/or Special
A-1	

## II. Major Accomplishments

### A. Development of New Fast Thermolysis Techniques.

Two new techniques based on fast heating of a film of sample to a high temperature combined with rapid-scan Fourier transform infrared spectroscopy were developed. These are called SMATCH/FTIR and T-jump/FTIR spectroscopy. T-jump/FTIR spectroscopy is the most widely applicable, and efforts are being made in a number of other laboratories to adopt this technique for combustion research.

### B. Validation that a Rapidly Heated Film of Sample is the "Snapshot" View of the Burning Surface.

The regression rates for selected energetic materials calculated from fast thermolysis of a 50 $\mu$ m thick film by SMATCH/FTIR spectroscopy closely resemble the regression rates measured on the bulk material in a strand burner at the same pressure. As shown in Table 1, this is true for NC, HMX, RDX, DNNC, GAP, and AP.

Table 1. Burn Rate Comparisons		
Compound	$\dot{r}$ , mm/sec (1 atm)	
	SMATCH	Strand burner
AP	0.16	0.25
HMX	0.37	0.5
RDX	0.38	0.38
DNNC	0.27	0.27
134N NC	0.3	0.4
GAP	1.35	1.7



C. Determination of the Major Decomposition Pathways and the First Strongly Exothermic Reaction in the Surface Reaction Zone.

By using T-jump/FTIR spectroscopy, the chemistry of a simulated surface reaction zone of many of the materials in Figure 1 was characterized. Of particular interest is the semi-global decomposition reactions of the parent molecule leading to the initial products (Table 2). These initial products become the reactants for the first strongly exothermic reaction which dominates in releasing heat in the bubbles and voids in the surface zone. This reaction strongly influences the burn rate of the material.

Table 2. A Summary of the Major Initial Decomposition Products and the Reactants for the First Large Heat Generation Reaction		
Compound	Initial Products	Heat Generation Reaction
HMX	CH <sub>2</sub> O + N <sub>2</sub> O + NO <sub>2</sub> + HCN	CH <sub>2</sub> O + NO <sub>2</sub>
RDX		
AN	NH <sub>3</sub> + NO <sub>2</sub> + HNO <sub>3</sub> N <sub>2</sub> O + NO	NH <sub>3</sub> + NO <sub>2</sub>
ADN		
DNNC	Complicated but similar to HMX and RDX	CH <sub>2</sub> O + NO <sub>2</sub>
AP	NH <sub>3</sub> , HClO <sub>4</sub>	HNO + HClO <sub>4</sub>
BAMO	RN + N <sub>2</sub>	RN decomposition
GAP		

III. Publications (Papers attached as appendices)

1. T. B. Brill and P. J. Brush, "Temperature Dependence of the Rapid Thermal Decomposition of Nitramines," Proc. 22nd International Conference of the ICT, Karlsruhe, FRG, July, 1991, p 12-1.

2. J. K. Chen and T. B. Brill "Thermal Decomposition of Energetic Materials 50. Kinetics and Mechanism of Nitrate Ester Polymers at High Heating Rates by SMATCH/FTIR Spectroscopy," Combust. Flame, 85, 479 (1991).
3. J. K. Chen and T. B. Brill "Thermal Decomposition of Energetic Materials 51. Kinetics of Weight-Loss from Nitrate Ester Polymers at Low Heating Rates," Thermochemica Acta, 181, 71 (1991).
4. S. F. Palopoli and T. B. Brill, "Thermal Decomposition of Energetic Materials 52. On the Foam Zone and Surface Chemistry of Rapidly Decomposing HMX," Combust. Flame, 87, 45 (1991).
5. D. G. Patil, J. K. Chen and T. B. Brill, "Thermal Decomposition of Energetic Materials 53. Kinetics and Mechanism of Thermolysis of Hexanitrohexaazaisowurtzitane," Combust. Flame, 87, 145 (1991).
6. J. K. Chen and T. B. Brill, "Thermal Decomposition of Energetic Materials 54. Kinetics and Near-Surface Products of AMMO, BAMO and GAP in Simulated Combustion," Combust. Flame, 87, 157 (1991).
7. J. K. Chen and T. B. Brill, "Chemistry and Kinetics of Hydroxyl-terminated Polybutadiene (HTPB) and Diisocyanate-HTPB Polymers during Slow Decomposition and Combustion Conditions," Combust. Flame, 87, 217 (1991).
8. T. B. Brill, "Connecting the Chemical Composition of a Material to its Combustion Characteristics," Prog. Energy Combust. Sci., 18, 91 (1992). (Invited).
9. T. B. Brill and P. J. Brush, "Condensed Phase Chemistry of Explosives and Propellants at High Temperature: HMX, RDX and BAMO," Phil. Trans. Royal Society, London, A, 339, 377 (1992) (Invited).
10. D. G. Patil, S. R. Jain and T. B. Brill, "Thermal Decomposition of Energetic Materials 56. On The Fast Thermolysis Mechanism of Ammonium Nitrate and its Mixtures with Magnesium and Carbon," Prop. Explos. Pyrotech., 17, 99 (1992).
11. T. B. Brill, P. J. Brush, K. J. James, J. E. Shepherd and K. J. Pfeiffer, "T-Jump/FTIR Spectroscopy. A New Entry into the Rapid, Isothermal Pyrolysis Chemistry of Solids and Liquids," Appl. Spectrosc., 46, 900 (1992) (feature article).
12. T. B. Brill, "Simulation Experimentale d'une Surface en Train de Bruler lors d'une Combustion ou d'une Explosion," Rev. Sci. Tech. Def. (France), 14, 37 (1992) (Invited and translated by J. Boileau).

13. T. B. Brill, P. J. Brush, D. G. Patil and J. K. Chen, "Reaction Pathways at a Burning Surface," Proc. 24th Symposium (International) on Combustion, The Combustion Institute, Pittsburgh, PA, 1992, p. 1907.
14. T. B. Brill, "Surface Chemistry of Energetic Materials at High Temperature" in Energetic Materials, R. W. Armstrong, J. G. Gilman and D. A. Liebenberg, Eds., Materials Research Society, Pittsburgh, PA, 1993, Vol. 296, p. 269.
15. T. B. Brill, P. J. Brush and D. G. Patil, "Thermal Decomposition of Energetic Materials 58. Chemistry of Ammonium Nitrate and Ammonium Dinitramide at the Burning Surface Temperature," Combust. Flame, 92, 178 (1993).
16. D. G. Patil and T. B. Brill, "Thermal Decomposition of Energetic Materials 59. Characterization of the Residue of Hexanitrohexaazaisowurtzitane," Combust. Flame, 92, 456, (1993).
17. T. B. Brill, P. J. Brush, and D. G. Patil, "Thermal Decomposition of Energetic Materials 60. Major Reaction Stages of a Simulated Burning Surface of  $\text{NH}_4\text{ClO}_4$ ," Combust. Flame, 94, 70 (1993).
18. T. B. Brill, D. G. Patil, J. Duterque, and G. Lengelle, "Thermal Decomposition of Energetic Materials 63. Surface Reaction Zone Chemistry of Simulated Burning 1,3,5,5-Tetranitrohexahydropyrimidine (DNNC or TNDA) Compared to RDX," Combust. Flame, in press.
19. T. B. Brill "FTIR Spectroscopy for Surface Pyrolysis and Flame Diagnostics," in Non-Intrusive Combustion Diagnostics, K. K. Kuo, Ed. Begell House, Inc. New York, 1993, in press. (Invited).
20. D. G. Patil and T. B. Brill, "Thermal Decomposition of Energetic Materials 64. Kinetics of Decomposition of Furazans[3,4,b]piperazine and its 1,4-Dinitro Nitramine Derivative," Thermochim. Acta, in press.

#### IV. Persons Supported

1. Dr. Dilip G. Patil was a post-doctoral associate supported Oct. 1989 to May, 1993. Dr. Patil is now Director of Research and Development of the Sabinsa Corp. Edison, NJ.
2. Dr. Jang Kang Chen was a graduate student with his own support from Chung Shan Institute of Science and Technology, Taiwan. The supplies and expendables for his Ph.D. research during 1989-1992 were covered on this grant.

3. Dr. Peter Brush was a Ph.D. student who was entirely supported on this project for 1989-1993. Dr. Brush is an analytical spectroscopist now employed by NIR Systems, Silver Springs, MD.

**V. A. Interactions and Consultations**

1. Federation of Analytical Chemistry and Spectroscopy Societies Meeting, Chicago, IL, October, 1989. (SMATCH/FTIR lecture presented)
2. SNPE - LeBouchet, France, January, 1990. (invited fast thermolysis lecture)
3. DRET - Paris, France, January, 1990. (invited fast thermolysis lecture)
4. Franco-German Research Institute (ISL), St. Louis, France, Jan., 1990. (invited fast thermolysis lecture)
5. American Defense Preparedness Association Meeting, Virginia Beach, VA, March, 1990. (invited fast heat-and-hold lecture)
6. Lawrence Livermore National Lab, April, 1990. (heat transfer in energetic materials discussed)
7. Los Alamos National Lab, May, 1990. (invited fast thermolysis lecture)
8. AFOSR/ONR Rocket Propulsion Meeting, June, 1990.
9. French-US Information Exchange on CL-20, China Lake, CA, June, 1990. (invited lecture on decomposition of CL-20)
10. Gordon Conference on "Chemistry of Energetic Materials", June, 1990. (chaired conference)
11. International Combustion Symposium, Orleans, France, July, 1990. (poster on SMATCH/FTIR)
12. Federation of Analytical Chemistry and Spectroscopy Societies Meeting, Cleveland, OH, October, 1990. (SMACH/FTIR lecture)
13. Zhongshan University, Guangzhou, Peoples Republic of China, November, 1990 (3 invited lectures on energetic materials).
14. Third Research Center, Japan Defense Agency, Tokyo Japan, November, 1990 (2 invited lectures on energetic materials).
15. Space Research Center, University of Arizona, December, 1990. (seminar on the burning surface)
16. State University of New York, Bringhamton, NY, December, 1990. (invited seminar on fast thermolysis)

17. Los Alamos National Laboratory, Los Alamos, NM, January, 1991. (invited lecture on energetic materials)
18. Pittsburgh Conference, Chicago, IL, March, 1991. (invited lecture on fast thermolysis techniques)
19. Naval Research Laboratory, Washington, DC, April, 1991. (invited lecture on energetic materials).
20. JANNAF CL-20 Symposium, China Lake, CA, May, 1991. (lecture on CL-20)
21. France-US Information Exchange, Paris, France, June, 1991. (two invited lectures on energetic materials)
22. AFOSR Contractor's Meeting, Boulder, CO, June, 1991.
23. 22nd International Conference of the ICT, Karlsruhe, Germany, July, 1991. (lecture on HMX)
24. Workshop on Propellant Flame Structure, University of Delaware, August, 1991. (organized workshop around O. Korobeinichev's visit)
25. T. B. Brill and P. J. Brush, "T-Jump/FTIR Spectroscopy as a Reaction Mechanism Tool," 18th FACSS/PAS Meeting, Anaheim, CA, October, 1991 (also chaired session).
26. T. B. Brill, "Condensed Phase Chemistry of Explosives and Propellants at High Temperature," Royal Society Discussion Meeting, London, England, November, 1991 (invited).
27. T. B. Brill, "Combustion/Explosion Chemistry of Bulk Materials," Workshop on Combustion and Explosion Phenomena of Energetic Materials, Los Alamos National Lab., March, 1992 (invited plenary lecture).
28. T. B. Brill and D. G. Patil, "Burning Surface Chemistry of Ammonium Dinitramide," Workshop on Combustion and Explosion Phenomena of Energetic Materials, Los Alamos National Laboratory, March, 1992 (poster).
29. T. B. Brill, "Chemistry of the Burning Surface: Possibilities for Analyzing Unsteady Processes," Propellant Flame Combustion Instability Modelling ONR Workshop, Naval Weapons Center, China Lake, CA, June, 1992 (invited).
30. T. B. Brill, "Chemistry of the Burning Surface: Possibilities for Analyzing Unsteady Processes," AFOSR Contractors' Meeting, La Jolla, CA, June 1992.
31. T. B. Brill, "Determination of the Dominant Heat Release Reactions at the Surface of Explosives and Propellants,"

Gordon Research Conference on Chemistry of Energetic Materials, New Hampton School, NH, June, 1992 (invited).

32. T. B. Brill, P. J. Brush, D. G. Patil, J. K. Chen, "Chemical Pathways at a Burning Surface" 24th Symp. (Int.) Combustion, Sydney, Australia, July, 1992.
33. T. B. Brill, "Surface Reactions of Energetic Materials at High Temperature," 1992 Fall Meeting of the Materials Research Society, Boston, MA, Dec., 1992 (invited).
34. Phillips Lab, Edwards AFB--Berge Goshgarian. Decomposition mechanisms of ADN, GAP, CL-20 and other nitramines, 1992.
35. Nellis AFB, NV--Conrad Dziejewski. Gas products from explosions to get environmental permits, 1992.
36. Dr. David Lee, Clark County Health District, NV. Information on explosion products for permits to Nellis AFB, 1992.
37. Hercules Research Center--Dr. Don Pivonka. Methods of fast thermolysis, 1992.
38. Thiokol Corporation--Dr. Bob Wardle. Thermal Decomposition data on CL-20, ADN, and AN, 1992.
39. Thiokol Corp., Elkton, MD--Dr. Steve Palopoli. Burn rate modifier mechanisms, 1992.
40. Idaho National Engineering Laboratory--Dr. John Davies. Decomposition products of Nitramines, TNT and PETN, 1992.
41. Naval Surface Warfare Center--Dr. Tom Russell. Decomposition of ADN, 1992.
42. NWC--Dr. May Chan. Decomposition mechanisms of NTO, CL-20, ADN, HMX, RDX, 1992.
43. National Defence Research Establishment, Sweden--Roland Sanden. Decomposition mechanisms of HTPB, NC, GAP, 1992.
44. ONERA, Fort Palaiseau, France--Drs. G. Lengelle, J. Duterrque, J. Trubert. Decomposition data on GAP, HMX, RDX, 1992 AGARD Lecturer.
45. SNPE, Le Bourdichet, France--Dr. Mark Piteau. Decomposition of nitramines, 1992.
46. T. B. Brill, "FTIR Studies of Surface Pyrolysis Phenomena and Flame Structure," Scheveningen, Holland, May, 1993 (invited plenary lecture).

47. T. B. Brill, "Chemistry of the Burning Surface," AFOSR Contractors Meeting on Propulsion, Atlantic City, NJ, June, 1993.
48. T. B. Brill, "Chemistry of a Burning Propellant Surface," Workshop on Combustion Efficiency and Air Quality, Hungarian Academy of Sciences, Budapest, Hungary, September, 1993 (invited).
49. T. B. Brill, "Spectroscopic Studies of Heterophase Reactions in Energetic Materials," Optical Society of America, National Meeting, Toronto, Canada, Oct., 1993 (invited).
50. T. B. Brill, "Chemistry of the Heterophase Surface Reaction Zone of Burning Nitramine Monopropellants," First Pacific International Conference on Aerospace Science and Technology, Tainan, Taiwan, December, 1993.
51. Chung Shan Institute of Science and Technology, Taipei, Taiwan, Dec., 1993 (invited lecture).

B. Inventions: None

from: 22<sup>nd</sup> International Conference of the ICT, Karlsruhe  
Germany, July, 1991.

12 - 1

**TEMPERATURE DEPENDENCE OF THE RAPID THERMAL DECOMPOSITION OF  
NITRAMINES**

Thomas B. Brill and Peter D. Brush

Department of Chemistry, University of Delaware, Newark,  
Delaware, 19716, USA

**ABSTRACT**

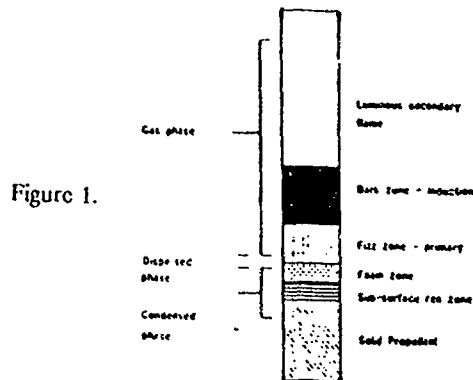
The T-Jump/FTIR spectroscopy technique will be described and the results for RDX presented. This device enables a thin film of sample to be heated at 2000°C/sec and held isothermally at a preselected temperature while the rapid decomposition process is studied. In this way, a controlled study is possible of energetic materials at temperatures far above the slow decomposition range. For example, the identity and relative concentration of the near surface gas products can be determined at temperatures characteristic of the burning surface. There is evidence that autocatalysis exists at high temperatures for RDX and that the formation of  $H_2O$  and  $NO_2$  are not directly coupled to the reactions that produce  $CH_2O$  and  $HCN$ . The temperature dependence of the  $H_2O/NO_2$  branching ratio of the nitramine group was determined.



### Introduction

The ultimate goal of modeling of combustion and combustion stability of rocket propellants requires, among other inputs, a chemical and physical description of the condensed phase/gas phase interface at the microscale level. Such detail has not been forthcoming from direct measurements during combustion. This is because the surface is transient, heterogeneous, non-equilibrium and is obscured by the flame. Therefore, it is necessary to design experiments that simulate the condensed phase and surface during combustion, but release the gases into a cool unreactive atmosphere where they quench and can be detected immediately.

Figure 1 is a diagram describing the interface zone of a typical propellant. Our objective is to experimentally simulate the foam and disperse regions where the condensed phase transits to the gas phase. The gases that are



formed in these zones feed the luminous flame and thus are responsible for the major features of propulsion. Hence, our research connects the formulation of a propellant or explosive to its combustion characteristics through the study of the basic chemical processes.

The challenge is how to simulate the conditions that are

present on the burning surface and to characterize the most important processes at the microscale level. The burning surface can be imagined to be a film of material 5-50 $\mu$ m thick in which a phase change occurs driven by chemical reactions and heat transfer. In effect, it is a "thin-film" reaction zone that regresses through the condensed phase on one side leaving gas products behind on the other side. Therefore, an instantaneous simulation of this reaction zone requires that the sample be a thin film, that the heating rate lie in the 1000-2000°C/sec range and that the pressure be atmospheric or higher. The choice of this heating rate of is based on work of Sakamoto and Kubota [1] with thermocouples imbedded in HMX propellants in which dT/dt in the condensed phase (foam) reaction zone appears to be 1000 $\pm$ 500°C/sec.

Both kinetics and mechanism information is needed at high heating rates and high temperature. However, no single technique appears to be able to provide a comprehensive picture at this time. For this reason, our approach has focused on the development of two new fast thermolysis methods: T-Jump Spectroscopy and Simultaneous Mass and Temperature Change/FTIR Spectroscopy (SMATCH/FTIR) [2,3]. Measurement of both high rate kinetics and the gas products released is important because these gas products feed the dark zone of the combustion region.

This paper will present one of two techniques, that of T-Jump/FTIR Spectroscopy, along with data on the fast decomposition process of HMX.

#### T-Jump FTIR Spectroscopy of HMX

The T-Jump/FTIR method is designed to permit heating of a sample at a high rate to a preselected final temperature. In this way, we minimize interfering chemical processes that are operative in decomposition studies at slow heating rates and that result from "cooking". A picture of the energetic material much closer to combustion is obtained. A heating rate of 2000°C/sec was chosen because it is the highest

heating rate that can be achieved with the device without overshooting the final filament temperature,  $T_f$ .

The experimental design is shown in Figure 2 in block form. The cell is an Al cylinder bored out so that an IR beam can pass through the long axis. ZnSe windows enclose the

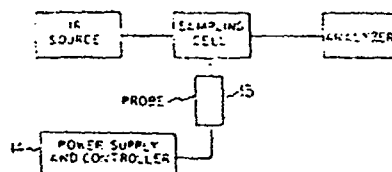
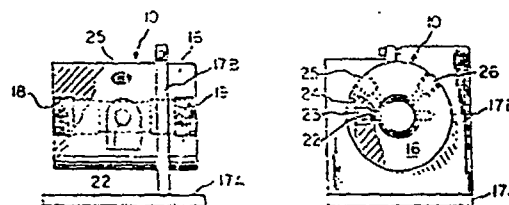


Figure 2.



cavity. The cell can be pressurized or evacuated as desired in the 1-1000 psi range. Ar is usually used as the atmosphere. The Pt ribbon filament that supports the thin film of sample is inserted from the side. A Nicolet 20SX FTIR spectrometer is used for the collection of rapid scan spectra of the gas products 2mm above the surface. A scan rate of ten scans per second is employed.

The heating experiment is built around a CDS Instruments 1000 controller. This device is able to heat the thin Pt ribbon filament under the conditions described above. It senses temperature by measuring the resistance of the filament as in a Pt resistance thermometer. The controller was modified in our laboratory so as to be able to record the very fast response control voltage that maintains a linear increase in the Pt resistance during the heating phase and a constant resistance during the hold phase. This control voltage was

amplified and channeled through an AD converter and recorded on an IBM-PC.

A powdered sample of about  $200\mu\text{g}$  is thinly spread or cast as a film on the filament. The circuit is fired simultaneously with the spectral trigger of the IR spectrometer. The added heat capacity of the filament with sample present or an endothermic event of the sample, such as melting, requires an increase (positive deflection) in the control voltage to maintain the desired filament resistance. An exothermic event is met with a decrease in the control voltage. Hence, endothermic and exothermic events of the sample can be tracked very sensitively and rapidly by the circuitry. Shown in Figure 3 is the control voltage trace of the bare filament superimposed on the trace when  $200\mu\text{g}$  of HMX are spread on the

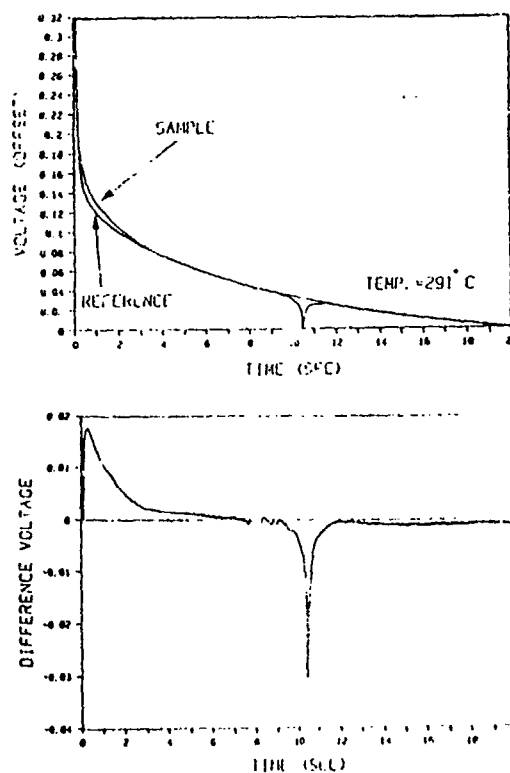
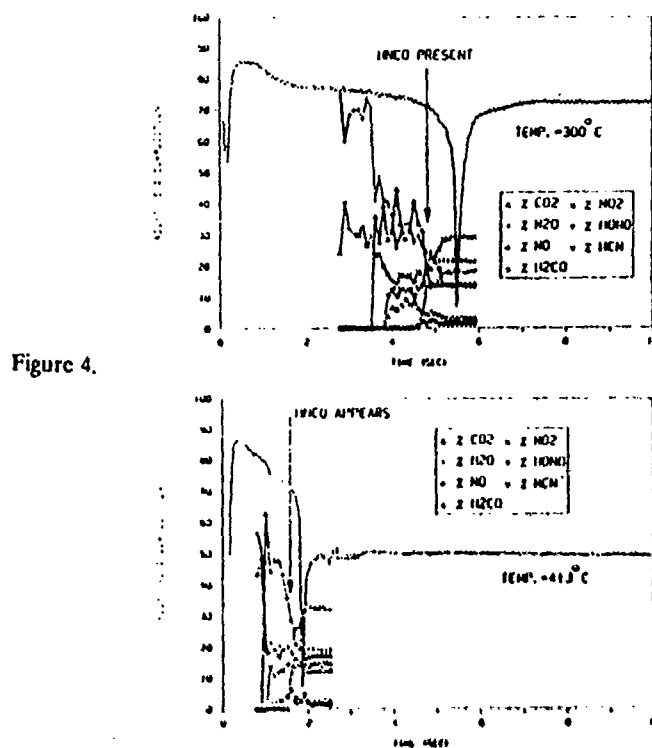


Figure 3.

filament. There is an initial endothermic departure (melting and heat capacity effects) followed by an exotherm. These events are seen more clearly in the difference trace (sample trace minus reference trace also shown in Figure 3).

Simultaneously, the gas products are measured in near-real time (maximum time delay is 0.1 sec) by the use of rapid-scan FTIR spectroscopy. Shown in Figure 4 are the results for HMX at two different values of  $T_f$ . The exotherm of HMX occurs at a different time because of the different filament temperatures. However, the time of appearance of the gas products and their relative concentration ratios gives new insight into the mechanism of decomposition.



The fact that gas products are detected in advance of the exotherm is strong evidence that autocatalysis is operative in HMX even at high temperature. The fact that  $\text{NO}_2$  and  $\text{N}_2\text{O}$  appear in advance of the fuels ( $\text{CH}_2\text{O}$  and  $\text{HCN}$ ) indicates that these fuel and oxidizer-producing reactions are not coupled. That is,  $\text{NO}_2$  and  $\text{HCN}$  are not produced in the same elementary reaction and  $\text{N}_2\text{O}$  and  $\text{CH}_2\text{O}$  are not produced in the same elementary reaction. Instead,  $\text{N}_2\text{O}$  and  $\text{NO}_2$  are released and  $\text{CH}_2\text{O}$  and  $\text{HCN}$  are then produced in later stage degradation of the residue. The fact that the gas product concentrations are not changing through the exotherm implies that the mechanism of decomposition before the exotherm and during the exotherm is essentially the same. More of the HMX is simply decomposing. Perhaps most useful is the new data available from this experiment on the gas product ratios as a function of temperature. The  $\text{N}_2\text{O}/\text{NO}_2$  ratio reflects the ratio of

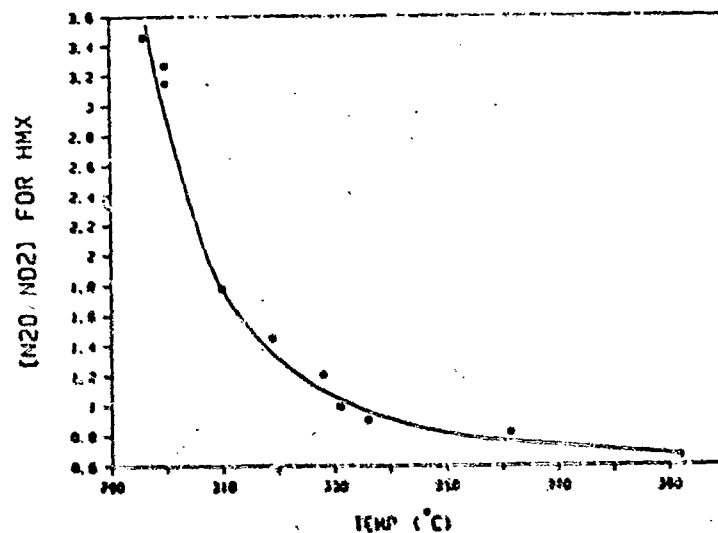
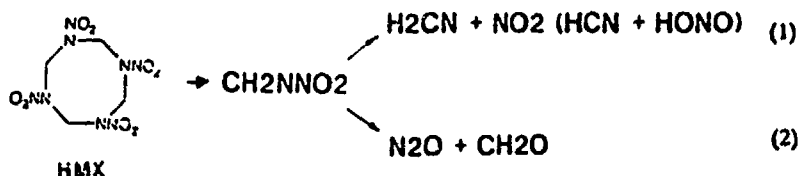


Figure 5.

rate constants for the two global decomposition paths of HMX, reactions (1) and (2).



At lower temperature reaction (1) dominates, while at higher temperature reaction (2) dominates. The rate constants are about equal at about 330°C. Temperatures in the range of 350°C are believed to exist on the surface of burning HMX propellants. Thus, the plot of  $\text{N}_2\text{O}/\text{NO}_2$  shown above gives the ratio of the rate constants that should be applied in models of the gas phase during the combustion of HMX and at different temperatures. This is highly valuable and heretofore unavailable data.

If completed in time of the conference, T-Jump FTIR studies of RDX and perhaps several other nitramines may be presented.

#### Acknowledgments

We are grateful to the Air Force Office of Scientific Research, Aerospace Sciences, for support of this work.

#### References

1. M. Kubota and S. Sakamoto, Prop. Explos. Pyrotech., 14, 6 (1989).
2. M.D. Timken, J.K. Chen and T.B. Brill, Appl. Spectroscopy, 44, 701 (1990).
3. J.K. Chen and T.B. Brill, Combust. Flame, in press.

## Thermal Decomposition of Energetic Materials 54. Kinetics and Near-Surface Products of Azide Polymers AMMO, BAMO, and GAP in Simulated Combustion

J. K. CHEN and T. B. BRILL\*

*Department of Chemistry, University of Delaware, Newark, DE 19716*

Kinetics of weight-loss during programmed heating at 150°C/s were determined by simultaneous mass and temperature change (SMATCH)/FTIR spectroscopy of the polymers 3-azidomethyl-3-methyloxetane (AMMO), 3,3'-bis(azidomethyl)oxetane (BAMO), and glycidyl azide polymer (GAP). The kinetics match the burn rate of GAP extrapolated to the same pressure and temperature range, which suggests that SMATCH/FTIR gives an instantaneous microscale simulation of macroscale combustion at those pressure and temperature conditions. SMATCH/FTIR spectroscopy enables the gases that leave the surface and form the earliest stage of the flame zone to be identified. Small molecules are formed by BAMO and GAP, but some large fragments are evolved by AMMO. Kinetic constants were determined for AMMO, BAMO, and GAP by isothermal and nonisothermal thermogravimetric analysis (TGA). Comparing these data to SMATCH/FTIR kinetics reveals that the accelerating rate of change of mass with time ( $da/dt$ ) at small  $\alpha$  controls the temperature dependence of the TGA rate constant, while the total mass present at a particular time ( $1 - \alpha$ ) controls the SMATCH/FTIR kinetics. Irrespective of chemistry differences at low and high heating rates, TGA kinetics would be expected to fail to predict the combustion behavior because the specific reaction rates in the lower and higher temperature ranges fail to connect by factor of several thousand.

### INTRODUCTION

Considerable progress is possible if microscale laboratory experiments on the thermal decomposition of materials can be designed to simulate macroscale combustion behavior, such as the burn rate. The simulation experiment might help establish some of the chemical processes at and near the surface that are impossible to study during actual combustion. Such a microscale simulation was our goal in developing simultaneous mass and temperature change (SMATCH)/FTIR spectroscopy [1, 2]. By using SMATCH/FTIR spectroscopy the dynamic mass and temperature changes of a 20-70- $\mu$ m-thick film are measured in real time at a fast heating rate while the near surface gas products are analyzed with the rapid-scan FTIR spectrum. Heating rates in the 100°-200°C/s range are employed.

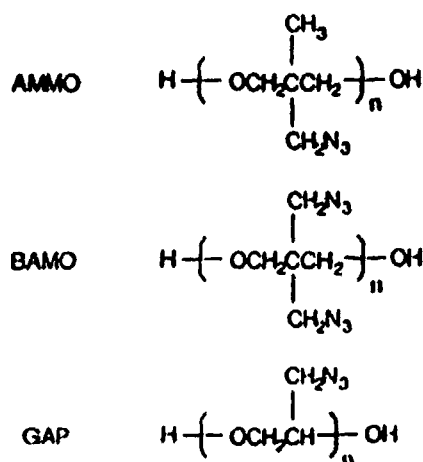
The kinetics of rapid weight loss are found to predict the burn rate of the material in the same pressure and temperature range [2]. Hence, the

thin film of rapidly decomposing material in the SMATCH/FTIR technique apparently simulates the heterogeneous surface reaction zone of a material burning at steady state. The gases evolved initiate the earliest stage of the flame during combustion, but have not been identifiable during combustion because they are rapidly consumed very close to the surface. By evolving the gases into a cool, nonreacting atmosphere of Ar, these species are quenched and quickly identified and quantified by the use of rapid-scan FTIR spectroscopy. The gas products are similar to those measured in our previous fast thermolysis/FTIR studies [3], which gives confidence in the fast thermolysis/FTIR technique as also being able to reveal many of the species that feed the early flame zone.

The SMATCH/FTIR concept was applied in this article to determine the kinetic constants and gas products at the condensed-phase/gas-phase interface during a combustion simulation of azide-containing polymers. The compounds studied were poly (azidomethylmethyl oxetane), AMMO; poly[bis(azidomethyl)oxetane], BAMO; and glycidyl azide polymer, GAP.

\* Corresponding author.





These polymers have potential as energetic binders and plasticizers in gun and rocket propellants, where a relatively low flame temperature and high mass impetus are sought [4, 5].

In addition to the decomposition kinetics at fast heating rates, AMMO, BAMO, and GAP were analyzed at slow heating rates. These data enable the relationship of kinetics expressions at slow and fast heating rates to be better understood. As a result, this project was able to connect the kinetics of fast thermal decomposition to the burn rate and to reveal some of the species in the surface reaction zone. It also showed that the factors controlling the thermal decomposition rates measured at slow rates are different from those at high rate heating and combustion conditions.

## EXPERIMENTAL

Samples of AMMO monomer (bp = 165°C) and BAMO polymer were supplied by G. E. Manser, Aerojet, Sacramento, CA. AMMO polymer was synthesized by Oyumi [6] by stirring AMMO monomer with  $\text{BF}_3 \cdot \text{Et}_2\text{O}$  in anhydrous MeOH for 24 h. A polymer of MW = 8000–10000 formed. GAP (MW = 2000–5000) was provided by D. O. Woolery, Rocketdyne, Canoga Park, CA.

The SMATCH/FTIR technique has been described elsewhere [1, 2]. The technique employs a cantilevered quartz tube whose vibrational frequency depends on the sample mass. Typically, 0.2–0.8 mg of sample (a film of 16–64  $\mu\text{m}$  thickness) was painted onto a metal tip attached to the tube. The metal end-tip was heated by RF

induction at a chosen rate in the 100°–200°C/s range. The sample atmosphere was 1 atm of Ar. The heating rate and film thickness are matched so that the heat transfer is fast enough to give a reasonably uniform temperature throughout the film [2]. The dynamic weight change of the sample was measured by the change in the vibrational frequency of the tube. Data were recorded at 160 Hz, which provides enough points on the weight-loss curve to be confident of fitting the shape. The temperature was measured by a type E thermocouple spot-welded to the metal end-tip and in contact with the sample film. Infrared spectra of the decomposition gases were measured about 3 mm above the metal end-tip by using a Nicolet 60SX FTIR spectrometer operating in the rapid-scan mode (10 scans/s, 4  $\text{cm}^{-1}$  resolution). The IR spectra were converted to the relative percent composition scale by integrating the absorption bands and converting them to a relative concentration scale by their absolute intensities [7]. IR-inactive species, such as  $\text{N}_2$  and  $\text{H}_2$ , are not detected and, therefore, are not included in the quantitation procedure. The gas evolution rate from these polymers was rather high, resulting in loss of resonance of the quartz tube in many cases. The film of polymer needed to be very uniform in thickness for best results. Still, the decomposition of BAMO was too exothermic to maintain resonance. For this reason, only AMMO and GAP were characterized by SMATCH/FTIR. However, the off-gassing process of GAP and, to some extent, AMMO was sufficiently vigorous that SMATCH/FTIR could be applied only to small sample sizes. Consequently, various electronic interferences intruded on the weight-loss curves.

The temperature profiling/FTIR spectroscopy technique has been described elsewhere [8]. About 2 mg of neat sample was placed on the nichrome ribbon filament. The cell was purged with argon and pressurized as desired. The infrared beam was focused several millimeters above the sample. With the spectrometer scanning at 10 scans/s and accumulating two spectra per file at 4  $\text{cm}^{-1}$  resolution, current was applied to the filament. During the initial 3–4 s, ramp heating occurred. After that time the final temperature was reached and remained constant for the remaining 10 s of data acquisition. As in SMATCH/FTIR, the spectra of the gas products were converted to the

relative percent composition, and IR-inactive species were not included.

Isothermal and dynamic thermogravimetry (TGA) were carried out on a DuPont Instruments 2000 thermal analyzer with a 951 thermogravimetric module. Dynamic thermogravimetry studies were run at a linear heating rate of 1°C/min. Between 1.5 and 2.5 mg of sample was used and a flow rate of 20 ml/min of Ar existed in all cases. The DuPont model 910 differential scanning calorimeter (DSC) was used to determine the enthalpy change of 2.5–3.5 mg of sample heated at a linear rate of 1°C/min under an Ar flow of 20 ml/min.

### KINETICS OF DECOMPOSITION

The kinetic constants of thermal decomposition of bulk samples of energetic materials are sensitive to a myriad of experimental and physical variables. Important experimentally controlled variables include the heating rate, sample temperature, and pressure. For example, low temperature and slow heating rate data on solids pertain to slow cook-off stability. Without empirical scaling [9], these data cannot be applied to the combustion regime where a high temperature and heating rate exist. We now have methods to measure kinetics at both low and high heating rates, which enables the relationship of the kinetics of slow and fast weight loss to be better understood.

#### Kinetics at 1°C/Min

The nonisothermal kinetics method is subject to criticism [10]. For this reason, the rate of gradual weight loss was compared under isothermal and nonisothermal conditions by TGA during the initial 20%–40% of weight loss where decomposition of the azide group dominates. The rate constants,  $k$ , for isothermal decomposition were

calculated from Eq. 1 and are given in Table 1. Approximate first-order kinetics is followed. The fractional weight  $\alpha$  is defined as  $(W_0 - W_t)/W_0$ , as is frequently done in TGA measurements [11].  $W_0$  is the initial sample weight and  $W_t$  is the weight at time,  $t$ . Figure 1 shows the Arrhenius plots and Table 2 gives the resulting activation energy  $E_a$ .

$$-\ln(1 - \alpha) = kt + c \quad (1)$$

and preexponential  $A$  values.

The kinetics were determined under non-isothermal conditions (TGA,  $dT/dt = 1^\circ\text{C}/\text{min}$ ) by the use of Eqs. 2 and 3 [12, 13].

$$\frac{d\alpha}{dt} = k(T)(1 - \alpha)^n, \quad (2)$$

where  $k(T) = Ae^{-E_a/RT}$ . Equation 2 can be simplified by the use of a linear heating rate  $dT/dt = \beta$  and integrated to yield Eq. 3 when  $n = 1$  [14]:

$$\ln \left[ \frac{-\ln(1 - \alpha)}{T^2} \right] = \ln \left[ \frac{AR}{\beta E_a} \left( 1 - 2 \left( \frac{RT}{E_a} \right) \right) \right] - \frac{E_a}{RT}. \quad (3)$$

Figure 2 shows the Arrhenius plots and Table 2 contains the Arrhenius constants. As can be seen, approximate first-order kinetics is followed. However, we caution that this fact tells little about the mechanism.

The Arrhenius constants in Table 2 are essentially the same within experimental error for both the isothermal and nonisothermal kinetics methods, which lends confidence in the use of non-isothermal methods for these azide polymers. The activation energies in Table 2 are in the range of those measured from the change of intensity of

TABLE I

Isothermal TGA Rate Constants ( $\text{s}^{-1}$ ) for Azide Polymers

Polymer	180°C ( $\times 10^5$ )	185°C ( $\times 10^5$ )	190°C ( $\times 10^5$ )	195°C ( $\times 10^5$ )	200°C ( $\times 10^5$ )	205°C ( $\times 10^5$ )	210°C ( $\times 10^5$ )
ANMO		4.83	8.21	13.00	19.27	31.36	50.50
BAMO		12.76	24.13	38.65	60.88	93.67	138.10
GAP	12.96	22.68	35.18	54.50	82.45	123.10	

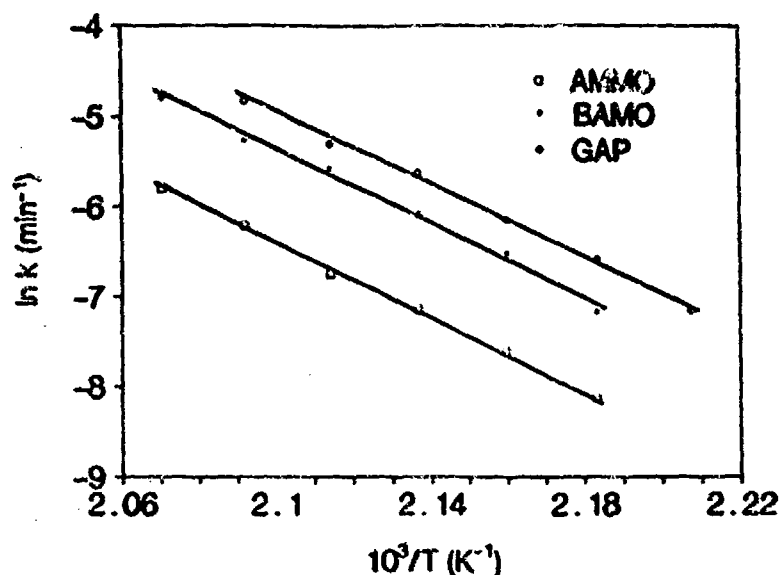


Fig. 1. Arrhenius plots for azideethyl polymers measured by the isothermal TGA method.

the  $N_2$  peak in the mass spectrum of these compounds [15] and by DSC [16] and DTA [17].

#### Kinetics at 150°C/s

Considerable care was taken with the SMATCH/FTIR experiments to employ a film thin enough to optimize temperature uniformity during the heating phase. A 20–60- $\mu$ m-thick film enables a heating rate of about 150°C/s to be achieved with a temperature gradient of <5°C across the film. This amount of material is sufficient to obtain the required mass change and spectral data. Rapid weight-loss kinetics were measured by SMATCH/FTIR for AMMO and GAP, but could not be determined for BAMO

because the heat release was so violent that the vibrating tube failed to maintain resonance. Figures 3 and 4 show the composite plots of the SMATCH/FTIR data for AMMO and GAP, respectively. The initial 80% of the weight-loss curve was fit to the polynomial Eq. 4 by using the coefficients given in Table 3. The harmonic noise in Figs. 3 and 4 is electrical interference and does not strongly affect the goodness of fit of the polynomial because the number of experimental data points in the weight-loss step (15–20) is sufficiently large to give a good representation with Eq. 4. The weight-loss curve was expanded in time so that the best fit could be obtained.

$$1 - \alpha = \sum_{i=0}^3 a_i t^i \quad (4)$$

TABLE 3  
TGA Kinetics Parameters for Azide Polymers<sup>a</sup>

Polymer	Isothermal TGA			Nonisothermal TGA <sup>b</sup>		
	$E_a$ (kcal/mol)	$\log A$ (s <sup>-1</sup> )	$T$ (°C)	$E_a$ (kcal/mol)	$\log A$ (s <sup>-1</sup> )	$T$ (°C)
AMMO	40.9 ± 0.8	14.2 ± 0.4	185–210	40.2 ± 0.5	13.6 ± 0.3	180–230
BAMO	40.8 ± 1.9	14.6 ± 0.9	185–210	39.9 ± 0.4	14.0 ± 0.2	180–224
GAP	39.4 ± 1.1	14.1 ± 0.5	180–205	39.4 ± 0.3	13.8 ± 0.2	180–220

<sup>a</sup> Errors are based on the standard deviation of the actual data points and the least square fit.

<sup>b</sup> Heating rate was 1°C/min under Ar at flow rate of 20 ml/min.

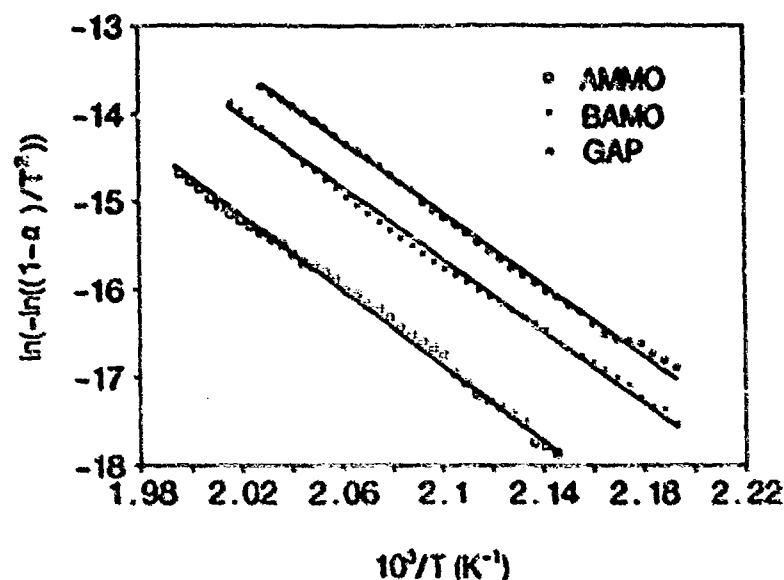


Fig. 2. Arrhenius plots measured by nonisothermal TGA methods for azidoazide polymers.

The derivative of Eq. 4 gives  $da/dt$ . In this way, Eq. 2 can be solved by the derivative method to yield Eq. 5 and obtain  $E_a$  and  $\log A$  after finding the value of  $n$  that linearizes the equation.

$$\log \left[ \frac{da}{dt} \frac{1}{(1-a)^n} \right] = \log A - \frac{E_a}{2.303RT} \quad (5)$$

As shown in Fig. 5,  $n = 2$  is appropriate. The temperature corresponding to each  $1 - a$  data point is taken from the digitized thermocouple data. Despite considerable effort to locate the best position to place the thermocouple to minimize the temperature lag due to slow heat transfer, there is an inevitable small temperature lag. In this experiment this lag affects  $A$  more than  $E_a$ . Table 4 gives the solutions of Eq. 5 for AMMO and GAP along with the temperature ranges in which these data were extracted. The value of  $n = 2$  does not imply that high rate decomposition of these polymers is a second-order process. The value of  $n$  in Eq. 2 is simply a parameter chosen to give normal Arrhenius behavior.

#### Comparison of Kinetics at Low and High Heating Rates

The specific reaction rates in Tables 2 and 4 measured by nonisothermal TGA and SMATCH/FTIR in different temperature ranges miss linking one another by several orders of magnitude [18]. On this basis alone TGA kinetics could not be expected to explain combustion behavior. SMATCH/FTIR kinetics (vide infra) are able to match burn rate data, suggesting that they are closely related to what occurs during the ignition/combustion process.

The fact that we have experimentally determined the forms of Eq. 2 at low (TGA) and high (SMATCH/FTIR) heating rates enables the details of the effect of the heating rate on the weight-loss kinetics to be understood more clearly. Since Eq. 3 is a special case of Eq. 2, the two experiments can be compared with Eq. 5. The temperature dependence of the reaction rate expressed by Eq. 5 depends on the product of the rate of weight change ( $da/dt$ ) and the total

TABLE 3

Polynomial Curve Fitting Coefficients for Azide Polymers Along with the Temperature Range Used

Polymer	$a_0$	$a_1$	$a_2$	$a_3$	$T$ (°C)
GAP	322.63	-636.64	727.09	-211.66	240-268
AMMO	457.49	-796.76	664.39	-40.33	256-280

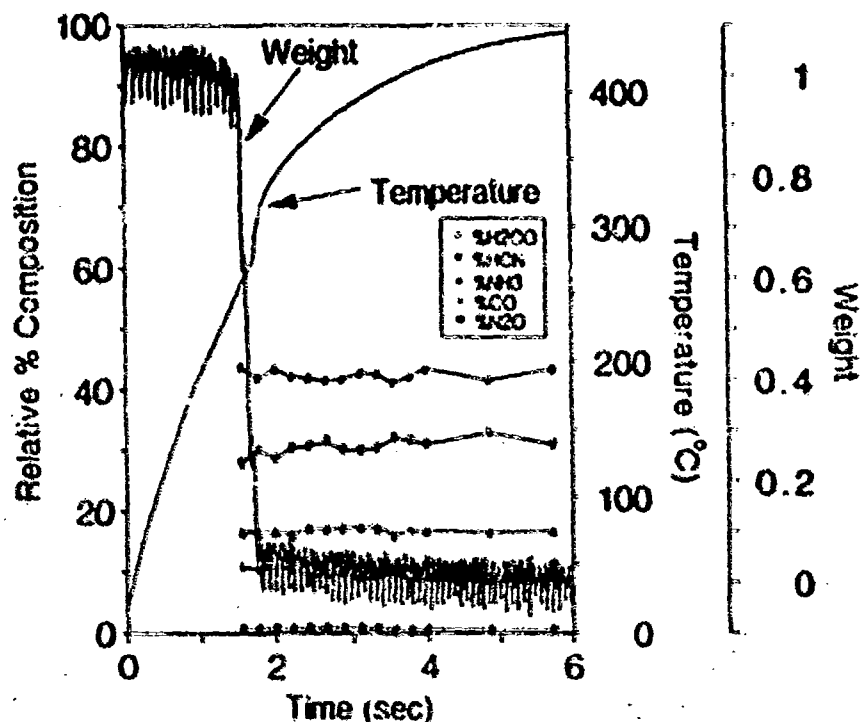


Fig. 3. SMATCH/FTIR results for AMMO showing the dynamic weight loss, temperature change, and the near-surface gas products that are IR active. The pressure was 1 atm. Ar, N<sub>2</sub>, and any H<sub>2</sub> were not detectable by IR spectroscopy.

weight of the sample  $(1 - \alpha)^n$  at any particular time. Figures 6 and 7 show how these two terms for AMMO depend on the temperature. In the slow heating rate TGA experiment, Fig. 6 reveals that  $da/dt$  is very sensitive to temperature because the weight change begins slowly and accelerates rapidly. In the fast heating rate SMATCH/FTIR experiment,  $da/dt$  remains relatively constant throughout the weight-loss process. Hence,  $da/dt$  strongly influences the temperature dependence of the reaction rate at low heating rates, but not at high heating rates. Figure 7 shows that the reverse is true of the  $(1 - \alpha)^n$  mass term. The mass changes slowly in the slow heating rate experiment and this has a minor effect on the rate constant, whereas at fast heating rates the  $(1 - \alpha)^n$  term is the overwhelming contributor to the temperature dependence of the rate constant. Consequently, the choice of  $n$  has a strong influence on the linearity of Eq. 5 at high heating rates. The TGA data are linearized with  $n = 1$ . If  $n = 1$  is used for the SMATCH/FTIR data, a negative value of  $E_a$  is produced in the lower temperature range. A value

of  $n = 2$  or higher is needed to linearize the SMATCH/FTIR data. In fact, we have found that  $n = 2$  is the smallest exponent that is able to linearize SMATCH/FTIR data for a wide range of compounds [2, 19]. Clearly, the value of  $n$  is merely a fitting parameter. Any relationship of  $n$  to a homogeneous molecular reaction order would be fortuitous.

#### Relationship of the SMATCH/FTIR Kinetics to the Burn Rate

The SMATCH/FTIR experiment attempts to mimic the temperature and heating rate conditions in the reaction zone of the condensed phase during combustion. If the simulation is accurate, the kinetic constants from SMATCH/FTIR should predict the burn rate of the material where the pressure and temperature are the same for both measurements. Burn rate data for GAP are available [17], which enables this analysis to be made.

Burn rates,  $\dot{r}$ , are expressible in Arrhenius-like form [20]. For straightforward use of the SMATCH/FTIR data to calculate a burn rate, we

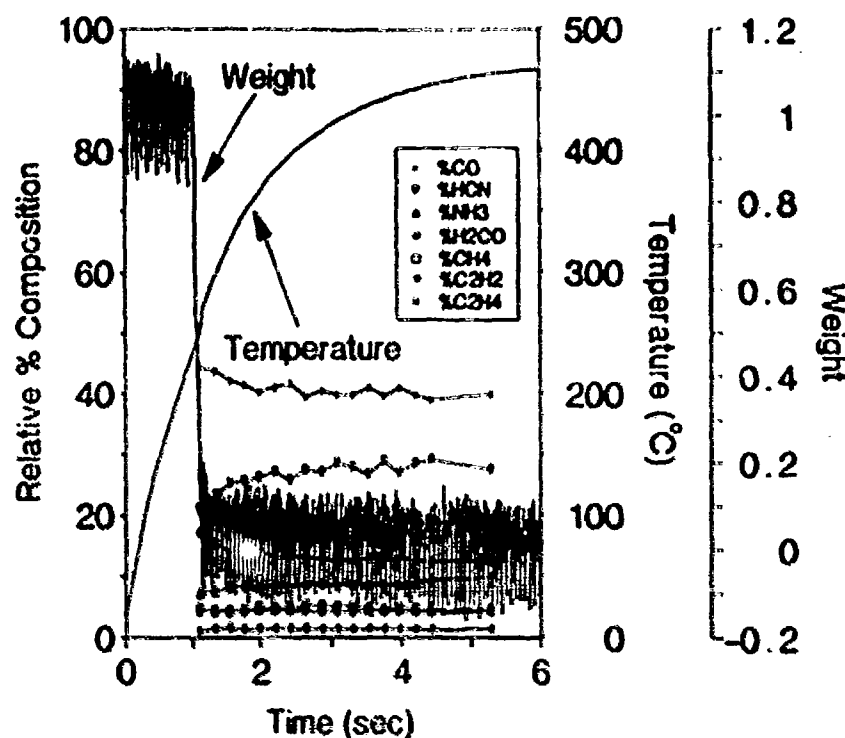


Fig. 4. SMATCH/FTIR data for GAP showing the weight and temperature change and the near-surface gas products.  $N_2$  and any  $H_2$  are not detected by IR spectroscopy. The pressure was 1 atm Ar.

have used an adaptation of this concept shown in Eq. 6, where  $h$  is the thickness of the film:

$$\dot{r}(\text{mm/s}) = Ake^{-E_a/RT} \quad (6)$$

This equation has validity if the film thickness is approximately the same as the reaction zone of the burning material at 1 atm. A 20-60- $\mu\text{m}$ -thick reaction zone is quite reasonable at this pressure. By using the Arrhenius constants in Table 4 for GAP, the experimental film thickness of 30  $\mu\text{m}$ , and  $T = 260^\circ\text{C}$  (Fig. 4), a value of  $\dot{r} = 1.35$  mm/s is calculated from the SMATCH/FTIR data at 1 atm. This regression rate compares quite well with the burn rate for GAP of  $\dot{r} = 1.7$  mm/s obtained by extrapolating the higher pressure data on temperature sensitivity plots of Kubota and Sonobe [17] to 1 atm. This is the same level of agreement as that for the burn rate calculated from SMATCH/FTIR data and measured for combustion of nitrocellulose samples [2]. Thus, the fact that the SMATCH/FTIR kinetics data can reasonably match burn rates measured in the same pressure and temperature range implies

that the film of sample in SMATCH/FTIR simulates the condensed-phase surface reaction region during combustion of the bulk material. The chemistry that is indicated by the gas products observed in SMATCH/FTIR spectroscopy is likely to be essentially the same as that occurring in the condensed phase during combustion.

Before describing the chemical information learned from SMATCH/FTIR, it needs to be emphasized that we do not propose to use the kinetic constants from SMATCH to predict the burn rates of materials outside of the pressure and temperature ranges where the SMATCH/FTIR data were measured. One reason is that  $n = 0$  in Eq. 5 for the burning of a propellant. This is because mass is constantly being replenished in the reaction zone by the propellant. In addition,  $d\alpha/dt$  is a constant for steady state combustion. The left side of Eq. 5 becomes the product of two constants. As a result, propellant burning behaves as a zero-order process. Instead, the purpose of the SMATCH/FTIR experiment is to simulate combustion in a criterion set of conditions where burn rates have been measured in order to give

TABLE 4

Kinetic Parameters of Azide Polymers for Thermal Decomposition at  $dT/dt = 150^\circ\text{C/s}$  by SMATCH/FTIR Spectroscopy

Polymer	$E_a$ (kcal mol <sup>-1</sup> ) <sup>a,b</sup>	log $A$ (s <sup>-1</sup> )	$T$ (°C)
GAP	42.3 ± 2.4	19.0 ± 0.9	242-260
AMMO	43.2 ± 2.8	18.9 ± 1.3	256-273

<sup>a</sup> Apparent reaction order  $n = 2$ .

<sup>b</sup> The average of two experiments.

insight into the species that form the earliest part of the flame zone. SMATCH/FTIR is not designed to predict burn rates over a wide range of pressures and temperatures.

### REACTION EVENTS

In both the kinetics data and the near-surface gas products, there is mechanistic information about the decomposition process of these polymers. According to the data in Table 1, the rate of decomposition is GAP > BAMO > AMMO. This trend follows the trend in the temperature of maximum heat release by DSC (Table 5). The correlation stems from the fact that the faster the decomposition rate, the faster heat is released, and, thus, the lower the temperature the heat release reaches its maximum point. Were these polymers not closely

related, this correlation might not exist.  $\Delta H$  of decomposition (the integral of the exotherm) would not be expected to, and does not, correlate with the reaction rate. Rather, Table 5 shows  $\Delta H$  follows the trend in the weight fraction of the azide group in the polymer, which indicates that the azide group controls the overall decomposition energy release.

The similarity of the activation energies in Table 2 to those of other alkylazides [21] suggests that the azide group largely controls the kinetics through reaction 7.



The nitrene intermediate, RN, is unstable and reacts further in ways that are analyzable by the gas products. Figures 3 and 4 show the quantifiable gas products from AMMO and GAP measured by SMATCH/FTIR.  $\text{N}_2$  is not shown because it is not IR active. It was gratifying to observe that the gas products sensed with the SMATCH/FTIR technique are very similar to those observed with our other fast thermolysis/FTIR methods [22]. Thus, the many previous studies of the relative concentrations of near-surface gas products of energetic materials [3] can be used to understand the thermolysis under combustion-like conditions. Since BAMO could not be studied by SMATCH/FTIR, the relative concentrations of the gas products were measured

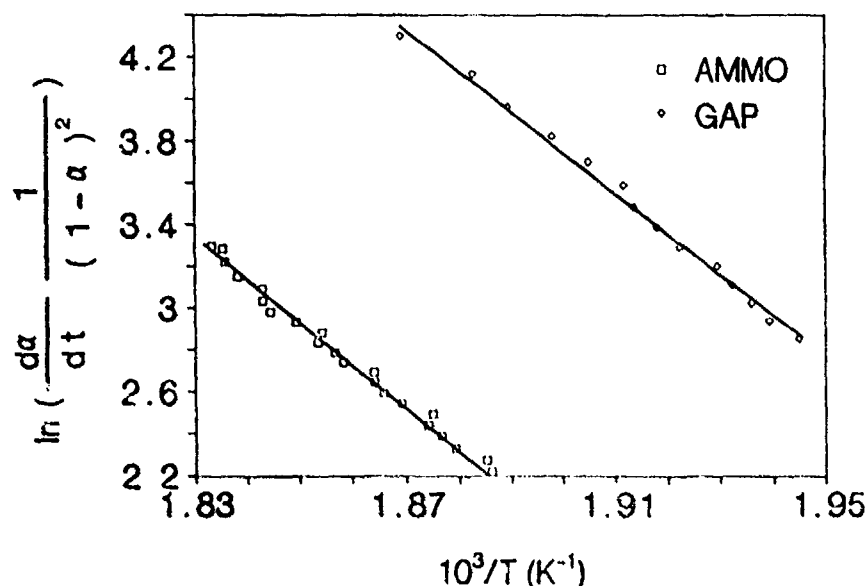


Fig. 5. Arrhenius plots for the kinetics of weight loss measured at about  $150^\circ\text{C/s}$  by SMATCH/FTIR spectroscopy of AMMO and GAP.

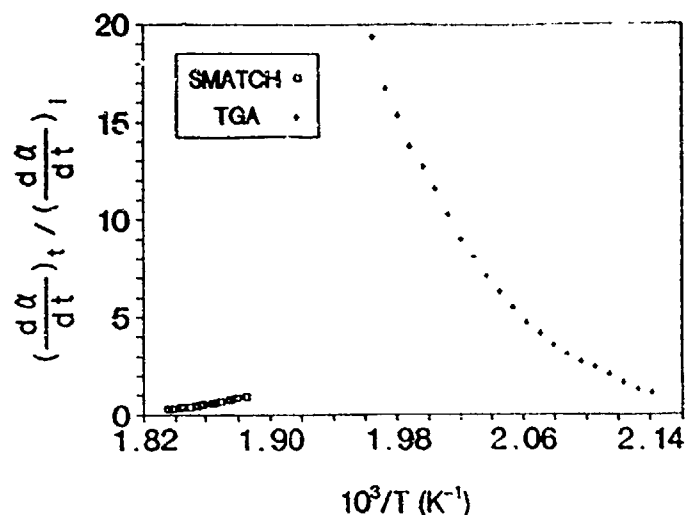


Fig. 6. The reduced value of  $d\alpha/dt$  measured by TGA and SMATCH/FTIR for AMMO.  $d\alpha/dt$  controls the temperature sensitivity of  $k$  at slow heating rates but has little effect at high heating rates. The data points shown are the actual experimental data points obtained by TGA and SMATCH/FTIR.

by the temperature profiling/FTIR method [8]. With this technique the dependence of the initial concentration of each gas on the static pressure of Ar in the cell can also be determined. These data are shown for AMMO, BAMO, and GAP in Figs. 8–10. Note that the data at 1 atm are very similar to those measured by SMATCH/FTIR (Figs. 3 and 4). Plots of this type shown in Figs. 8–10 were constructed previously [6], but differ mostly in the fact that a more accurate quantitation factor for HCN is now being used. There is very little pressure dependence in the product concentrations, indicating minimal heterogeneous gas-phase/condensed-phase redox chemistry for these polymers [23].

The higher energy polymers, BAMO and GAP,

produce small hydrocarbon fragments, along with CO and  $\text{CH}_2\text{O}$  from the backbone. These products form from reactions associated with the condensed phase as opposed to the gas phase [24]. Since the nitrene functional group in reaction 7 is formed in the methylene azide side chain, the formation of both HCN and  $\text{NH}_3$  indicates that the nitrene has two decomposition branches. Based on the higher relative concentration of HCN, the dominant branch involves C–C fission, while the lesser branch involves C–N fission and hydrogen migration to liberate  $\text{NH}_3$ .

AMMO has the lowest  $\Delta H$  of decomposition of the three azidopolymers. The lower energy of decomposition leads to a somewhat different fragmentation process.  $\text{CH}_2\text{O}$  dominates the quan-

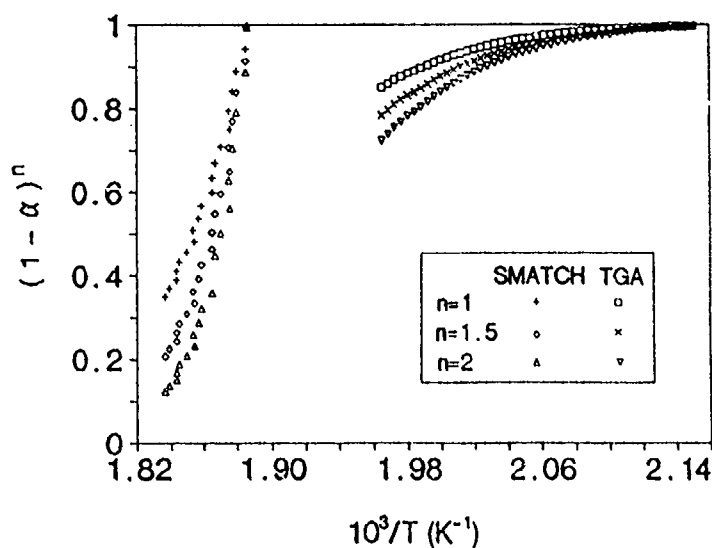


Fig. 7. The temperature sensitivity of  $k$  at high heating rates is mostly controlled by the total mass present at a particular time whereas the total mass changes slowly at a slow heating rate. Several values of  $n$  are shown to illustrate the effect of  $n$ .



TABLE 5

Thermochemical Data for Azide Polymers Measured by DSC

Polymer	$T_{max}$ (°C)	$\Delta H$ (J/g)	%N
AMMO	233	-1550	33
GAP	221	-2060	42
BAMO	224	-2670	50

tifiable products. The low-molecular-weight hydrocarbons found with BAMO and GAP are absent. In their place are one or more higher molecular weight products which can be identified, but not quantified. As shown in Figure 11, absorbances are present at 901, 1168, 1370, 1448,

1610, 1649, and 1708  $\text{cm}^{-1}$ , along with additional intensity at 1103  $\text{cm}^{-1}$  (some of which is from  $\text{CH}_2\text{O}$ ), and absorbances in the 2700-3000  $\text{cm}^{-1}$  range not associated with  $\text{CH}_2\text{O}$ . With the exception of the mode at 1610  $\text{cm}^{-1}$  all of these modes closely match those of bis(2-methylallyl)amine,  $[\text{H}_2\text{C} = \text{C}(\text{CH}_3)\text{CH}_2]_2\text{NH}$  [25]. The mode at 1610  $\text{cm}^{-1}$  could be the  $\text{N} = \text{N}$  stretch of the azo derivative of the 2-methylallyl group,  $[\text{H}_2\text{C} = \text{C}(\text{CH}_3)\text{CH}_2\text{N}]_2$ . These products are readily rationalized in the decomposition scheme. Following the decomposition of the azide group of AMMO, it can be seen that clipping the backbone at the dashed lines shown below pro-

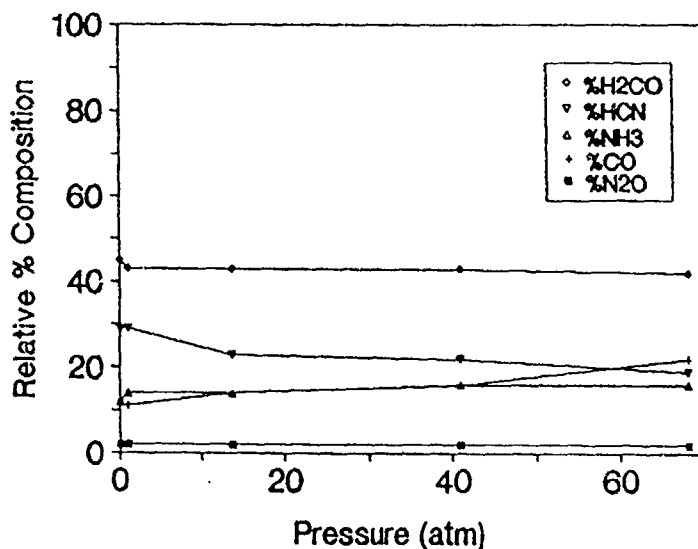


Fig. 8. The dependence of the initial concentrations of the quantifiable gas products of AMMO on the Ar pressure in the cell.

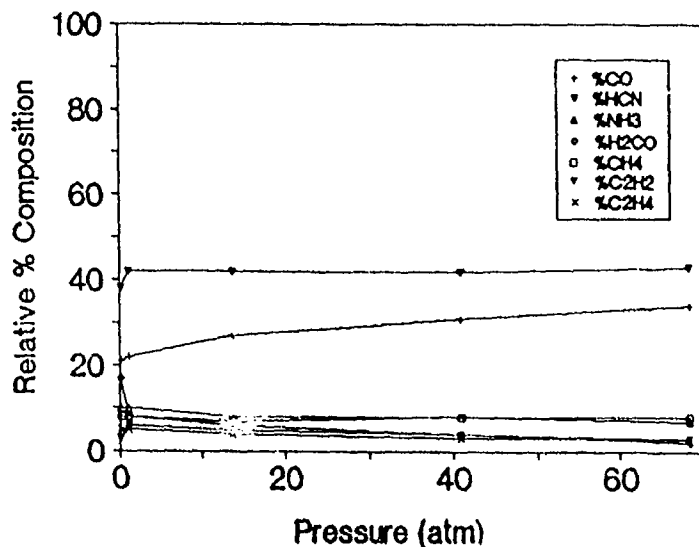


Fig. 9. The dependence of the initial concentrations of the quantifiable gas products of BAMO on the Ar pressure in the cell.

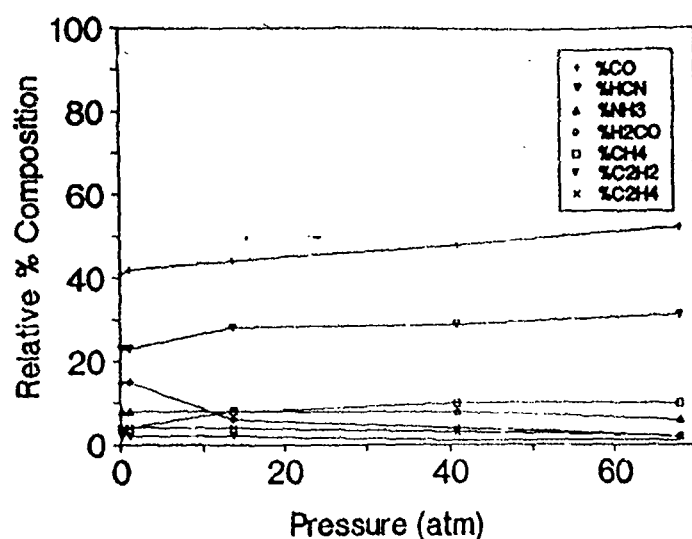
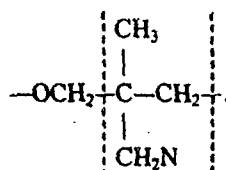


Fig. 10. The dependence of the initial concentrations of the quantifiable gas products of GAP on the Ar pressure in the cell.

duces  $\text{CH}_2\text{O}$  and the required 2-methylallyl derivative:



Recombination of the coordinately unsaturated N atoms would produce the azo compound, while

the secondary amine would form by recombination after an N atom is eliminated and H is scavenged. The fact that HCN,  $\text{NH}_3$ , and CO are significant products from AMMO shows that a portion of the backbone also degrades into smaller fragments and would provide a sink for N and a source of H atoms. The 2-methylallyl nitrene might not completely recombine to the amine or the azo derivative during the actual combustion of AMMO. The formation of these specific stable

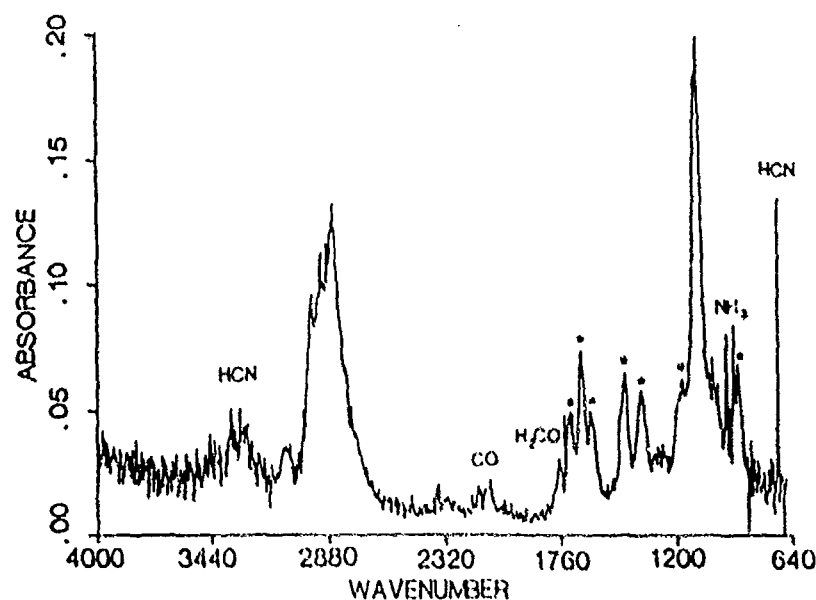


Fig. 11. The IR spectrum of the gas phase above AMMO heated at  $140^\circ\text{C/s}$  under 1 atm Ar. The spectrum was taken 2.2 s after the onset of heating. The starred absorbances are from the 2-methylallyl derivatives described in the text.

molecules may result from the fact that no flame is present. The important point is that the 2-methylallyl nitrene is implicated as a reactant in the combustion of AMMO.

The identification and partial quantitation of the gas products, along with  $N_2$  and, possibly,  $H_2$ , evolving from the condensed phase of these polymers under conditions that simulate combustion helps connect the chemistry of the condensed phase to the combustion behavior. These gas products are present in the earliest stage of the flame zone and are the reactants for the combustion process.

*We are grateful to the Air Force Office of Scientific Research, Aerospace Sciences, for support of this work on AFOSR-89-0521.*

#### REFERENCES

1. Timken, M. D., Chen, J. K., and Brill, T. B., *Appl. Spectrosc.* 44:701-706 (1990).
2. Chen, J. K., and Brill, T. B., *Combust. Flame*, 85:479-488 (1991).
3. Brill, T. B., in *Chemistry and Physics of Molecular Processes in Energetic Materials* (S. Bulusu, Ed.), Kluwer, Boston, 1990, p. 277.
4. Manser, G. E., Guimet, J., and Ross, D. L., *Proc. JANNAF Propulsion Mtg.*, CPIA Publ. 340, 1981, p. 29.
5. Flanagan, J. E., and Gray, J. C., *US Patent* 4, 288, 262, Sept. 8, 1981.
6. Oyumi, Y., and Brill, T. B., *Combust. Flame* 65:127-135 (1986).
7. Oyumi, Y., and Brill, T. B., *Combust. Flame* 62:213-224 (1985).
8. Cronin, J. T., and Brill, T. B., *Appl. Spectrosc.* 41:1147-1151 (1987).
9. Hart, R. W., and McClure, F. T., *J. Chem. Phys.* 30:1501-1514 (1959).
10. Arnold, M., Veress, G. E., Paulik, J., and Paulik, F., *Thermochim. Acta* 52:67-81 (1982).
11. Zsako, J., Kekedy, E., and Varhelyi, Cs., *Thermal Analysis Vol. II, Proc. Third ICTA, Davos, 1971*, pp. 487-499.
12. Sharp, J. H., and Wentworth, S. A., *Anal. Chem.* 41:2060-2062 (1969).
13. Carroll, B., and Manche, E. P., *Anal. Chem.* 42:1296-1297 (1970).
14. Coates, A. W., and Redfern, J. P., *Nature* 201:68-69 (1964).
15. Farber, M., Harris, S. P., and Srivastava, R. D., *Combust. Flame* 55:203-211 (1984).
16. Goshgarian, B. B., AFRPL-TR-82-040, Edwards AFB, CA, June, 1982.
17. Kubota, N., and Sonobe, T., *Prop. Explos. Pyrotech.* 13:172-176 (1988).
18. We thank a reviewer for pointing this out.
19. Chen, J. K., and Brill, T. B., *Combust. Flame*, in press.
20. Varney, A. M., and Strahle, W. C., *Combust. Flame* 16:1-8 (1971).
21. Gieseler, G., and Konig, W., *Z. Phys. Chem. (Leipzig)* 227:81-92 (1964).
22. Brill, T. B., in *Chemistry and Physics of Molecular Processes in Energetic Materials* (S. Bulusu, Ed.), Kluwer, Boston, 1990, p. 255.
23. Oyumi, Y., and Brill, T. B., *Combust. Flame* 68:209-216 (1987).
24. Palopoli, S. F., and Brill, T. B., *Combust. Flame*, in press.
25. *Aldrich Handbook of Infrared Spectra*, 3rd ed., Aldrich Chemical Co., Milwaukee, WI, 1981.

*Received 1 March 1991; revised 26 June 1991*

## Thermal Decomposition of Energetic Materials 50. Kinetics and Mechanism of Nitrate Ester Polymers at High Heating Rates by SMATCH/FTIR Spectroscopy

J. K. CHEN and T. B. BRILL\*

Department of Chemistry, University of Delaware, Newark, DE 19716

Kinetics and mechanism studies of the fast thermal decomposition of 9.45%, 11.7%, and 13.4% N nitrocellulose, poly(vinyl nitrate), poly(glycidyl nitrate) and poly(nitratomethylmethyloxetane) are described by the SMATCH/FTIR technique. Kinetic constants were calculated from the weight loss and temperature traces of thin films heated in the 100°-150°C/s range. The power rate law  $-d\alpha/dt = A(1-\alpha)^n \exp(-E_a/RT)$  was solved nonisothermally and linearized with  $n = 2$ .  $E_a$  values of 31-34 kcal/mol and log  $A$  values of 14.7-16.9 s<sup>-1</sup> were obtained. The similarity of the values among the compounds suggests that the same processes control the weight loss in all these compounds. The kinetic constants from SMATCH/FTIR predict the burn rate of the sample when the pressure and temperature conditions are the same. The relatively stable gas products that are detected during the reaction interval indicate that an extensive amount of the decomposition chemistry occurs in the condensed phase. The decomposition reactions at the beginning of the weight loss are similar to those near the end based on the constancy of the relative concentrations.

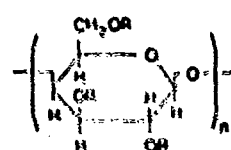
### INTRODUCTION

When a solid material burns, a steep temperature gradient is produced at the surface. In the condensed phase this region can be thought of as a continuously regenerated thin film of material in which heat and mass transfer are driven by phase changes and chemical reactions. The reaction zone in the condensed phase is thin, transient, and nonisothermal [1]. Accordingly, the physico-chemical processes are extremely complicated. The net result of these condensed phase processes is the release of gas products that form the flame zone. The identity, concentration, and rate of release of these products are important components in the combustion characteristics of the solid.

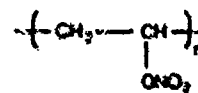
The complexity and transient nature of the surface reaction zone makes experimental measurements nearly impossible to conduct under combustion conditions. Therefore, it has been helpful to gain insight about the chemistry by using techniques that attempt to simulate some of the conditions [2, 3]. For example, rapid heating of a thin film of sample while detecting the dynamic mass change, temperature change, and near-surface gas products in real or near real-time is a promising strategy [4, 5]. SMATCH/FTIR spectroscopy (Simultaneous Mass and Temperature Change/FTIR) was developed with these

types of measurements as the goal [5]. Films of 20-70  $\mu$ m thickness have been heated at rates up to 320°C/s while the mass and temperature changes are measured simultaneously. Rapid-scan FTIR spectroscopy is used to identify the gas products near the surface and to determine their relative concentration in near real-time. The kinetics of mass change can be determined from the mass and temperature change profiles by using a nonisothermal model. The gas products give an indication of the decomposition mechanism under fast heating conditions.

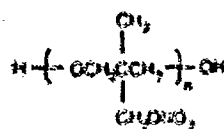
This article describes SMATCH/FTIR studies of polymers containing energetic nitrate ester groups: nitrocellulose (NC), poly(glycidyl nitrate) (PGN), poly(vinyl nitrate) (PVN), and poly(nitratomethylmethyloxetane) (NMMO). The gas products from



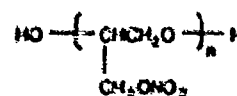
NC (R=H or NO<sub>2</sub>)



PVN



NMMO



PGN

\*Corresponding author

the rapid decomposition [6] and combustion [7] of NC have been reported, but kinetics data at high heating rates do not appear to have been measured. Kinetics studies of the decomposition of NMMO, PVN, and PGN at low heating rates are now available [8], and the gas products from fast thermolysis of NMMO have been discussed [6]. Considerable research on the kinetics of decomposition of NC under isothermal or slow heating rate ( $\leq 5^\circ\text{C}/\text{min}$ ) conditions has been reported [9-16]. TGA, DSC, and vibrational spectroscopy have been used for these studies and indicate that a first-order autocatalytic rate expression applies to the initial half of the decomposition, followed by a second-order rate expression for the remainder. The activation energies cluster in the 39-45 kcal/mol range with  $\log A$  of 16-17.5  $\text{s}^{-1}$ . The results have been interpreted as showing that O-NO<sub>2</sub> bond homolysis occurs in the first phase followed by chain cleavage in the later stage [12, 14]. Likewise, PVN follows the first-order autocatalytic rate expression in the initial 50% of weight loss [8]. On the other hand, PGN and NMMO require only a first-order rate expression without autocatalysis, perhaps because of their lower oxygen balance, viscosity, and different backbone structure [8]. These slow-heating or isothermal decomposition studies apply to the conditions of slow cook-off [17], but it is not known if they also apply to the fast heating rates that are more representative of the foam and fizz zone during ignition and combustion of the solid propellant.

Kinetic studies of thermal decomposition at high heating rates are described in this article in an attempt to address the question of how the condensed phase of nitrate esters degrade under fast heating conditions. The heating rates achieved are within an order of magnitude of heating rates of the foam/surface region during combustion of typical rocket propellants [18], and are 3-4 orders of magnitude faster than those of TGA and DSC measurements. The results reveal that the weight-loss kinetics at fast heating rates are different from those measured at slow heating rates.

## EXPERIMENTAL

Samples of the compounds studied in this work were generously provided by others: nitrocellulose (Dr. Y. P. Carignan, Picatinny Arsenal),

poly(vinyl nitrate), (Mr. A. Becuwe, SNPE, Le Bouchet, France), poly(glycidyl nitrate) (Dr. R. L. Willer, Thiokol Corp.), and poly(nitratomethylmethyloxetane) (G. Manser, Aerojet). NC and PVN were dissolved in acetone and acetonitrile, respectively, and carefully painted onto the metal end tip described below. The tube was dried under vacuum at room temperature for 1 h. PGN and NMMO were painted on as neat samples. The sample thickness was estimated by weighing the tube before and after application of the film to determine the amount of sample applied and using the area of the end-tip. Films were typically 20-70  $\mu\text{m}$  in thickness.

The SMATCH/FTIR technique has been described elsewhere [5] so only a brief description is given here. The dynamic weight change was measured by the change in the vibrational frequency of a cantilevered quartz tube. The stainless-steel end tips attached to the quartz tube were approximately 7 mm in length and were flattened with a lab press. A minimum of high-temperature ceramic was used to fix the flattened end tip to the quartz tube. A type E thermocouple (0.1 mm bead diameter) was spot-welded to the upper center of the stainless-steel end tip and wrapped around the outside. A typical sample tube weighed approximately 65 mg and resonated near 130 Hz when cantilevered to a length of 75 mm.

Initially, the empty quartz sample tube was mounted in the cantilever support between a phototransistor and an LED, and positioned to optimize vibration feedback and control. Heating was effected with a specially designed radio frequency induction coil situated close to the metal end tip. The desired heating rate (or final temperature) was set by adjusting the output level of the RF power supply. A reference thermal trace was obtained by heating the vibrating, empty quartz tube for 6 s; the thermocouple data were stored in an IBM PC.

The empty quartz tube was removed and weighed on a Cahn electrobalance. Typically, ca. 0.2-1 mg of sample was applied to the tube as a thin film. The tube was weighed to determine the initial sample mass, and mounted on the cantilever support. The IR cell was placed over the end tip. While vibrating the tube at resonance, the frequency voltage converter (FVC) output sensed by the phototransistor was adjusted to provide a 0.1 V dc level. This adjustment kept

the FVC output level in the proper range (0 to +5V) for AD conversion. The initial resonance frequency was measured by using a Hewlett-Packard 5300B period meter. This measurement correlated the initial sample mass, the initial resonance frequency, and the initial FVC output level.

The entire sampling device and the gas cell were independently purged with argon gas and maintained at 15 psi Ar. Following the purge, the SMATCH/FTIR experiment was quickly initiated by starting the rapid-scan FTIR data collection. Ramp heating of the end tip typically occurred during the first 5-6 s, after which time a stable final temperature was reached. Throughout the 6-s experiment, IR spectra were collected at 10 scans/s and 4  $\text{cm}^{-1}$  resolution, and FVC and thermocouple data were collected at about 160 data points per sec into the IBM PC. At the end of the experiment with nitrocellulose, the frequency of the tube was again measured, and the tube was reweighed to determine the final sample mass. The total sample mass loss was obtained as the difference between the initial and final mass. Intermediate sample masses were calculated from the FVC output data by using the linear relationship between the mass change and the square of the period of the vibration [5]. For the other nitrate ester polymers, the weight loss was converted to a  $(1 - \alpha)$  percent scale. IR spectra of the gas products were converted to the percent composition relative to  $\text{CO}_2$  of each gas by a method described previously [19].  $\text{H}_2\text{O}$  and any IR-inactive species were not quantified in this procedure.

### TRANSPORT PHENOMENA

The SMATCH/FTIR technique enables the dynamic weight change of the sample to be recorded as a function of time and temperature as the sample is rapidly heated. However, the microscopic detail of the thin film is expected to be complicated because gasification is not instantaneous. At any time during degradation, the film may be partly in contact the heat source and partly separated by a very thin gas layer. As a result, the heat and mass transfer are difficult to analyze. In the worst scenario, the solid sample falls off the end-tip without reacting. Another failed experiment would occur if the sample gasifies more vigorously on one side of the filament

than another and pushes the tube out of resonance. These difficulties are readily recognized in the weight-loss curves as sharp spikes or slope breaks. Experiments in which this occurs are discarded. These problems are minimized when the thin film is uniformly deposited on the end-tip. Therefore, considerable care was taken in the preparation of the sample tubes.

### Heat Transfer

To relate the kinetic parameters to the true behavior of the material during decomposition, the temperature and the mass change at that temperature must be genuinely related. That is, the relaxation rate of the temperature in the film must be at least as fast as the heating rate so that the film maintains a constant temperature. If this condition is met, then the measured temperature is characteristic of the chemistry taking place in the bulk sample. The maximum heating rate for which the temperature is uniform in a film of thickness  $l$  in meters is given by

$$t_r = \frac{C_p \rho l^2}{\lambda} \quad (1)$$

where  $t_r$  is the relaxation time for the temperature gradient in a film of the polymer,  $C_p$  is the heat capacity (1.25 kJ/kg · K at 120°C for 13%N NC [20]),  $\rho$  is the nominal density ( $1.5 \times 10^3$  kg/m<sup>3</sup> for NC), and  $\lambda$  is the thermal conductivity ( $2.3 \times 10^{-4}$  kJ/s · m · K for 12%N NC [21]). In a qualitative way, the heating rate and film thickness can be related by Eq. 1.  $t_r = 4 \times 10^{-2}$  s for a film thickness of 70  $\mu\text{m}$ . This is the approximate time at which the film is able to equilibrate a change in temperature. If 1K accuracy in the temperature data is sought, then  $dT/dt$  can be no faster than  $1/t_r$ , or 25 K/s. If 4-K accuracy is sought, then  $dT/dt$  can be about 100 K/s. Since the heating rate in the SMATCH/FTIR experiment during decomposition was typically 140°C/s, this analysis indicates that the film thickness should be  $\leq 30$   $\mu\text{m}$  for 1-K accuracy. As a result, attempts were made to achieve a film thickness in this range. The nitrocellulose films were usually somewhat thicker than 30  $\mu\text{m}$ , while the other nitrate ester films studied were 30  $\mu\text{m}$  or less in thickness.

### Mass Transfer

The effect of mass transfer on these fast heating experiments was tested by determining the sensitivity of the weight-loss curves to the initial sample mass. No effect was found for masses less than 1 mg, indicating that in the design of SMATCH/FTIR, mass transfer is not an important factor provided the sample mass is small and the film is thin and uniformly deposited.

### GAS PRODUCT ANALYSIS

#### NC

Many of the previous studies of the chemistry of thermal decomposition of nitrocellulose have been reviewed [22]. Three samples differing in the percent nitration were studied here. In 13.4% N NC, 2.73/3 of the OH groups of the  $\beta$ -1,4-glucoside unit are nitrated. NC samples with 11.7%N have 2.16/3 nitrated OH sites, and 9.45%N has 1.57/3 nitrated sites. All three compounds vigor-

ously decomposed on heating and gave similar SMATCH/FTIR results. Phillips et al. [9] also reported that the %N had little effect on the kinetics of decomposition of NC at low heating rates. Although the temperature rise in the exotherm of the sample containing 13.4% N is somewhat greater than in the samples with the less N, the shapes of the weight-loss curves are similar. Therefore, only the SMATCH/FTIR data for 13.4%N NC is shown (Fig. 1). The gas products are detected simultaneously with the onset of weight loss at 175°C. This temperature closely resembles the onset of weight loss by TGA. The gas products from all three samples are quite similar. NO dominates NO<sub>2</sub> as the oxidizer reaching the gas phase. The extensive amount of reduction of NO<sub>2</sub> results in a large amount of carbon oxidation as evidenced by the CO and CO<sub>2</sub> liberated. HCOOH and CH<sub>2</sub>O are also significant products. CH<sub>2</sub>O was found to form in relatively higher concentration as the percent N in the sample decreases. It has been

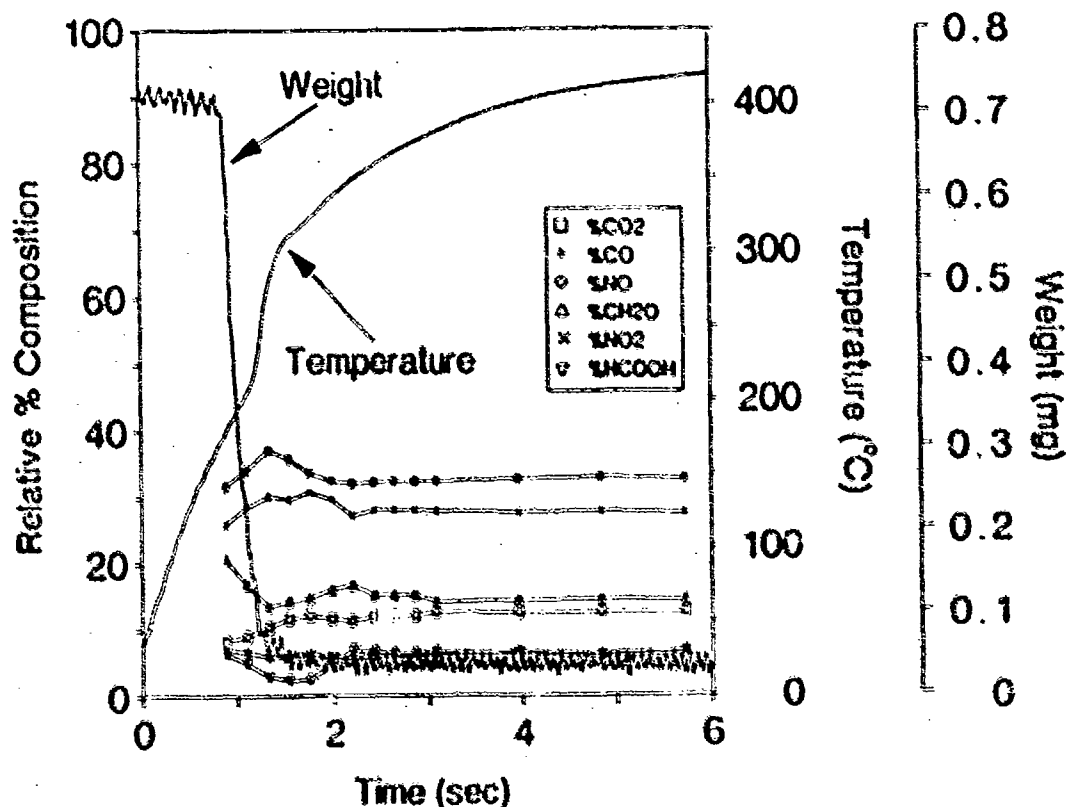


Fig. 1. SMATCH/FTIR data for 13.4%N nitrocellulose. The weight change, temperature change and near surface gas products were measured simultaneously under 15 psi Ar.

shown that nitration of the  $-\text{CH}_2\text{OH}$  sites of the cellulose backbone is favored over the secondary  $-\text{OH}$  sites [23].  $\text{CH}_2\text{O}$  has been proposed to form from the  $-\text{CH}_2\text{ONO}_2$  groups [24]. Hence,  $\text{CH}_2\text{O}$  is expected to be, and is, relatively more prevalent in the less nitrated samples.

$\text{HCOOH}$  has been identified previously as a product of decomposition of NC [24-27]. SMATCH/FTIR studies of NC samples having an even lower percent nitration indicate that  $\text{HCOOH}$  forms after most of the other gas products appear. This suggests that  $\text{HCOOH}$  is produced by the residue after most of the energetic nitrate ester sites have decomposed.

#### PVN, PGN, and NMMO

Figures 2-4 show SMATCH/FTIR data for PVN, PGN and NMMO, respectively.  $\text{CH}_2\text{O}$  is the

dominant product from PGN and NMMO, which contain only  $-\text{CH}_2\text{ONO}_2$  sites.  $\text{CH}_2\text{O}$  is relatively less prevalent from PVN which possesses no primary alkyl nitrate sites. The fact that  $\text{CH}_2\text{O}$  forms at all from PVN indicates that  $\text{CH}_2\text{O}$  is not solely formed by these primary alkyl nitrate sites. As with the NC samples, CO and NO are major products. However, for both PVN and PGN, HONO, as well as  $\text{NO}_2$ , are detected.

The gas products liberated from NC, PGN, and NMMO contain large amounts of NO, CO, and  $\text{CO}_2$  and lesser amounts of  $\text{NO}_2$  and HONO. This finding indicates that an extensive amount of reaction takes place in the condensed phase before the products are released [6, 28]. It is widely believed that  $\text{O}-\text{NO}_2$  homolysis is the initial step in the thermal decomposition of nitrate esters (reaction 2) [9-16]. However, except when reaction 2 occurs on the surface, the  $\text{NO}_2$  must

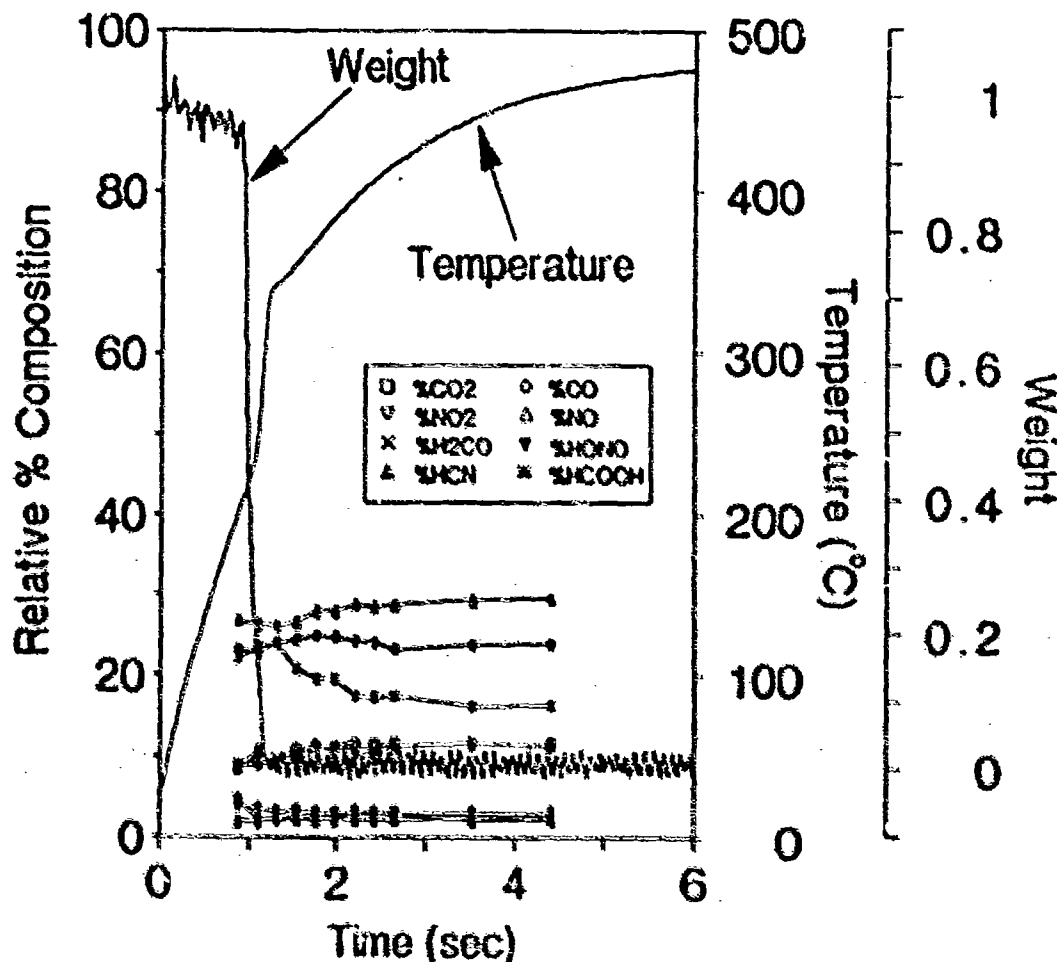


Fig. 2. SMATCH/FTIR data for poly(nitro) esters under 15 psi. The weight loss is expressed as a percent conversion (1 - w).



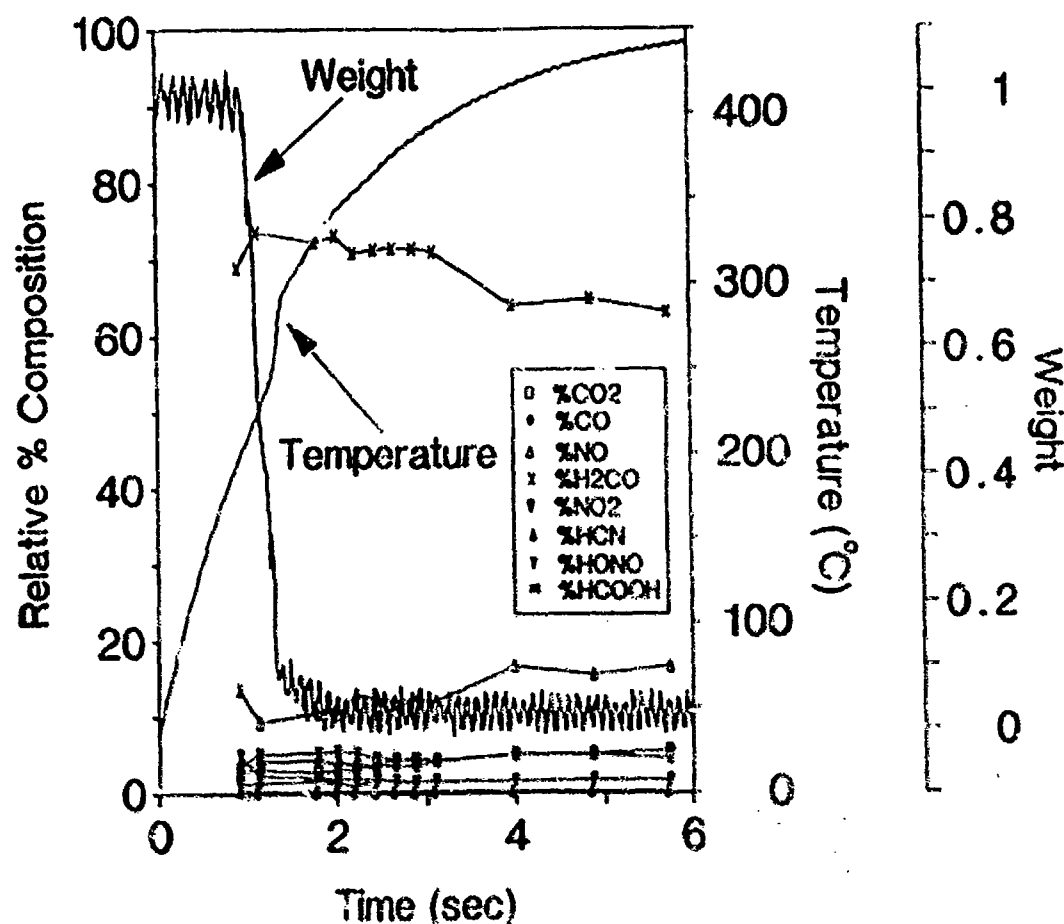


Fig. 3. SMATCH/FTIR data for poly(glycidyl nitrate) under 15 psi Ar. The weight loss is expressed in terms of the percent conversion  $(1 - \alpha)$ .

migrate through the polymer matrix



before it is detected. Because of its reactivity with organic polymers at elevated temperatures, it is not surprising that most of the nitrogen appears as NO rather than  $\text{NO}_2$ .

It is interesting to note that the relative product concentrations do not change dramatically from the beginning to the end of the weight-loss step. The minor initial fluctuations are primarily the result of convective mixing of the gases. We interpret this to mean that the same decomposition reactions dominate from the beginning to the end of the decomposition of the sample, but that an increasing amount of sample is involved in these reactions as the temperature increases. Consistent with this is the fact that a plot of the total IR absorbance of the products shown in Figs.

1-4 vs. time shows that the absorbance of the gas products smoothly increases through the weight-loss step and levels off sharply at the end of the weight-loss step.

#### KINETIC ANALYSIS

The kinetic parameters for the thermogravimetric weight loss were calculated using

$$\frac{d\alpha}{dt} = k(T)f(\alpha), \quad (3)$$

$$\alpha = (W_0 - W_t)/(W_0 - W_f), \quad (4)$$

where  $\alpha$  is the degree of conversion,  $W_0$  is the initial weight of the sample,  $W_t$  is the weight of sample at time  $t$ ,  $W_f$  is the final weight,  $t$  is the time,  $k$  is the rate constant, and  $f(\alpha)$  is the function which describes the degree of conversion. The temperature dependence of the rate

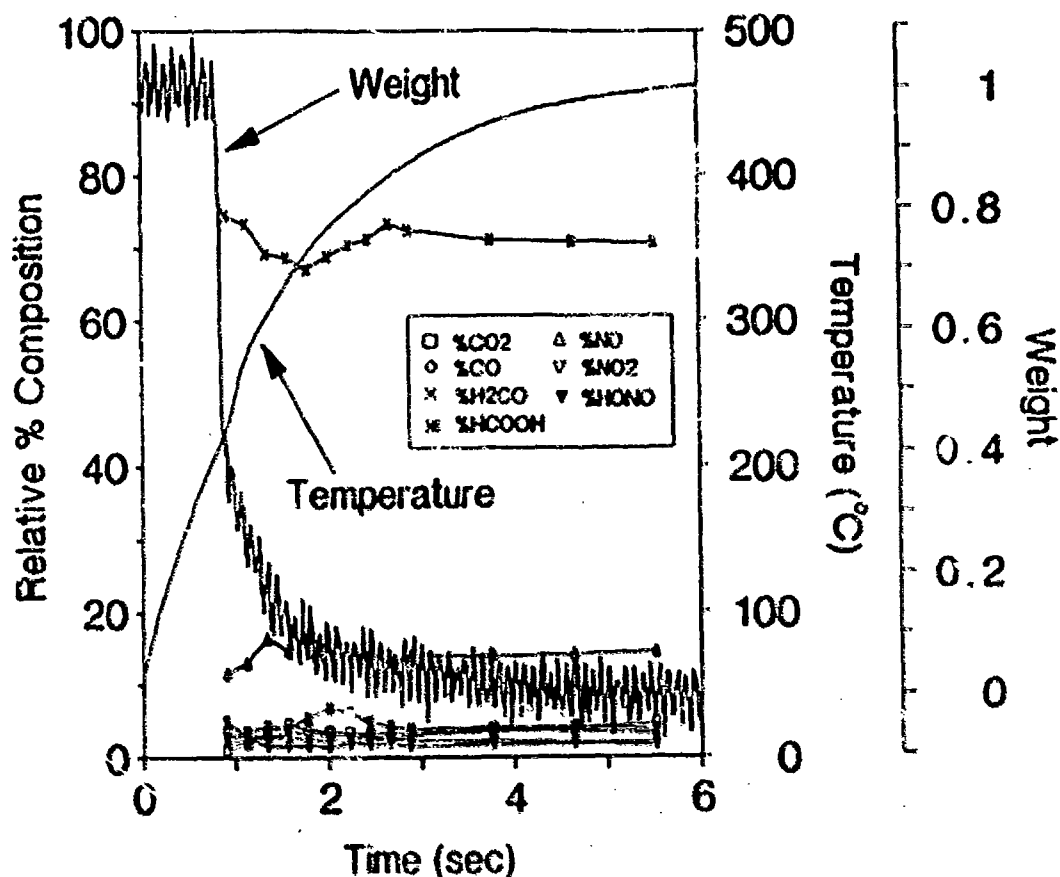


Fig. 4. SMATCH/FTIR data for poly(nitramethylmethyloxazone) under 15 psi Ar. The weight loss is expressed in terms of the percent conversion  $(1 - \alpha)$ .

constant  $k$  obeys the Arrhenius equation,

$$k(T) = Ae^{-E_a/RT} \quad (5)$$

where  $E_a$  is the activation energy,  $R$  is the gas constant, and  $A$  is a preexponential factor. Equation 3 then becomes

$$\frac{d\alpha}{dt} = f(\alpha) Ae^{-E_a/RT} \quad (6)$$

which is the basic kinetics equation of nonisothermal thermogravimetry.

In the SMATCH/FTIR experiment, the mass change, temperature, and time are measured simultaneously. However, owing to the high heating rate (100–150°C/s), the experiments were not carried out at a constant heating rate. During the decomposition the material may absorb or release heat. Therefore, the sample temperature  $T(t)$

became a complicated function of time  $t$ . The derivative method [29, 30] may be applied in this case. Equation 6 can be rearranged to

$$\ln\left(\frac{d\alpha}{dt} \frac{1}{f(\alpha)}\right) = \ln(A) - \frac{E_a}{RT} \quad (7)$$

The conversion function  $f(\alpha)$  is considered in its simplest form (Eq. 8),

$$f(\alpha) = (1 - \alpha)^n \quad (8)$$

where  $n$  is the apparent order of the process. Therefore, by using Eqs. 4 and 8 the value of  $n$  and  $f(\alpha)$  at each time  $t$  can be calculated. The  $d\alpha/dt$  can be obtained by using polynomial curve fitting to express  $(1 - \alpha)$  as a function of time (Eq. 9 and Table I). Figure 2 shows the calcu-

TABLE I  
Polynomial Curve Fitting Coefficients of Nitrate  
Ester Polymers

Polymer	$a_0$	$a_1$	$a_2$	$a_3$
NC(13.4%N)	14.68	-31.02	22.18	-5.38
NC(11.7%N)	5.85	-9.83	6.13	-1.54
NC(9.45%N)	6.77	-11.63	7.13	-1.74
PVN	35.35	-64.48	29.52	
PGN	6.75	-8.24	2.45	
NMNO	35.29	-74.04	39.15	

lated and experimental weight-loss curve used in this analysis for 13.4%N nitrocellulose.

$$(1 - \alpha) = \sum_{i=0}^j a_i t^i \quad (j = 2 \text{ or } 3) \quad (9)$$

$$-\frac{d\alpha}{dt} = \sum_{i=1}^j i a_i t^{i-1} \quad (10)$$

The time-derivative of Eq. 9 is shown in Eq. 10. Therefore, only a single thermogram is required for the determination of the kinetic parameters in the SMATCH/FTIR experiment. By using trial-and-error modification of  $n$ , a straight line is achieved when the left side of Eq. 7 is plotted against  $1/T$  in the initial 50% of weight-loss. When  $n = 2$ , the plots are shown in Fig. 6 for the three samples of nitrocellulose. The intercept gives the value for  $A$  and the slope yields a value for  $E_a$  (Table 2). The terms "activation energy" and "reaction order" are carried over from the nomenclature of homogeneous systems even

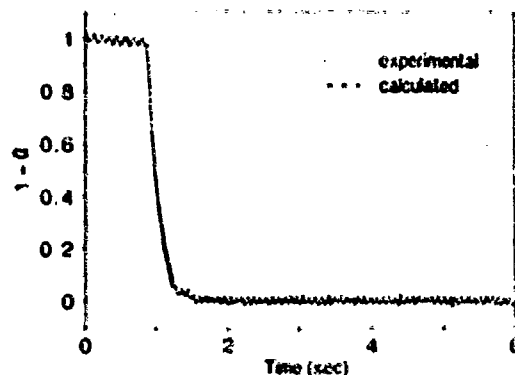


Fig. 5. The experimental weight loss curve for 13.4% N NC and the calculated curve fit using polynomial regression.

though they do not necessarily have the same meaning when applied to these heterogeneous decomposition processes [31].

The kinetics data analysis described above differs from the models used previously to interpret thermogravimetric data for NC when  $dT/dt < 5^\circ\text{C}/\text{min}$ . At slow heating rates, a first-order autocatalytic reaction in the induction step followed by simple second-order kinetics is able to fit the global weight-loss curve. When a first-order kinetic expression is applied to the SMATCH/FTIR data in Figs. 1-4, the activation energy is negative in the lower temperature range. Negative  $E_a$  values can occur but are unlikely under the conditions that are present in the SMATCH/FTIR experiment. Thus, the global decomposition processes of these nitrate esters heated at  $> 100^\circ\text{C}/\text{s}$  are better described by Eqs. 7 and 8 with  $n = 2$  than by the first-order model. The fact that linear functions are obtained

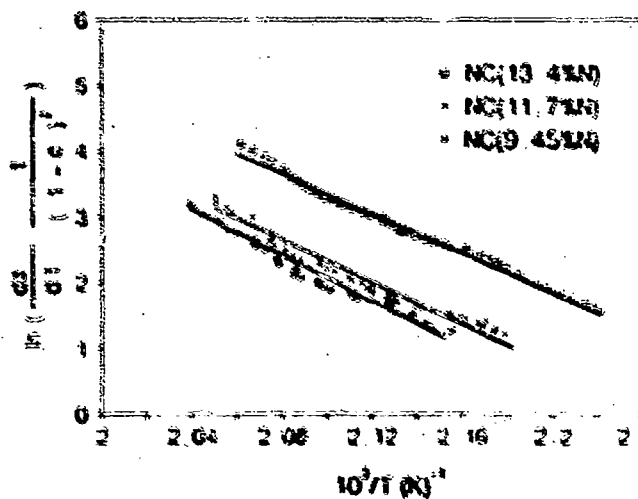


Fig. 6. Arrhenius plots for the initial 50% of weight loss for three nitrocellulose samples that differ in the percent nitrogen.

TABLE 2

Kinetic Parameters of Nitrate Ester Polymers for Thermal Decomposition at  $dT/dt > 100^\circ\text{C/s}$  by SMATCH/FTIR Spectroscopy

Polymer	$E$ (kcal/mol) <sup>a, b</sup>	$\log A$ (s) <sup>-1</sup>
NC(13.4%N)	$32.6 \pm 0.8$	$16.4 \pm 0.4$
NC(11.7%N)	$33.7 \pm 1.3$	$16.9 \pm 1.0$
NC(9.45%N)	$33.8 \pm 2.3$	$16.7 \pm 0.8$
PVN	$32.1 \pm 0.2$	$15.9 \pm 0.3$
PGN	$31.1 \pm 2.1$	$14.7 \pm 0.7$
NMMO	$33.5 \pm 1.5$	$16.4 \pm 0.5$

<sup>a</sup>Apparent reaction order  $n = 2$ .

<sup>b</sup>The average of two experiments.

(Fig. 6) with  $n = 2$  does not mean that the decomposition process is necessarily second-order in the usual sense of chemical kinetics. The thermal decomposition of these nitrate esters is a heterogeneous process in which all of the reactions and diffusion terms are lumped. The value of  $n = 2$  is only an empirical parameter chosen to linearize the power rate law. The similarity of the values of  $E_a$  and  $\log A$  for the six nitrate ester polymers decomposed at a high heating rate suggests that the global kinetics of decomposition is dominated by the same processes. The similarity of the values is not an artifact of the method because other classes of compounds yield different values [32].

This study shows that the expressions that linearize the rate data for the thermal decomposition of nitrate esters depend on the heating rate. This is because the left side of Eq. 7 has two variables. At slow heating rates ( $\leq 5^\circ\text{C/min}$ ), the weight loss of most nitrate esters is first-order or first-order autocatalytic through the first 50%, followed by a second-order process in the latter 50% [8, 12, 14]. The two steps are separated by a discontinuity that has been interpreted as meaning that  $\text{C}-\text{NO}_2$  homolysis dominates initially followed by the dominance of chain cleavage [12, 14]. When the decomposition takes place at a higher heating rate ( $\geq 100^\circ\text{C/s}$ ), the rate expression has the form of apparent second-order process in the initial 50% of weight loss. We stress that this does not imply that a second-order elementary reaction is taking place because mass loss is a global heterogeneous process involving many parallel reactions as well as diffusion. The most important point is that the  $da/dt$  and  $f(\alpha)$

terms in Eq. 7 have different importance at slow and fast heating rates.

It is well known that the kinetics determined with slow thermal decomposition techniques do not explain combustion data. We were interested in establishing whether the fast decomposition kinetics from SMATCH/FTIR spectroscopy apply to combustion. Indeed, they match the regression rate measurements of double base propellants (mostly NC) during combustion, but apply only in the range of pressure and temperature where the kinetics were measured.

Various surface temperatures in the  $175\text{--}300^\circ\text{C}$  range have been reported for double base propellants at 15 psi [33]. Despite the high heating rates employed in SMATCH/FTIR, the decomposition temperature range achieved is  $180\text{--}200^\circ\text{C}$  at the lower end of this range. Still, this permits a comparison to be made of the kinetic constants to the burn rate expression. The  $da/dt f(\alpha)^{-1}$  term in Eq. 7 expresses the rate of regression of mass in the temperature range of the SMATCH experiment. The regression (burn) rate,  $\dot{r}$ , of materials is expressible in a form similar to Eq. 7, but with units appropriate for the burn rate (Eq. 11), where  $h$  is the sample thickness.

$$\dot{r}(\text{mm/s}) = A h e^{-E_a/RT} \quad (11)$$

By using the thickness of  $70\text{ }\mu\text{m}$ ,  $T = 180^\circ\text{C}$ , and the parameters for 13.4%N NC in Table 2, a value of  $\dot{r} = 0.3\text{ mm/s}$  is obtained. This is close to the regression rate ( $0.4\text{ mm/s}$ ) for a double base propellant under the same pressure and temperature conditions [33].

## CONCLUSIONS

1. The gas products evolved from the fast thermal analysis of these nitrate ester polymers indicate that an extensive amount of reaction has taken place in the condensed phase before the gases appear. The global kinetics are controlled by these reactions.
2. The decomposition reactions at the beginning of the weight loss produce the same products as those later in the degradation based on the similarity of the initial products and the final, steady-state products.
3. The  $-\text{CH}_2\text{ONO}_2$  groups contribute greatly to the amount of  $\text{CH}_2\text{O}$  formed. However,  $\text{CH}_2\text{O}$  is formed to some extent even when

this primary alkyl nitrate pendant group is absent as evidenced by its presence in the thermolysis of PVN.

4. Weight-loss measurements at slow and fast heating rates produce different kinetic rate expressions. A second-order power rate law linearizes the data in the first 50% of weight-loss at high heating rates, whereas at low heating rates, a first-order autocatalytic rate-law applies.
5. The similarities of  $E_a$  and  $\log A$  for these nitrate esters decomposed at high heating rates suggest that similar overall reactions and transport properties dominate the decomposition process under these fast heating conditions.
6. The kinetic constants from SMATCH measurements on NC predict the measured burn rate in the same pressure and temperature range.

*We are grateful to the Air Force Office of Scientific Research, Aerospace Sciences, for support of this work on AFOSR-89-0521. We thank A. Becuwe, Y. P. Carignan, G. E. Manser and R. L. Willer for providing samples.*

## REFERENCES

1. Kubota, N., *Prog. Astronaut. Aeronaut.* 90:1 (1984).
2. Brill, T. B., *Chemistry and Physics of Energetic Materials* (S. Bulusu, Ed.), NATO ASI, Series C, Vol. 309, Kluwer, Dordrecht, 1990, p. 255.
3. Brill, T. B., *Chemistry and Physics of Energetic Materials* (S. Bulusu, Ed.), NATO ASI, Series C, Vol. 309, Kluwer, Dordrecht, 1990, p. 277.
4. Skocypec, R. D., Erickson, K. L., Renlund, A. M., and Trott, W. M., *Proceedings of the 26th JANNAF Combustion Meeting*, JPL, Pasadena, CA, October 1989.
5. Timken, M. D., Chen, J. K., and Brill, T. B., *Appl. Spectrosc.* 44:701 (1990).
6. Oyumi, Y., and Brill, T. B., *Combust. Flame* 66:9 (1986).
7. Fifer, R. A., and Lannon, J. A., *Combust. Flame* 24:369 (1975).
8. Chen, J. K., and Brill, T. B., *Thermochim. Acta* (in press).
9. Phillips, R. W., Orlick, C. A., and Steinberger, R., *J. Phys. Chem.* 59:1034 (1955).
10. Manelis, G. B., Rubtsov, Y. I., Smirnov, L. P., and Dubovitskii, F. I., *Kinet. Katal.* 3:42 (1962).
11. Duswalt, A. A., *Thermochim. Acta* 8:57 (1974).
12. Eisenreich, N., and Pfeil, A., *Thermochim. Acta* 61:13 (1985).
13. Volltrauer, H. N., and Fontijn, A., *Combust. Flame* 41:313 (1981).
14. Eisenreich, N., Krause, H. H., and Pfeil, A., *Thermochim. Acta* 85:395 (1985).
15. Jutier, J.-J., and Prud'homme, R. E., *Thermochim. Acta* 104:321 (1986).
16. Ho, S. Y., and Fong, C. W., *Combust. Flame* 75:139 (1989).
17. Pakulak, J. M., Jr. NWC TP 6660, Naval Weapons Center, China Lake, CA, June 1988.
18. Kubota, N., and Sakamoto, S., *Prop. Explos. Pyrotech.* 14:6 (1989), and personal communication of S. Sakamoto, 1990.
19. Oyumi, Y., and Brill, T. B., *Combust. Flame*, 62:213 (1985).
20. Decker, L. J., Ward, J. R., and Freedman, E., *Thermochim. Acta*, 8:177 (1974).
21. Dobratz, B. M., LLNL Explosives Handbook, UCRL-52997, Lawrence Livermore National Laboratory, March, 1981, p. 19-95.
22. Fifer, R. A., *Prog. Astronaut. Aeronaut.* 90:177 (1984).
23. Wu, T. K., *Macromolecules* 13:74 (1980).
24. Shafizadeh, F., and Wolfrom, M. L., *J. Am. Chem. Soc.* 80:1675 (1958).
25. Wolfrom, M. L., Frazer, J. H., Kuhn, L. F., Dickey, E. F., Olin, S. M., Bower, R. S., Maher, G. G., Mulach, J. D., Chaney, A., and Carpenter, E., *J. Am. Chem. Soc.* 78:4695 (1956).
26. Wolfrom, M. L., Chaney, A., and McWain, P., *J. Am. Chem. Soc.*, 80:946 (1958).
27. Shafizadeh, F., Wolfrom, M. L., and McWain, P., *J. Am. Chem. Soc.*, 81:122 (1959).
28. Oyumi, Y., and Brill, T. B., *Combust. Flame* 68:209 (1987).
29. Sharp, J. H., and Wentworth, S. A., *Anal. Chem.* 41:2060 (1969).
30. Carroll, B., and Manche, E. P., *Anal. Chem.* 42:1296 (1970).
31. Garn, P. D., *Thermochim. Acta* 28:183 (1979).
32. Chen, J. K., and Brill, T. B. (to be published).
33. Beckstead, M. W., *Proceedings 26th JANNAF Combust. Meeting*, JPL, Pasadena, CA, October 1989.

*Received 5 September 1990; revised 17 January 1991*

**THERMAL DECOMPOSITION OF ENERGETIC MATERIALS.  
PART 51. KINETICS OF WEIGHT LOSS FROM NITRATE ESTER  
POLYMERS AT LOW HEATING RATES**

J.K. CHEN and T.B. BRILL \*

*Department of Chemistry, University of Delaware, Newark, DE 19716 (U.S.A.)*

(Received 4 September 1990)

**ABSTRACT**

The kinetics of weight loss of six polymeric nitrate esters is described by the non-linear least-squares fit of non-isothermal TGA weight-loss curves. In the first 50% of weight loss, nitrocellulose (9.45%, 11.7%, and 13.4% nitrogen) and poly(vinyl nitrate) undergo first-order autocatalytic decomposition. Poly(glycidyl nitrate) and poly(nitratomethylmethyloxethane) exhibit simple first-order kinetics. The tendency to become autocatalytic follows the trend toward higher oxygen balance, higher viscosity, and the increased presence of secondary alkyl nitrate sites in the molecules.

**INTRODUCTION**

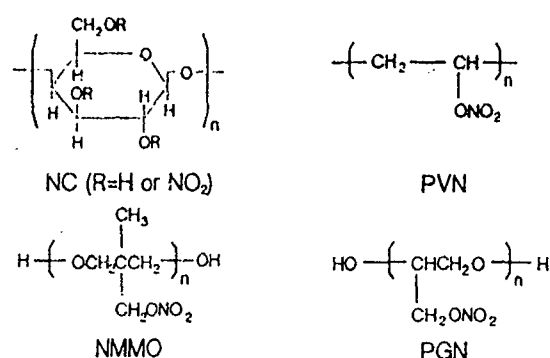
Studies of the decomposition of nitrocellulose under slow heating conditions ( $dT/dt < 5^\circ\text{C min}^{-1}$ ) have been extensive [1-7]. For instance, the kinetics of weight loss measured by TGA reveals that the decomposition process initially follows a first-order rate law that may be associated with O-NO<sub>2</sub> homolysis as in reaction (1) [4,5]



Autocatalysis, perhaps as a result of  $\cdot\text{NO}_2$  reacting with  $\text{RO}\cdot$ , then becomes increasingly important. After about 50% of the weight is lost, a discontinuity occurs in the weight-loss curve and a second-order rate expression best describes the process [4,5]. This latter stage has been interpreted as indicating that backbone cleavage reactions are occurring [8].

Recently, the decomposition kinetics of thin films of nitrocellulose (NC), poly(vinyl nitrate) (PVN), poly(glycidyl nitrate) (PGN), and poly(nitromethylmethyloxethane) (NMMO) have been studied at heating rates exceeding  $100^\circ\text{C sec}^{-1}$  [9]. The rate laws that describe the weight loss from NC at

\* Author for correspondence.



slow and fast heating rates are different. Unlike the first-order autocatalytic model that describes NC at low heating rates, the first 50% of weight lost at high heating rates is best described by a simple second-order power rate law. Because no previous kinetic studies of PVN, PGN and NMMO were found, comparisons of the high rate decomposition kinetics with low rate decomposition data could not be made for these compounds. Low heating rate TGA kinetics data would also enable more general comparisons to be made of the kinetics of decomposition of nitrate ester polymers. Therefore, this paper describes the kinetics of weight loss measured by TGA for three samples of NC that differ in the percent N, and for PVN, PGN and NMMO. The initial 50% of weight loss is considered. In this early part of the decomposition, the induction process is emphasized. The later stage of weight loss where the residue reactions dominate was not studied here.

#### EXPERIMENTAL

Samples of nitrocellulose were supplied by Y.P. Carignan of Picatinny Arsenal, NJ. PVN, PGN and NMMO were provided by A. Becuwe (SNPE, Le Bouchet, France), R.L. Willer (Thiokol, Elkton, MD), and G. Manser (Aerojet, Sacramento, CA), respectively.

Thermogravimetric analysis was conducted using a Dupont Instruments Model 951 TGA at 0.5 or 1°C min<sup>-1</sup> under Ar at a flow rate of 20 ml min<sup>-1</sup>. Samples of 1.75–2.55 mg were used in all cases. The first-order weight-loss curves were fit by the non-linear regression subroutine RNSSQ contained in the International Mathematical and Statistical Library.

#### KINETIC MODELS

The first-order autocatalytic model that describes the TGA weight-loss curves during the thermal decomposition of NC at  $dT/dt \leq 1^\circ\text{C min}^{-1}$  is

well known [2,4,5]. As a check on how our TGA methods compared with previous work, we reinvestigated samples of 13.4 %N NC for comparison with published data. The data, especially those of Eisenreich and Pfeil [4] on 13.3 %N NC, are fully reproducible in our laboratory. We employed the non-linear least-squares model for non-isothermal decomposition that they used. In their approach they searched directly for the least-squares fit of the temperature integral of the Arrhenius equation. Since multiple solutions of this integral are possible, we wished to determine whether their converged values were the appropriate ones. Therefore, the Coats and Redfern approximation [10] was used to obtain an initial guess of the solution. The final, converged values of the least-squares calculation were found to be the same as those of Eisenreich and Pfeil indicating that their direct search procedure had converged at the most reasonable solutions. Thus, no further elaboration of this published kinetic model is needed here. The weight-loss data for all samples of NC and the sample of PVN were analyzed by the model.

The weight-loss curves for PGN and NMMO were found not to require the first-order autocatalytic model. Only a simple first-order model was found to be necessary. In this model, the rate of weight loss,  $d\alpha/dt$  is given by

$$d\alpha/dt = k(T)(1 - \alpha) \quad (2)$$

where  $\alpha$  and  $k(T)$  are defined by eqns. (3) and (4)

$$\alpha = (W_0 - W_t)/(W_0 - W_f) \quad (3)$$

$$k(T) = A e^{-(E/RT)} \quad (4)$$

If a linear heating rate is employed, then  $dT/dt = \beta$ . Therefore

$$\int_0^\alpha \frac{d\alpha}{(1 - \alpha)} = \frac{A}{\beta} \int_{T_0}^T e^{-(E/RT)} dT \quad (5)$$

Redefining  $T_0 = 0$ , the temperature integral  $S(T)$  is given by

$$S(T) = \int_0^T e^{-(E/RT)} dT \quad (6)$$

Since eqn. (6) has no closed solution, it can be solved as an asymptotic expansion, eqn. (7), [10,11]

$$S(T) = \frac{RT^2}{E} e^{(-E/RT)} \left[ 1 - 2\left(\frac{RT}{E}\right) + 6\left(\frac{RT}{E}\right)^2 - 24\left(\frac{RT}{E}\right)^3 + \dots \right] \quad (7)$$

If only the first two terms of the expansion of eqn. (7) are considered [12] then

$$\ln\left(\frac{-\ln(1 - \alpha)}{T^2}\right) = \ln\left[\frac{AR}{\beta E} \left(1 - 2\left(\frac{RT}{E}\right)\right)\right] - \frac{E}{RT} \quad (8)$$



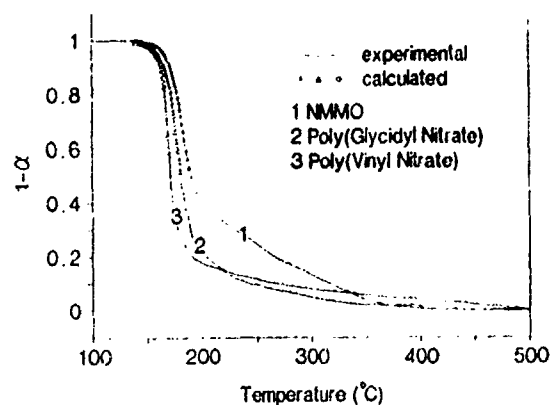


Fig. 1. The experimental and kinetically modelled TGA weight-loss curves for three nitrate ester polymers. The first 50% of conversion was modelled.

Using eqn. (8) to obtain an initial estimate of  $E$  and  $A$ , the non-linear least-squares method can then be used to solve eqn. (9) and obtain more accurate values of  $E$  and  $A$

$$(1 - \alpha) = \exp \left[ -\frac{ART^2}{\beta E} e^{-(E/RT)} \left( 1 - 2\left(\frac{RT}{E}\right) + 6\left(\frac{RT}{E}\right)^2 - \dots \right) \right] \quad (9)$$

## RESULTS

Figure 1 shows the weight-loss curves for NMMO, PVN and PGN. By using these data and those for 9.45%, 11.7% and 13.4 %N NC, Arrhenius plots were constructed from eqn. (8). Figure 2 shows these plots for PVN, PGN and NMMO. Figure 3 shows the plots for the three samples of NC.

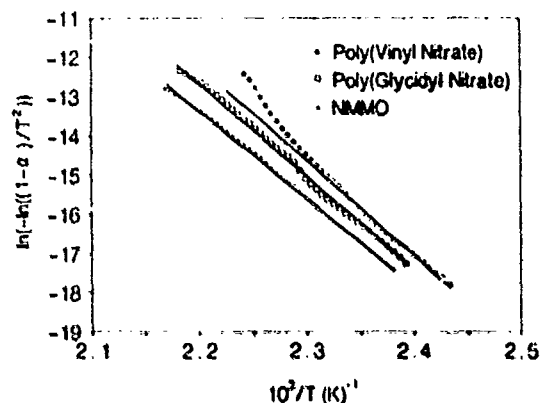


Fig. 2. Arrhenius plots for three nitrate ester polymers showing first-order behavior, except for PGN at higher temperature, where autocatalysis becomes important.

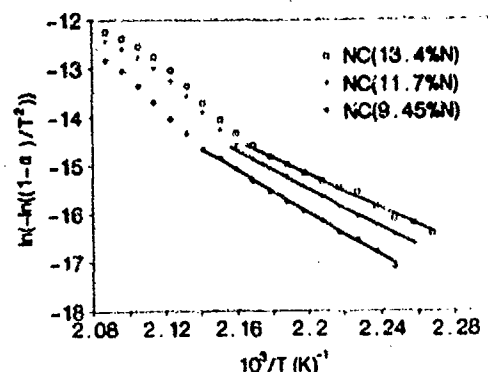


Fig. 3. Arrhenius plots for three nitrocellulose samples showing first-order behavior at lower temperature with autocatalysis becoming important at higher temperatures.

Note that NC and PVN follow first-order kinetics only in the low temperature range (138–160°C for PVN, 169–190°C for NC). The autocatalytic process then becomes important. This behavior requires the use of a first-order autocatalytic model to calculate the kinetic constants given in Table 1. On the other hand, PGN and NMMO follow simple first-order kinetics throughout the initial 50% of weight loss (144–180°C) without undergoing autocatalysis. The final  $E$  and  $A$  values in Table 1 were calculated from eqn. (9). The weight-loss curves calculated from these models are shown on Fig. 1 for comparison with the experimental data.

Three factors in these compounds may be responsible for their different kinetic behavior: the differences in phase, energy content (oxygen balance), and number of primary and secondary alkyl nitrate groups. With regard to the phase, NC and PVN are amorphous solids up to the decomposition temperature, whereas PGN and NMMO are viscous fluids at room temperature. The ease with which the gaseous products, especially  $\text{NO}_2$ , can escape

TABLE I

TGA kinetic parameters of nitrate ester polymers

Polymer	Heating rate (°C min <sup>-1</sup> )	First-order step		Autocatalytic step	
		$E$ (kcal mol <sup>-1</sup> )	log $A$ (sec <sup>-1</sup> )	$E$ (kcal mol <sup>-1</sup> )	log $A$ (sec <sup>-1</sup> )
NC(13.4 %N)	0.5	40.6	15.1	41.0	16.0
NC(11.7 %N)	0.5	40.8	15.2	41.1	16.0
NC(9.45 %N)	0.5	41.7	15.4	41.2	15.9
PVN	1.0	47.7	20.2	46.0	19.9
PGN	1.0	46.2	19.3		
NMMO	1.0	44.2	18.0		

the condensed phase would be expected to be greater for PGN and NMMO. Hence, the concentration of  $\text{NO}_2$  may not build up to the level needed to create significant autocatalysis. The more rigid NC and PVN matrices may retain the  $\text{NO}_2$  to a greater extent and enable autocatalysis to become important. Consistent with this, Phillips et al. [1] found that the decomposition of NC followed first-order kinetics below 200 mm Hg, but more complicated kinetics were followed at high pressures. The decomposition gases would be expected to escape from the sample more readily at lower pressure. Were this physical mechanism entirely responsible for the kinetics differences, the concentration of  $\text{NO}_2$  in the gas phase would be expected to be higher for PGN and NMMO than for the other samples. This is not found experimentally [9], and illustrates the value of performing IR analysis of the near-surface products when conducting these types of experiments.

A second explanation for the apparently different kinetic behavior of these compounds upon thermolysis lies in the oxygen balance. Figure 3 shows that the deviation from first-order behavior of NC decreases as the oxygen balance (or percent N) decreases. The acceleratory effect of  $\text{NO}_2$  on the degradation of the sample at higher temperature depends on a threshold amount of  $\text{NO}_2$  in the sample being reached relative to the other products. Otherwise, the reaction might continue to follow global first-order behavior as suggested by reaction (1). PGN and NMMO have an even lower oxygen balance than 9.45 %N NC. On this basis they would be expected to tend toward the dominance of first-order kinetics, in accordance with what is found experimentally. Thus, it appears that the oxygen balance (amount of  $\text{NO}_2$  available relative to the other products) may play a role in the reaction rate. A higher oxygen balance favors first-order autocatalysis while a lower oxygen balance favors simple first-order kinetics.

A third factor may be the position of the nitrate ester group on the backbone. The preferential site for nitration of NC is the primary alcohol [13]. Thus, the ratio of primary/secondary alkyl nitrate groups is higher in 9.45 %N NC than 13.4 %N NC. As the percent N in NC decreases, autocatalysis occurs to a lesser extent (Fig. 3) suggesting that autocatalysis is favored by the presence of the secondary nitrate groups. In keeping with this pattern, PVN, which possesses only secondary alkyl nitrate groups decomposes autocatalytically while PGN and NMMO, which possess only primary alkyl nitrate groups follow simple first-order kinetics.

ignore  
!!  
All three of the above observations may be contributing factors in the different kinetics of decomposition of these nitrate ester polymers. However, the first-order or first-order autocatalytic models do not satisfactorily fit the weight-loss kinetics at heating rates exceeding  $100^\circ\text{C sec}^{-1}$  [9], where a simple second-order expression was found to be necessary.

#### ACKNOWLEDGEMENTS

We are grateful to the Air Force Office of Scientific Research, Aerospace Sciences, for support of this work on AFOSR-89-0521. Samples of compounds were generously supplied by Y.P. Carignan, A. Becuwe, R. Willer and G. Manser.

#### REFERENCES

- 1 R.W. Phillips, C.A. Orlick and R. Steinberger, *J. Phys. Chem.*, 59 (1955) 1034.
- 2 G.B. Manelis, Y.I. Rubtsov, L.P. Smirnov and F.I. Dubovitskii, *Kinet. Katal.*, 3 (1962) 42.
- 3 A.A. Duswalt, *Thermochim. Acta*, 8 (1974) 57.
- 4 N. Eisenreich and A. Pfeil, *Thermochim. Acta*, 61 (1983) 12.
- 5 J.-J. Jutier and R.E. Prud'homme, *Thermochim. Acta*, 104 (1986) 321.
- 6 H.N. Volthamer and A. Fontijn, *Combust. Flame*, 41 (1981) 313.
- 7 For a review of product analysis studies see R.A. Fifer, *Fundamentals of Solid Propellant Combustion*, in K.K. Kuo and M. Summerfield (Eds.), *Prog. Astronaut. Aeronaut.*, 90 (1984) 177.
- 8 N. Eisenreich, H.H. Krause and A. Pfeil, *Thermochim. Acta*, 85 (1985) 395.
- 9 J.K. Chen and T.B. Brill, *Combust. Flame*, in press.
- 10 P. Murray and J. White, *J. Trans. Brit. Ceram. Soc.*, 54 (1955) 204.
- 11 G. Gyulai and E.J. Greenhow, *Thermochim. Acta*, 6 (1973) 239.
- 12 A.W. Coats and J.P. Redfern, *Nature*, 201 (1964) 68.
- 13 T.K. Wu, *Macromolecules*, 13 (1980) 74.

**THERMAL DECOMPOSITION OF ENERGETIC MATERIALS 53. KINETICS  
AND MECHANISM OF THERMOLYSIS OF  
HEXANITROHEXAZAISOWURTZITANE**

by

**D. G. PATIL and T. B. BRILL**

Reprinted from *Combustion and Flame*  
Volume 57 Number 2 November 1994

# Thermal Decomposition of Energetic Materials 53. Kinetics and Mechanism of Thermolysis of Hexanitrohexazaisowurtzitane

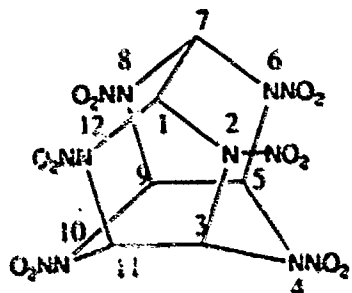
D. G. PATIL and T. B. BRILL\*

Department of Chemistry, University of Delaware, Newark, DE 19715

The kinetics of thermal decomposition of hexanitrohexazaisowurtzitane (HNIW) were measured by the isothermal weight loss (TGA) and absorbance changes in the FTIR spectrum at 1 atm. Below 204°C, the initial 50% of decomposition follows the power rate expression  $k(T)(1 - \alpha)^n$  with  $n = 1, 2$ . The activation energy is  $36.3 \pm 0.6$  kcal/mol and  $\log A$  of  $13.6 \text{ s}^{-1}$  for  $n = 1$ . The data do not fit an autocatalytic decomposition model. Thermolysis in the 250°-400°C range was studied by the fast-heat-and-hold/FTIR technique.  $\text{N}-\text{NO}_2$  homolysis dominates the decomposition rate in the lower temperature range and  $\text{NO}_2$  is the major gas product. Several later stage decomposition reactions of HNIW are proposed in light of the nature of the gas products, their concentration ratios as a function of temperature, and information on the residue. The  $\text{NO}/\text{NO}_2$  ratio shows that oxidation of the residue by  $\text{NO}_2$  becomes increasingly important at higher temperatures.

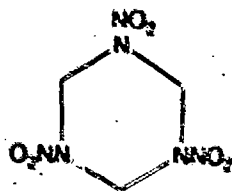
## INTRODUCTION

The three-dimensional cage structure of the polycyclic nitramine, hexanitrohexazaisowurtzitane, HNIW, provides a variable not commonly present in a nitramine molecule.

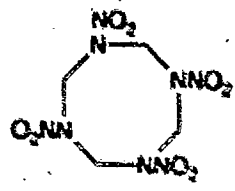


(HNIW)

Unlike the two-dimensional cyclic nitramine molecules, RDX and HMX, where decomposition by  $\text{N}-\text{NO}_2$  homolysis lowers the barrier to  $\text{C}-\text{N}$  fission [1],



(RDX)



(HMX)

radical recombination in the backbone of HNIW following  $\text{N}-\text{NO}_2$  homolysis could stabilize the  $\text{C}-\text{N}$  bond by multiple bond formation and polymerization. As a result, HMX and RDX produce only gas products upon combustion at 1 atm, whereas HNIW produces an ash along with gas products.

Previous HMX and RDX studies counsel that the experimental conditions are likely to influence the decomposition behavior of bulk sample of HNIW. In addition, the number of parallel and sequential reactions is likely to be large enough to make the full picture very difficult to develop. Our focus in this study was to determine the global thermal decomposition kinetics and gas products of a bulk sample of HNIW under isothermal conditions at low and high temperature. The goal was to gain a more specific understanding of how these kinetics are connected to the decomposition reactions of HNIW.

## EXPERIMENTAL

HNIW ( $\text{C}_6\text{H}_6\text{N}_{12}\text{O}_{12}$ ) was supplied by Dr. W. Koppes of NSWC. It was shown by IR and NMR spectroscopy to contain a negligible amount of oxo impurities and  $\text{H}_2\text{O}$ .

The essential principles of the fast-heat-and-hold experiment have been described elsewhere [2]. However, a new variation of this method has been developed [3] based on the CDS 1000 pyro-

\*Corresponding author.

probe controller incorporating a Pt ribbon filament. Typically 200  $\mu\text{g}$  of sample is thinly spread on the filament and the thermolysis is conducted in the usual manner in an Ar atmosphere [4]. A heating rate of 2000°C/s to a specified filament temperature was used. The IR beam of a Nicolet 20SX FTIR spectrometer passed several millimeters above the filament so that the gas products are detected in near real time by the rapid scan mode (10 scans/s, 4  $\text{cm}^{-1}$  resolution). Products for which IR intensities are available were quantified and shown here as relative percent concentrations [4]. HNCN was detected but could not be quantified because no intensity data are available. Endothermic and exothermic events of the sample are detected by monitoring the control voltage of the filament. The control voltage is applied to maintain a constant heat rate and final filament temperature. Hence, no thermocouple is needed. The difference trace of the control voltage (control voltage with sample present minus the control voltage with no sample present) gives the clearest representation of the thermal events.

The kinetics of solid-phase decomposition of HNIW were studied in air in the 190°-200°C range by using the Nicolet 60SX FTIR spectrometer. The HNIW sample was dissolved in  $\text{CH}_3\text{CN}$  and spread onto a NaCl plate. The solvent was then evaporated to form a thin film. This plate was then placed uncovered in the solid-phase IR cell described before [5] so that the decomposi-

tion gases could escape. The temperature was maintained isothermally by a time-proportioning controller. Thirty-two interferograms were summed per spectrum. The changes in the N-NO<sub>2</sub> modes (1605, 1325, 1266, 941, and 876  $\text{cm}^{-1}$ ) and CH stretch (2915  $\text{cm}^{-1}$ ) with time afforded the rate data.

TGA studies in air were conducted on a DuPont Instruments 951 Analyzer in the temperature range 190°-204°C. Between 1 and 2 mg of sample was used with a temperature control of  $\pm 1^\circ\text{C}$ .

### ISOTHERMAL KINETICS

The decomposition kinetics of HNIW at temperatures where the reaction is relatively slow were studied isothermally by thermogravimetrically measuring the rate of weight loss (TGA), and by quantitating the absorbance changes in the transmission IR spectrum. The relatively narrow temperature range employed for such studies is typical of energetic materials. For example, with HNIW, the reaction is very slow below 190°C while the reaction becomes quite rapid above 204°C.

Figure 1 shows the rate of the initial 50% decomposition of HNIW in air at several temperatures as measured by the rate of weight loss. These data represent the composite rate of all of the gas evolution reactions and of mass diffusion.

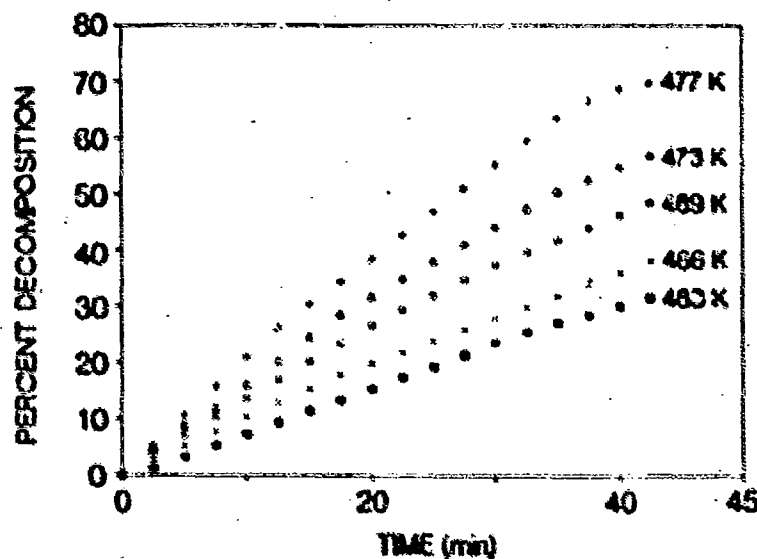


Fig. 1. Weight-loss data for HNIW at four temperatures as measured by TGA.

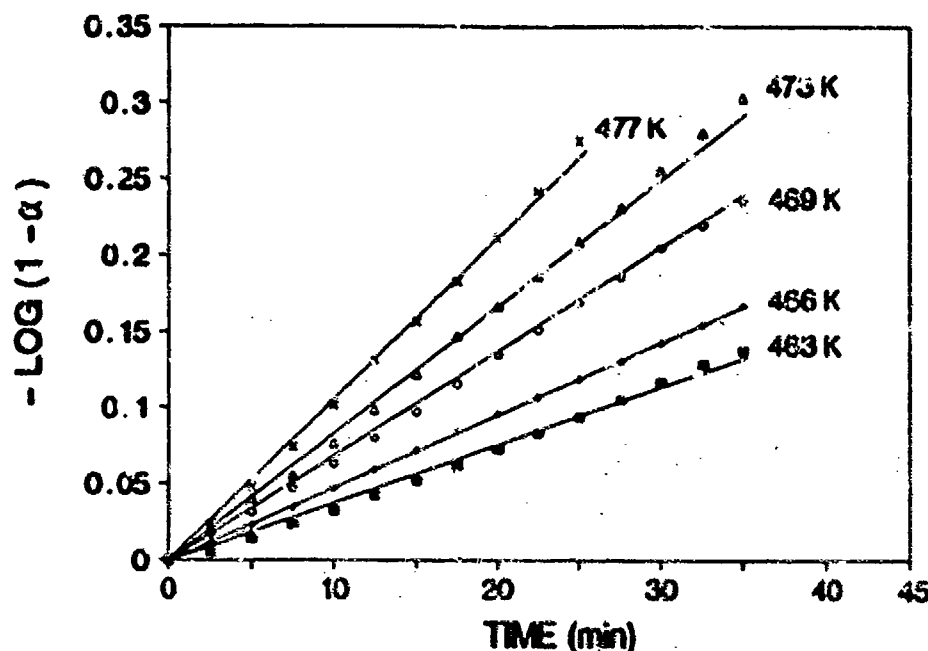


Fig. 2. The rate data for the initial 50% of decomposition on HNIW plotted with the Coats-Rossiter equation, where  $n = 1$ .

The power rate equation (Eq. 1) fits the rate of decomposition equally well when  $n = 1$  (Eq. 2) and  $n = 2$  (Eq. 3) [6].

$$\frac{d\alpha}{dt} = k(T)(1 - \alpha)^n \quad (1)$$

$$-\ln(1 - \alpha) = kt + c \quad (2)$$

$$(1 - \alpha)^{-1} - 1 = kt + c \quad (3)$$

The fraction of weight lost,  $\alpha$ , is defined as  $\alpha = (W_0 - W_t)/W_0$ . The time is  $t$ ,  $k$  is the rate constant, and  $n$  is the apparent order of the reaction.  $W_0$  is the initial sample weight and  $W_t$  is the weight at time  $t$ . Figure 2 shows the results for  $n = 1$  and Table I gives the rate constants for  $n = 1$  and  $n = 2$ . Nitramines sometimes display autocatalysis upon decomposition [7]. HNIW does

not undergo autocatalysis, as evidenced by the fact that the data do not fit the Prout-Tomkins autocatalytic model [8]. A plot of  $\log k$  vs  $1/T$  gives the apparent activation energy,  $E$ , and pre-exponential factor,  $A$ , shown in Table 2.

More detail about the relationship of the global kinetics of slow thermal decomposition to the individual reactions of HNIW is available through analysis of the changes in the IR spectrum of HNIW as a function of time at several temperatures. Since the spectral changes of interest involve the decrease in intensity of modes due to the gas-producing reactions, the variable-temperature transmission IR cell used in our work [5] was modified to permit controlled heating of a thin film of sample while allowing the gases to

TABLE I

Rate Constants ( $s^{-1}$ ) for the Decomposition of HNIW by TGA Calculated with Two Forms of the Power Rate Law (Eq. 1)

Temp (K)	$k(n=1) \times 10^4$	$k(n=2) \times 10^4$
463	0.73	1.93
466	0.87	2.34
469	1.12	2.79
473	1.47	3.60
477	2.06	5.13

TABLE 2

Activation Constants for Isothermal Decomposition of HNIW in 1 atm of Air

Decomposition	$E$ (kcal/mole)	$\log A$ ( $s^{-1}$ )
TGA	36.1 ( $n=2$ )	13.6
	33.7 ( $n=2$ )	13.1
$\alpha_{(NO_2)_1}$	36.5	13.0
$\alpha_{(NO_2)_2}$	38.3	13.2
	37.7	13.0
$\alpha_{(NO_2)_1}$	38.1	13.0
$\alpha_{(NO_2)_2}$	38.7	13.0
$\alpha_{(CH_2)}$	49.1	19.1



escape. Upon heating,  $\beta$ -HNIW converts to  $\gamma$ -HNIW so that decomposition occurs from the  $\gamma$ -polymorph. The IR spectrum of  $\gamma$ -HNIW shown in Fig. 3 reveals that modes associated with the external bonds [the C—H stretch, and bending ( $\delta$ ) and stretching ( $\nu$ ) of  $\text{NNO}_2$ ] dominate. The cage modes (C—C and C—N) are relatively weak owing to the high pseudosymmetry of the cage. The modes assigned to the  $\text{NO}_2$  group are not entirely pure  $-\text{NO}_2$  modes because of coupling with the N—N motions [9].

The rate of decrease of the area,  $A$ , of each mode assigned in Fig. 3 as a function of time was followed for the first 50% of decomposition at four temperatures.  $k$  was calculated from Eq. 2 by using  $\alpha = (A_0 - A_t)/A_0$ . The Arrhenius constants were calculated for each mode and are shown in Table 2. The values for the bending and stretching motions of the  $-\text{NO}_2$  group are the same within experimental error. The fact that the Arrhenius constants for the first 50% of decomposition measured by TGA are very similar to those for the motions of the N— $\text{NO}_2$  group is good evidence that N— $\text{NO}_2$  homolysis dominates the global rate constant for decomposition in this temperature range. On the other hand, the kinetic constants for the C—H bond (Table 2) are different which implies that the degradation of the C

—H bonds of HNIW does not control the global decomposition kinetics under these conditions.

A small amount of black amorphous residue is formed upon thermal decomposition at 1 atm. Krautle [10] has investigated this residue and found it to have the approximate stoichiometry  $\text{H}_2\text{C}_3\text{N}_2\text{O}_2$ . The IR spectrum of the residue formed at 215°C shows absorbances characteristic of C=O (1821, 1703  $\text{cm}^{-1}$ ), C=N (1594  $\text{cm}^{-1}$ , broad), and NH (3277  $\text{cm}^{-1}$ , broad). The presence of the C=O, the broad absorbance centered at 1594  $\text{cm}^{-1}$  and absorbances at 1348 and 1297  $\text{cm}^{-1}$  could be used as evidence of amides in the residue. The intensities of the absorbances vary depending on the conditions of the decomposition. No further work on this residue was performed.

The kinetics data on HNIW described above were gathered in the temperature range where decomposition occurs over a period of minutes. Of course, combustion applications involve much higher temperatures and shorter time scales. Hence, it has been necessary to develop methods to investigate the thermolysis of HNIW at higher temperatures where the decomposition rate is much faster. A useful method for such studies is the fast-heat-and-hold/FTIR spectroscopy technique [2]. Recent improvements [3] enable the

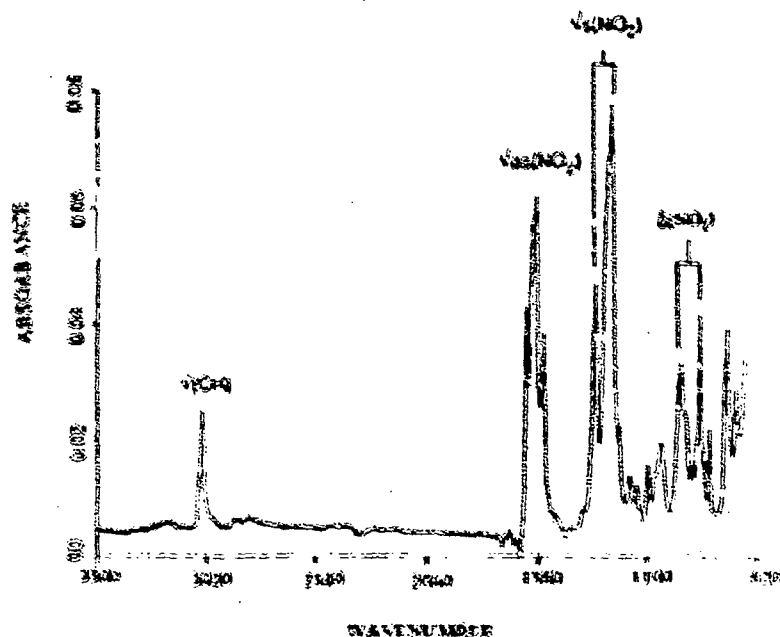


Fig. 3. The IR spectrum of a thin film of  $\gamma$ -HNIW (175°C) showing the vibrational modes whose changes in absorbance were quantified as a function of time.

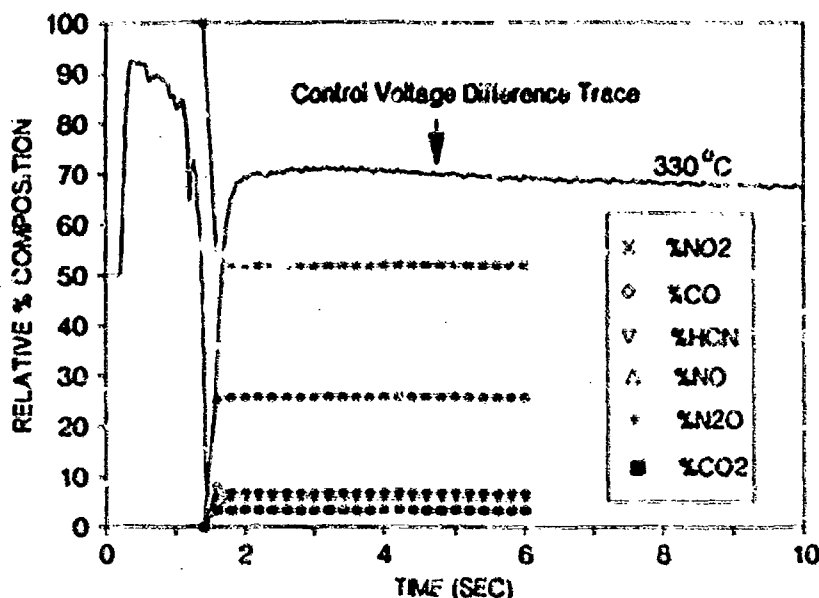


Fig. 4. The filament control voltage trace and the gas products formed several mm above the surface when 200  $\mu$ g of HNIW is heated at 2000°C/s to 330°C under 1 atm Ar.

heating rate and final temperature of a thin Pt ribbon filament to be controlled independently. A heating rate of 2000°C/s to a prescribed temperature  $T_f$  can be achieved without overshooting  $T_f$ . In this way, the sample can be heated rapidly to a known, constant temperature that is substantially higher than that available in the TGA or IR experiments described above. HNIW decomposes under near isothermal conditions with a minimal cooking time. Endothermic and exothermic events are sensed by the change in the resistance of the filament rather than by a thermocouple. A very rapidly responding control voltage is applied to the filament to maintain the heating rate and  $T_f$  in the presence of endotherms and exotherms of the sample. An endotherm requires a positive control voltage while an exotherm requires a negative control voltage to maintain a linear increase of constant filament resistance.

Figure 4 shows the control voltage trace of the filament and the quantified gas products from 200  $\mu$ g of HNIW heated at 2000°C/s to 330°C under 1 atm of Ar. The strongly exothermic decomposition reaction is shown as a negative spike in the control voltage. No gas products are detected in advance of the exotherm, indicating that autocatalysis is at most a minor process. This observation is consistent with the results of kinetics of slow decomposition described above.  $\text{NO}_2$  is the

dominant product, which is also consistent with the aforementioned  $\text{N}-\text{NO}_2$  homolysis reaction being the major initial decomposition step.

In fast-heat-and-hold/FTIR experiments at several temperatures covering the 250°–400°C range, the ratios of the final concentrations of most of the gas products remain relatively constant. Hence, the mechanism of decomposition of HNIW is qualitatively the same over this temperature range and the rate coefficients of the parallel reactions have a similar temperature dependence. The notable exception is the  $\text{NO}/\text{NO}_2$  ratio, which increases with increasing temperature (Fig. 5). Since  $\text{NO}_2$  is a primary product and  $\text{NO}$

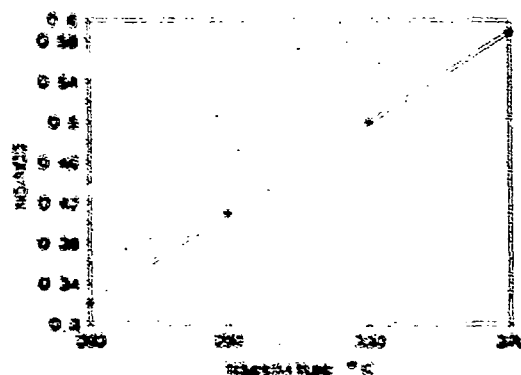
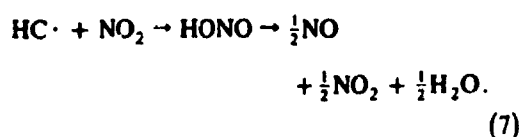
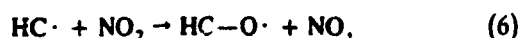
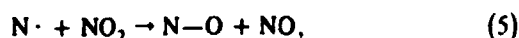
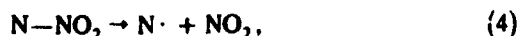


Fig. 5. The temperature dependence of the  $\text{NO}/\text{NO}_2$  gas product ratio from HNIW.

forms from the  $\text{NO}_2$ , the  $\text{NO}/\text{NO}_2$  ratio is an indication of the relative importance of secondary reactions involving  $\text{NO}_2$ . Even though  $\text{NO}_2$  is a primary product, most of it forms in a matrix of condensed phase material! As a result it can react further with other radicals in the decomposition sequence, e.g., by Eqs. 4-7. The reactions are accentuated by higher temperatures.

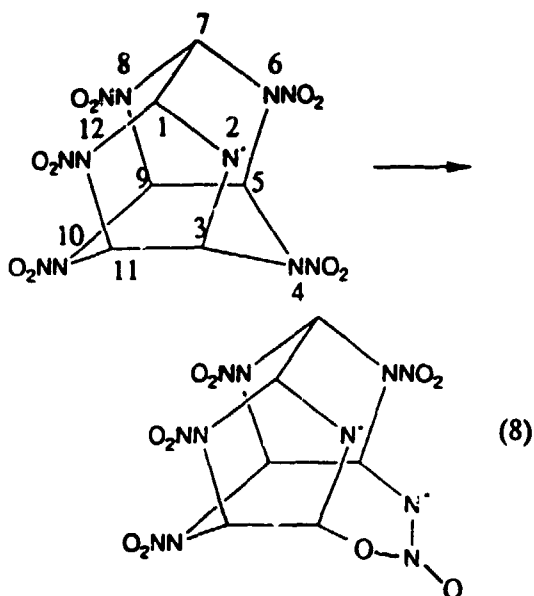


Hence, the  $\text{NO}/\text{NO}_2$  ratio is larger at higher temperatures. As noted above, the residue from the decomposition of HNIW has modes characteristic of  $\text{>C=O}$  which can form via reaction 6. The high O and N content and low C and H content of the gas products are consistent with the formation of a residue containing more C and H and less N and O, as found in the analysis performed by Krautle [10].

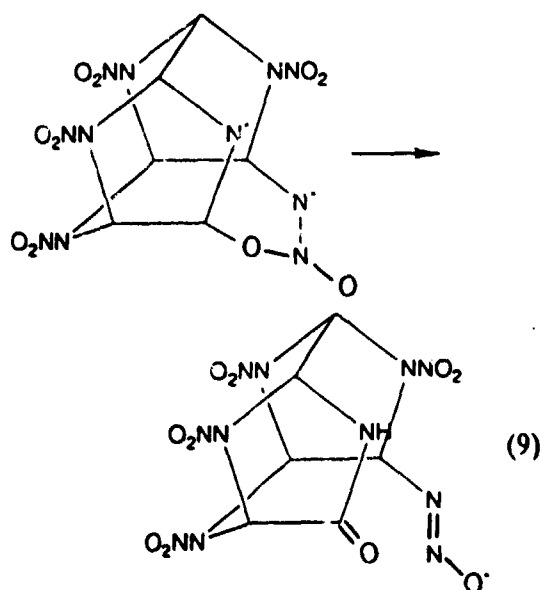
### THERMOLYSIS REACTIONS OF HNIW

As with the cyclic nitramines, HMX and RDX, many parallel reactions occur during the thermal decomposition of the polycyclic nitramine HNIW. The study described here suggests several plausible steps that take place.  $\text{N}-\text{NO}_2$  homolysis is the major step in the initial 50% of decomposition of HNIW on the basis of the large amount of  $\text{NO}_2$  liberated and the global kinetic constants. Much of the  $\text{NO}_2$  is released to the gas phase, but the T dependence of the  $\text{NO}/\text{NO}_2$  ratio indicates that the  $\text{NO}_2$  increasingly reacts with radical sites that form in the backbone at higher temperature according to Eqs. 5-7. These reactions are responsible in part for the formation of the  $\text{>C=O}$  and  $\text{>C=N-}$  bonds found in the residue.

Following the  $\text{N}-\text{NO}_2$  homolysis, many reactions of the backbone cage can occur. Several that are consistent with the data obtained in this work are shown in reactions 8-10.

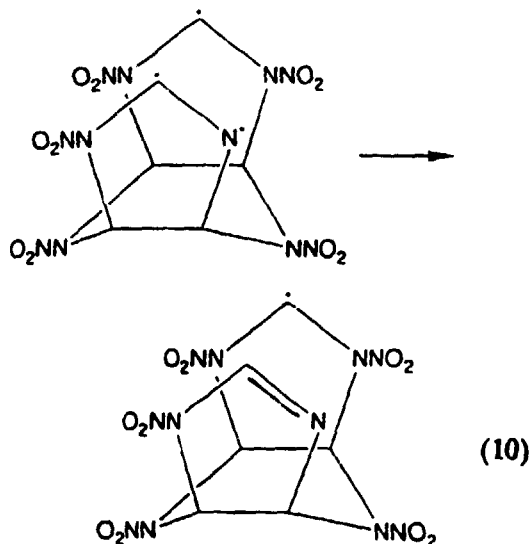


By analogy to the behavior of HMX and RDX [1],  $\text{N}-\text{NO}_2$  homolysis at (for example) N(2) would result in the weakening of the  $\text{C}(3)-\text{N}(4)$  bond. This would facilitate insertion of the  $\text{NO}_2$  unit into the bond as shown in reaction 8. This intermediate product could react further in several ways, including reaction 9, which could be a source of  $\text{N}_2\text{O}$ , as well as some of the carbonyl containing residue. In addition, a  $\text{C}-\text{C}$  bond such as  $\text{C}(1)-\text{C}(7)$ .



could cleave leading to adjacent radical sites which might recombine to form  $\text{>C=N-}$ , as in

reaction 10. The IR spectrum of the residue shows modes in the C=N region.



The formation of a small amount of HONO was sometimes observed and is understandable as a result of radical scavenging in these systems by  $\cdot\text{NO}_2$  [11], as in reaction 7. HNCO appears to be formed from nitramines by the decomposition of amide residues in the condensed phase [12], such as could form in reaction 9. HCN and CO are products commonly formed during nitramine decomposition and can arise in many ways from HNIW.

## SUMMARY

1. A power rate law equation with  $n = 1$  or  $2$  fits the rate of the initial 50% of weight loss equally well. Autocatalysis does not appear to occur during the decomposition of HNIW.
2. The global kinetics of slow decomposition of HNIW is dominated by N- $\text{NO}_2$  homolysis. The residue that forms from this reaction con-

tains C=O, C=N, and NH bonds, whose formation is understandable in terms of reactions expected of radical sites in the polycyclic cage.

3. The NO/ $\text{NO}_2$  gas products ratio depends on the temperature and favors NO at higher temperature. This pattern is consistent with increased oxidation of the residue by  $\text{NO}_2$  as the temperature at which decomposition occurs is raised.

*We are grateful to Dr. W. Koppes for supplying a sample of HNIW, and to the Air Force Office of Scientific Research, Aerospace Sciences, for support of this work on AFOSR-89-0521.*

## REFERENCES

1. Melius, C. F., and Binkley, J. S., *Twenty-First Symposium (International) on Combustion*, The Combustion Institute, Pittsburgh, PA, 1986, pp. 1953-1963.
2. Brill, T. B., and Brush, P. D., *Proceedings of the Ninth Symposium (International) Detonation*, Portland, OR, vol. 1, pp. 228-234 (1989).
3. Brush, P. D., and Brill, T. B., to be published.
4. Oyumi, Y., and Brill, T. B., *Combust. Flame* 62:213-224 (1985).
5. Karpowicz, R. J., and Brill, T. B., *Appl. Spectrosc.* 37:79-81 (1983).
6. Coats, A. W., and Redfern, J. P., *Nature* 201:68-69 (1964).
7. Dubovitskii, F. I., and Korsunskii, B. L., *Russ. Chem. Rev.* 50:958-978 (1981).
8. Prout, E. G., and Tompkins, F. C., *Trans. Farad. Soc.* 42:468-472 (1945).
9. Trinquesco, C., Rey-Lafon, M. and Forel, M. T., *J. Chim. Phys.* 72:689-696 (1975).
10. Krautle, K. J., NWC, personal communication, 1990.
11. Brill, T. B., and Oyumi, Y., *J. Phys. Chem.* 90:6848-6853 (1986).
12. Palopoli, S. F., and Brill, T. B., *Combust. Flame*, in press.

*Received 31 January 1991; revised 26 June 1991*

## Chemistry and Kinetics of Hydroxyl-terminated Polybutadiene (HTPB) and Diisocyanate-HTPB Polymers during Slow Decomposition and Combustion-like Conditions

J. K. CHEN and T. B. BRILL\*

*Department of Chemistry, University of Delaware, Newark, DE 19716*

The decomposition chemistry and kinetics of hydroxyl-terminated polybutadiene (HTPB), hydroxyl-terminated polyethyleneglycol adipate (HTPA), and diisocyanate cross-linked HTPB (diisocyanates = TDI, IPDI, and DDI) were determined by TGA, DSC, and IR spectroscopy at 10°C/min and by SMATCH/FTIR at 250°–350°C/s. At 10°C/min, the first step (300°–400°C) for diisocyanate-HTPB is fission of the urethane cross-link bonds. The diisocyanate cross-linking agent is vaporized to an extent that is controlled by its vapor pressure. The HTPB polymer then exothermically cross-links and cyclizes, but also depolymerizes to yield volatile products. The overall exothermicity of these steps is proportional to the number of double bonds in the parent polymer. Above 400°C, the final major stage is endothermic decomposition of the mostly saturated residue of HTPB formed in the 300°–400°C range. The kinetics of this final step are independent of whether the original polymer contained urethane cross-links or not. SMATCH/FTIR spectroscopy simulates the conditions in the condensed phase during combustion at 15 psi, as evidenced by the fact that the regression rates calculated for HTPB (from the SMATCH/FTIR kinetics at 250°–350°C/sec fall within the range of combustion-like regression rates of IPDI-HTPB and similar polymers (0.05–0.2 mm/s at 15 psi). SMATCH/FTIR spectroscopy establishes that under combustion-like conditions, the urethane cross-links cleave in the first step, but that less cyclization of the residual HTPB occurs because of the shorter time available. Hence, no initial exotherm appears. Instead, HTPB skips directly to depolymerization, giving up butadiene, butadiene oligomers, and CH<sub>2</sub>O to the first stage of the flame zone.

### INTRODUCTION

Diisocyanate cross-linked hydroxyl-terminated polybutadiene (HTPB) is the most commonly used binder in solid composite rocket propellants. Aside from providing favorable mechanical properties after highly loading the polymer matrix with particulate aluminum and NH<sub>4</sub>ClO<sub>4</sub> (AP), curing of the HTPB with a diisocyanate cross-linking agent can be effected at a low enough temperature to prevent decomposition of the AP. Moreover, the decomposition products of the binder contribute additional fuel to the flame zone during combustion. The kinetics and mechanism of degradation of these polymers is the major topic of this article. Insight into the binder pyrolysis reactions is especially important in combustion modeling because models, such as BDP [1] and the leading edge flame model [2], consider the binder and oxidizer products to be spatially

separated for a short distance above the surface before they mix to become the diffusion flame.

Considerable effort has been devoted to heating polymers rapidly enough to enable calculation of kinetics relevant to combustion [3–15]. In turn, inferences about the chemical mechanisms have been made from these data. Beck recently evaluated much of this work [16]. A common aspect of all of these past kinetic studies is that chemical mechanisms tend to be inferred without any chemical measurements actually having been made. In fact, the designs of all of these fast heating methods are poorly suited for simultaneous measurement of the reaction rate and products in any connected way. This disadvantage makes the mechanistic inferences about chemistry almost entirely speculative.

To enable the fast kinetics to be measured simultaneously with chemical analysis, the Simultaneous *MA*ss and *TE*mperature *CH*ange (SMATCH)/FTIR technique was developed [17]. With SMATCH/FTIR spectroscopy, a thin film of material can be heated at a rate of 100°–

\*Corresponding author.

350°C/s with the simultaneous measurements of dynamic mass change, temperature change, and near-surface gas products. The thin film of rapidly heated polymer is a "snapshot" simulation of the condensed phase at a burning surface. The mass and temperature data enable Arrhenius constants for the regression of the surface reaction zone to be determined [18, 19]. Confidence that this simulation of the surface reaction zone during combustion is reasonably accurate is bolstered by the fact that the Arrhenius constants from SMATCH/FTIR predict the experimental burning rates of energetic nitrate ester [18] and organoazide [19] polymers at the same pressure and temperature conditions. The gas products detected near the surface should, therefore, be very similar to those that leave the surface and initiate the flame zone, were a flame to be present. It is also gratifying that the products detected by SMATCH/FTIR are very similar to those observed by our other fast thermolysis/FTIR techniques [20], which implies that fast thermolysis/FTIR spectroscopy also gives a reasonably good indication of the gases that leave the surface and enter the earliest stages of the flame zone during combustion.

In addition to high-rate kinetics studies, the kinetics and products of thermolysis of HTPB and diisocyanate cross-linked HTPB were determined at a low heating rate by DSC, TGA, and gas- and condensed-phase IR spectroscopy. It is widely cautioned that such studies should not be routinely used to describe the combustion regime [5, 8, 11, 13, 19], but they may be applicable in some instances [21]. At the very least establishment of the different processes that occur with these polymers as a function of the heating rate gives insight into the relative roles of the many possible decomposition branches.

## EXPERIMENTAL

### Materials

A sample of HTPB (ARCO R45M, Lot 003097) was obtained from S.F. Palopoli, Thiokol Corp., Elkton, MD. Its equivalent weight based on OH is 1300. Samples of TDI, IPDI, and DDI were also supplied by S.F. Palopoli and were protected from moisture. The equivalent weights of TDI, IPDI, and DDI are 87, 111, and 300, respec-

tively. HTPA was provided by B. Goshgarian, AFAL, Edwards AFB, CA. HTPB was heated to 60°C under vacuum in a rotary evaporator for 2 h to remove any water. It was then stored in a desiccator. The diisocyanate-HTPB cross-linked polymers were prepared by mixing HTPB and the diisocyanate in an OH:NCO ratio of 1:1 and curing at 60°C for 10 days. For the SMATCH/FTIR and solid-phase studies, the samples were partially cured at 60°C and the gumstock was smeared directly onto an NaCl plate or the metal end-tip of the SMATCH device. The curing process was then continued for a total of 10 days. Pure HTPB and HTPA were smeared directly onto the end-tip or NaCl plate for decomposition studies of these samples.

### TGA-DSC Measurements

Thermogravimetric analysis (TGA), differential thermogravimetric analysis (DTG), and differential scanning calorimetry (DSC) measurements were made on a DuPont Instruments 2000 Analyzer with a model 951 TGA module and 910 DSC module. A linear heating rate of 10°C/min and 4–6 mg of sample were used in all cases. An Ar flow rate of 5 ml/min was used for DSC while 20 ml/min was used for TGA.

### IR Spectra of the Solid Phase

The residues of the cross-linked and pure HTPB samples were studied by placing the sample directly onto an NaCl plate. The plate was then heated in the TGA furnace at a 10°C/min linear heating rate with a 20 ml/min Ar flow rate. At the desired temperature, the plate was removed and the IR spectrum was recorded on a Nicolet 60SX FTIR spectrometer at 2 cm<sup>-1</sup> resolution and 32 accumulated scans. A fresh sample was used for each temperature.

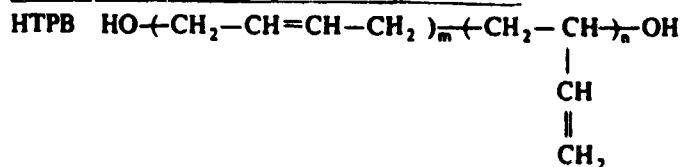
### SMATCH/FTIR Spectroscopy

The SMATCH/FTIR technique has been described before [17, 18]. A cantilevered quartz tube whose natural frequency depends on the sample mass coating the metal end-tip was set into motion by a vibration exciter. Typically, 0.2–0.8 mg of sample was used giving a film thickness of 22–88 μm. The metal end-tip was heated by RF induction at a chosen rate in the

250°–350°C/s range by using a 1-KW RF power supply. The film thickness and heating rate are matched so that the heat transfer across the film is fast enough to give a reasonably uniform temperature [18]. The dynamic weight change during the decomposition step was measured by the rate of change of the vibrational frequency of the tube. The temperature was simultaneously monitored by a type E thermocouple spot-welded to the metal end-tip and in contact with the sample film. The IR beam of the Nicolet 60SX FTIR spectrometer operating in the rapid-scan mode (10 scans/s, 2 spectra per file, and 4 cm<sup>-1</sup> resolution) was focused within 3 mm of the top surface of the end-tip. In this way the gas products evolve into the cool atmosphere of Ar in the cell. The pressure on the sample was 15 psi. Considerable care was taken to obtain a uniform thickness of the sample film because a nonuniform film resulted in a poorly shaped weight-loss curve.

#### Fast Thermolysis/FTIR Spectroscopy

Gas products from these samples were also monitored by the fast thermolysis/FTIR technique



The amount of each of these three units can be controlled in the synthesis, but all three structural components are present in propellant-grade HTPB. OH groups terminate the chains. Considerable work has been conducted on the thermal decomposition of polybutadiene at a heating rate of several °C/min [23–30] and at high temperature [14]. These results are quite useful for characterizing the behavior of HTPB. In fact, Du [31] recently extended these polybutadiene studies to HTPB by using DSC, TGA, gas chromatography, and mass spectrometry. The sample used had somewhat different composition from the one employed in this project. Several parameters for our sample compared with those of Du (parenthetical values) are equivalent weight = 1300 g/Eq (2300), % trans = 54.8 (62), % cis = 20.2 (14), % vinyl = 25 (21), and % weight remaining at 500°C = 2 (14). The general features of decomposition of the two samples are

[22]. About 2 mg of the sample was placed on the nichrome ribbon filament. The cell was purged with Ar and adjusted to 15 psi. The IR beam of the Nicolet 60SX was focused several millimeters above the surface of the sample. With the spectrometer scanning at 10 scans/s and accumulating two spectra per file at 4 cm<sup>-1</sup> resolution, voltage was applied to the filament. Ramp heating occurred for the first 3–4 s until the final filament temperature was reached. This temperature was then maintained for about 10 s. The temperature of the filament was monitored in real time by a type E thermocouple that was spot welded to the underside. The output was amplified, passed into an AD converter and to an IBM PC. The spectral files and thermocouple trace were correlated by time.

## RESULTS AND DISCUSSION

### Thermolysis of HTPB at 10°C/min

HTPB, whose connectivity is shown below, consists of a mixture of cis and trans units in the *m* portion of the molecule and 1,2-vinyl units:

similar, but differ in some of the details. Also, our kinetic analysis procedure is different. A reinvestigation of pure HTPB was undertaken so that the effect of urethane cross-linking of HTPB could be determined.

Figure 1 shows the TG, DTG, and DSC traces of HTPB heated at 10°C/min to 550°C. As noted by Du [31], the DTG trace shows that weight is lost in two main steps, although further substeps are evident in the overall process. By DSC, the initial weight loss step is net exothermic, while the second step is endothermic overall. The initial exotherm results from the positive energy balance of the endothermic depolymerization process and the exothermic cyclization and cross-linking process of the HTPB that has not undergone depolymerization. The sample loses weight during this first step because lower-molecular-weight hydrocarbons, such as 1,3-butadiene (C<sub>4</sub>H<sub>6</sub>) and 4-

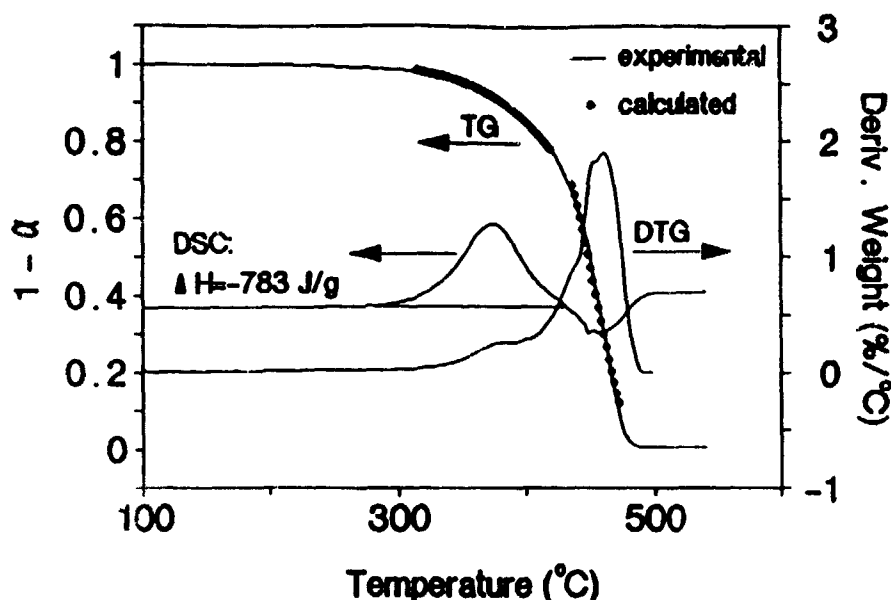


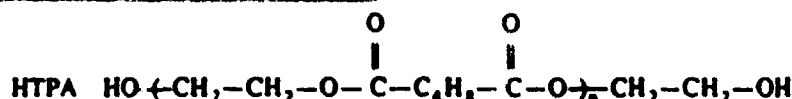
Fig. 1. TGA, DTG, and DSC traces for HTPB at a heating rate of 10°C/min under a 5–20-ml/min flow of Ar.

vinylcyclohexene ( $C_8H_{12}$ ), volatilize. These processes are essentially the same as those that occur with polybutadiene [14, 23–30].

The second main weight-loss step of HTPB is mostly the result of depolymerization of the cross-linked residue formed in the cyclization and cross-linking reactions of the first decomposition step. Du noted that butadiene continues to be released in the first part of this second step [31],

indicating that some unsaturation remains in the residue after the initial exothermic step ends. The second step is endothermic because of the predominance of bond-breaking (depolymerization) in the residue and desorption of the fragments.

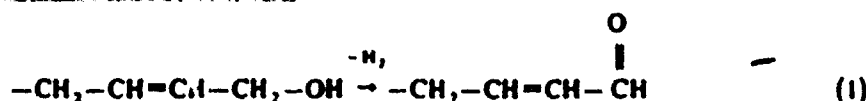
A study of hydroxyl-terminated polyethyleneglycol adipate (HTPA) was undertaken to help confirm the essential features of the decomposition scheme proposed



for HTPB. HTPA lacks unsaturation in the hydrocarbon backbone. Accordingly, no exothermic first stage process should occur because cross-linking and cyclization involving the backbone are not possible. Only the endothermic second stage of decomposition resulting from depolymerization and desorption should be present. Figure 2 verifies these expectations and supports the scheme described above for HTPB.

Further details about the chemical events in HTPB were gained from the IR spectrum of the condensed phase and gas products as a function

of temperature. Figure 3 shows the main changes in the mid-IR spectrum of films of HTPB heated to four temperatures covering most of the decomposition temperature range. At 240°C, which is below the temperature range where detectable weight loss occurs, an absorbance appears at 1694  $\text{cm}^{-1}$  that is characteristic of an  $\alpha, \beta$ -unsaturated carbonyl group. Reactions 1 and 2 are the main reasons. The absorption intensity of  $\nu$  ( $\text{C}=\text{O}$ ) is very large, which explains why  $\nu$  ( $\text{C}=\text{O}$ ) can be detected even though there





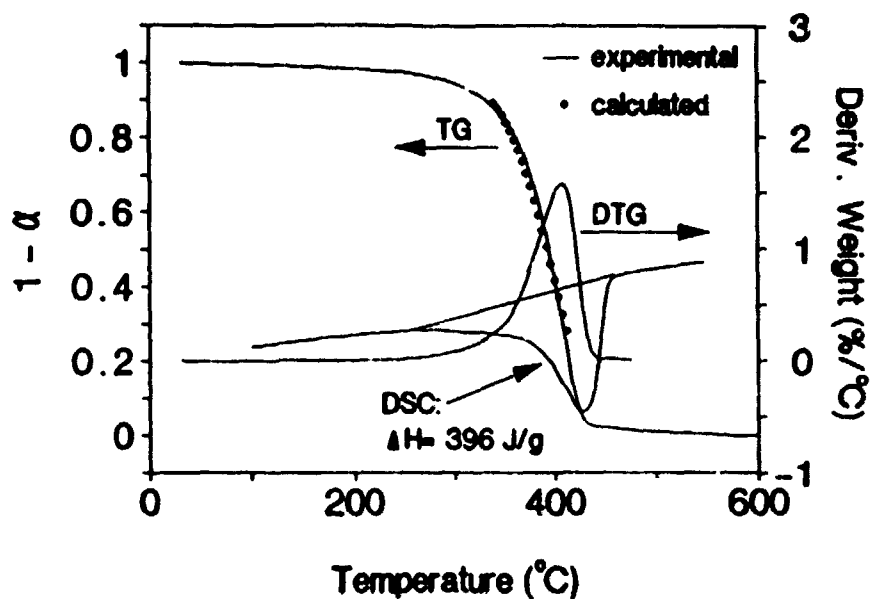


Fig. 2. TGA, DTG, and DSC traces for HTPA at a heating rate of  $10^{\circ}\text{C}/\text{min}$  under a 5-20-ml/min flow of Ar.

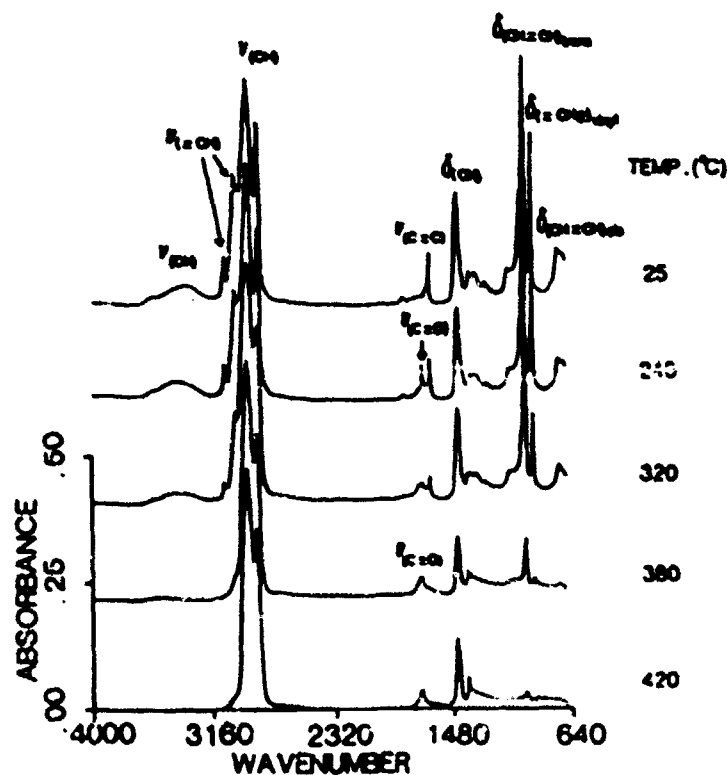
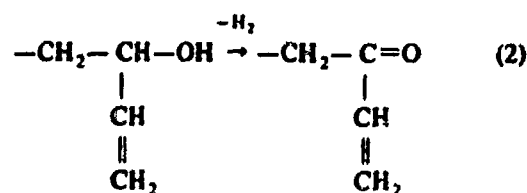
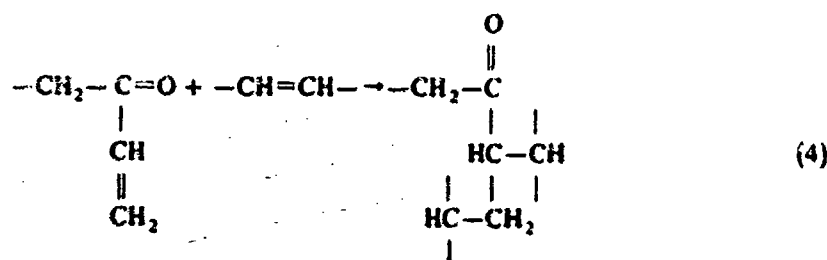
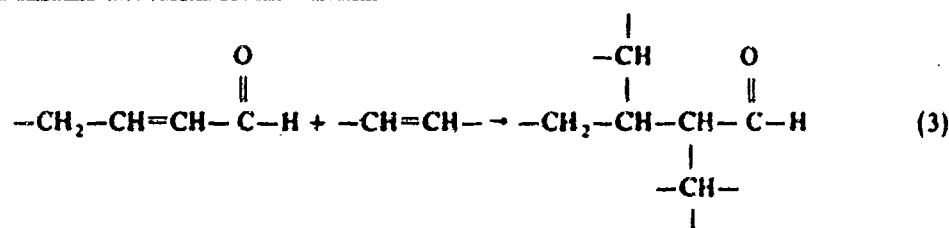


Fig. 3. IR spectra of the residue of HTPB heated to the temperatures shown at  $10^{\circ}\text{C}/\text{min}$  in TGA furnace under an Ar atmosphere.



is only one -OH group per 24 butadiene units in the sample used for this work. The weight of  $\text{H}_2$  lost from the polymer in reactions 1 and 2 is too

small to be detected clearly by TGA. At  $320^\circ\text{C}$  during the exotherm, the cross-linking and cyclization reactions leading to saturation of the  $\text{C}=\text{C}$  double bonds in the products of reactions 1 and 2 are indicated by the appearance of a new  $\text{C}=\text{O}$  mode at  $1704\text{ cm}^{-1}$ . A carbonyl stretching frequency will increase when an adjacent double bond becomes saturated. Cross-linking reactions of the type shown in reactions 3 and 4 explain the  $\text{C}=\text{O}$  frequency shift from  $1694$  to  $1704\text{ cm}^{-1}$ .



In keeping with the cross-linking and saturation reactions 3 and 4, modes characteristic of  $\text{C}=\text{C}$  are absent at  $420^\circ\text{C}$ . The indicative modes that disappear are *cis*- $\text{RCH}=\text{CHR}$  ( $721\text{ cm}^{-1}$ ),

$\text{CH}=\text{CH}_2$  ( $909$  and  $991\text{ cm}^{-1}$ ), *trans*- $\text{RHC}=\text{CHR}$  ( $963\text{ cm}^{-1}$ ),  $\text{C}=\text{C}$  ( $1637\text{ cm}^{-1}$ ), and  $=\text{CH}_2$  ( $3001$ ,  $3072\text{ cm}^{-1}$ ). Volatilization of unsaturated fragments, such as butadiene and 4-

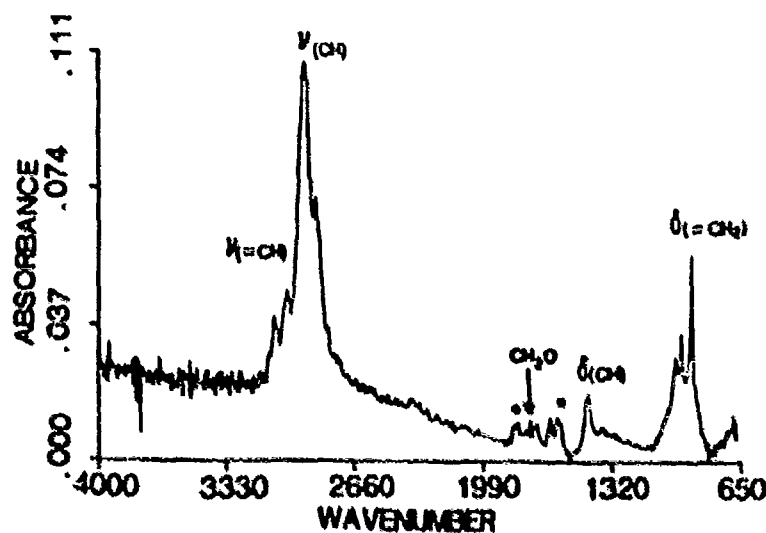
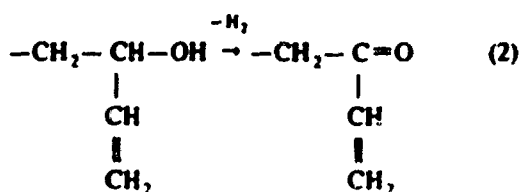
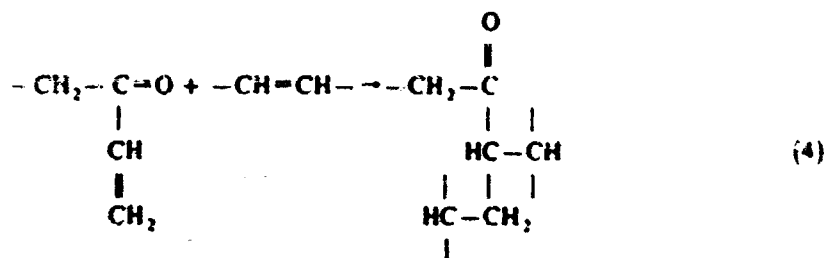
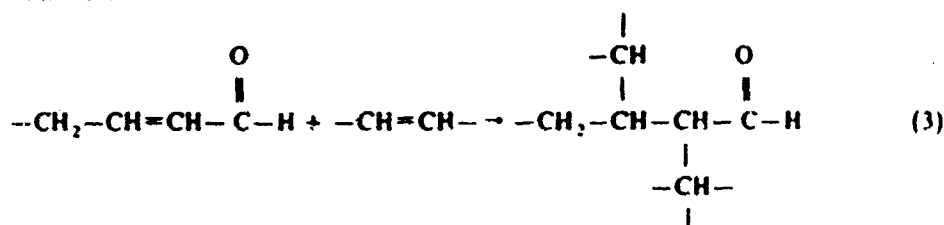


Fig. 4. The IR spectrum of the gas products 3 mm above the surface of a sample of HTPB during heating of the sample at  $100^\circ\text{C}/\text{s}$ . The sample was at  $450^\circ\text{C}$  when this spectrum was recorded. Both butadiene and 4-vinylcyclohexene are present. The starred peaks are from butadiene.



is only one -OH group per 24 butadiene units in the sample used for this work. The weight of  $\text{H}_2$  lost from the polymer in reactions 1 and 2 is too

small to be detected clearly by TGA. At  $320^\circ\text{C}$  during the exotherm, the cross-linking and cyclization reactions leading to saturation of the  $\text{C}=\text{C}$  double bonds in the products of reactions 1 and 2 are indicated by the appearance of a new  $\text{C}=\text{O}$  mode at  $1704\text{ cm}^{-1}$ . A carbonyl stretching frequency will increase when an adjacent double bond becomes saturated. Cross-linking reactions of the type shown in reactions 3 and 4 explain the  $\text{C}=\text{O}$  frequency shift from  $1694$  to  $1704\text{ cm}^{-1}$ .



In keeping with the cross-linking and saturation reactions 3 and 4, modes characteristic of  $\text{C}=\text{C}$  are absent at  $420^\circ\text{C}$ . The indicative modes that disappear are  $\text{cis-RHC}=\text{CHR}$  ( $721\text{ cm}^{-1}$ ).

$\text{CH}=\text{CH}_2$  ( $909$  and  $991\text{ cm}^{-1}$ ),  $\text{trans-RHC}=\text{CHR}$  ( $963\text{ cm}^{-1}$ ),  $\text{C}=\text{C}$  ( $1637\text{ cm}^{-1}$ ), and  $=\text{CH}_2$  ( $3001$ ,  $3072\text{ cm}^{-1}$ ). Volatilization of unsaturated fragments, such as butadiene and 4-

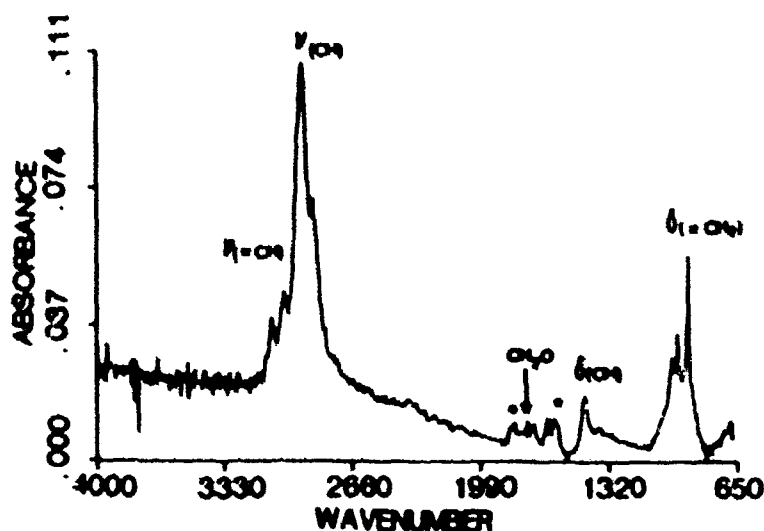


Fig. 4. The IR spectrum of the gas products 3 mm above the surface of a sample of HTPB during heating of the sample at  $100^\circ\text{C}/\text{s}$ . The sample was at  $430^\circ\text{C}$  when this spectrum was recorded. Both butadiene and 4-vinylcyclohexene are present. The starred peaks are from butadiene.

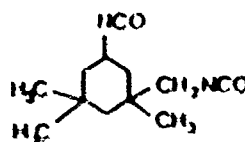
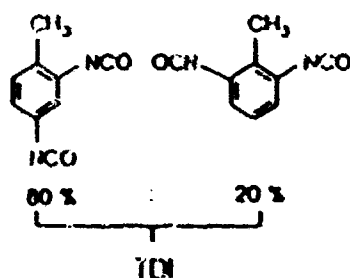
vinylcyclohexene, also occurs by this temperature and contributes to the disappearance of modes associated with unsaturation. The  $^1\text{H}$  NMR spectrum corroborates these observations. The  $-\text{CH}=$  ( $\delta = 5.4$  ppm),  $=\text{CH}_2$  ( $\delta = 5.0$  ppm), and  $-\text{CH}_2\text{C}=$  ( $\delta = 2.0$  ppm) signals of an authentic sample of HTPB disappear when the sample is heated to  $420^\circ\text{C}$ . The  $^1\text{H}$  NMR spectrum of the residue contains only a broad signal covering the  $\delta = 0.4$ – $3.0$ -ppm range that arises from various nonequivalent, saturated  $\text{CH}_2$  and  $\text{CH}$  groups.

The IR spectrum of the gas-phase products that appear several millimeters above the surface of a sample of HTPB heated at about  $100^\circ\text{C/s}$  to about  $450^\circ\text{C}$  is shown in Figure 4. The spectrum was taken as the sample reached  $450^\circ\text{C}$ . The absorbances in Fig. 4 closely match those of

butadiene and the dimer of butadiene, 4-vinylcyclohexene [27]. The 4-vinylcyclohexene could form from stabilization of the dibutadiene biradical or by a Diels-Alder cyclization reaction of two butadiene molecules [22].  $\text{CH}_2\text{O}$  is also detected, indicating how the alcohol chain terminus is liberated.

#### Thermolysis of Diisocyanate Cross-Linked HTPB at $10^\circ\text{C/min}$

Composite rocket propellants are cast with HTPB and cured to a solid by the addition of a diisocyanate cross-linking agent. Several diisocyanates of interest are dimethyl diisocyanate (DDI), toluene diisocyanate (TDI), and isophorone diisocyanate



(IPDI). In practice, IPDI and DDI are most frequently used. After the addition of one equivalent of the diisocyanate, the HTPB was cured for 10 days at  $60^\circ\text{C}$ . The urethane linkage shown in reaction 5 forms and is responsible for hardening of the polymer



Figure 5 shows the TG, DTG, and DSC traces of the three types of cross-linked polymers heated at  $10^\circ\text{C/min}$  in a flow of Ar. HTPB samples cured with TDI and IPDI have two clearly resolved weight loss steps in the first stage of decomposition (the depolymerization, cross-linking, and cyclization stage of pure HTPB). The temperature at which these events occur depends on the cross-linking agent. More than one step probably exists for the DDI-HTPB sample, but the temperatures are not different enough to dis-

tinguish the steps. The first step is most likely associated with cleavage of the urethane cross-links and the second step is the cross-linking and depolymerization of the HTPB backbone.

The presence of these overall reactions is confirmed by the IR spectrum of the residue of each sample heated to a set temperature. These spectra are shown in Figs. 6–8. In all cases the spectra are consistent with cleavage of the urethane cross-link (the reverse of reaction 5) being the first major reaction in the decomposition sequence. This is because an absorbance characteristic of  $-\text{NCO}$  at  $2265\text{ cm}^{-1}$  either formed or grew by  $220^\circ\text{C}$ . Between  $220^\circ$  and  $300^\circ\text{C}$  further dissociation of the urethane linkage is evident in the decrease of the IR absorptions at  $3338\text{ cm}^{-1}$  ( $\text{NH}$ ),  $1704\text{ cm}^{-1}$  ( $\text{C}=\text{O}$ ),  $1510\text{ cm}^{-1}$  ( $\text{CNH}$ ), and  $1232\text{ cm}^{-1}$  ( $\text{C}-\text{O}$ ). Others have concluded that the urethane linkage of cured HTPB is the first bond to cleave during thermal decomposition [12, 33, 34]. The present data reinforce this

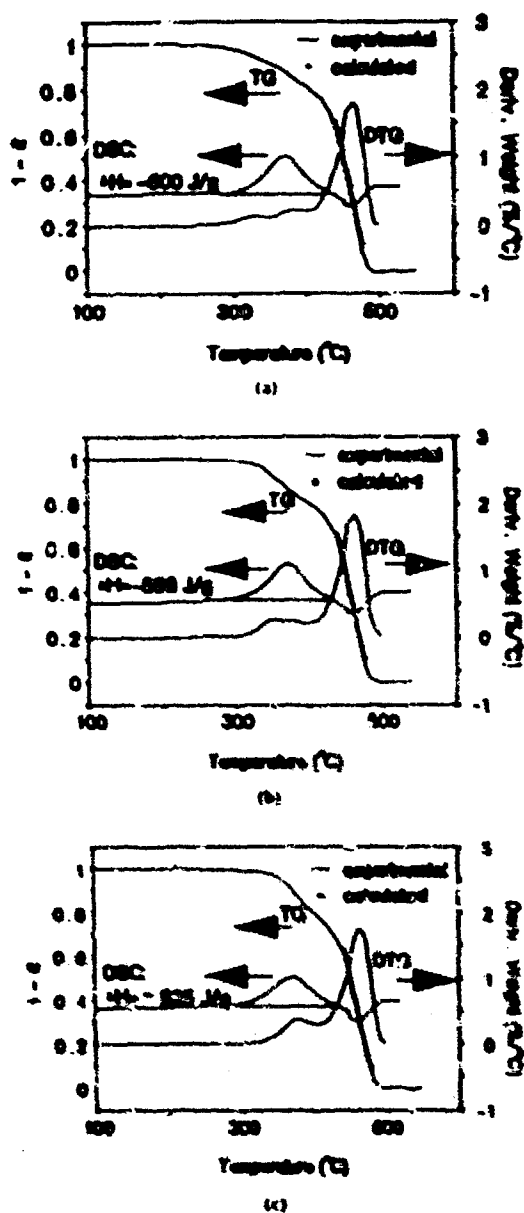


Fig. 5. The TGA, DTG, and DSC traces of TDI-HTPB (a), IPDI-HTPB (b) and DDI-HTPB (c) heated at 10°C/min under a 5–20 ml/min flowing atmosphere of Ar.

Also, saturation and volatilization of fragments containing C=C bonds occur as indicated by the loss of intensity of the absorbances characteristic of C=C given in the previous subsection. It is interesting to note that the residues of all three products at 420°C in Figs. 6–8 have the same IR spectrum as that of the residue from pure HTPB shown in Fig. 3. This result indicates that once the urethane linkages cleave and the parent

diisocyanate volatilizes, the HTPB residue behaves essentially as though it had never been urethane cross-linked.

The gas products that appear in near real-time several millimeters above the surface of these cross-linked polymers add further support for the reaction scheme described above. These gas products are shown in Figs. 9–11 and occur from a sample of each polymer heated at about 100°C/s to 450°C. The most important point is illustrated with the data for TDI-HTPB. The initially detected products contain the —NCO group and CO<sub>2</sub>. The —NCO group comes from cleavage and volatilization of the isocyanate cross-linking agent. CO<sub>2</sub> can form by decarboxylation of the urethane linkage as shown in reaction (6):



After these products from the urethane linkage appear, absorptions associated with the HTPB backbone fragments begin to appear at higher temperature. The separation of these events is less clear in the IPDI-HTPB and DDI-HTPB data shown in Figs. 10 and 11 because of the lower volatility of IPDI and DDI as discussed below.

The temperature of the onset of weight loss in these cross-linked polymers follows the order TDI-HTPB < IPDI-HTPB < DDI-HTPB according to Fig. 5. This trend follows the boiling temperatures of the parent isocyanate: TDI (121°C at 1.33 kPa) < IPDI (158°C at 1.3 kPa) < DDI (nonvolatile). Thus, the urethane linkages dissociate on heating in part to give the parent isocyanate molecule whose rate of escape from the matrix is controlled by its vapor pressure.

According to the DSC data in Figs. 1 and 5 the exothermicity of the first stage of decomposition follows the order HTPB > TDI-HTPB > IPDI-HTPB > DDI-HTPB. The trend follows the weight fraction of HTPB in the polymers, which is summarized in Table I. As the amount of HTPB in the sample decreases, the number of C=C bonds decreases, which suggests that the number of C=C bonds in the polymer mainly controls the amount of energy released in the first step. The exothermicity results from the energy released in the cross-linking and cyclization involving the C=C bonds of the HTPB backbone.

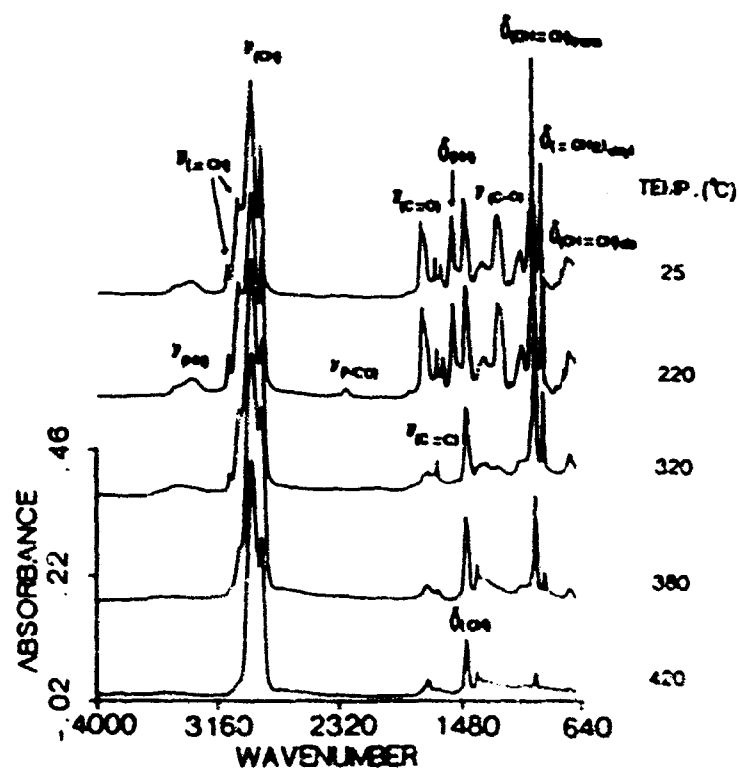


Fig. 6 IR spectrum of the residue of TDI-HTPB heated to the temperature shown at 10°C/min in an Ar atmosphere.

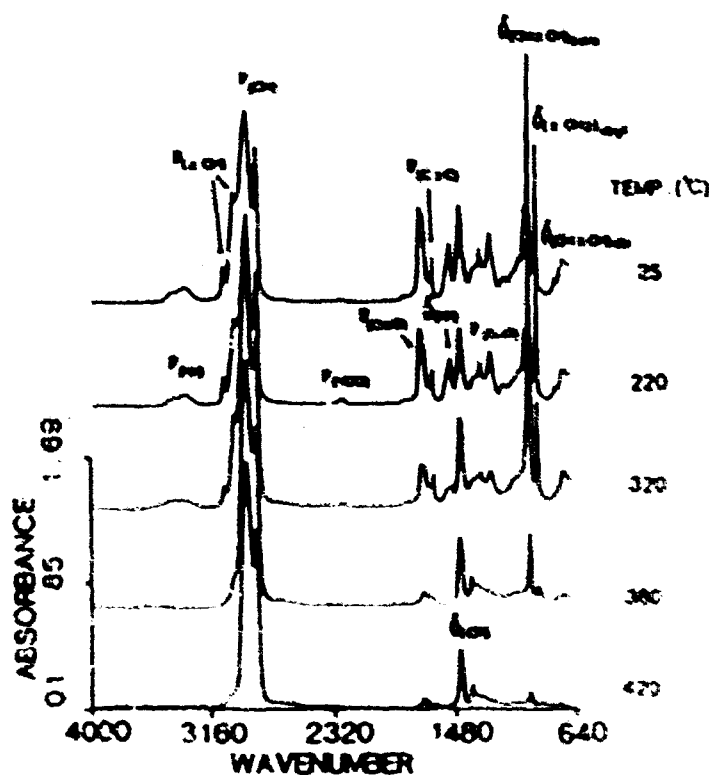


Fig. 7 IR spectrum of the residue of HTPB-HTPB heated to the temperature shown at 10°C/min in an Ar atmosphere.

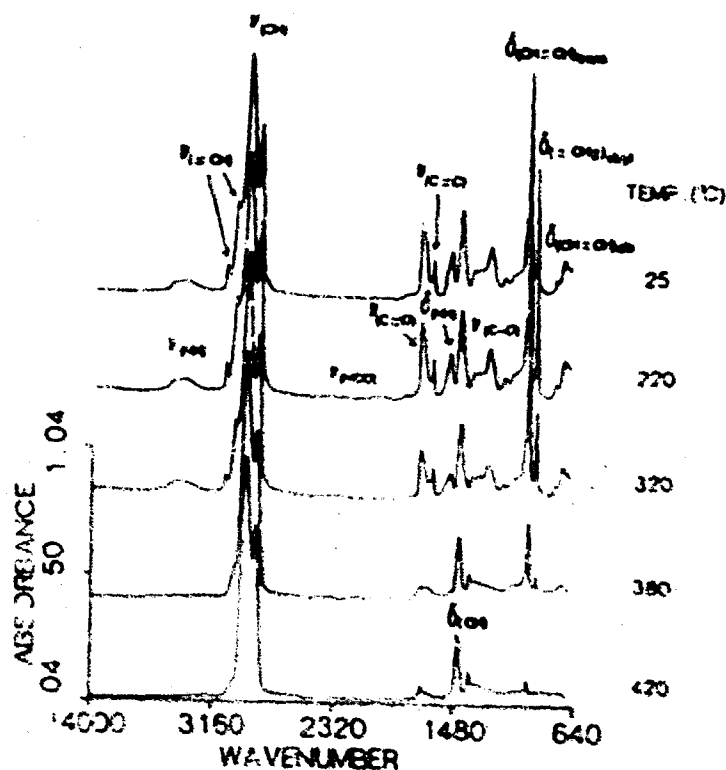


Fig. 8. IR spectra of the residue of LDI HTPB heated to the temperatures shown at 10°C/min in 10 psi Ar atmosphere.

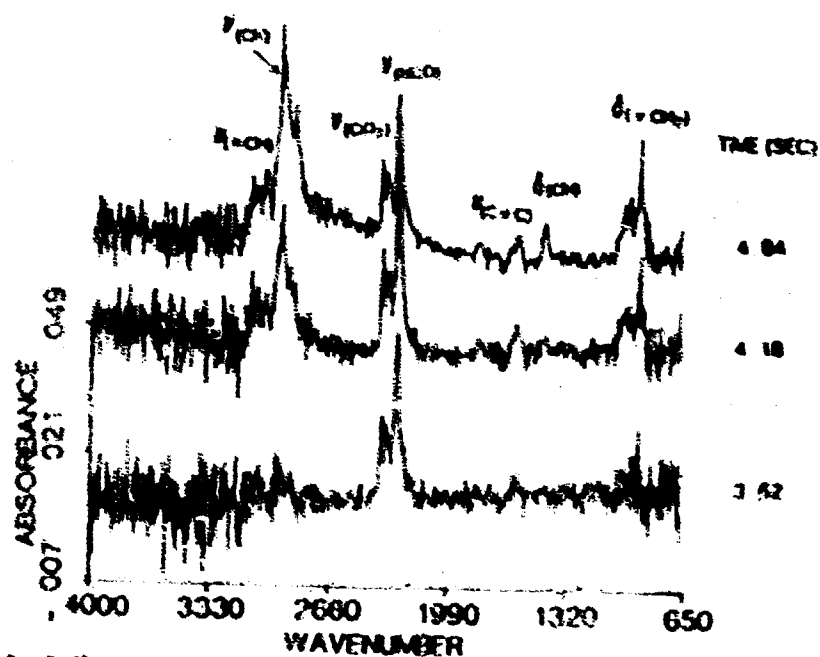


Fig. 9. IR spectra of the gas products from the surface of LDI HTPB at the times shown. The sample of LDI HTPB is heated at 100°C/s under 15 psi Ar. The time shown is the time after the onset of burning.

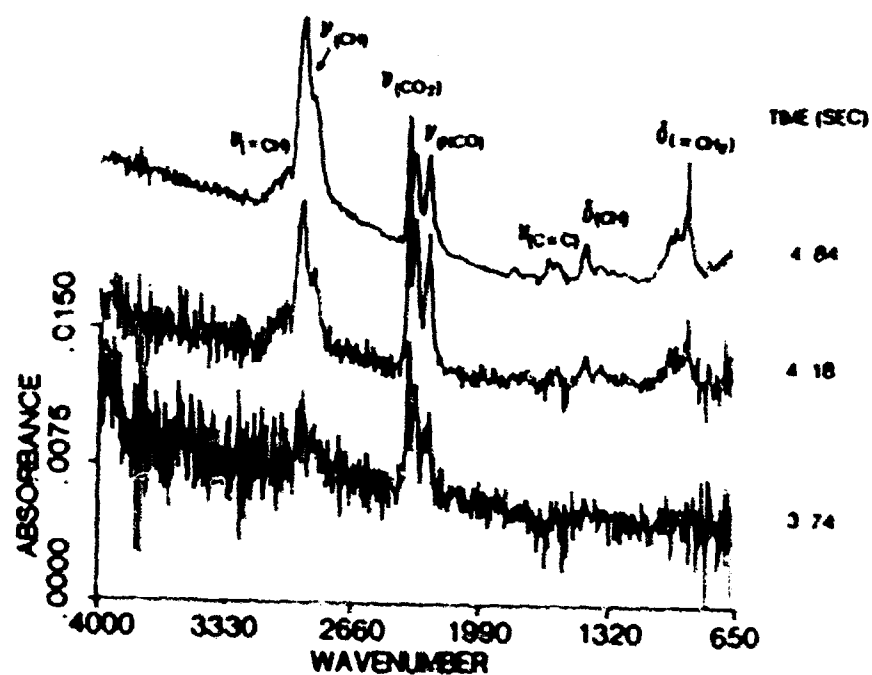


Fig. 10 IR spectra of the gas products 3 mm above the surface when a sample of HTPB HTPB is heated at 100°C/s under 15 psi Ar. The time shown is the time after the start of heating.

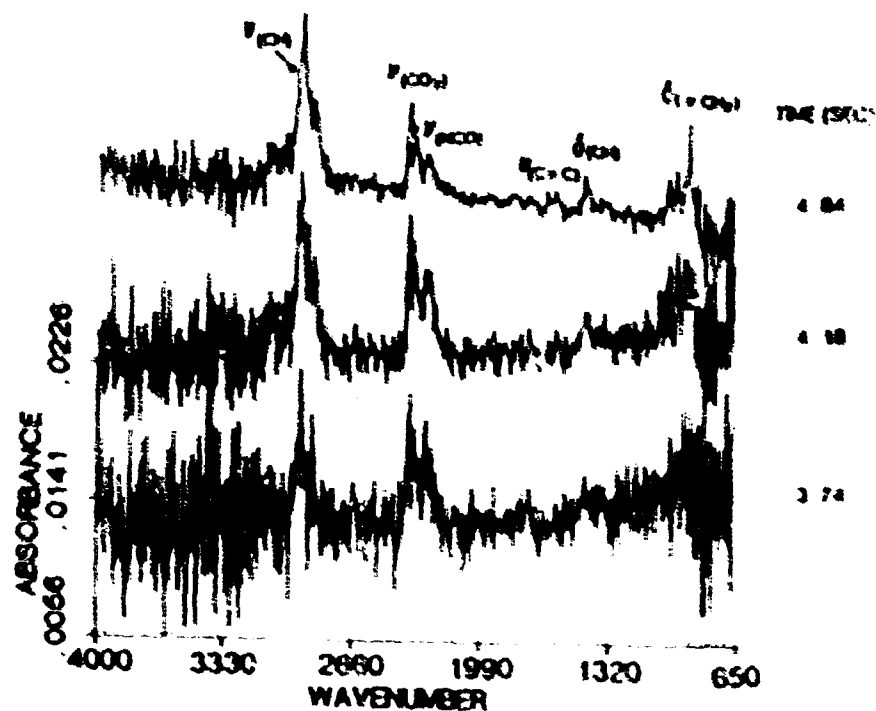


Fig. 11 IR spectra of the gas products 3 mm above the surface when a sample of HTPB HTPB is heated at 100°C/s under 15 psi Ar. The time shown is the time after the start of heating.



TABLE I  
Effect of the Unsaturation in the Polymer Backbone  
(% HTPB) on the Enthalpicity of the First Step  
of Decomposition

Polymer	Weight Fraction of HTPB (%)	$\Delta H$ (J/g)
HTPB	100	-783
TDI-HTPB	93.7	-800
IPDI-HTPB	92.1	-586
ODI-HTPB	81.3	-525

#### Kinetics of Decomposition at 10°C/min

The kinetic parameters for the thermal decomposition of HTPB, HTPA, and the diisocyanate-HTPB samples were extracted by using a nonlinear least squares fit of the weight loss curves shown in Figs. 1, 2, and 5. In each case the calculated curve is shown on the TGA trace. The Coats and Redfern approximation [35]

$$\ln\left(\frac{-\ln(1-\alpha)}{T^2}\right) = \ln\left[\frac{AR}{BE}\left(1 - 2\left(\frac{RT}{E}\right)\right)\right] - \frac{E}{RT} \quad (7)$$

was used to obtain an initial estimate of the activation energy,  $E$ , and preexponential value,

$A$ , of the Arrhenius equation.  $\beta$  is the linear heating rate. Because of the complex multiple steps in the first stage of decomposition of the diisocyanate cross-linked HTPB samples, an Arrhenius plot was made only for pure HTPB in this step. All four samples were analyzed in the second step of decomposition. Figure 12 shows the Arrhenius plot from which the kinetic constants in Table 2 were calculated. Data for HTPA are also given in Table 2 for comparison.

Since these Arrhenius parameters are the composite of many reactions and transport processes, it is not useful to attempt to dissect the data in Table 2 further. However, one important point can be made. As noted in the spectroscopy of the previous subsection, the residues of the HTPB polymers are all essentially the same following the first stage of decomposition. Consistent with and in support of this observation, the kinetic constants in Table 2 for the second step of decomposition involving these residues are all essentially the same.

#### Kinetics and Mechanism at 250-350°C/s

The kinetics and mechanisms described above for HTPB and its diisocyanate cross-linked derivatives can be used in any situation where low heating rates apply, such as in slow cook-off. The

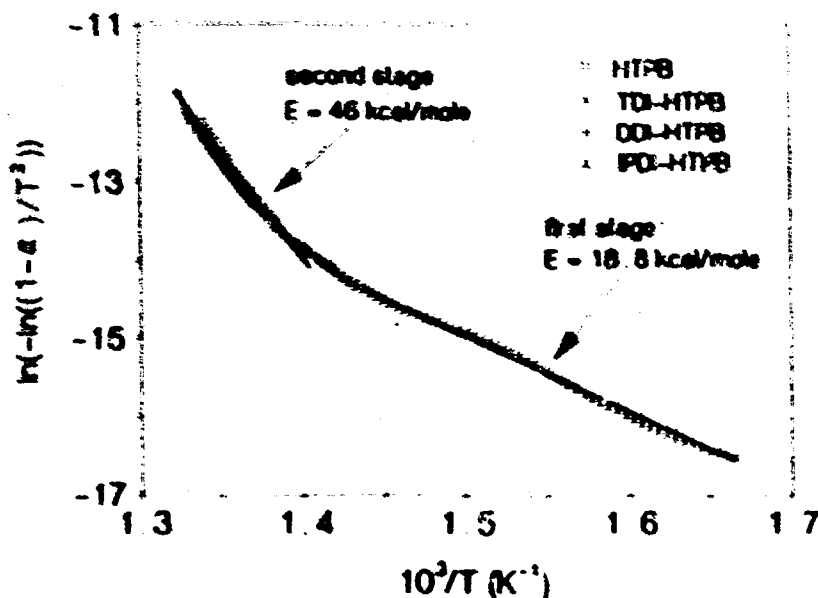


Fig. 12. Arrhenius plots for HTPB and the diisocyanate cross-linked HTPB polymers for the kinetics of weight loss compared by TGA. The second stage of decomposition is very similar for all of the materials.

TABLE 2

Arrhenius Parameters for HTPA, HTPB, and Diisocyanate Cross-linked HTPB Measured by the Nonisothermal TGA Method at a Heating Rate of 10°C/min

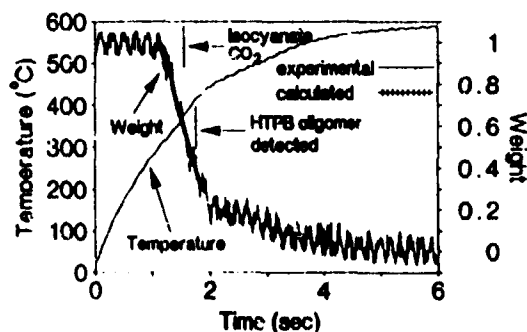
Polymer	First Stage			Second Stage		
	$E_a$ (kcal/mol)	$\log A$ (s <sup>-1</sup> )	$T$ (°C)	$E_a$ (kcal/mol)	$\log A$ (s <sup>-1</sup> )	$T$ (°C)
HTPA	23.5	3.4	348-398			
HTPB	18.8	1.1	328-420	46.6	10.1	436-470
TDI-HTPB				45.6	9.7	436-470
DDI-HTPB				45.6	9.7	436-470
IPDI-HTPB				46.0	9.8	436-470

data cannot be routinely extended to describe the polymers under the conditions that the condensed phase experiences during combustion. To establish the behavior under high heating rate conditions, SMATCH/FTIR studies in Ar were undertaken.

Because of the high heating rates employed in SMATCH/FTIR studies, care must be taken to produce a film of material that is thin enough to prevent a large temperature gradient from developing during heating [18]. If this condition is met, then the kinetics of mass loss will be controlled predominately by molecular processes rather than by heat transfer. Films of approximately 60  $\mu\text{m}$  thickness and 0.8 mg mass were used in this study, ensuring that the temperature difference across the film will be no larger than 10°-15°C.

Figure 13 shows a typical composite plot of the SMATCH/FTIR data for TDI-HTPB. The weight-loss ( $1-\alpha$ ) was fit as a function of time by the polynomial equation 8 using the coefficients given in Table 3:

$$1 - \alpha = \sum_0^3 a_i t^i \quad (8)$$



The calculated curve for TDI-HTPB is shown on Figure 13. Differentiation of Eq. 8 yields  $d\alpha/dt$ . The values of  $1 - \alpha$  and  $d\alpha/dt$  at each  $T$  from the temperature trace as a function of time are used in Eq. 9 to compute  $E$  and  $\log A$ . The value of  $n$  was chosen so as to linearize

$$\ln \left[ \frac{d\alpha}{dt} \frac{1}{(1 - \alpha)^n} \right] = \ln A - \frac{E}{RT} \quad (9)$$

$n = 2$  has been found to linearize SMATCH/FTIR data and has been rationalized elsewhere [19]. Figure 14 shows the Arrhenius plots and Table 4 summarizes the resulting constants.

The regression (burn) rates,  $\dot{r}$ , of energetic nitrate ester and organoazide polymers can be calculated from the kinetics data determined by SMATCH/FTIR spectroscopy [18, 19]. The regression rates at 15 psi agree well with the values obtained by extrapolation of combustion data at higher pressure [18, 19]. By using the kinetic constants for the polymers in Table 4, the nominal SMATCH film thickness of  $h = 60 \mu\text{m}$ , a decomposition temperature of 350°C, and a modified version of the pyrolysis law (Eq. 10), the

Fig. 13. SMATCH/FTIR data for TDI-HTPB showing the experimental and polynomial curve fit weight-loss data, the temperature trace, and the time of appearance of the gas products. The details of these gas products are shown in Fig. 9 at a somewhat lower heating rate. The atmosphere was 15 psi of Ar.

TABLE 3

Polynomial Curve Fitting Coefficients for HTPA, HTPB, and Diisocyanate Cross-linked HTPB

Polymer	$a_0$	$a_1$	$a_2$	$a_3$	$T(^{\circ}\text{C})$
HTPA	2.989	-3.321	1.577	-0.321	303-430
HTPB	1.957	-1.780	0.584	-0.065	325-440
DDI-HTPB	6.217	-8.854	4.111	-0.583	325-425
IPDI-HTPB	4.883	-6.731	3.438	-0.634	317-430
TDI-HTPB	3.004	-1.847	0.021	0.105	315-430

regression rates given in Table 4 were determined under 15 psi of Ar:

$$r(\text{mm/s}) = Ahe^{-E/RT} \quad (10)$$

The film thickness of 60  $\mu\text{m}$  is similar to the thickness expected of the surface reaction zone during combustion at this pressure. The burn rate of IPDI-HTPB measured at higher pressures [36] and extrapolated to 15 psi is 0.19 mm/s. This is in excellent agreement with the value determined here of 0.21 mm/s. As an additional check, the linear pyrolysis rates of several other hydrocarbon-based polymers can be estimated by extrapolation of higher temperature data to 350°C. For example, polystyrene with a molecular weight of 21,000 has a regression rate of about 0.2 mm/s at 350°C [37]. The value for poly(methylmethacry-

late) is about 0.05 mm/s [37]. A butadiene-styrene copolymer extrapolates from higher temperature to about 0.06 mm/s at 350°C [37]. The fact that the regression rates for the polymers shown in Table 4 fall into this general range of 0.05-0.2 mm/s combined with the good agreement of the IPDI-HTPB data gives confidence in the use of the SMATCH/FTIR data to characterize the mechanism of degradation HTPB under conditions resembling those of combustion.

The low values of  $E$  and  $A$  in Table 4 indicate that chemical bond breaking is not the controlling process in the decomposition of these polymers at high heating rates. This is one of the major differences between the kinetics and mechanisms obtained at the low heating rates described in the previous three subsections and those obtained by SMATCH/FTIR at fast heating rates. Low activation energy values have been obtained by others when materials are heated at a high rate. The low values have been interpreted as indicating that desorption of fragments is rate-controlling [4, 6, 7, 37, 38], while others propose that subsurface processes dominate [39-41]. Through the following facts, SMATCH/FTIR spectroscopy supports the surface desorption interpretation. The IR spectrum of the gases liberated from the polymer film (Figs. 9-11) reveals that only butadiene, vinylcyclohexene (the dimer of

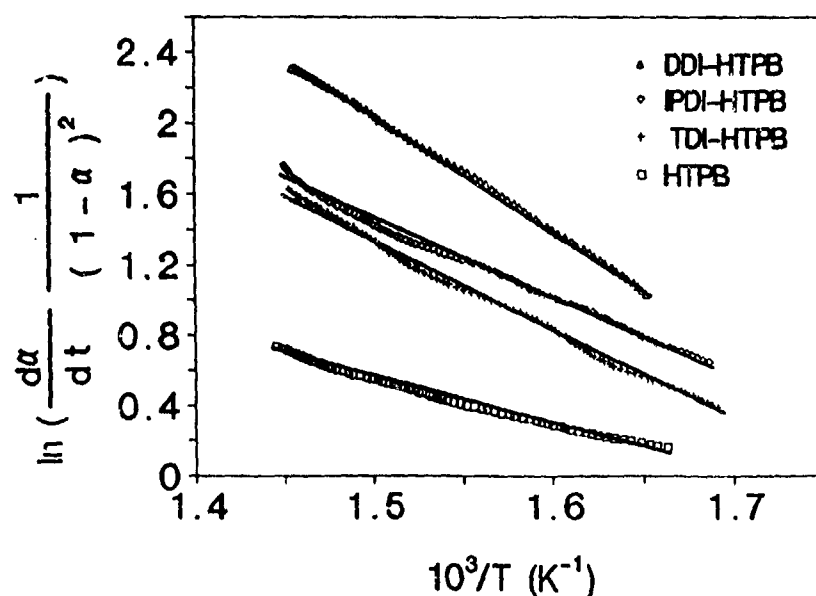


Fig. 14. The Arrhenius plots for HTPB and diisocyanate cross-linked HTPB measured by SMATCH/FTIR at about 250°C/s under 15 psi of Ar.

TABLE 4

Arrhenius Parameters for HTPA, HTPB,  
and Diisocyanate Cross-linked HTPB Measured  
by SMATCH/FTIR Spectroscopy  
(regression rate calculated by Eq. 10)

Polymer	$E$ (kcal/mol) <sup>a, b</sup>	$\log A$ (s <sup>-1</sup> )	$\dot{r}$ (mm/s)
HTPA	7.8 ± 0.7	3.1 ± 0.1	0.14
HTPB	8.3 ± 1.2	3.1 ± 0.4	0.09
DDI-HTPB	12.5 ± 0.3	4.9 ± 0.2	0.20
IPDI-HTPB	11.3 ± 2.4	4.5 ± 0.9	0.21
TDI-HTPB	9.2 ± 1.3	3.6 ± 0.4	0.14

<sup>a</sup> Apparent reaction order  $n = 2$ .

<sup>b</sup> The average of two experiments.

butadiene),  $\text{CH}_2\text{O}$ , an isocyanate and  $\text{CO}_2$  are formed on rapid thermolysis. Hence, the product gases are clipped fragments of the polymer and the cross-linking agent.  $\text{CO}_2$  probably forms by reaction 6. There is very little time for the exothermic cross-linking and cyclization reactions to take place in the polymer matrix, as they do when these polymers are slowly heated. In keeping with this, there is no evidence of an initial exotherm in the thermal trace at the high heating rate of Fig. 13, as there is in the DSC traces of Figs. 1 and 5 at a low heating rate. Furthermore, TDI appears in the gas phase in advance of the HTPB fragments, whereas IPDI and DDI are detected at about the same time as the polymer fragments. This observation is consistent with the data obtained at slow heating rates where the volatility of the isocyanate cross-linking agent plays an important role in the thermal stability of the cross-linked polymers. Thus, the low apparent activation energy, the absence of an exotherm, and the appearance of clipped polymer fragments support desorption as the process that dominates the regression rate of HTPB and diisocyanate-HTPB polymers.

The diisocyanate cross-linked HTPB samples are predicted to have somewhat higher regression rates than pure HTPB according to the SMATCH/FTIR kinetics data in Table 4. The values of  $\dot{r}$  at 15 psi calculated for the HTPB samples by equation 10 are given in Table 4. The cross-linked polymers are more rigid, and there is a pattern of higher regression rates with higher rigidity in linear pyrolysis studies of other polymers [37]. The cross-linked HTPB samples would not be expected to have vastly different regression rates that pure HTPB because the urethane cross-

link is the weakest bond in the molecule. It is useful to note that the burn rates for AP-HTPB composite propellants cured with IPDI and DDI are available in the 2-12 MPa (290-1740 psi) range [34, 36]. The burn rate of the IPDI-cured propellant is slightly higher than that of the DDI-cured propellant. Table 4 shows that the SMATCH/FTIR kinetics predicts the same trend although the burn rates are very similar for these two polymers. Hence, despite the different heating rates, the conditions that the condensed phase experiences during combustion appear to be well simulated by SMATCH/FTIR spectroscopy.

We wish to stress again that the major gas products detected with SMATCH/FTIR spectroscopy are very similar to those obtained with our other fast thermolysis/FTIR methods [20]. Therefore, this previous work covering a large range of other materials identifies the major gas products that feed the first stage of the flame zone during combustion of those materials. As the decomposition products leave the rapidly reacting condensed phase and enter the cool atmosphere of the cell, any highly reactive species will have reacted further to form more stable molecules. Thus, some additional thought may be needed before the gas product data from fast thermolysis/FTIR techniques are transferred to flame models, where, rather than being quenched in a cool atmosphere, the gas products enter an even hotter zone. In the case of HTPB the gas products are straightforward. Butadiene monomer and dimer are the major products that leave the surface and enter the hotter flame zone during combustion. The actual dimer of butadiene that is observed is 4-vinylcyclohexene. This molecule is the stabilized form of the butadiene dimer and may be present primarily because of the cool Ar atmosphere. In the reality of combustion the higher temperature of the flame zone would cause the butadiene monomer and dimer that leave the surface to pyrolyze in the gas phase into smaller fragments before mixing with the oxidizer gases. In accordance with this expectation, the IR emission spectrum of an AP-HTPB flame at 15 psi contains evidence of low-molecular-weight hydrocarbon fragments [42].

*We are grateful to the Air Force Office of Scientific Research, Aerospace Sciences, for support of this work on AFOSR-89-0527.*

## REFERENCES

1. Beckstead, M. W., Derr, R. L., and Price, C. F., *AIAA J.* 8:2200-2207 (1970).
2. Price, E. W., Sigman, R. K., Beiler, C., Lee, S. T., Markou, C., Chiang, H. J., and Prasad, K., *Proceedings of the 27th JANNAF Combustion Meeting*, CPIA Publ. 557, Vol. III, pp. 31-56 (1991).
3. Schultz, R. D., and Dekker, A. O., *Fifth Symposium (International) on Combustion*, The Combustion Institute, Pittsburgh, 1955, pp. 260-267.
4. Chaiken, R. F., Anderson, W. H., Barsh, M. K., Mishuck, E., Moe, G., and Schultz, R. D., *J. Chem. Phys.* 32:141-146 (1960).
5. McAlevy, R. F., and Hansel, J. G., *AIAA J.* 3:244-249 (1965).
6. Hansel, J. G., and McAlevy, R. F., *AIAA J.* 4:841-848 (1966).
7. McAlevy, R. F., Lee, S. Y., and Smith, W. H., *AIAA J.* 6:1137-1142 (1968).
8. Cheng, J.-H., Ryan, N. W., and Baer, A. D., *Twelfth Symposium (International) on Combustion*, The Combustion Institute, Pittsburgh, 1968, pp. 525-537.
9. Steinheil, E., *Proc. 3rd ICTA*, Davos, 1971, Vol. 1, pp. 187-192.
10. Youren, J. W., and Smith, D. A., *Proc. 3rd ICTA*, Davos, 1971, Vol. 1, pp. 209-214.
11. Bouck, L. S., Baer, A. D., and Ryan, N. W., *Fourteenth Symposium (International) on Combustion*, The Combustion Institute, Pittsburgh, 1973, pp. 1165-1176.
12. Cohen, N. S., Fleming, R. W., and Derr, R. L., *AIAA J.* 12:212-218 (1974).
13. Baer, A. D., Hedges, J. H., Seader, J. D., Jayakar, K. M., and Wojcik, L. H., *AIAA J.* 15:1398-1404 (1977).
14. Ericsson, I., *J. Chromatogr. Sci.* 16:340-344 (1978).
15. Price, E. W., Sigman, R. K., Powers, R. J., Markou, C., and Sambamurthi, Final Report, ONR, Contract N00014-79-C-0764, 1986.
16. Beck, W. H., *Combust. Flame* 70:171-190 (1987).
17. Timken, M. D., Chen, J. K., and Brill, T. B., *Appl. Spectrosc.* 44:701-706 (1990).
18. Chen, J. K., and Brill, T. B., *Combust. Flame* 85:479-488 (1991).
19. Chen, J. K., and Brill, T. B., *Combust. Flame* (in press).
20. Brill, T. B., in *Chemistry and Physics of Energetic Materials* (S. Bulusu, Ed.), Kluwer, Boston, 1990, p. 277.
21. Lengelle, G., *AIAA J.* 8:1989-1996 (1970).
22. Cronin, J. T., and Brill, T. B., *Appl. Spectrosc.* 41:1147-1151 (1987).
23. Shono, T., and Shinra, K., *Anal. Chim. Acta* 56:303-307 (1971).
24. Golub, M. A., and Gargiulo, R. J., *Poly. Lett.* 10:41-49 (1972).
25. Grassie, N., and Heaney, A., *Poly. Lett.* 12:89-94 (1974).
26. Kiran, E., and Gillham, J. K., *Anal. Chem.* 47:983-995 (1975).
27. Tamura, S., and Gillham, J. K., *J. Appl. Poly. Sci.* 22:1867-1884 (1978).
28. Brazier, D. W., and Schwartz, N. V., *J. Appl. Poly. Sci.* 22:113-124 (1978).
29. McCreedy, K., and Keskkula, H., *Polymer* 20:1155-1159 (1979).
30. Radhakrishnan, T. S., and Rama, R. M., *J. Poly. Sci.* 19:3197-3208 (1981).
31. Du, T., *Thermochim. Acta* 138:189-197 (1989).
32. Benson, S. W., *Thermochemical Kinetics*, Wiley, New York, 1976, p. 110.
33. Benow, A. W., and Cullis, C. F., *Combust. Flame* 24:217-230 (1975).
34. Fong, C. W., and Hamshire, B. L., *Combust. Flame* 65:61-69 (1986).
35. Coat, A. W., and Redfern, J. P., *Nature* 201:68-69 (1964).
36. Stacer, R. G., Eisele, S., and Eisenreich, N., *Twenty-First International Annual Conference of the ICT*, Karlsruhe, FRG, July 1990, paper 80.
37. Anderson, W. H., Bills, K. W., Mishuck, E., Moe, G., and Schultz, R. W., *Combust. Flame* 3:301-317 (1959).
38. Gullett, B. K., and Smith, P., *Combust. Flame* 67:143-151 (1987).
39. Houser, T. J., *J. Chem. Phys.* 45:1031-1037 (1966).
40. Rabinovitch, B., *Tenth Symposium (International) on Combustion*, The Combustion Institute, Pittsburgh, (1965), pp. 1395-1404.
41. Kumar, R. N., and Stickler, D. B., *Thirteenth Symposium (International) on Combustion*, The Combustion Institute, Pittsburgh, 1971, pp. 1059-1072.
42. Klotz, S., Thynell, S. T., Huang, I. T., and Kuo, K. K., *26th Joint Propulsion Conference of the AIAA/SAE/ASME/ASEE*, July 16-18, 1990, Orlando, FL, AIAA-90-1850.

Received 30 April 1991; revised 27 July 1991

## Thermal Decomposition of Energetic Materials 52. On the Foam Zone and Surface Chemistry of Rapidly Decomposing HMX

S. F. PALOPOLI and T. B. BRILL\*

*Department of Chemistry, University of Delaware, Newark, DE 19716*

Studies designed to perturb selected surface and foam zone reactions characteristic of burning HMX are described. This was done by determining the gas product ratios from carefully controlled fast thermal decomposition ( $> 100$  K/s) of a thin film of HMX in atmospheres of Ar,  $H_2$ ,  $O_2$ , CO, NO,  $NO_2$ , and  $NH_3$ . The results are correlated with experimental combustion data and thermochemical modeling studies of nitramines. A consistent picture about some of the probable reactions in the heterogeneous foam and fizz zones emerges.  $H_2$ , CO,  $O_2$ , and NO affect the secondary thermolysis reactions in these zones.  $NH_3$  appears to affect both the primary and secondary reactions, while  $NO_2$  is directly involved in primary decomposition reactions. HNCO and  $CH_2O$  appear to be products from secondary condensed phase reactions. The results suggest that  $NH_x$  sites and  $NO_2$  are catalyzable species for burn-rate modification of nitramine propellants.

### INTRODUCTION

A conspicuous aspect of the combustion of nitramine propellants is the insensitivity of the burn rate and pressure exponent to combustion modifiers. A systematic approach to understanding this problem requires an accurate description of the fast thermolysis/combustion mechanism. Changes in the physical aspects of the burning surface as a function of pressure are an accepted explanation for the pressure dependence of nitramine combustion [1-4]. Chemically, H atoms appear to be important in the rate-controlling step both in the condensed phase [5] and the gas phase [6]. Most of the heat is proposed to have been released in the gas phase, which would suggest that the burn rate is dominated by the secondary flame [7]. If too much of the exothermic chemistry occurs in the secondary flame away from the burning surface, then the heat feedback to the surface will be small. Other investigators [8] have concluded that nitramines intrinsically decompose to more stable products and produce relatively small amount of catalyzable species, such as  $NH_x$  and  $NO_x$ , thus explaining their insensitivity to burn-rate modifiers.

Identification of the catalyzable species under

fast thermolysis conditions is needed in order to apply chemical modifiers to propellant combustion. Ten IR-active gas products are detected by real-time FTIR spectroscopy during high-rate thermolysis of HMX. These gas products are  $NO_2$ , NO,  $N_2O$ , HONO, HNCO, HCN,  $CH_2O$ , CO,  $CO_2$ , and  $H_2O$  [9]. Infrared-inactive species  $H_2$ ,  $N_2$ , and  $O_2$  may also be present. Although a complex set of reactions produces these products, recent progress [5-7, 9-12] coupled with past work [13-24], permits a semiempirical scenario of the decomposition process to be developed. The chemical processes occurring at the heterogeneous condensed-phase-gas-phase interface of HMX can be probed by perturbing them with atmospheres of several of the known decomposition gases, i.e.,  $H_2$ , CO,  $O_2$ , NO, and  $NO_2$ . In addition, the  $NH_3$  atmosphere was studied. Although  $NH_3$  is not a product of HMX decomposition, species containing NH bonds may play a role as intermediates in the elementary reactions.

Previous studies [24-29] of nitramine decomposition in the presence of one of these gases have produced contradictory results about the global reaction rate. Reaction rates have been measured by weight loss or gas evolution, but no decomposition product analysis was reported.  $NO_2$  and  $CH_2O$  were found to be both accelerating and inhibiting [24-28].  $O_2$  inhibits [24, 29] while NO [24, 28] and  $NH_3$  [29] enhance the

\* Corresponding author.

global decomposition rate. Water vapor, CO, and  $N_2O$  had no effect on the rate relative to decomposition in an inert atmosphere (Ar or  $N_2$ ). These previous experiments were performed isothermally below the melting point of the nitramine or at low heating rates near the melting point. Rather than true melting, HMX is known to undergo condensed phase liquefaction with concomitant decomposition [30, 31]. The heterogeneous liquefaction phase is initially composed of some solid nitramine, molten nitramine, decomposition fragments, and evolving gases. Some of the contradictions in the previous findings on the sensitivity of the reaction rate to the atmosphere may stem from the difficulty of defining and controlling the reaction zone. Therefore, rather than to study rates, we have focused on the products of the reaction in this article.

Figure 1 defines the reaction zones of propellant combustion in one dimension. The chemistry of the foam and dispersed phase are nearly impossible to study directly during combustion, and yet this surface region is vitally important because it connects the gas phase to the condensed phase. Therefore, the experiments described in this article attempt to perturb the reactions in a simulation of the foam and disperse zone and thereby gain insight into the important surface chemistry. This objective was approached by performing near real-time in situ, IR analysis of the

gases evolved during high-rate ( $> 100$  K/s) thermolysis of a thin film of HMX in various reactive atmospheres. In doing so, the catalyzable species and the nature of the reactions are better defined. We fully realize that the process we have studied is very complicated. Therefore, classes of elementary reactions are given whose known rates make them plausible contributors under the conditions of this experiment. In this way, the work helps bridge some of the experimental combustion observations [32] and thermochemical modeling studies [7].

## EXPERIMENTAL

HMX was used in this study for experimental convenience. Its higher liquefaction/decomposition temperature results in no detectable sublimation at 1 atm pressure under the heating conditions used. Nitramine aerosol, if present, complicates the quantitation of  $NO_2$  and HONO. HMX recrystallized from ACS grade acetonitrile was dissolved in hot, reagent grade, glacial acetic acid and slowly cooled to yield  $\alpha$ -HMX. This procedure is effective for removing traces of RDX from HMX [33]. A third recrystallization from spectrophotometric grade acetone converted the  $\alpha$ -HMX back to  $\beta$ -HMX, which is the highest-density, most stable polymorph at STP [34]. The triply recrystallized HMX was redissolved in acetone and the solvent removed by rotary evaporation, yielding a free-flowing, fine powder.

The gases used in this study were obtained from Matheson or Union Carbide Linde and were used as received. The gases and their purities were Ar (UHP, 99.999% min.),  $O_2$  (research, 99.997% min.), CO (C.P., 99.5% min.),  $NH_3$  (anhydrous, 99.99% min.),  $H_2$  (pre-purified, 99.99% min.), NO (C.P., 99% min.), and  $NO_2$  (C.P., 99.5% min.).

The high heating rate thermolysis experiments were conducted in a modified IR transmission cell (Foxboro Analytical Model 40 Pyro-Chem). The Ni-plated cell has a free internal volume of about  $25\text{ cm}^3$  and can be filled with the gas of choice at pressures of  $10^{-3}$ –1000 torr. The bottom plate of the cell incorporated electrical feedthroughs for mounting a nichrome IV ribbon heater filament. The overall dimensions of the filament are  $2.5 \times 0.6 \times 0.012$  cm. The bottom plate was sealed against the cell body with a silicone-rubber gas-

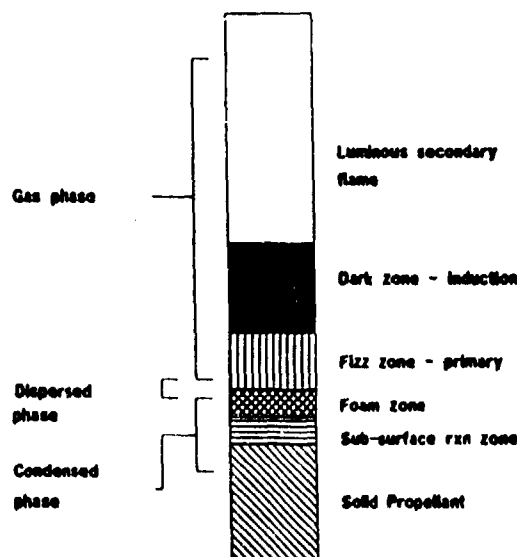


Fig. 1. A schematic depiction in one dimension of the major regions of reaction during nitramine propellant combustion.

ket. All of the other seals and gaskets in the system, including those in the manifold described below, were made of Teflon, viton, or Kel-F. The standard valve was replaced with a stainless-steel (SS) Whitney severe service, union bonnet valve. The cell was modified to accept a 3D Instruments Precision vacuum gauge (0.5% accuracy). The internal surfaces of this corrosion resistant gauge are SS and Inconel X-750. A corrosive service lecture bottle regulator (Matheson Model 3332) was used with NO, NO<sub>2</sub>, and NH<sub>3</sub>.

A gas manifold was constructed for filling the cell with the desired atmosphere. The manifold consisted of a 304 SS cross, the four arms of which are connected, respectively, to the pyrolysis cell, a LN<sub>2</sub> trapped vacuum line, an Ar gas cylinder, and the cylinder of the reagent gas. The lines to the Ar and the reagent gas cylinders were coiled lengths of  $\frac{1}{8}$ -in o.d. 316 SS tubing incorporating protective SS check valves. The line to the cell was a 12-in length of a  $\frac{1}{4}$ -in i.d. SS flexible bellows tube.

In a typical experiment, 1 mg of powdered HMX was thinly spread in the cusp of the  $2.5 \times 0.6 \times 0.012$  cm nichrome filament. The cell was filled with the desired atmosphere and placed in the sample compartment of a Nicolet 60SX FTIR spectrometer equipped with an MCT-B detector. The cell was positioned such that the IR beam passed a few millimeters above and parallel to the long axis of the filament. The pathlength of the cell was 5 cm. The IR beam at the focal point is 3 mm diameter. Varying the height of the beam relative to the sample causes some time delay effects but the product concentrations are not greatly altered [9]. The heating rate and final filament temperature were controlled by varying the current setting. The sample of HMX melted to a thin film immediately. Spectra of the evolved decomposition products were recorded in situ as a function of time using the rapid-scan mode. Decomposition was monitored for 10 s. The spectrometer was set to collect 10 scans per second, co-adding two spectra per file. These collection parameters result in a wavenumber resolution of  $4 \text{ cm}^{-1}$  and a temporal resolution of 200 ms.

The baseline thermolysis studies in an inert atmosphere of Ar were run at heating rates of 40 to 180 K/s, with corresponding final filament temperatures of 600–1000 K. Calibration of the

filament temperature was made with melting points of Aldrich standards. The heating response is not linear throughout the 10-s run. The quoted heating rates are the initial heating rates during the first 1–2 s of the run, when the response is nearly linear. For the studies in reactive atmospheres an initial heating rate of 140 K/s was used. The corresponding final filament temperature was 900 K. The filament temperature as a function of time was calibrated by spot-welding a fine Type J thermocouple to the filament and recording the output on a digital storage oscilloscope. The temperature-time profile for an initial heating rate of 140 K/s is shown in Fig. 2.

For the experiments in an IR-active atmosphere (CO, NO, NO<sub>2</sub>, NH<sub>3</sub>), it was necessary to correct the decomposition spectra by digital subtraction with reference spectra. The relatively intense characteristic absorptions of the reagent gas must be removed to obtain a baseline satisfactory for quantifying the adjacent absorptions of the HMX decomposition products. Also, when the nichrome filament was fired, the surrounding reagent gas heated during the 10-s run resulting in slightly broadened absorption bands. Good spectral subtractions with minimal artifact required reference spectra measured under the same conditions. Thus, a set of reference spectra were collected for each IR-active gas by filling the cell with the desired gas, firing the empty filament for 10 s, and recording the spectra as described above. The spectra of the thermolysis products from the decomposition of HMX in an atmosphere of an IR-active gas were corrected by digital subtraction.

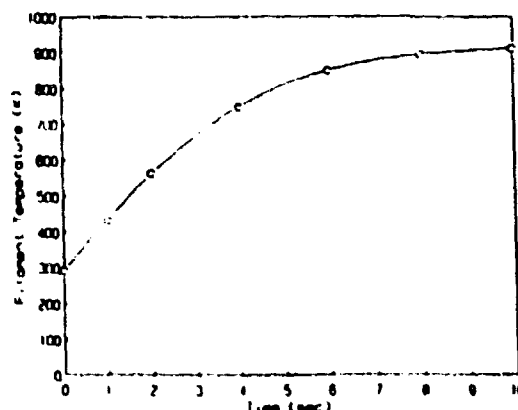


Fig. 2. The temperature response of the nichrome filament during studies of HMX decomposition at an initial heating rate of 140 K/s.



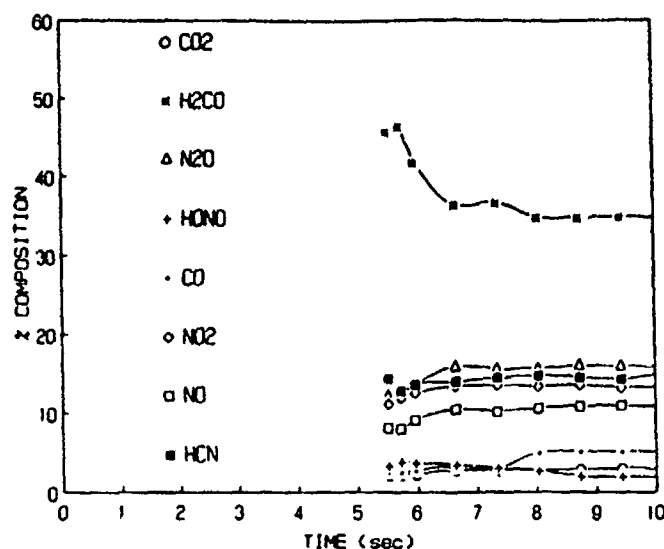


Fig. 3. The gas composition vs. time profiles for HMX under an initial heating rate of 40 K/s and 1 atm Ar.

tives indirectly during low-temperature nitramine decomposition using GC-MS [37] or via HPLC of nitramine combustion residues [38]. There is no evidence for nitrosoamines in the present work. This may be due to low volatility, obscuration of the characteristic nitrosoamine IR bands by the other products, or concentrations below the limit of detection.

Under the conditions of this experiment, most of the HCN, NO<sub>2</sub>, and N<sub>2</sub>O arise from skeletal breakup of HMX or pyrolysis species, such as O<sub>2</sub>NNCH<sub>2</sub> or the AMNA radical suggested above. CH<sub>2</sub>O results from intramolecular or intermolecular O-atom transfer or reaction of OH

with skeletal derived -CH<sub>2</sub>-. Study of a large series of nitramines has shown that the initial amounts of HONO can be correlated with the H/NO<sub>2</sub> ratio of the parent nitramine [39]. HONO forms predominantly from adventitious contact with H radicals or NO<sub>2</sub> abstraction of H from weakly bound hydrogenated species such as H<sub>2</sub>CN.

Previous investigators [13-24] have speculated on the importance or extent of reactions based on C-N bond homolysis versus N-N bond homolysis. It is commonly believed that CH<sub>2</sub>O and N<sub>2</sub>O form from coupled processes, such as (1) intramolecular O-atom transfer from the -NNO<sub>2</sub>

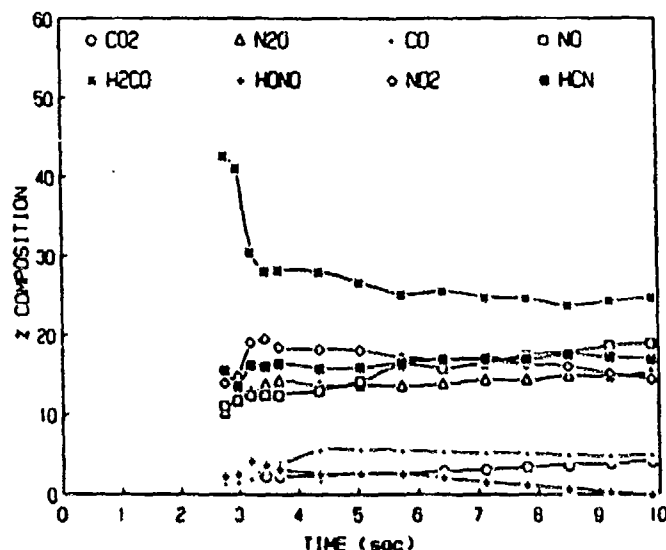


Fig. 4. The gas composition vs. time profiles for HMX under an initial heating rate of 90 K/s and 1 atm Ar.

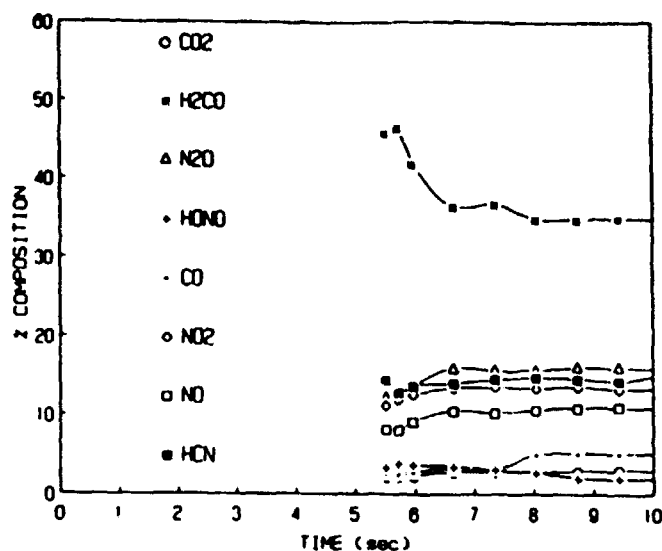


Fig. 3. The gas composition vs. time profiles for HMX under an initial heating rate of 40 K/s and 1 atm Ar.

tives indirectly during low-temperature nitramine decomposition using GC-MS [37] or via HPLC of nitramine combustion residues [38]. There is no evidence for nitrosoamines in the present work. This may be due to low volatility, obscuration of the characteristic nitrosoamine IR bands by the other products, or concentrations below the limit of detection.

Under the conditions of this experiment, most of the HCN, NO<sub>2</sub>, and N<sub>2</sub>O arise from skeletal breakup of HMX or pyrolysis species, such as O<sub>2</sub>NNCH<sub>2</sub> or the AMNA radical suggested above. CH<sub>2</sub>O results from intramolecular or intermolecular O-atom transfer or reaction of OH

with skeletal derived -CH<sub>2</sub>-. Study of a large series of nitramines has shown that the initial amounts of HONO can be correlated with the H/NO<sub>2</sub> ratio of the parent nitramine [39]. HONO forms predominantly from adventitious contact with H radicals or NO<sub>2</sub> abstraction of H from weakly bound hydrogenated species such as H<sub>2</sub>CN.

Previous investigators [13-24] have speculated on the importance or extent of reactions based on C-N bond homolysis versus N-N bond homolysis. It is commonly believed that CH<sub>2</sub>O and N<sub>2</sub>O form from coupled processes, such as (1) intramolecular O-atom transfer from the -NNO<sub>2</sub>

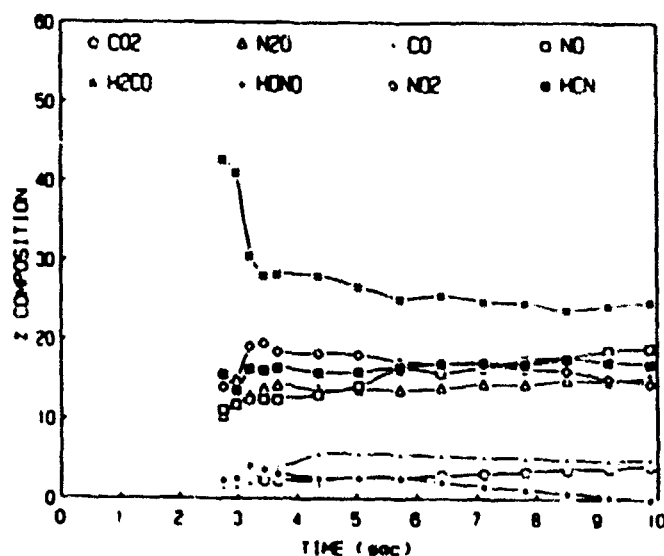


Fig. 4. The gas composition vs. time profiles for HMX under an initial heating rate of 90 K/s and 1 atm Ar.

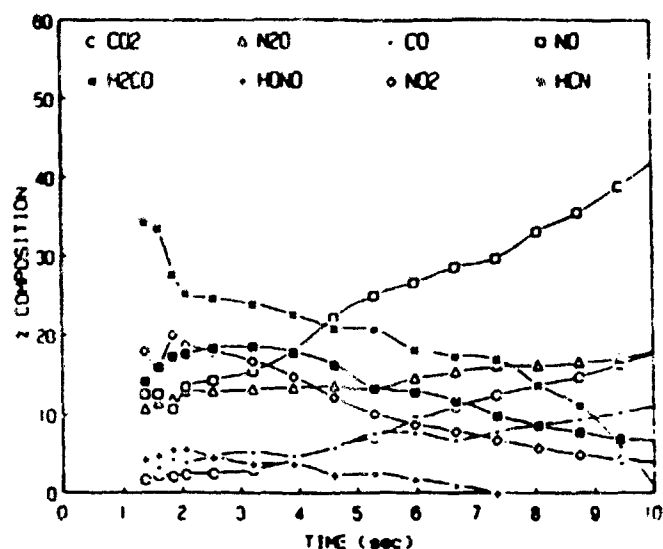


Fig. 5. The gas composition vs. time profiles for HMX under an initial heating rate of 180 K/s and 1 atm Ar.

group to  $-\text{CH}_2-$  in HMX and concomitant C-N bond scissions [22], (2) unimolecular decomposition of a  $\text{H}_2\text{CNNO}_2$  fragment via a similar process [11], or (3) a bimolecular OH-catalyzed decomposition of  $\text{H}_2\text{CNNO}_2$  [7]. High-rate thermolysis coupled with real-time product analysis can shed some light on these questions.

Examination of Figs. 3-5 shows that products of both C-N and N-N bond homolysis reactions are important. Because of their higher reactivity,  $\text{NO}_2$  and  $\text{CH}_2\text{O}$  may be less reliable indicators of the relative importance of N-N versus C-N scissions. HCN (product of N-N scission) and  $\text{N}_2\text{O}$  (product of C-N scission) are very stable except at the higher heating rates and decomposition (filament) temperatures. The ratio of these two species early in the thermolysis should provide some insight. As the heating rate and decomposition temperature are raised, the  $\text{HCN}/\text{N}_2\text{O}$  ratio increases, suggesting an increase in the importance of N-N bond homolysis at higher temperatures. This is consistent with estimated kinetic and thermochemical parameters [7, 20] and with studies of isothermal decomposition at high temperatures [40].

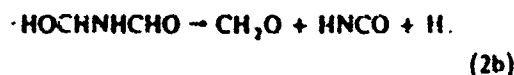
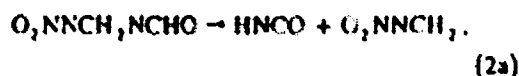
According to the nonisothermal gas evolution data in Figs. 3-5, more  $\text{CH}_2\text{O}$  is generated than  $\text{N}_2\text{O}$ . This casts doubt on the existence of a coupled (concerted) mechanism of oxygen transfer leading to  $\text{N}_2\text{O}$  and  $\text{CH}_2\text{O}$ . Furthermore, in isothermal decomposition studies,  $\text{CH}_2\text{O}$  evolution follows that of  $\text{N}_2\text{O}$  [40]. The data suggest

that  $\text{CH}_2\text{O}$  forms largely in the condensed phase "melt," probably from one or more of the carbonyl-nitramine decomposition species that are observed in the 200-600-ms period early in the run. This period also coincides with the highest concentrations of  $\text{CH}_2\text{O}$ .  $\text{CH}_2\text{O}$  may form from decomposition of amide species such as HMFA:

$$\text{HOCH}_2\text{NHCHO} \rightarrow \text{CH}_2\text{O} + \text{HCN} + \text{H}_2\text{O} \quad (1)$$

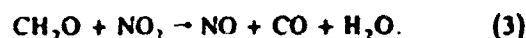
Note that the highest initial  $\text{CH}_2\text{O}$  concentration occurs at the lowest heating rate. Under these conditions there is more time for low temperature aging of the "melt" and formation of the amide species [36].

It is proposed that HNCO arises from a similar condensed phase mechanism. As noted earlier, the initial observation of HNCO coincides with the disappearance of the carbonyl and/or carbonyl-nitramine fragment species. AMNA and HMFA or the related radicals shown in reactions 2a and 2b may be sources of HNCO. Fragmentation could also be aided by H-atom abstraction by  $\text{NO}_2$  or OH.

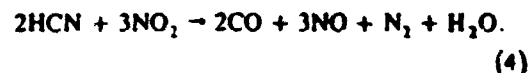


Other observations regarding HMX decomposition in Ar can be summarized as follows. Under

1 atm of Ar, no decomposition products are detectable in 10 s for final filament temperatures less than 550 K. This temperature corresponds closely to the decomposition temperature of HMX [13]. At heating rates below 90 K/s, corresponding to final filament temperatures below 780 K, the products result primarily from condensed-phase decomposition. Little change occurs in the composition-time profiles beyond the first 800 ms of decomposition. At higher temperatures the influence of condensed-phase-gas-phase interactions increases. At higher temperatures progressively more  $\text{CH}_2\text{O}$  is oxidized by  $\text{NO}_2$ :



At heating rates of 140 K/s or greater, some of the relatively stable HCN is oxidized in the following net reaction:



$\text{NO}_2$  is also controlled by reaction 5 as increasing temperature shifts the equilibrium to the right:



In addition to reactions 3-5, NO is produced by the decomposition of HONO (reaction 6) and by reaction 7:



As shown in Fig. 5, NO concentration rises steeply at a heating rate of 180 K/s. As the final filament temperature is raised, the total production of CO and  $\text{CO}_2$  also increases. On going from a filament temperature of 600-1000 K the  $\text{CO}_2/\text{CO}$  ratio changes from 0.6/1 to 1/1 to > 1.5/1 as reaction 7 becomes more important:



It should be noted that oxidation reactions 3, 4, 6, and 7 are net reactions. The elementary steps involve HNO and the radical species H, OH, and HCO [7, 41, 42]. The initial and final amounts of  $\text{N}_2\text{O}$  are essentially the same regardless of the heating rate or filament temperature. This is consistent with its formation primarily from skeletal HMX bond scissions and its stability at the conditions investigated.

There is a microscopic film of nonvolatile residue remaining on the filament after thermolysis. This material is presumably a (CN)<sub>x</sub> coke

with little H or O content. It fumes off when the filament is fired in air at 1200 K.

#### Relevance to Combustion Experiments and Modeling

The thermolysis experiments described here simulate the chemistry occurring in the heterogeneous foam zone (liquefaction layer) and the dispersed-phase interface region with the fizz zone (primary flame) during nitramine combustion (Fig. 1). Under rocket motor conditions, combustion occurs at pressures of 500-1000 psia with heating rates of  $10^3$ - $10^6$  K/s. Obviously, we cannot draw conclusions about the significance of our experiments compared with these conditions. However, we can make qualitative comparisons to experimental and theoretical studies of nitramine combustion at low pressures.

Kubota and Sakamoto [32] recently studied the flame (combustion wave) structure of HMX at pressures of 1-10 atm. Pellets of HMX were burned in a window bomb pressurized with  $\text{N}_2$ . Temperature profiles of the combustion wave were measured with embedded microthermocouples. The burning surface, burn rate, and gas-phase reaction zone thickness were observed using high-speed video.

The condensed-phase temperature early in the foam zone is approximately 700 K and is relatively insensitive to pressure. Temperature rises at an equivalent heating rate of ca.  $10^3$  K/s in the foam zone [??] to a burning surface temperature of < 900 K near atmospheric pressure. The temperature gradient in the gas phase just above the burning surface is large and pressure dependent ( $10^3$ - $10^5$  K/s). The measurements indicate that the heat flux produced in the foam zone is approximately equal to the heat transferred back from the gas phase (predominantly from the primary flame). The luminous secondary flame rapidly approaches the burning surface as pressure is increased, but the burning rate appears to be independent of the luminous flame reaction. These HMX combustion studies at 1 atm demonstrate that the filament temperatures in our pyrolysis experiments (600-1000 K) are in the same range as the temperatures observed in the "foam" zone and the early fizz zone. Although our heating rates are lower, they are within an order of magnitude of those observed in the surface zone

of the condensed phase during combustion at low pressure [32].

Melius has performed thermochemical modeling of nitramine decomposition, ignition, and combustion [7, 43]. The most detailed studies involved RDX combustion at pressures of 0.5, 1, and 17 atm. RDX was used for computational convenience. The foam zone pyrolysis and the gas-phase fizz zone chemistry are essentially the same for RDX and HMX, but their relative importance is different. Quantitatively, the gas-solid boundary mass and energy conditions will be different due to the higher decomposition temperature of HMX and its significantly lower volatility. Because of the latter behavior the condensed-phase foam zone chemistry and autocatalysis by products (e.g.,  $H_2O$  and  $CH_2O$ ) are more important for HMX than RDX. These differences do not negate a qualitative comparison of computational RDX combustion behavior at 1 atm and our high-rate HMX thermolysis results.

The calculated combustion product profiles [7] as a function of temperature (position in flame) share many of the features observed in our thermolysis product profiles. The thermolysis product profiles are consistent with the reaction networks of the model that are dominant during condensed-phase decomposition and the early regions of the fizz zone. HCN, NO,  $N_2O$ , CO, and  $CO_2$  concentrations increase and/or level off with increasing temperature. Initially the concentrations of  $CH_2O$ , HONO, and  $NO_2$  rise rapidly and then progressively decrease. At the highest heating rates with final filament temperatures of 900 K or more, relatively stable HCN is consumed via reaction 4. A similar decrease in HCN concentration is predicted by the model at flame temperatures in excess of 1100 K. The model also suggests that the following species, which are either not detectable or quantifiable, are important under the conditions of thermolysis:  $H_2O$ ,  $N_2$ ,  $H_2$ , and HNO.

One of the major differences between modeling and experiment is the high HCN/ $N_2O$  ratio predicted by the (RDX) model. This high ratio is not unexpected for RDX. However for HMX, condensed-phase pyrolysis mechanisms are more important including those favoring C-N bond homolysis. For example, Melius [43] has shown that coconversion of  $H_2CNNO_2$  to  $CH_2O$  and  $N_2O$  (C-N bond scission) can be enhanced in the

condensed phase by a water-catalyzed concerted reaction. In our HMX thermolysis experiments HCN and  $N_2O$  are equally important products. For volatile RDX, unimolecular gas-phase reactions involving N-N bond homolysis become more important.

In the RDX flame model [7] HNCO results from the oxidation of HCN in the secondary (luminous) flame zone at temperatures in excess of 1000 K. Although this may be a source of HNCO, HNCO is detected early in the fast thermolysis of HMX and RDX under all of the conditions studied [9, 44]. The high-rate thermolysis studies point to a condensed-phase mechanism of HNCO generation. Reactions such as 7a and 2b need to be recognized in modeling as condensed phase sources of HNCO.

The RDX flame model includes reaction networks involving the formation of cyanogen,  $C_2N_2$ , from HCN in the combustion region of the primary flame (fizz zone) and the subsequent regeneration of HCN from cyanogen in a post-zone reign of the primary flame [7]. If cyanogen were formed to a significant extent, then its characteristic IR absorptions would be readily apparent. Cyanogen has not been detected during the thermolysis of HMX or RDX under any of the conditions investigated. It may be that the formation of cyanogen occurs late enough in the fizz zone (particularly at low pressures) that it is outside of the combustion regime simulated in high-rate thermolysis studies.

#### HMX Thermolysis in Reactive Atmospheres

The thermolysis of HMX was examined in atmospheres of  $H_2$ , CO,  $O_2$ , NO,  $NO_2$ , and  $NH_3$  to gain insight into the effect of an excess of each species on the chemistry occurring in the heterogeneous foam zone and its interface with the gas-phase fizz zone.

As described in the experimental section, these thermolysis studies were conducted at an initial heating rate of 140 K/s, corresponding to a final filament temperature of 900 K. These conditions were chosen to be relevant to HMX combustion at atmospheric pressure [32] and to provide a reaction regime that simulates the dispersed regime of the flame (Fig. 1).

The discussion focuses on comparison of HMX decomposition in a specific reactive atmosphere

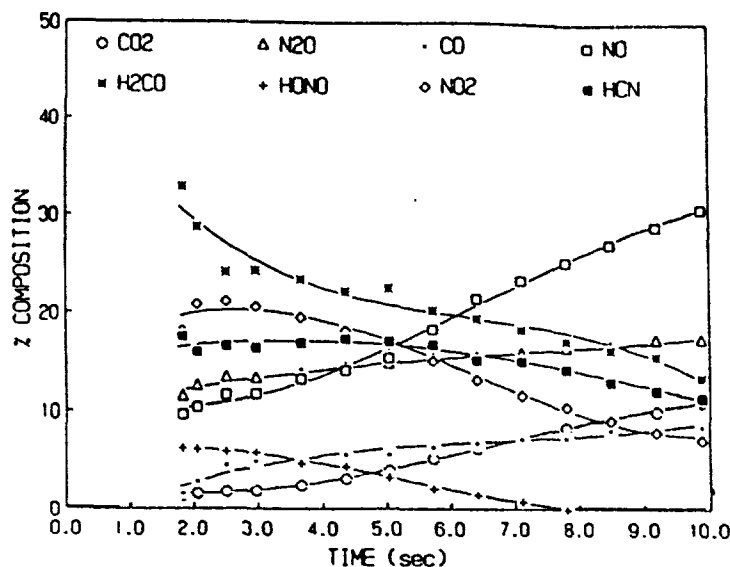


Fig. 6. The gas composition vs. time profiles for HMX under an initial heating rate of 140 K/s and 1 atm Ar.

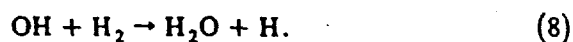
to HMX decomposition under the same conditions in an Ar atmosphere (the control). The composition-time profiles for decomposition of HMX in Ar are shown in Fig. 6 under the same conditions as the reactive atmospheres discussed below.

The reactions cited in explaining the effects of the reactive atmospheres are generally those relevant combustion reactions that are kinetically (high preexponential factors, zero or low activation energies) and/or thermodynamically more favorable [7, 41-43, 45, 46].

**Thermolysis Under  $H_2$ .** The product profiles for HMX decomposition under  $H_2$  are shown in

Fig. 7. Relative to thermolysis in Ar (Fig. 6), higher concentrations of  $CH_2O$  and HCN are observed. The terminal  $CO_2/CO$  ratio has gone from 1.3 to 0.6 with the concentration of CO remaining essentially the same. The overall  $NO_2$  concentration is lower, although the decay behavior is similar. These observations may be attributed to the processes described below.

The excess  $H_2$  present scavenges OH radical arising from pyrolysis (reaction 8).



This reaction is exothermic ( $-63.2$  kJ/mol) [41]. The H atoms generated can mediate several

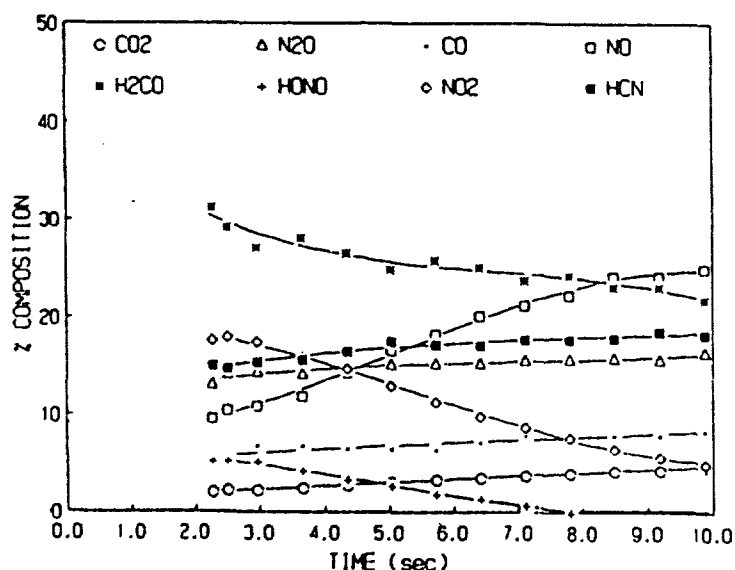
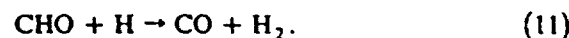


Fig. 7. The gas composition vs. time profiles for HMX under an initial heating rate of 140 K/s and a 380 torr  $H_2$ /380 torr Ar atmosphere.

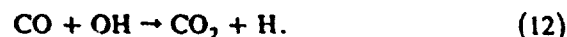
reactions, including regeneration of OH (reaction 9a):



The higher amounts of  $\text{CH}_2\text{O}$  and  $\text{HCN}$  are due to less OH available for oxidation reactions, and in the case of  $\text{HCN}$ , reactions 9a, 9b, and 10. Additional water produced via reaction 8 may increase the condensed-phase formation of  $\text{CH}_2\text{O}$  by water catalyzed conversion of  $\text{H}_2\text{CNNO}_2$  [43]. The competitive reduction in available OH results in less CO burning in  $\text{CO}_2$ , which requires a strong oxidant. However, H atom abstractions by H provide a mechanism for generation of CHO from  $\text{CH}_2\text{O}$  and subsequently CO formation (reaction 11). These reactions also regenerate  $\text{H}_2$ .

**Thermolysis Under CO.** Figure 8 shows the product profiles for decomposition under an atmosphere of CO. Higher amounts of  $\text{CH}_2\text{O}$  are observed and the oxidative decay of  $\text{CH}_2\text{O}$  and  $\text{HCN}$  is reduced. The disappearance rate of  $\text{NO}_2$  is similar to that under Ar. Lower amounts of  $\text{CO}_2$  are observed and the concentration of  $\text{CO}_2$  does not progressively increase with time

(increasing filament temperature). Most of the  $\text{CO}_2$  produced results from oxidation of the added CO rather than from HMX-bound carbon. The added CO competitively reacts with OH produced from pyrolysis:



This results in an environment richer in H atoms similar to that produced in an atmosphere of  $\text{H}_2$ .

**Thermolysis Under  $\text{O}_2$ .**  $\text{O}_2$  is a minor product of HMX combustion and its generation and reactions are normally more important in the luminous secondary flame. The product profiles for HMX thermolysis under  $\text{O}_2$  are shown in Fig. 9. At first glance the profiles are surprising for decomposition in an "oxidizing" atmosphere. The concentration of  $\text{CH}_2\text{O}$  is higher than that observed for thermolysis under Ar, and the oxidative decays for  $\text{CH}_2\text{O}$  and  $\text{HCN}$  are lower. Although the total  $\text{CO}_x$  generation and the concentration of  $\text{CO}_2$  are lower, somewhat more CO is observed ( $\text{CO}_2/\text{CO} = 0.4$ ). The buffer atmosphere of  $\text{O}_2$  masks the generation of NO, from oxidation reactions involving  $\text{NO}_2$ , due to equilibrium reaction 5.

The apparent inhibiting effect of  $\text{O}_2$  on the course of the oxidation reactions can be explained in the following way.  $\text{O}_2$  reacts with H (reaction 13) or with species containing weakly bound hydrogen (reaction 14) to produce  $\text{HO}_2$  radicals. Reaction 13 will play a larger role at elevated

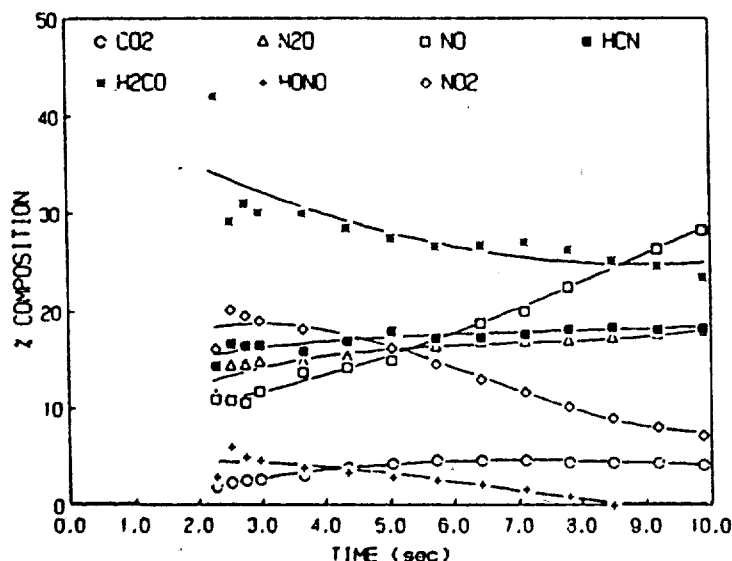


Fig. 8. The gas composition vs. time profiles for HMX under an initial heating rate of 140 K/s and 1 atm CO.

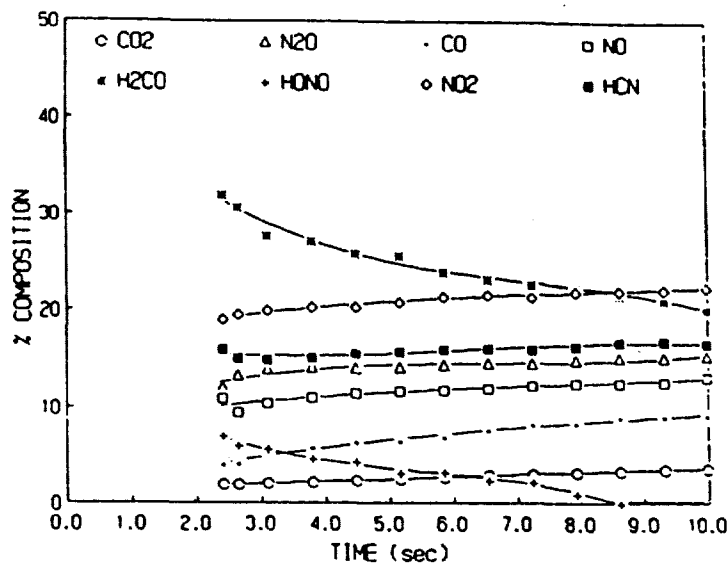
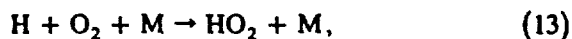


Fig. 9. The gas composition vs. time profiles for HMX under an initial heating rate of 140 K/s and 1 atm  $O_2$ .

pressures or in the condensed phase (e.g.,  $M = H_2O$ ):



$O_2$  and  $HO_2$  are relatively poor oxidants compared with  $OH$ . Comparison of the rate constant for  $CO$  oxidation by  $OH$ ,  $HO_2$ , and  $O_2$  indicates that the rate constant for oxidation by  $OH$  is 3 orders of magnitude greater than that for  $HO_2$  and 7 orders of magnitude greater than that for  $O_2$  [7, 41].  $O_2$  competes with  $NO_2$  in reactions involving pyrolysis fragments containing weakly bound hydrogen.  $HO_2$  is produced at the expense

of the more powerful oxidant  $OH$ . This results in the lower oxidative decay rates and decreased production of  $CO_2$  from  $CO$  which requires a strong oxidant.

**Thermolysis Under  $NO$ .** Under an atmosphere of  $NO$  (Fig. 10), HMX thermolysis results in a higher level of  $HCN$  throughout the experiment and no net  $HCN$  decay.  $CH_2O$  concentrations are higher due to little decay from oxidation. The  $CO_2/CO$  ratio is similar to that observed under  $Ar$ , but the total  $CO_x$  yield is the lowest observed in all of the experiments. This behavior can best be explained by reactions involving  $HNO$ . Relatively short-lived (ca. 0.1 s)

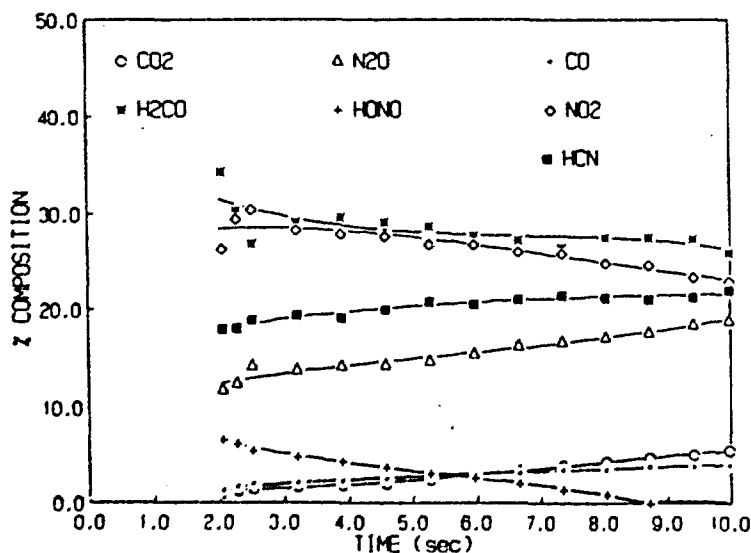
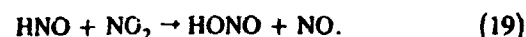
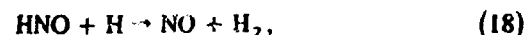
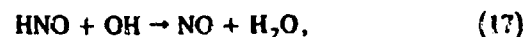
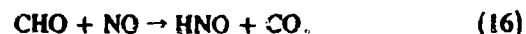
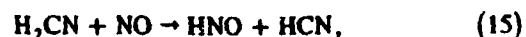


Fig. 10. The gas composition vs. time profiles for HMX under an initial heating rate of 140 K/s and 1 atm of  $NO$ .



HNO is believed to be an important species in nitramine decomposition. Modeling studies suggest it is present at instantaneous concentrations similar to those of the more stable species  $\text{NO}_2$  and  $\text{CH}_2\text{O}$  (at  $T < 1000 \text{ K}$ ) [7].



NO readily abstracts H atoms from large radical fragments of HMX decomposition [43], and other species containing weakly bound hydrogen, generating HNO. Abstraction of a methylene proton from large radical fragments or  $\text{H}_2\text{CN}$  increases the generation of HCN (reaction 15). HNO thus generated can react with OH, H, and  $\text{NO}_2$  (reactions 17–19, respectively). In particular, HNO (via NO) interferes with the oxidation of  $\text{H}_2\text{CO}$  and HCN by competitively reacting with OH and  $\text{NO}_2$  (e.g., reaction 6). NO is a poor oxidant at the temperatures of our experiment. It is an important oxidant in the high-temperature regions of the luminous flame during nitramine combustion [7].

**Thermolysis Under  $\text{NO}_2$ .** In the thermolysis studies above the effect of the added gas is primarily on the secondary reactions among the

pyrolysis products, i.e., reactions that occur primarily in the dispersed-phase region of the flame (Fig. 1). Examination of the composition-time profiles (Figs. 6–10) indicates that the initial concentrations of the products are essentially the same for HMX thermolysis under Ar,  $\text{H}_2$ ,  $\text{CO}$ ,  $\text{O}_2$ , and NO (added NO does appear to influence the yield of HCN slightly). This suggests that at a pressure of 1 atm these added gases have little effect on the initial pyrolysis reactions in the condensed phase. The results with added  $\text{NO}_2$  stand in stark contrast to this observation.

As shown in Fig. 11, the initial concentrations of  $\text{CH}_2\text{O}$ , HCN,  $\text{N}_2\text{O}$ , and HONO are significantly higher than the concentrations observed for thermolysis under Ar (Fig. 5). The  $\text{CH}_2\text{O}$  produced is consumed rapidly, although little HCN decay is observed. The terminal  $\text{CO}_2/\text{CO}$  ratio is 0.4 (versus 1.0 for Ar) and the total  $\text{CO}_x$  concentration is slightly lower. These dramatic effects occur in an initial atmosphere that contains only 25 torr of  $\text{NO}_2$  diluted with Ar to a total pressure of 760 torr.

The results suggest that the added  $\text{NO}_2$  is involved with the incipient pyrolysis reactions occurring in the condensed phase. This interaction is enhanced by the higher solubility and reactivity of  $\text{NO}_2$  in the heterogeneous liquefaction phase. The added  $\text{NO}_2$  may initiate HMX decomposition via skeletal methylene proton abstraction, mediate the pyrolysis of HMX via further H-atom abstracts from the initial large radical fragments, and

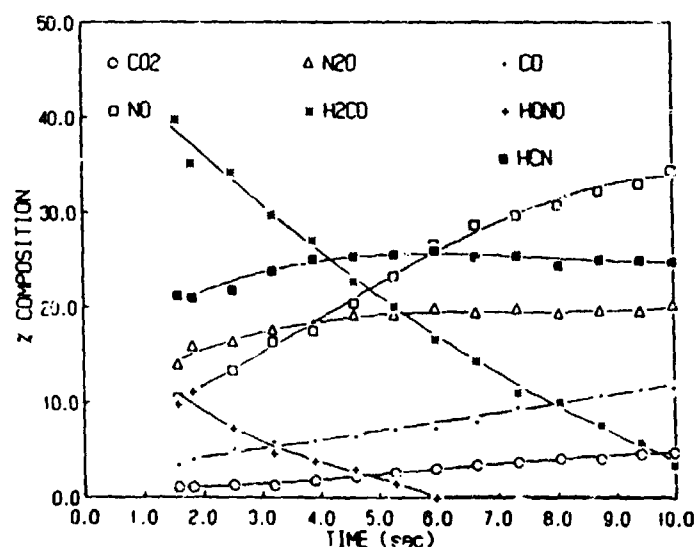
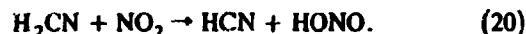


Fig. 11. The gas composition vs time profiles for HMX under an initial heating rate of 140 K/s and a 25 torr  $\text{NO}_2$ /735 torr Ar atmosphere.

possibly aid in breaking up "cage" effects in the condensed phase [35]. H-atom abstractions from large radicals or secondary fragments like  $\text{H}_2\text{CN}$  account for the high initial concentration of HONO and the overall increase in HCN generation (reaction 20).



The high initial concentration of HONO and its subsequent decomposition [11] yield an effective source of OH that rapidly consumes the  $\text{CH}_2\text{O}$  generated.

**Thermolysis Under  $\text{NH}_3$ .** HMX decomposition under  $\text{NH}_3$  (Fig. 12) produces dramatic differences relative to decomposition under Ar. The initial concentration of HCN is the same as that produced under Ar, but significantly less  $\text{CH}_2\text{O}$  is present. Both  $\text{CH}_2\text{O}$  and HCN decay rapidly to undetectable levels.  $\text{NO}_2$  is also consumed completely. Total  $\text{CO}_x$  production is somewhat lower which is consistent with the lower initial amount of  $\text{CH}_2\text{O}$ . HONO and HNCO are not detected. There is an unusual plateau in the NO product profile. The very high  $\text{N}_2\text{O}$  concentration probably results more from the  $\text{N}_2\text{O}$  produced by reaction of  $\text{HN}_x$  and  $\text{NO}_x$ , than effects that generate more skeletal derived  $\text{N}_2\text{O}$ .

The extensive involvement of  $\text{NH}_3$  ( $\text{NH}_x$ ) with secondary pyrolysis products makes it difficult to assess clearly its influence on the condensed phase chemistry. However, like  $\text{NO}_2$  it is highly

reactive and should have higher solubility in the liquefaction phase than the other gases studied.  $\text{NH}_3$  cannot directly initiate HMX decomposition but should react rapidly with radical mediators like OH.

$\text{NH}_3$  present during incipient HMX pyrolysis and liquefaction may scavenge OH and provide a source of H atoms for abstraction by other fragment radicals. The absence of HNCO and the reduced concentration of  $\text{CH}_2\text{O}$  may result from a shunting of the condensed phase chemistry.  $\text{NH}_3$  could provide a source of H atoms to fragment radicals in the "melt," such as those proposed in reactions 2a and 2b, and hinder their future fragmentation of  $\text{CH}_2\text{O}$  and HNCO. This scenario is consistent with secondary condensed-phase chemistry being responsible for HNCO and much of the  $\text{CH}_2\text{O}$ .

The most important reactions involving  $\text{NH}_x$  species under the conditions of this experiment are given below. All of the  $\text{NH}_x$  reactions have rate constants greater than  $10^{11} \text{ cm}^3 \text{ mol}^{-1} \text{ s}^{-1}$  and are exothermic [41, 45, 46]:

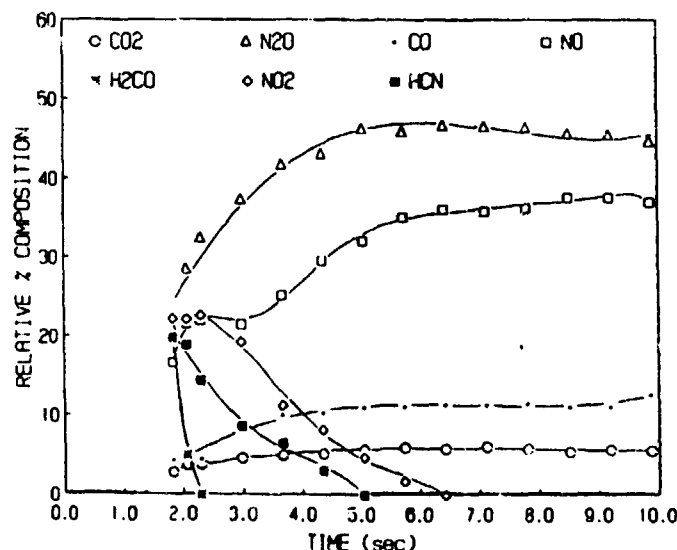
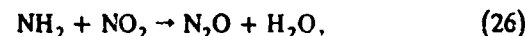
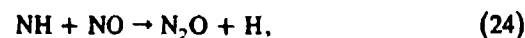
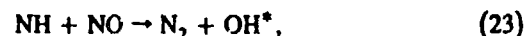
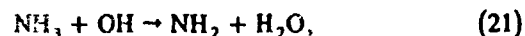
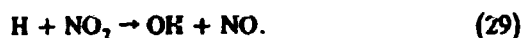
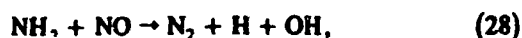


Fig. 12. The gas composition vs time profiles for HMX under an initial heating rate of 140 K/s and a 380 torr  $\text{NH}_3$ /380 torr Ar atmosphere.



These reactions account for the consumption of  $\text{NO}_2$  and the larger amounts of  $\text{N}_2\text{O}$  generated. Reaction 23 is important in explaining the complete oxidation of HCN. As noted earlier in the section on HMX decomposition in Ar, HCN is relatively stable. Its decay is normally only observed at the highest heating rates and filament temperatures. The observation is consistent with modeling studies [7] that show HCN to be oxidized primarily in the hotter secondary flame during HMX combustion. Why then (under the fuel-rich  $\text{NH}_3$  atmosphere) is HCN rapidly oxidized and completely consumed? Laser diagnostic studies of ammonia flames indicate that reaction of HN with NO (reaction 23) can result in vibrationally excited "hot" OH [46]. It is proposed that "hot" OH is responsible for the oxidation of the HCN. Reference to Fig. 12 shows that HCN is initially produced at a concentration similar to that observed during thermolysis under Ar. Its concentration increases slightly during the next 400 ms. Then abruptly, the concentration of HCN decays rapidly. This rapid decay region corresponds directly to the plateau feature in the NO concentration profile, which supports the suggested "hot" OH mechanism.

#### Time of Decomposition Product Appearance

Review of the thermolysis product profiles (Figs. 6-12) reveals that there are reproducible differences in the time of appearance of the first quantifiable spectrum of products. Under an inert Ar atmosphere pyrolysis products appear 1.8 s after the onset of heating. Calibration shows that the temperature of the filament is near 550 K at this point, which corresponds closely to the decomposition temperature of HMX [13]. Under the reactive atmospheres products appear as early as 1.6 s ( $\text{NO}_2$ ,  $\text{NH}_3$ ) and as late as 2.4 s ( $\text{O}_2$ ).

The data available do not provide a strong basis to suggest that the time of product appearance is related to the accelerating or inhibiting effect of the added gas. Although heat and mass transfer play a role, the variations in product

appearance for these experiments cannot be explained on the basis of differences in the transport properties of the gases. The transport properties (mean free path, viscosity, thermal conductivity) for all of the gases studied, except  $\text{H}_2$ , are similar [47, 48]. The thermal conductivity of  $\text{H}_2$  is an order of magnitude greater than the other gases and it has a significantly lower viscosity. Despite these differences, the time of product appearance is the same for thermolysis under CO and  $\text{H}_2$ . The largest variation (relative to Ar) is observed for thermolysis under  $\text{O}_2$ . A temperature calibration check in an  $\text{O}_2$  atmosphere indicates no difference in the heating rate of the filament temperature relative to that under Ar. Products reproducibly appear 200 ms earlier under an atmosphere containing 25 torr of  $\text{NO}_2$  in Ar (3.3 vol.%  $\text{NO}_2$ ) compared with thermolysis under neat Ar.

Collisional energy transfer efficiencies are also not a factor. The relative efficiencies for all of the gases studied are low and of the same magnitude [49]. The most important species for collisional energy transfer are  $\text{H}_2\text{O}$  and other large pyrolysis products arising from the sample. We do not have a consistent explanation for the variations in time of appearance of products at this time.

#### SUMMARY

This work has furthered the understanding of many aspects of high-rate thermal decomposition of HMX and its relationship to combustion. These are the first studies to probe the effects of reactive gases on HMX thermolysis by analyzing the evolved decomposition products. The work supports the belief that high-rate thermolysis under these conditions simulates the heterogeneous condensed-phase foam zone chemistry and the chemistry of the early fizz zone of energetic materials. The results are qualitatively consistent with experimental combustion and modeling studies of HMX performed under 1 atm pressure.

$\text{H}_2$ , CO,  $\text{O}_2$  and NO do not appear to perturb the initial decomposition pathways, but play a role in the secondary pyrolysis reactions in the foam zone and the early fizz zone. The most dramatic perturbations are induced by atmospheres of  $\text{NO}_2$  and  $\text{NH}_3$ . This is attributed to their higher reactivity and higher solubility in the liquefaction phase.  $\text{NH}_3$  reacts with the first and

subsequent pyrolysis products, while  $\text{NO}_2$  perturbs the initial decomposition pathways.

The products of  $\text{HNCO}$  and  $\text{CH}_2\text{O}$  arise primarily from condensed-phase reactions. Conditions that promote condensed phase reactions (low heating rates, low temperatures) and "aging" of the melt yield higher amounts of  $\text{CH}_2\text{O}$ . Pathways for  $\text{CH}_2\text{O}$  and  $\text{HNCO}$  formation were proposed. A ready source of abstractable hydrogen atoms ( $\text{NH}_3$ ) may quench these reactions.

Decomposition of HMX results predominantly in the generation of more stable products, such as  $\text{N}_2\text{O}$ ,  $\text{HCN}$ , and  $\text{NO}$ . These species largely pass through the primary flame zone without further reaction and are converted to final combustion products in the hotter luminous flame (farther from the burning surface). Our studies indicate that the so-called catalyzable species  $\text{NO}_2$  and  $\text{HN}_x$  [8] are important. These species are reactive in the condensed phase and the primary flame. Ballistic modifiers that could increase the amount of  $\text{NO}_2$  generated in the condensed phase may increase the burn rate.  $\text{NH}_x$  species are not produced in significant amounts during HMX thermolysis. The highest amounts are probably produced in the luminous secondary flame. These thermolysis experiments demonstrate that  $\text{NH}_x$  species can effectively react with  $\text{NO}$  at the lower temperatures of the dispersed phase, generating heat closer to the burning surface and liberating a potent oxidizer  $\text{OH}$ . This may increase heat feedback to the burning surface and ultimately increase burn rate.

The most efficient formulation-based approach to introduce  $\text{NH}_x$  would be to replace the hydrocarbon or polyether binder with a binder system containing  $\text{NH}_x$  functionality. Developing an  $\text{NH}_x$ -containing binder that is chemically compatible and possesses suitable aging and mechanical properties presents a challenge. Ballistic modifiers based on heterogeneous catalysts known to be effective for  $\text{NO}_x$  reduction [44, 50, 51] should be evaluated in conjunction with a source of  $\text{NH}_x$ .

*We are grateful to the Thiokol Corp. for support of this work on an independent research and development program. The encouragement of Dr. D. A. Flanigan was most appreciated. Partial support of the Air Force Office of Scientific Research on AFOSR-85-*

*0356 and 87-0033 is also gratefully acknowledged.*

## REFERENCES

1. Cohen, N. S., Derr, R. L. and Price, C. F., Ninth JANNAF Combustion Meeting, CPIA Publ. 231, Dec. 1972, Vol. II, pp. 25-42.
2. Cohen, N. S. and Price, C. F., 13th AIAA Meeting, AIAA Paper 75-238, Jan. 1975.
3. Kumar, R. N., and Strand, L. P., AFATL-TR-74-155, Air Force Rocket Propulsion Laboratory, Edwards AFB, CA, Sept. 1974.
4. Kumar, R. N., and Strand, L. P., 13th AIAA Meeting, AIAA Paper 75-239, Jan. 1975.
5. Shackelford, S. A., Coolidge, M. B., Goshgarian, B. B., Loving, B. A., Rogers, R. N., Janney, J. L., and Ebinger, M. H., *J. Phys. Chem.* 89:3118-3126 (1984).
6. Melius, C. F., and Binkley, J. S., *Twenty-First Symposium (International) on Combustion*, The Combustion Institute, Pittsburgh, 1986, pp. 1953-1963.
7. Melius, C. F. in *Chemistry and Physics of Molecular Processes in Energetic Materials* (S. Bulusu, Ed.), Kluwer, Boston, 1990, pp. 51-78.
8. Jones, M. L., Elrick, D. E., Herriott, G. E., Mühlfeith, C. M., and McCarty, K. P., AFRPL-TR-82-79, Air Force Rocket Propulsion Laboratory, Edwards AFB, CA, 1983.
9. Oyumi, Y., and Brill, T. B., *Combust. Flame* 62:213-224 (1985).
10. Perry, R. A., *J. Chem. Phys.* 82:5485-5488 (1985).
11. Zhao, X., Hintsa, E. J., and Lee, Y. T., *J. Chem. Phys.*, 88:801-810 (1988).
12. Behrens, R., Jr., Proceedings of the 24th JANNAF Combustion Meeting, CPIA Publ. 476, 1987, Vol. I, 333-342.
13. Boggs, T. L., *Prog. Astronaut. Aeronaut.* 90:121-175 (1984).
14. Filer, R. A., *Prog. Astronaut. Aeronaut.* 90:177-237 (1984).
15. McCarty, K. P., AFRPL-TR-78-73, Air Force Rocket Propulsion Laboratory, Edwards AFB, CA, 1978.
16. Goshgarian, B. G., AFRPL-TR-78-73, Air Force Rocket Propulsion Laboratory, Edwards AFB, CA, 1978.
17. Schroeder, M. A., Proceedings of the 16th JANNAF Combustion Meeting, CPIA Publ. 308, 1979, Vol. II, pp. 17-34.
18. Schroeder, M. A., Proceedings of the 17th JANNAF Combustion Meeting, CPIA Publ. 329, 1980, Vol. II, pp. 493-503.
19. Schroeder, M. A., Proceedings of the 18th JANNAF Combustion Meeting, CPIA Publ. 347, 1981, Vol. II, pp. 395-413.
20. Schroeder, M. A., BRL-TR-2673, Army Ballistic Research Laboratory, Aberdeen, MD, 1985.
21. Caveny, L. H., and Ben Reuven, M., *AIAA J.* 19:1276-1285 (1981).
22. Shaw, R., and Walker, F. E., *J. Phys. Chem.* 81:2572-2576 (1977).

23. Cosgrove, J. D., and Owen, A. J., *Combust. Flame*, 22:13-18 (1974).
24. Batten, J. J., *Aust. J. Chem.* 24:945-954 (1971).
25. Batten, J. J., *Aust. J. Chem.* 24:2025-2029 (1971).
26. Maksimov, Y. Y., *Tr. Mosk. Khim. Tekhnol.* 53:73-84 (1967).
27. Debenham, D. F., and Owen, A. J., *Proc. Symp. Stab. Explos.* 4:201-220 (1977).
28. Cosgrove, J. D., and Owen, A. J., *Combust. Flame* 22:19-22 (1974).
29. Kraeutle, K. J., Proceedings of the 17th JANNAF Combustion Meeting, CPIA Publ. 329, 1980, Vol. VIII, pp. 509-525.
30. Karpowicz, R. J., and Brill, T. B., *AIAA J.* 20:1586-1591 (1982).
31. Brill, T. B. and Karpowicz, R. J., *J. Phys. Chem.* 86:4260-4265 (1982).
32. Kubota, N., and Sakamoto, S., *Prop. Explos. Pyrotech.* 14:6-11 (1989), and personal communication of S. Sakamoto, 1990.
33. Rogers, R. N., personal communication to F. Goetz and T. Brill, 1982.
34. Tectsov, A. S., and McCrone, W. C., *Microsc. Cryst. Front.* 15:13-29 (1965).
35. Northrup, S. H., and Hynes J. T., *J. Chem. Phys.* 71:871-893 (1979).
36. Karpowicz, R. J., and Brill, T. B., *Combust. Flame* 56:317-325 (1984).
37. Behrens, R., Jr., Proceedings of the 26th JANNAF Combustion Meeting, CPIA, 1989, Vol. I, pp. 39-48.
38. Schroeder, M. A., Fifer, R. A., Miller, M. S., and Peace-Rodriguez, A., BRL-MR-3845, Ballistic Research Laboratory, Aberdeen Proving Ground, MD, 1990.
39. Brill, T. B., and Oyumi, Y., *J. Phys. Chem.* 90:6848-6853 (1986).
40. Brush, P. J., and Brill T. B., *Proceedings of the 9th Symposium on Detonation*, Portland, OR, Vol. I, pp. 228-234, 1989.
41. Gardiner, W. C., Jr. (ed.), *Combustion Chemistry*, Springer-Verlag, New York, 1984.
42. Wagner, H. G., *Fourteenth Symposium (International) on Combustion*, The Combustion Institute, Pittsburgh, 1973, pp. 27-35.
43. Melius, C. F., in *Chemistry and Physics of Molecular Processes in energetic Materials* (S. Bulusu Ed.), Kluwer, Press, Boston, 1990, pp. 21-49.
44. Palopoli, S. F., and Brill T. B., *Combust. Flame* 72:153-158 (1988).
45. Gehring, M., Hoyermann, K., Schacke, H., and Wolfrum, J., *Fourteenth Symposium (International) on Combustion*, The Combustion Institute, Pittsburgh, 1973, pp. 99-105.
46. Dean, A. M., Chou, M. S., and Stern, D., in *Chemistry of Combustion Processes*, ACS Symposium series 249 (T. M. Sloane, Ed.), Washington, D.C., 1984, pp. 71-86.
47. Moore, W. J., *Physical Chemistry*, Prentice-Hall, Englewood Cliffs, NJ, 1972, p. 154.
48. Braker, W., and Mossman, A. L., *Matheson Gas Data Book*, Matheson Gas Products, East Rutherford, NJ, 1971.
49. Gardiner, W. C., Jr., *Rates and Mechanisms of Chemical Reactions*, Benjamin, Menlo Park, CA, 1972, p. 117.
50. Palopoli, S. F., Geib, S. J., Rheingold, A. L., and Brill, T. B., *Inorg. Chem.* 27:2963-2971 (1988).
51. Stoner, C. E., Jr., Rheingold, A. L., and Brill, T. B., *Inorg. Chem.* 30:360-364 (1991).

Received / December 1990; revised 4 June 1991

## SIMULATION EXPÉRIMENTALE D'UNE SURFACE EN TRAIN DE BRÛLER LORS D'UNE COMBUSTION OU D'UNE EXPLOSION

Pr. T. B BRILL <sup>(1)</sup>

Traduction : J. BOILEAU

**RÉSUMÉ.** — *Il est essentiel d'avoir une description physique et chimique précise de la zone de la surface en réaction pendant la combustion d'un propergol, pour établir tout modèle détaillé de cette combustion. Comme les compositions chimiques détaillées n'ont pu être déterminées dans une combustion réelle, deux expériences de simulations ont été mises au point pour déterminer les cinétiques et les mécanismes. La vitesse de combustion peut être prédite par les mesures de cinétiques. De ce fait, les produits gazeux observés sont très probablement à l'origine de la première étape de la zone de flamme.*

**ABSTRACT.** — *A chemical and physical description of the surface reaction zone during propellant burning is essential to any advanced model of combustion. Because chemical details have not been obtainable during actual combustion, two simulation experiments have been developed to determine the kinetics and mechanisms. The burn rate is predicted by the measured kinetics. The observed gas products, therefore, very probably initiate the first stage of the flame zone.*

### DISCUSSION TECHNIQUE

La mise au point de nouveaux propergols à haute énergie, sans combustibles métalliques, représente un défi considérable pour la communauté des fabricants de propergols. Les problèmes des instabilités de combustion, de la sécurité des allumages, et des réglages sur mesure doivent tous être surmontés. La modélisation va jouer un rôle majeur comme guide au développement étant donné les coûts élevés des essais en vraie grandeur.

L'objectif final de la modélisation de la combustion des propergols et de sa stabilité exige, parmi d'autres

données d'entrée, une description physique et chimique de la surface de combustion à l'échelle microscopique. Celle-ci ne peut actuellement être obtenue par des mesures directes pendant la combustion : c'est dû au fait que la surface de combustion est transitoire, hétérogène, hors d'équilibre, elle est en outre obscurcie par la flamme. Il est donc nécessaire de monter des expériences qui simulent la phase condensée et la surface en cours de combustion, tout en dégageant les gaz dans une atmosphère inerte et froide, où ils sont figés et détectés aussitôt.

On peut imaginer la surface en combustion comme un film de produit d'épaisseur 20 à 100  $\mu\text{m}$  dans lequel se produit un changement de phase entraîné

<sup>(1)</sup> Département de Chimie, Université de Delaware Newark, DE 19716, ÉTATS-UNIS.

par les réactions chimiques et le transfert de chaleur. En effet, il s'agit d'une zone de réaction en « film mince » qui régresse à travers la phase condensée d'un côté et qui produit des gaz en arrière, de l'autre côté. C'est pourquoi une simulation instantanée de cette zone de réaction pourrait être un film mince de propergol subissant une montée en température de 100 à 2000°C/s à la pression atmosphérique ou sous une pression plus élevée. Le choix de cette vitesse de montée en température de 100 à 2000°C/s est fondé sur un récent travail de Sakamoto et Kubota avec des thermocouples incorporés dans des propergols à base d'octogène; leurs mesures indiquent que dans la zone de réaction en phase condensée (« mousse ») la valeur de  $dT/dt$  est de l'ordre de  $1000 \pm 500^\circ\text{C/s}$ .

Deux approches pour cette simulation ont été développées :

- l'une appelée T-jump/FTIR (saut en T/spectroscopie infrarouge à transformée de Fourier).
- l'autre appelée SMATCH/FTIR (mesure simultanée du changement de masse et de température/spectroscopie infra-rouge à transformée de Fourier).

La mesure à la fois des cinétiques ultra-rapides et des produits gazeux dégagés est importante car il faut démontrer que la cinétique peut prévoir la vitesse de combustion afin de vérifier que les produits gazeux observés sont effectivement ceux qui alimentent la zone sombre dans la région de la combustion.

La méthode Fast-Head-and-Hold T-Jump/FTIR est agencée pour permettre un chauffage d'un échantillon à une vitesse de 2000°C/s jusqu'à une température finale choisie à l'avance. De cette façon, on minimise la plupart des processus chimiques parasites qui interviennent dans les études de décomposition à chauffage lent et ceux qui résultent de la « carbonisation ». La figure 1 illustre le principe de la méthode. Le tracé de la réponse thermique de l'échantillon est obtenu à partir de la régulation de la tension qui est prévue pour maintenir constante la résistance du ruban chauffant de platine. Les produits gazeux se dégagent dans une atmosphère froide d'argon, qui les fige, et ils sont identifiés et dosés par absorption d'un rayonnement infrarouge enregistré sur spectromètre à transformée de Fourier à balayage rapide. La figure 2 représente la superposition de ces enregistrements pour de l'octogène porté à 300°C par chauffage à 2000°C par seconde. L'exotherme d'allumage est le pic très fin négatif représentant la régulation de la tension.

Le fait que les produits gazeux soient détectés avant l'apparition de l'exotherme d'allumage est une forte évidence pour l'existence d'un phénomène d'autocatalyse dans l'octogène.

Le fait que  $\text{NO}_2$  et  $\text{N}_2\text{O}$  apparaissent avant les combustibles ( $\text{HCHO}$  et  $\text{HCN}$ ) montre que les réactions produisant des oxydants et celles produisant des combustibles ne sont pas couplées :  $\text{NO}_2$  et  $\text{HCN}$  ne sont pas produits au cours de la même réaction élémentaire, il en est de même pour  $\text{N}_2\text{O}$  et  $\text{HCHO}$ ;

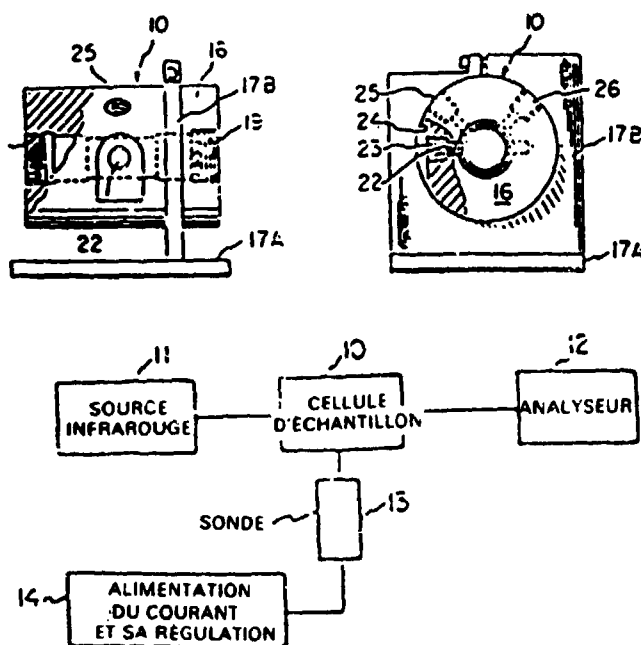


FIG. 1. — Schéma de l'appareil T-jump/FTIR (à gauche) et dessus de la cellule. Un mince film de 200 µg d'échantillon est placé sur un ruban de platine et inséré au point 22 via la paroi de la cellule.

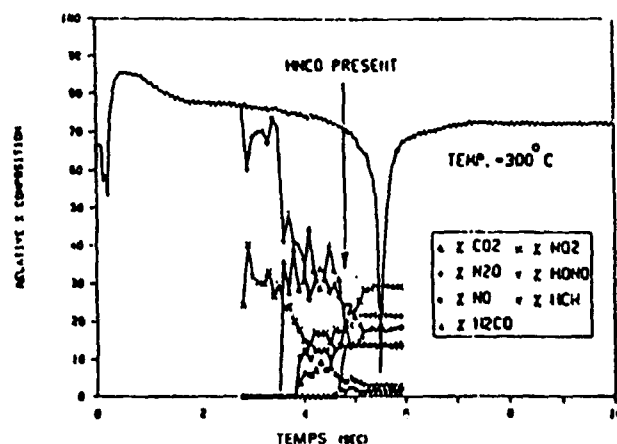


FIG. 2. — Réponse en tension de la régulation du filament de platine superposée aux courbes de composition relative des gaz produits à partir de 200 µg d'octogène. La vitesse de chauffage était de 2000°C/s jusqu'à une température de 300°C. Le pic négatif est l'exotherme de l'octogène. Pour plus de détails, voir le texte.

au contraire  $\text{N}_2\text{O}$  et  $\text{NO}_2$  sont dégagés et c'est seulement ensuite que  $\text{HCHO}$  et  $\text{HCN}$  sont produits, à un stade ultérieur de la dégradation du résidu. Le fait que les concentrations respectives des produits gazeux ne changent pas lorsque l'exotherme (de l'allumage) a lieu implique que les mécanismes de décomposition avant l'exotherme et pendant l'exotherme sont essentiellement les mêmes d'un bout à l'autre. Simplement une plus grande quantité d'octogène est décomposée.

L'une des données les plus intéressantes à partir de ce type d'expériences est la proportion des gaz produits en fonction de la température. Le rapport

$N_2O/NO_2$  (voir fig. 3) reflète la proportion des vitesses de réaction pour les deux voies globales de décomposition de l'octogène : la branche  $N_2O + HCHO$  et la branche  $NO_2 + HCN$ . A plus basse température, la première est prépondérante, la seconde le devient à plus haute température. On pense qu'à la surface de propergols à base d'octogène, les températures en surface sont de l'ordre de  $350^\circ\text{C}$ . Ainsi la figure 3 donne un rapport des constantes de vitesse des deux réactions pilotes, qui peuvent être utilisées comme données d'entrée dans des modèles concernant la phase gazeuse pendant l'allumage de l'octogène.

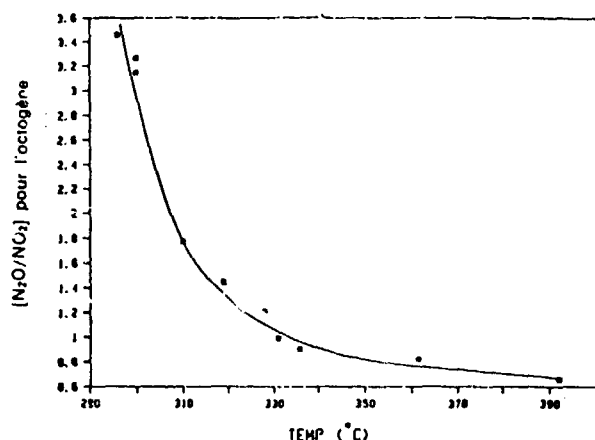


FIG. 3. — Proportion des deux branches  $N_2O-HCHO/NO_2-HCN$  provenant de la décomposition de l'octogène, en fonction de la température. Les vitesses de ces deux réactions sont approximativement égales à la température de la surface de combustion de l'octogène ( $340-360^\circ\text{C}$ ).

La technique SMATCH/FTIR rend possible l'enregistrement de la variation de la masse de l'échantillon en fonction du temps et de la température quand celui-ci est chauffé rapidement; on en tire une simulation cinétique de la surface de combustion; on obtient simultanément l'enregistrement par spectroscopie infrarouge à grande vitesse et balayage rapide, des gaz produits près de la surface de combustion.

Il a été trouvé récemment que les constantes d'Arrhénius obtenues à partir d'expériences SMATCH/FTIR sur films minces permettent de prédire correctement la vitesse de combustion  $\dot{r}$  mesurée dans les mêmes domaines de pression et de température. La figure 4 montre pour une nitrocellulose à 13 % de taux d'azote, l'acquisition simultanée de la perte de masse, de l'élévation de température et des données de composition des produits gazeux à la surface de combustion.

Partant des constantes d'Arrhénius obtenues à partir d'un modèle cinétique non isotherme et de l'épaisseur connue de l'échantillon, on prévoit une vitesse de combustion de  $0,3 \text{ mm/s}$ ; elle est en très

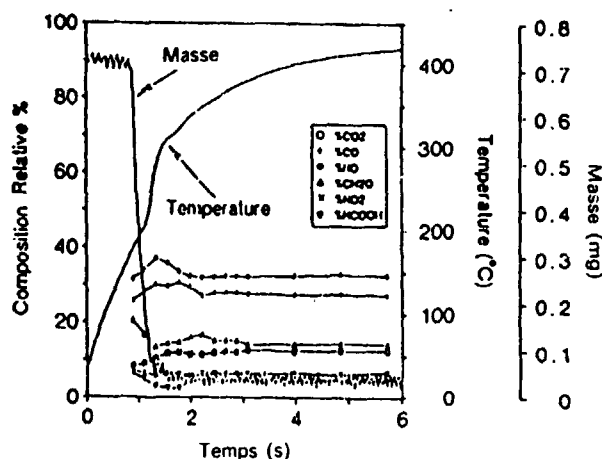


FIG. 4. — Données obtenues par SMATCH-FTIR sur un film de  $30 \mu$  d'épaisseur de nitrocellulose à 13 % d'azote, montrant les variations dynamiques de la masse, de la température et les produits gazeux de combustion. La variation de masse et le profil de la courbe de température permettent d'appliquer un modèle de cinétique non isotherme. Les produits sont les espèces chimiques s'échappant de la surface dans cette situation de simulation de la combustion.

bon accord avec la valeur expérimentale  $\dot{r}$  de  $0,4 \text{ mm/s}$  pour un propergol à double base (80 % de nitrocellulose) mesurée dans les mêmes conditions de pression.

La méthode SMATCH/FTIR pour le PAG (polyazide de glycidyle) prédit pour  $\dot{r}$  une vitesse de  $1,35 \text{ mm/s}$ , à comparer avec la valeur expérimentale de  $1,7 \text{ mm/s}$  dans les mêmes conditions de pression. Cette bonne concordance entre vitesses calculées et mesurées donne confiance pour dire que les produits gazeux aux concentrations mesurées par SMATCH/FTIR sont les réactifs intervenant dans la flamme au cas où une flamme serait présente.

Les produits gazeux obtenus par les 2 méthodes décrites (SMATCH/FTIR et Fast Heat and Hold/FTIR), ainsi que par toutes nos méthodes de thermolyse rapide associée à la FTIR que nous utilisons précédemment sont essentiellement les mêmes. Il en résulte que l'on commence à pouvoir trouver la connexion entre la composition chimique d'un matériau et les caractéristiques terminales de la flamme de sa combustion.

#### Notes du traducteur :

1) On pourra aussi consulter l'article de T. Brill et F. D. Brush publié dans les Actes du 22<sup>e</sup> Symposium International de l'ICT Karlsruhe (2-5 juillet 1991) pages 12-1 à 8.

2) Cet exposé du Pr. T. Brill a été présenté dans une réunion plus restreinte sur la combustion des propergols le 4 juin 1991, mais son intérêt dans le domaine des explosifs et la présence du Pr. Brill aux journées du 6-7 juin nous ont incités à publier ce texte.



## CONNECTING THE CHEMICAL COMPOSITION OF A MATERIAL TO ITS COMBUSTION CHARACTERISTICS

THOMAS B. BRILL

*Department of Chemistry, University of Delaware, Newark, DE 19716, U.S.A.*

*Received 9 August 1991*

**Abstract**—The chemistry in the surface region during combustion of a solid is extraordinarily difficult to determine. Understanding is important because molecules of the parent material break up in this zone to form the initial reactants for the flame. Hence, the surface reaction zone ties the composition of the material to the flame chemistry. The validity of using fast thermolysis of a thin film of the material to simulate the surface reaction zone is assessed. Sub-global chemical details are extracted by the use of rapid-scan Fourier transform infrared spectroscopy. Such microscale laboratory simulations help establish molecular structure details of nitramines that influence the formation of near-surface flame reactants like  $\text{NO}_2$ ,  $\text{HONO}$ ,  $\text{CH}_2\text{O}$  and  $\text{N}_2\text{O}$ . The effects of pressure and temperature on the surface reaction zone can be probed experimentally. Other infrared spectral methods designed to probe the condensed phase and gas phase are discussed.

### CONTENTS

1. Introduction	91
2. Simulation of the Disperse Region	92
3. Simultaneous Mass and Temperature Change/FTIR Spectroscopy (SMATCH/FTIR)	93
4. Rapid-Scan FTIR Spectroscopy	96
5. Near Surface Gas Product Analysis	96
5.1. Cell design and methods	97
5.2. Quantitation processes	97
5.3. Some characteristics of the evolved products	99
5.4. Structure/decomposition relationships	101
5.4.1. Tendency to form $\text{NO}_2(\text{g})$	102
5.4.2. Tendency to form $\text{HONO}(\text{g})$	103
5.4.3. Tendency to form $\text{N}_2\text{O}(\text{g})$	104
5.4.4. Tendency to form $\text{CH}_2\text{O}(\text{g})$	105
5.4.5. Other studies of energetic compounds	106
5.5. The use of decomposition product data in combustion modelling	106
6. Temperature profiling/FTIR Spectroscopy	106
7. The Effect of Pressure on the First Detected Products	109
8. Isothermal Decomposition at High Temperature	110
9. Studies on the Submicrosecond Timescale	112
10. FTIR Measurements of Flames	112
11. Summary	114
Acknowledgements	114
References	115

### 1. INTRODUCTION

New opportunities to advance the field of rocket propulsion are possible if important combustion characteristics can be predicted simply from the composition of the propellant. The achievement of this objective requires a detailed knowledge of many factors, among which is a thorough understanding of the relationship between the formulation of the condensed phase and the gases available to react in the flame zone.

In recent decades spectroscopy has played an increasing role in the identification of reactants and products, the measurement of temperature and reaction rates, and the description of physical phenomena during the thermal decomposition, com-

bustion and explosion of materials. When a solid propellant burns, the luminous flame is the most prominent feature. The luminous flame (diffusion or monopropellant) can be successfully interrogated by laser diagnostics which provides reaction rates, constituent species and temperatures. To achieve the desired understanding, the flame is frequently optimized by the choice of the reactants, the use of a single phase, and the use of a pressure below that of a rocket combustion chamber. Impressive advances have been made and have been overviewed elsewhere.<sup>1</sup>

A critically important zone for propellants and explosives is the heterogeneous reaction region that connects the condensed phase to the gas phase (Fig. 1). Despite its well-recognized importance, this zone has resisted detailed chemical study. The main focus

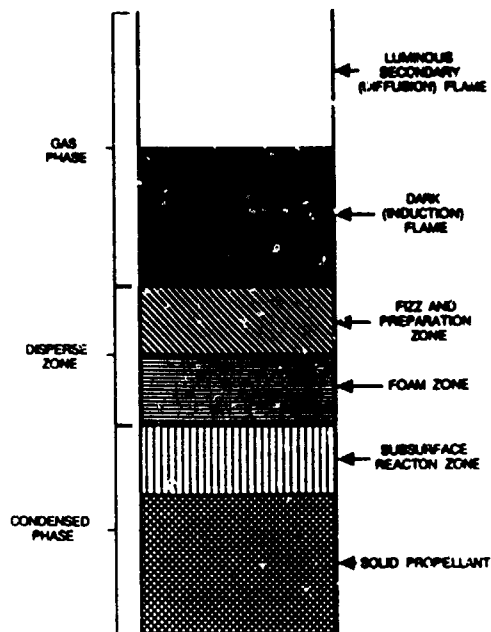


FIG. 1. A one-dimension microscale picture the main reaction zones at the surface of a solid propellant component during combustion.

of this article is to describe infrared absorption spectroscopy as a viable method to study this heterogeneous transition zone. When a bulk material is burned, a thin heterogeneous reaction zone develops at the surface where the reactants form and enter the flame zone. This process is extremely complex because thermochemistry, kinetics, condensed phase species, surface phenomena, and heat and mass transport are all important. The reaction zone is also very thin (5–200  $\mu\text{m}$ ) which makes studies very difficult to conduct under combustion conditions. Therefore, studies that simulate the conditions of this zone are the most promising alternate approach to gaining key information about how the composition of a material relates to its combustion characteristics. However, because of the complexity of the chemical and physical processes involving bulk samples, less temporal resolution, less quantitative data and more global information frequently have to be traded for interpretable data. Consequently, uncertainty exists as to how closely the microscale experiments simulate the conditions of a full scale combustion of explosion process.

Recently, it has been found that the burn rate of various energetic materials calculated from the kinetics constants measured with Simultaneous Mass and Temperature Change (SMATCH)/Fourier transform infrared spectroscopy (FTIR)<sup>1</sup> at 15 psi closely matches the experimental linear burn rate measured at or extrapolated to the same conditions.<sup>11</sup> Some comparisons are given in Table I and the experimental details are described later in Section 3. The important point is that this connection provides confi-

TABLE I. Regression (burn) rate data for various energetic and non-energetic materials at 15 psi calculated from SMATCH/FTIR kinetics and measured by combustion or linear pyrolysis experiments

Compound	r, mm/sec	
	SMATCH/FTIR	Engineering Test
Nitrocellulose	0.3	0.4*
Glycidyl azide polymer	1.35	1.7†
RDX	0.38	0.3‡
HTPB	0.21	0.05–0.2§

\* Extrapolated to 180°C from double base propellant data given by M. W. Beckstead, *Proc. 25th JANNAF Combust. Mtg.*, JPL, Pasadena, CA (October, 1985).

† Extrapolated to 15 psi from higher pressure data given by N. Kubota and S. Sonobe, *Prop. Explos. Pyrotech.* 13, 172 (1988).

‡ V. V. Aleksandrov, R. K. Tukhtaev, V. U. Boldyrev, and A. V. Boldyreva, *Combust. Flame* 35, 1 (1979).

§ Values for polymethylmethacrylate and polystyrene at 350°C given by W. H. Anderson, K. W. Bills, E. Mishuck, G. Moe and R. W. Schultz, *Combust. Flame* 3, 301 (1959).

dence in the use of SMATCH/FTIR and other fast thermolysis/FTIR methods<sup>4–10</sup> to identify many of the species that exist in the disperse zone shown in Fig. 1 and enter the primary flame zone. Thus, fast thermolysis/FTIR techniques provide a method for connecting the formulation or composition of a solid or liquid energetic material to its combustion or explosion characteristics. This is because the nature and concentration of the decomposition gases are important in controlling the flame and other later stage energy release reactions. Hence, this information should be useful for modelling the combustion and explosion of energetic materials.

To illustrate how these data might be used, a description is given of the use of fast thermolysis/FTIR methods to establish the relationship of the molecular structure and composition of a series of nitramine molecules to the nature of gas products that are liberated. As burn rates and near-surface flame structure data become available for nitramines, the relationship of the gas products to some of the combustion properties could be developed. In turn, the general combustion behaviour might be predictable for hypothetical formulations. The article is concluded by an overview of how infrared absorption and emission measurements can be used to characterize the flame zone.

## 2. SIMULATION OF THE DISPERSE REGION

Direct chemical measurements of the disperse zone of Fig. 1 during combustion have not been performed and, should they be possible, would be unrealistic to perform on hundreds of samples in the near future. Therefore, experimental methods that attempt to simulate important conditions in this region are a good alternative for obtaining this information. Of course, there is no ideal experimental method

that simulates and tells the detailed condensed phase chemistry and physics and the near surface processes during combustion or an explosion. Trade-offs must be made in experiments with respect to temporal resolution, the size and position of the spectral window, the number of species probed at one time, the configuration of the sample, the method of heating, the temperature, the pressure, etc.

Various sample configurations can be imagined that enable the important conditions of the burning surface to be simulated. For instance, an instantaneous picture of the burning surface would show a film of material with a steep and accelerating temperature gradient from within the condensed phase to the gas phase. Hence, a thin film of material subjected to a high heating rate is representative. The use of a small amount of sample facilitates the heat transfer. Even if a polycrystalline sample is used, the sample frequently melts to a thin film upon heating. Because chemical information in the simulation was our goal, we chose to optimize the amount of spectral information first and then to heat as rapidly as possible. Thus, our heating rates (100–350°C/sec for most experiments) are one to three orders of magnitude slower than actual propellant combustion heating rates. However, they are one to three orders of magnitude faster than those employed by conventional thermal analysis techniques, such as TGA and DSC. Pressure is another important variable. Pressures in the 15–3000 psi range are relevant to ignition and combustion of rocket propellants. To probe the effect of pressure on the decomposition process, the static gas pressure in the cell was varied in the 1–1000 psi range to examine its effect.

While not perfectly representative of the conditions of the disperse zone during combustion of rocket propellants, the conditions appear to be close enough to connect the linear burn rate kinetics to the mass loss kinetics from fast thermolysis measured at the same temperature and pressure. By inference, then, the spectroscopic data from fast thermolysis experiments tell a lot about the chemistry under these conditions.

#### 1. SIMULTANEOUS MASS AND TEMPERATURE CHANGE/FTIR SPECTROSCOPY (SMATCH/FTIR)

As discussed above, the regression rates of the thin film of sample calculated from the SMATCH/FTIR technique are similar to those measured or extrapolated from combustion or linear pyrolysis measurements at the same temperature and pressure. Thus, SMATCH/FTIR gives an instantaneous microscale simulation of some of the important conditions that the surface reaction zone experiences during steady-state macroscale combustion. The SMATCH/FTIR technique<sup>2</sup> is presented first even though it is the most complicated fast thermolysis techniques that we have developed so far. It forms the basis for using other simpler fast thermolysis/FTIR methods to identify

the gas products that feed the first stage of a flame zone.

SMATCH/FTIR spectroscopy enables the mass and temperature changes of a thin film (20–60 μm thickness) of a material to be measured simultaneously at a high heating rate (100–350°C/sec). Non-isothermal kinetics analysis of the mass and temperature data provides Arrhenius constants that can be used in a modified version of the pyrolysis law to predict a burn rate for the material. In addition the gas products leaving the surface are measured in near real-time, simultaneously with the mass and temperature measurements. These products are formed under conditions that the condensed phase experiences during combustion, at the same pressure and temperature.

A block diagram of the mass and temperature measurement portions of the SMATCH/FTIR experiment is shown in Fig. 2. In the experiment, a film of sample with a uniform thickness in the 20–60 μm range is applied to a stainless steel end-tip which is fixed to the free end of a cantilevered quartz tube. The tube serves as the resonant element in a feedback loop that consists of a light emitting diode/phototransistor pair, a voltage amplifier, an audio amplifier, and a vibration exciter. This electromechanical feedback circuit senses the motion of the vibrating tube and drives it into transverse oscillation at its natural resonance frequency (ca. 130 Hz).

The resonance frequency of the quartz tube is sensitive to the mass of sample on the end-tip; mass measurements rely upon this sensitivity. The frequency of the fundamental vibrational mode can be described by Eq. (1).

$$F = \frac{1}{2\pi} \sqrt{\frac{3EI}{L^3(m + 0.23m_s)}} \quad (1)$$

$F$  is the natural frequency of the tube,  $E$  is Young's modulus for the tube,  $I$  is the area moment of inertia of the tube,  $L$  is the length of the tube,  $m$  is the mass of the load (end-tip plus sample), and  $m_s$  is the mass of the tube. This equation rearranges to Eq. (2), which shows the linear relationship between the sample mass and the square of the period of the vibration ( $m_s$  is the mass of the end-tip and  $m$  is the sample mass). A plot of  $1/F^2$  vs the sample mass was found to be linear.<sup>2</sup>

$$\frac{1}{F^2} = \frac{4\pi^2 L^3}{3EI} (m_s + m + 0.23m_s) \quad (2)$$

Radio-frequency induction is used to heat the stainless steel end-tip. As the sample is heated and loses mass due to thermal decomposition, the tube oscillation shifts to increasingly higher natural resonance frequencies, as described by Eq. (2). By continuously monitoring the frequency changes for the heating period, rapid mass changes due to sample thermolysis can be followed.

The sample temperature is monitored by attaching a microthermocouple directly to the end-tip. This

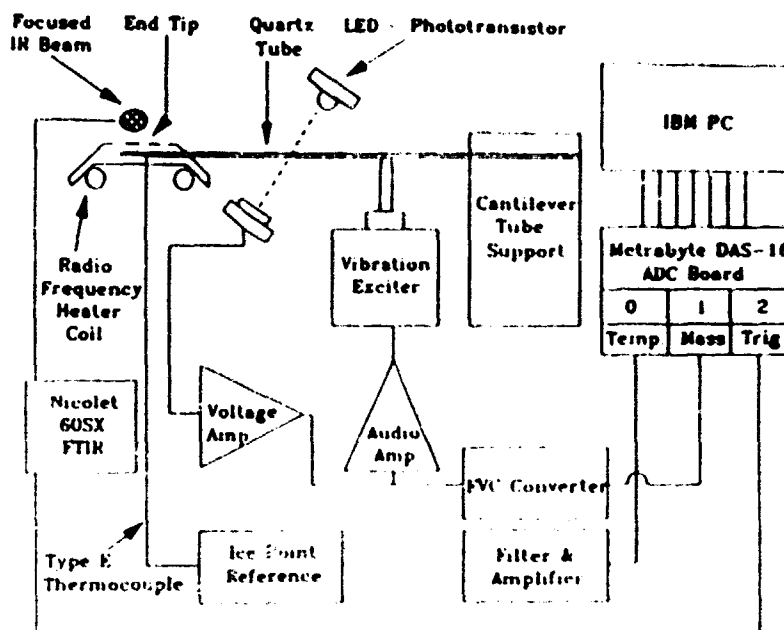


FIG. 2. A block diagram for the SMATCH/FTIR experiment.

direct attachment allows the thermocouple to sense temperature changes due to exothermic or endothermic steps during thermolysis of the sample.

The SMATCH/FTIR technique enables the dynamic weight change of the sample to be recorded as a function of time and temperature as the sample is rapidly heated. However, the microscopic detail of the thin film is expected to be complicated because gasification is not instantaneous. At any time during degradation, the film may be partly in contact with the heat source and partly separated by a very thin gas layer. As a result, the heat and mass transfer are difficult to analyze. In the worst scenario, the solid sample falls off the end-tip without reacting. Another failed experiment would occur if the sample gasifies more vigorously on one side of the end-tip than another and pushes the tube out of resonance. These difficulties are readily recognized in the weight-loss curve as a sharp spike or a slope break. Experiments in which this occurs are discarded. These problems are minimized when the thin film is uniformly deposited on the end-tip. Therefore, considerable care was taken in the preparation of the sample tubes.

To relate the kinetic parameters to the true behavior of the material during decomposition, the temperature and the mass change at that temperature must be genuinely related. That is, the relaxation rate of the temperature in the film must be at least as fast as the heating rate so that the film maintains a constant temperature. If this condition is met, then the measured temperature is characteristic of the chemistry taking place in the bulk sample. The maximum heating rate for which the temperature is uniform in a film of thickness  $l$  in meters is given by Eq. (1). Nitrocellulose (NC) is used here to illustrate

this analysis.

$$t_r = \frac{c_p \rho l^2}{\lambda} \quad (3)$$

$t_r$  is the relaxation time for the temperature gradient in a film of the polymer,  $c_p$  is the heat capacity (1.25 kJ/kg · K at 120°C for 13%N NC<sup>(1)</sup>),  $\rho$  is the nominal density ( $1.5 \times 10^3$  kg/m<sup>3</sup> for NC) and  $\lambda$  is the thermal conductivity ( $2.3 \times 10^{-4}$  kJ/sec · m · K for 12%N NC<sup>(1)</sup>). In a qualitative way, the heating rate and film thickness can be related by Eq. (3). By using the data given here for NC,  $t_r = 4 \times 10^{-2}$  sec for a film thickness of 70  $\mu$ m. This is the approximate time at which the NC film is able to equilibrate a change in temperature. If one degree accuracy in the temperature data is sought, then  $dT/dt$  can be no faster than  $1/t_r$  or 25°C/sec. If 4°C accuracy is sought then  $dT/dt$  can be about 100°C/sec. Because the heating rate during decomposition in the SMATCH/FTIR experiment was typically in the range of 150°C/sec, this analysis indicates that the film thickness should be  $\leq 30 \mu$ m for one degree accuracy in the temperature. As a result, attempts were made to achieve a film thickness in this range.

The effect of mass transfer on these fast heating experiments was tested by determining the sensitivity of the weight-loss curve to the initial sample mass. No effect was found for masses less than 1 mg indicating that in the design of SMATCH/FTIR, mass transfer is not an important factor provided the sample of the film is thin and uniformly deposited.

As indicated in Fig. 2, the thermocouple and mass measurement outputs at about 160 Hz are multiplexed to separate channels of a PC-based data acquisition system, which provides enough data for

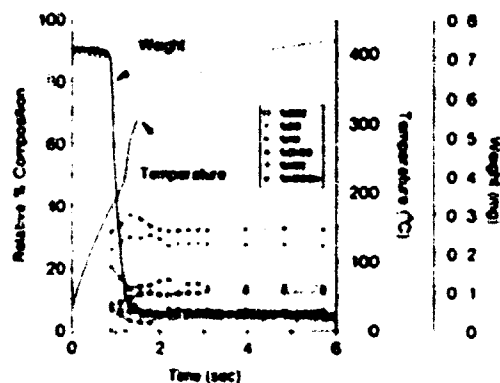


Fig. 3 SMATCH/FTIR data for 13.4% N nitrocellulose

accurate simultaneous determination of mass and temperature changes with time.

SMATCH/FTIR spectroscopy so far has been used to determine the rapid thermal decomposition kinetics and mechanism of energetic nitrate ester<sup>1</sup> and azide<sup>2</sup> polymers, several crystalline oxidizers<sup>11</sup> and several non-energetic polymer binders<sup>3</sup> used in rocket propellants. In all cases, the kinetics of rapid weight-loss can be calculated from the power rate law Eq. (4),

$$-\frac{dw}{dt} = k w^n \quad (4)$$

where  $w = (m - m_f)/(m_0 - m_f)$ ,  $m_0$  is initial sample weight,  $m_f$  is the final sample weight and  $m$  is the weight at any time  $t$ ,  $n$  is the apparent reaction order. Figure 3 shows the SMATCH/FTIR data for 13.4% N nitrocellulose. Heating of the sample occurs at an initial rate of about 150°C/sec. At its decomposition temperature, NC essentially completely decomposes in about 0.3 sec. A temperature rise occurs due to the exothermicity of the process.  $dw/dt$  was numerically obtained by polynomial regression analysis of the weight-loss curve through the initial 50% of the weight loss.

The temperature dependence of the rate constant  $k$  is given by the Arrhenius Eq. (5), where  $E_a$  is the activation energy

$$k = A e^{-E_a/RT} \quad (5)$$

Therefore, for the power rate law form the weight loss, Eq. (6) is followed. By applying the differential method to Eq. (6),

$$\frac{dw}{dt} = A w^n e^{-E_a/RT} \quad (6)$$

the reaction rate can be expressed as Eq. (7)

$$\ln \left( \frac{dw/dt}{w^n} \right) = \frac{E_a}{RT} + \ln A \quad (7)$$

By linearizing Eq. (7) through the appropriate choice

TABLE 2. Kinetic parameters and temperature ranges for the thermal decomposition of various materials measured at 100–250°C/sec by SMATCH/FTIR spectroscopy

Polymer	$E_a$ (kcal/mol)	$\log A$ (sec <sup>-1</sup> )	$T$ (°C)
NC(13.4%N)	32.6 ± 0.8	16.4 ± 0.4	177–215
NC(11.7%N)	33.7 ± 1.1	16.9 ± 1.0	186–215
NC(9.45%N)	33.8 ± 2.1	16.7 ± 0.8	192–217
PVN	32.1 ± 0.2	15.9 ± 0.3	200–220
PGN	31.1 ± 2.1	14.7 ± 0.7	220–240
NMMO	33.5 ± 1.5	16.4 ± 0.5	210–225
GAP	42.3 ± 2.4	19.0 ± 0.9	242–260
AMMO	43.2 ± 2.8	18.9 ± 1.3	256–273
HTPA	7.8 ± 0.7	3.1 ± 0.1	330–400
HTPB	8.3 ± 1.2	3.1 ± 0.4	329–421

\* Apparent reaction order  $n = 2$

† The average of two experiments

of  $n$ ,  $E_a$  and  $\ln A$  can be calculated from the rapid weight-loss curve.

Similar studies have been conducted on other samples of nitrocellulose having different percent nitration, and on poly(vinyl nitrate) (PVN), poly(glycidyl nitrate) (PGN) and poly(nitratomethylmethyloxetane) (NMMO).<sup>1</sup> The azide polymers azido-methylmethyloxetane (AMMO), beta-azidomethyl-oxetane (BAMO) and glycidyl azide polymer (GAP) have been studied.<sup>2</sup> The SMATCH/FTIR technique has also been applied to the decomposition of pure non-energetic propellant binders, such as hydroxy-terminated polybutadiene (HTPB), hydroxy terminated polyethyleneglycoladipate (HTPA), and diisocyanate crosslinked HTPB polymers.<sup>3</sup> The results for the non-energetic polymers are very different from those of the energetic polymers. Compared to NC shown in Fig. 3, the weight-loss curves of non-energetic polymers have a more gradual slope, and the temperature rises more slowly during decomposition reflecting the fact that these polymers do not have energetic functional groups. A value of  $n = 2$  was found to linearize Eq. (7) for the calculation of  $E_a$  and  $\log A$ . It should be emphasized that this value of  $n$  does not imply a second order reaction, but rather is merely a curve-fitting parameter. Further discussion of the role of  $n$  is given elsewhere.<sup>12</sup>

The kinetics constants for the polymer compounds are summarized in Table 2. Note that the activation energies for the nitrate ester and azide polymers are in the range expected when bond breaking and chemical reactions dominate the overall process. On the other hand, those for HTPA and HTPB are much smaller. Their values are more typical of desorption than chemical bond breaking. The appearance in the gas phase of fragments clipped from the HTPA and HTPB polymers is consistent with their Arrhenius values and with desorption.

The Arrhenius constants calculated from the high rate mass loss data and the corresponding temperature data measured by SMATCH/FTIR can be used to calculate a linear regression (burn) rate,  $r$ , in

mm/sec for the material by using a modified version of the pyrolysis law, Eq. (8), where  $h$  is the film thickness in mm.

$$i = A h e^{E_a/RT} \quad (8)$$

For the use of Eq. (8) to be valid, the film thickness must be essentially the same as the thickness of the surface reaction zone of the condensed phase during combustion at 15 psi. A reaction zone depth of 20–60  $\mu\text{m}$  is typical and this was the film thickness employed in our work. The temperature for Eq. (8) was taken from the thermal trace.

As shown in Table I, there is a good correlation between the measured (or extrapolated) values of  $i$  from combustion and those calculated from SMATCH/FTIR kinetics. It should be emphasized that this match applies only to the temperature and pressure conditions where the SMATCH data were measured. The value of  $i$  represents one data point on the burn rate curve. *The SMATCH/FTIR Arrhenius constants should not be used to calculate  $i$  in other pressure and temperature ranges.* However, the close match of the data from the two types of experiments in Table I implies that the condensed phase experiences similar conditions and that the chemical processes are likely to be closely related in the two experiments.

The chemistry of the reaction zone is inferred from the final portion of the SMATCH/FTIR experiment, which is the simultaneous analysis of evolved gases by rapid-scan FTIR spectroscopy. This is accomplished by positioning the cantilevered tube so that the metal end-tip was located 2–4 mm below the focal point of the infrared beam of the spectrometer. An IR gas cell was positioned above the end-tip in order to confine the gases that are produced upon thermal decomposition. By triggering the SMATCH portion of the experiment with the interferometer, correlation of gas products, thermal events, and mass loss can be made. It is gratifying to find that the gas products detected by SMATCH/FTIR are, for all intents and purposes, the same as those obtained with our other fast thermogravimetric techniques<sup>11</sup> that are described below. Hence, the gas products obtained over the years by these other techniques can be used with confidence to characterize the IR active species that leave the surface during the first stage of decomposition during combustion. These early products are an historical record of the reactions in the condensed phase.

The fast thermolysis/FTIR techniques described below are of simpler design and are easier to use than the SMATCH/FTIR technique. As a result, the major part of this article is devoted to describing relationships developed with these techniques. Of particular interest is the connection between the parent molecular structure and the decomposition gases that leave the surface. The methods for measuring these spectra and quantitating the products are described next.

#### 4. RAPID-SCAN FTIR SPECTROSCOPY

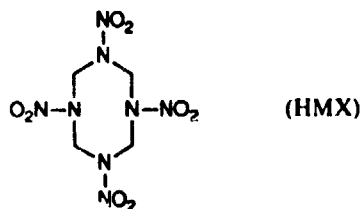
Chemical information about the condensed phase and the simulated burning surface is obtained from rapid-scan FTIR spectroscopy of the gas products evolved from the surface. FTIR spectroscopy has the advantage over dispersive IR methods when high energy throughput, rapid data acquisition and broadband IR spectra are required.<sup>12</sup> The layout of the optical benches of various FTIR spectrometers<sup>13</sup> should be consulted for details of how these advantages are achieved. For real or near real-time data acquisition, a research grade rapid-scanning FTIR spectrometer (RSFTIR) is invaluable. In general, thermal decomposition studies of bulk energetic materials are not well suited to conventional time-resolved IR spectroscopy because the physical and chemical events are neither reversible in the same experiment nor exactly recreatable in successive experiments. Step-scanning instruments<sup>14</sup> may have use in this field but have not been applied as yet to study physicochemical process in energetic materials. Time-resolved infrared spectral photography (TRISP) described in Section 9 is beginning to be applied to rapidly heated energetic materials.<sup>15</sup>

The rapid-scan FTIR spectrometer takes advantage of the fact that both the forward and reverse motions of the moving mirror of the interferometer can generate all of the spectral information. This fact, coupled with a rapid mirror velocity and a very stable interferometer, allows mid-IR spectra to be collected at 60–80 scans per sec with 16–32  $\text{cm}^{-1}$  resolution. This resolution is inadequate for studies of the decomposition of most energetic materials. As noted below, higher resolution is required for most analyses. A mercury-cadmium-telluride (MCT) semiconductor detector and digital signal processing provide a low noise signal in which absorbances are clearly evident in single-scan spectra. The interferograms acquired in this way are stored independently by fast analog-to-digital (AD) transfer with a precise and accurate time record attached to each file. At a later time, the interferograms are transformed. The operator can manipulate many of the parameters of the data collection and Fourier transformation to optimize the scan speed, resolution and spectra details. We settled on a scan speed of 10 scans/sec at 4  $\text{cm}^{-1}$  resolution as optimal for this research. However, a faster scan speed could have been chosen with a sacrifice in resolution, because the number of data points that can be collected per second is lower at higher scan rates. In short, the choice of the spectrometer parameter settings depends on the instrument and the problem under study. There is no perfect parameter file. Modifications to the sample compartment may also be required to be compatible with the conditions of the experiment. For example, a high temperature flame can heat the optics and cause an interference pattern (channeling) on the spectrum unless precautions are taken to use wedge shaped windows.

### 5. NEAR SURFACE GAS PRODUCT ANALYSIS

FTIR spectroscopy has been used extensively to identify and quantify gases produced by reactions of solids and liquids. A separation technique is sometimes involved, as in gas chromatography/FTIR. When studying ignition, combustion and explosion phenomena, the important variation on evolved gas analysis methods incorporating FTIR spectroscopy is to perform the analysis with minimal delay in the time between the event and analysis. Hence, the IR beam is focused as close to the reacting sample as possible (1–5 mm away) and the data are collected by RSFTIR. Since the delay time between the reaction and the analysis is kept to a minimum, many relatively reactive species are observed with concentrations more close to the original than when longer time delays exist. Of course, the time delay is still large compared to many of the elementary reaction rates. Nevertheless, the instantaneous relative concentrations of the gases observed are more typical of those that feed the flame zone (were a flame to be present and fed continuously by the condensed phase) than is the case if the time delay is introduced. Analysis of the gas products can be made if the flame is present (Section 10), but the flame zone products tend to dominate the reactive, near-surface products in this case.

The first in-beam FTIR analysis of rapid decomposition of a propellant or explosive appears to be the work of Flanigan and Stokes<sup>17</sup> who packed octahydro-1,3,5,7-tetranitro-1,3,5,7-tetrazacene (HMX) into a platinum screen, through which a current could



be passed, and positioned the screen in an IR beam. Filament pyrolysis employing FTIR spectroscopy as the diagnostic was first described by Liebman *et al.*<sup>18</sup> We have subsequently investigated more than two hundred energetic materials by filament pyrolysis in which the IR beam is passed over the surface of a rapidly heated sample. The basic cell design is described below. For these experiments the desire is to decompose the sample rapidly, but to avoid ignition or initiation of the sample. If the latter processes occur, the final, thermodynamically stable products tend to dominate in the infrared spectrum.

#### 5.1. Cell Design and Methods

More complete descriptions of the basic fast thermolysis/FTIR cell are given elsewhere.<sup>6-8,19</sup> Figure 4

gives the essential design features. The anti-reflection coated 0.5" × 1" diameter ZnSe windows are held in a 7.5 cm diameter aluminum cylinder by brass end caps. ZnSe was used because it is transparent in the mid-IR portion of the spectrum where modes occur that indicate the chemical behavior of energetic materials. It also has a high tensile strength so that it can be operated at high pressure. The cell was designed to withstand a static internal pressure up to 5000 psi, but is used only in the 1–1000 psi range. The heater filament is a slightly creased nichrome IV ribbon (2.5 × 0.6 × 0.012 cm) supported on pressure-tight feed-through insulators. Although studies were not conducted on a wide range of compounds, a detailed study of a liquid gun propellant LGP1845, which is expected to be especially sensitive to catalysis by metals, revealed little dependence of the thermolysis products on the filament material.<sup>9</sup> Typically, 1–2 mg of sample (solid, liquid or mixture) was heated on the filament using a Foxboro 40 Pyrochem controller. The constant voltage-variable current feature of the controller has special value in the temperature profiling experiments described in Section 6. In principle, any reasonable heating rate of the sample could be achieved, but < 400 °C/sec was chosen because the spectral collection rate does not distinguish processes at higher heating rates. The argon gas pressure in the cell was adjusted as desired in the 1–1000 psi range. Because of the importance of collecting IR spectra at high temporal resolution, the rapid-scan mode of a Nicolet 20SX and 60SX FTIR spectrometer was used in all of these studies. With the beam focused several mm above the filament surface, the IR active gas products from the fast heated sample can be detected in near real-time. No significant change of pressure in the cell occurred from the evolved gases because of the small sample size. If smoke or an aerosol with particle diameters less than 50 μm forms during thermolysis, wavelength-dependent dispersion can cause the baseline to slope upward, usually toward the shorter wavelength side. However, the gas product concentrations can still be calculated in most cases.

#### 5.2. Quantitation Processes

The relative percent concentrations of the gas products were obtained by a procedure employing the effective width factors and absolute intensities of non-interfering absorbances for each product.<sup>6</sup> In some cases only the P, Q, or R branch was used in order to minimize interference by other peaks. The effective width factors were determined from a greatly expanded, 2 cm<sup>-1</sup> resolution spectrum of the decomposition gases. For most of the products, the area of the absorption band of interest was measured and divided by the peak height. This gave an effective width factor for the absorption which was then divided by the absolute intensity to obtain

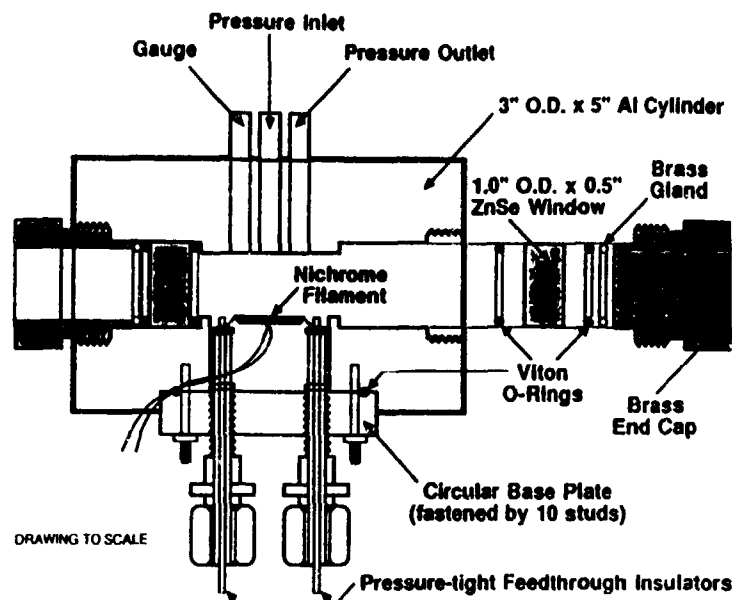


FIG. 4. The essential features of the fast thermolysis/FTIR cell. The pressure gauge and ports are drawn in abstraction.

a scaling factor. The scaling factor for each of the gases was then divided by the scaling factor for  $\text{CO}_2$  to obtain the relative percent concentrations based on  $\text{CO}_2$  as the standard. Several known mixtures of gases were compared to the scaling factors derived in this way and gave similar results. For all subsequent studies, this scaling factor needed only to be multiplied by the peak height for the gas in question to obtain the relative percent concentration of that gas.

The theoretical basis for the above procedure is based on Beer's Law. The concentration,  $C$ , is related to the absorption area,  $A$ , the pathlength,  $l$ , and the intensity,  $I$ , by Eq. (9).

$$C = \frac{1}{Al} \int \ln \frac{I_0}{I} dv \quad (9)$$

Since  $\text{CO}_2$  is the standard for determining the relative percent concentration of all other gases,  $x$ , in our work, Eq. (10) gives the ratioing process.

$$\begin{aligned} \frac{C_x}{C_{\text{CO}_2}} &= \frac{\frac{1}{A_x} \int \ln \left( \frac{I_0}{I} \right)_x dv_x}{\frac{1}{A_{\text{CO}_2}} \int \ln \left( \frac{I_0}{I} \right)_{\text{CO}_2} dv_{\text{CO}_2}} \\ &\approx \frac{A_{\text{CO}_2}}{A_x} \left( \frac{H_x \cdot \bar{W}_x}{H_{\text{CO}_2} \cdot \bar{W}_{\text{CO}_2}} \right) \end{aligned} \quad (10)$$

The integrated area,  $A$ , under the absorption curve was divided by the height,  $H$ , to give an effective width  $\bar{W}$ . When  $\bar{W}$  is divided by  $A$  for each absorption and then divided by  $\bar{W}_{\text{CO}_2}/A_{\text{CO}_2}$ , the factor  $F$  is obtained for each absorbance (Eq. (11)).

$$\frac{A_{\text{CO}_2}}{A_x} \left( \frac{H_x \cdot \bar{W}_x}{H_{\text{CO}_2} \cdot \bar{W}_{\text{CO}_2}} \right) = F \left( \frac{H_x}{H_{\text{CO}_2}} \right) \quad (11)$$

The factors,  $F$ , calculated in this way are shown in Table 3 and permit the relative percent concentrations to be computed from the peak heights.

There are several potential sources of error. Pressure broadening can change the peak height. Experimentally, it was found that HCN was most affected by pressure above 200 psi and so a correction was needed at higher pressures. Occasionally, the desired absorption overlapped another absorption. This problem was overcome by estimating the curve profiles of each component and using the desired one. Given the uncertainty in some of the literature values

TABLE 3. The multiplicative factor  $F$  used in relative percent concentration calculations (eq. 11)

Gas	Absorption* $\text{cm}^{-1}$	$F$
$\text{CO}_2$	2349(R)	1†
$\text{N}_2\text{O}$	2224(R)	2
CO	2143(P)	25
NO	1876(R)	32
$\text{CH}_2\text{O}$	1744(R)	15
$\text{HNO}_2$	1709	8
$\text{NO}_2$	1621	2
$\text{HCOOH}$	1103	3.7
$\text{NH}_3$	968(Q)	5
$\text{HONO (cis)}$	856(Q)	3.2†
$\text{HONO (trans)}$	794(Q)	
HCN	713(Q)	3
$\text{CH}_4$	3020(Q)	11
$\text{C}_2\text{H}_4$	949	7.5
$\text{C}_2\text{H}_2$	729	3.4
HCl	2974(R)	4

\* The meaning of R, Q and P branches for these modes can be found in G. Herzberg *Infrared and Raman Spectra*, D. Van Nostrand, Co., New York (1945).

† Reference compound.

‡ Sum of *cis* and *trans* intensity.



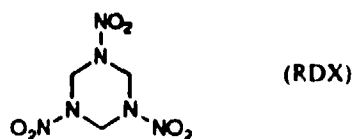
of the absolute intensities and the other approximations in this quantitation procedure, there is an absolute error of about  $\pm 10\%$  in the concentrations, but the relative changes in concentration within a given concentration vs time plot have lower error.

Another procedure that could be used for quantitation of a gas product is to measure the individual absorbance values at various partial pressures of each gas and to compare them to the product gas absorbance in a thermolysis experiment. This procedure has the value of giving the absolute rather than the relative concentration. The absorbance values measured in this way depend on the pathlength and most likely depend on the cell window material and thickness, and the type of spectrometer. Also, some of the gases of interest in energetic material research are difficult or dangerous to work with, especially at higher pressure (e.g.  $\text{HN}_3$ ,  $\text{CH}_2\text{O}$ ,  $\text{HCN}$ ,  $\text{HONO}$ ,  $\text{HNCO}$ ,  $\text{NH}_2\text{CN}$ ,  $\text{HNO}_3$ ).

### 5.2. Some Characteristics of the Evolved Products

In the above experiment the time delay between thermolysis and the detection of the evolved gases is insignificant compared to the scan speed of the spectrometer because the gases travel only 1–4 mm from the sample to reach the IR beam. The gas products rise by convection into the cooler Ar atmosphere of the cell where they are momentarily quenched during the detection stage. Based on the relative intensities of the P and R branches, the gases are in their ground state by the time they reach the IR beam. The choice of the atmosphere in the cell depends on the problem being studied. A relatively inert gas such as He, Ar or  $\text{N}_2$  is the atmosphere of choice if the intrinsic thermolysis characteristics of the parent compound are desired. If the thermolysis is performed in air, then the intrinsic thermolysis process of the compound is intermixed with the reactions with  $\text{O}_2$  and  $\text{H}_2\text{O}$ . Of course, an air atmosphere would be desirable if the decomposition of the material is likely to occur in air in practice. Other applications can be imagined that would call for a fuel-rich or oxidizer-rich atmosphere in the cell. If necessary, spectral subtraction can be used to remove unwanted absorbances caused by the background atmosphere.

Figure 5 illustrates for a 2 mg sample of RDX that



good quality spectra can be obtained by RSFTIR under rapid thermolysis conditions. When heated at  $dT/dt \geq 170^\circ\text{C}/\text{sec}$  from room temperature, the initial gases from RDX are first detected in about 1.15 sec because the thermal decomposition of RDX leading to gas products occurs at about  $200^\circ\text{C}$ . The

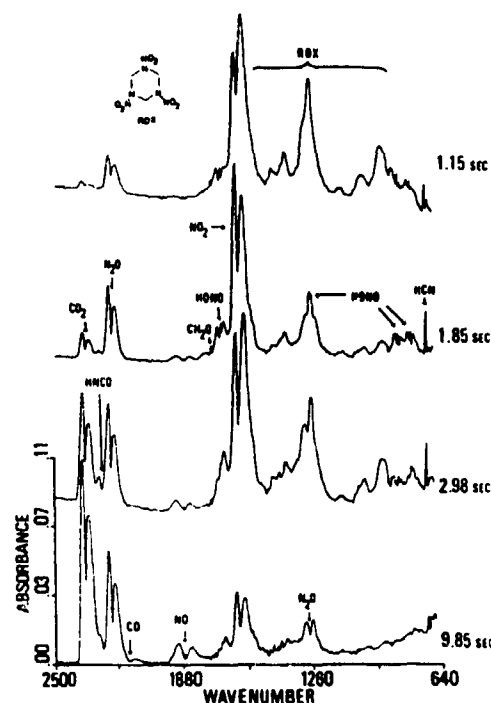


FIG. 5. Selected rapid-scan IR spectra of the gas phase 3 mm above a 2 mg sample of RDX heated at  $170^\circ\text{C}/\text{sec}$  under 15 psi Ar. The times shown follow the onset of heating at  $t = 0$  sec.

absorbance values for most compounds rise very steeply during the initial second of decomposition. An estimate of the rate of decomposition is illustrated by the SMATCH experiment data as shown in Fig. 3. By using the absolute IR intensity method, the absorptions can be converted to relative percents of the IR active gases. Figure 6 shows relative composition vs time profiles for the gas products from RDX obtained by this method. These concentrations are calculated by the method in Section 5.3, and are most closely related to the percent concentration based on volume.  $\text{H}_2\text{O}$  is relatively difficult to quantify because  $\text{H}_2\text{O}(\text{g})$  has extensive rotation-vibration fine-structure. Many materials that volatilize and then readily condense

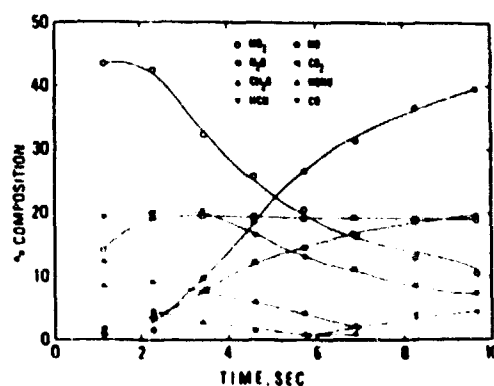
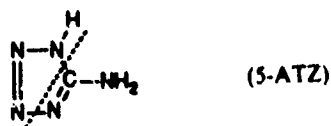


FIG. 6. The relative percent composition of the quantified gas products from the spectrum of RDX shown in Fig. 5.  $\text{HNCO}$  and RDX aerosol are not included.

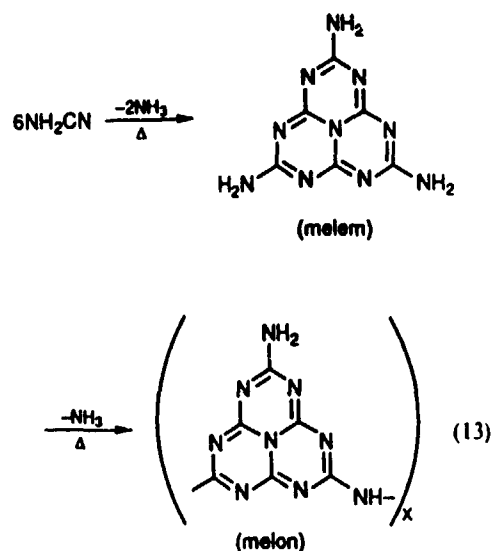
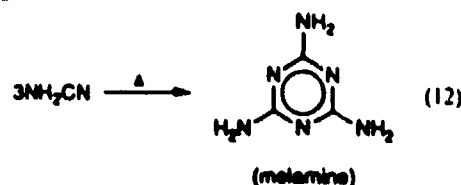
(e.g. some parent molecular compounds and alkylammonium nitrate salts) or polymerize (e.g.  $\text{HNCO} \rightarrow$  cyanuric acid;  $\text{NH}_2\text{CN} \rightarrow$  dicyandiamide  $\rightarrow$  melamine) can readily be detected, but are difficult to quantify. Of course, IR inactive molecules, such as homonuclear diatomics, will not be detected. The importance of near real-time analysis of the gas products in fast thermolysis research is evident from Fig. 6.  $\text{NO}_2$  is the dominant early decomposition product of RDX, but, because of secondary redox reactions, decreases rapidly in concentration, while  $\text{NO}$  increases. Note that  $\text{NO}$  has a low concentration at the onset of decomposition. As a result, if the time delay between the analysis and the onset of thermolysis were to exceed five seconds, then different and potentially incorrect conclusions about the thermal decomposition process of RDX could be drawn. The changes in the gas concentrations with time often indicate secondary reactions among the gases, while the initial gas concentrations are most closely related to the thermolysis of the parent molecule. Based on extensive studies of the thermolysis of nitramines in various reactive atmospheres, the evidence is very strong that the processes leading to the initial gas products occur in the condensed phase.<sup>20</sup> Thus, condensed phase processes are largely separated from purely gas phase processes in this experiment.

5-ATZ illustrates what can be learned about the thermolysis process when very few of the gas products can be quantified.<sup>21a</sup> With literature searching for reasonable products and thermolysis studies on authentic samples of potential products, the vaporized materials from 5-ATZ can be identified and the main decomposition processes understood.

Figure 7 shows selected IR spectra of the gas phase taken 3 mm above a 1 mg sample of 5-ATZ heated at about  $100^\circ\text{C}/\text{sec}$  under 15 psi Ar.  $\text{HN}_3$  and  $\text{NH}_2\text{CN}$  are the initially detected products. Their spectra closely match the spectra of authentic samples of these compounds.<sup>21b,22</sup>  $\text{NH}_3$  also forms, but its concentration is very low compared to  $\text{HN}_3$  and  $\text{NH}_2\text{CN}$ . The atom connectivities of 5-ATZ indicate how  $\text{HN}_3$  and  $\text{NH}_2\text{CN}$  can form.



$\text{HN}_3$  dominates  $\text{NH}_2\text{CN}$  in the gas phase indicating that some of the  $\text{NH}_2\text{CN}$  is detained in the condensed phase on the hot filament. There reactions (12) and (13) can occur leading to various cyclic azines.



In keeping with this, melamine-like products (absorptions at  $1400\text{--}1650\text{ cm}^{-1}$ <sup>23,29</sup> and  $\text{NH}_3$  begin to volatilize after  $\text{HN}_3$  appears. The filament temperature is about  $350^\circ\text{C}$  when the absorptions of the cyclic azines are first detected. Melamine-like products readily form at this temperature.<sup>23,29</sup> According to Fig. 7, these products grow in concentration as the filament temperature increases further. However, simultaneously with these cyclic azines, the absorbances of  $[\text{NH}_4]\text{N}_3$  aerosol appear. The Fermi resonance triplet of  $\nu_{\text{NH}_4^+}$ <sup>30</sup> at  $3133$ ,  $2997$  and  $2827\text{ cm}^{-1}$ , and  $\delta_{\text{NH}_4^+}$  at  $1435\text{ cm}^{-1}$  appear. The modes assignable to  $\nu_{\text{N-N}}$  are found at  $2040$  and  $1812\text{ cm}^{-1}$ . All of these frequencies agree well with those of an authentic sample of  $[\text{NH}_4]\text{N}_3$ .<sup>31</sup>  $\text{NH}_4\text{N}_3$  is formed by the reaction (14).



Note that the baseline slopes upward toward higher wavenumber when the  $\text{NH}_4\text{N}_3$  and cyclic azine absorptions become pronounced. This indicates that these products are aerosols. Solid melon was scraped from the filament following thermal decomposition of 5-ATZ and identified by the comparison of its IR spectrum to an authentic sample.

Several of the decomposition events become more dramatic when 5-ATZ is rapidly thermolized under 850 psia of Ar. The higher gas density at higher pressure carries heat away from the filament so that the sample does not reach as high a temperature as at lower pressure. Figure 8 shows that the relative concentration of  $\text{NH}_4\text{N}_3$  continues to increase slightly but remains constant after 5.1 sec. Hence, Fig. 8 shows spectra only up to 5.06 sec. The high concentration of  $\text{NH}_4\text{N}_3$ , compared to lower pressure is accounted for by a shift of reaction (14) to the right at higher pressure.  $\delta_{\text{NH}_4^+}$ , azide modes, and the Fermi resonance triplet from  $\nu_{\text{NH}_4^+}$  are clearly evident given the higher concentration of  $\text{NH}_4\text{N}_3$ , now present.

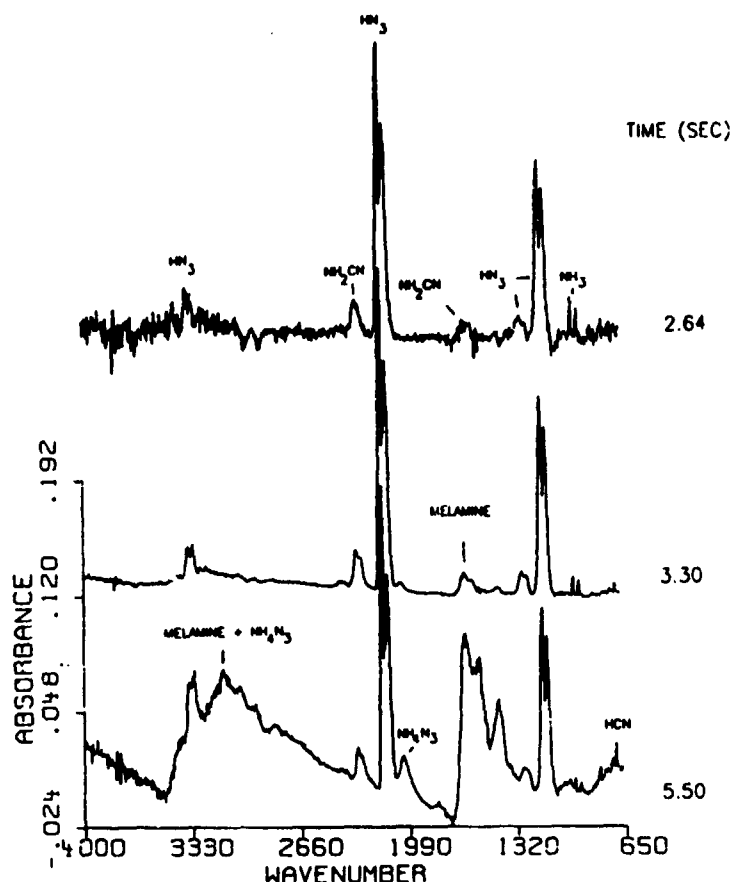
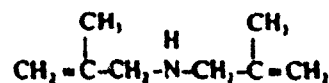


FIG. 7. Selected gas phase spectra 3 mm above S-ATZ heated at an initial rate of about 100°C/sec under 15 psi Ar.

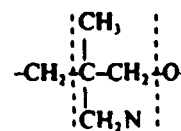
The amount of melamine in the gas phase is less because the sample temperature is not as high. Melamine would be expected to form under combustion conditions, but  $\text{NH}_4\text{N}_3$  forms because of the high pressure conditions in the cell.

Caution and chemical sense are always advisable when applying the gas product information from these experiments to the flame zone. This is because the gas products from rapid thermal decomposition are evolved into a cool inert atmosphere rather than a hotter flame zone. In many cases the gas products detected are the ones that will burn in the flame zone. However, in some cases products are seen that have most likely formed from reactive fragments that have recombined to more stable molecules in the cooler atmosphere. An example of this is the appearance of bis(2-methylallyl)amine, shown below, as a gas product from the fast thermolysis of AMMO.<sup>4</sup> This amine undoubtedly is



formed from further reactions of the unstable nitrene fragment shown between the dashed lines in the

repeating unit of the AMMO



polymer. The nitrene is the product of decomposition of the azide by release of  $\text{N}_2$ . The amine probably is observed because the nitrene self-reacts to stabilize itself perhaps in the cooler Ar atmosphere. Were combustion of AMMO actually occurring, the nitrene fragment is the more probable flame reactant because it would have been evolved into the hotter reactive atmosphere and not necessary have self-reacted.

#### 5.4 Structure/Decomposition Relationships

Many uses can be made of the relative concentrations of the near-surface gas products. An example is to relate the parent molecular structure or elemental composition of the reactant to the near-surface gas products. This connection provides a way to relate the formation of the condensed phase to the combustion characteristics. A more detailed description of the relationship of gas products to structure is compiled elsewhere.<sup>11</sup>

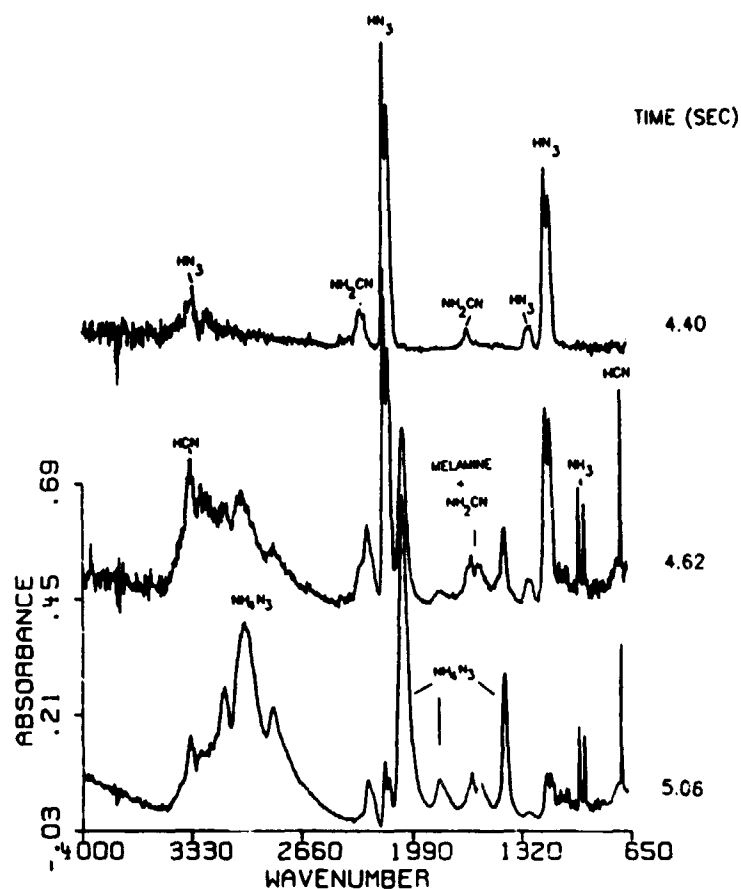


FIG. 8. Selected spectra of the gas phase at 3 mm above 5-ATZ heated at an initial rate of about 120°C/sec under 850 psi Ar.

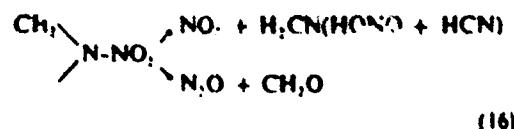
The near-surface gas products and their relative concentrations contain a rich historical record of the condensed phase decomposition reactions and physical processes. These gases dominate the pre-ignition and ignition chemistry of the sample. In turn, the products of ignition control the flame chemistry. If connections can be uncovered between the molecular structure of the parent material and the gas products released, then the work of the synthesis chemist could be guided by the combustion and explosives scientist and vice versa. Aside from the connection made with the SMATCH/FTIR results, confidence that the thermolysis products acquired by RSFTIR at least approach the combustion situation comes from the fact that the findings for nitramines qualitatively resemble the stable products observed by quartz microprobe-mass spectrometry<sup>23</sup> and planar laser induced fluorescence (PLIF)<sup>24</sup> studies of nitramine flames. The PLIF experiments show that NO<sub>2</sub> dominates close to the surface and that NO forms in the hotter part of the flame. The products also resemble many aspects of the theoretical gas product profiles computed by Melius.<sup>25</sup>

Compounds containing the nitramine functional group (15) are among the most important energetic materials. Some of the major gas products that are

produced by decomposition of



nitramine molecules are NO<sub>2</sub>, HONO, N<sub>2</sub>O, CH<sub>2</sub>O and HCN. These oxidizer and fuel gases feed the flame zone. The detection of some of these products in the concentrations that realistically represent the breakup of the parent compound requires the near real-time detection afforded by fast thermolysis/FTIR spectroscopy. The nitramine functional group (15) can be the source of NO<sub>2</sub> (HONO) and HCN or N<sub>2</sub>O or N<sub>2</sub>O and CH<sub>2</sub>O depending on the temperature and structure of the molecule (reaction 16).



#### 5.4.1. Tendency to form NO<sub>2</sub>(g)

The formulation of NO<sub>2</sub> by reaction (16) is of major importance in nitramine combustion because it is an oxidizer in the primary (near surface) flame zone. Although not previously discussed as such, it seems

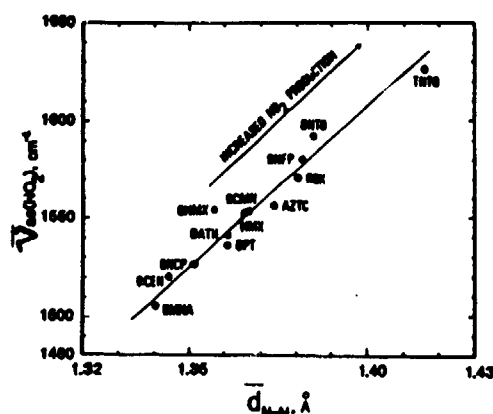


FIG. 9. The average asymmetric  $\text{NO}_2$  stretching frequency compared to the average N-N bond distance for a series of secondary nitramines. Compounds on the right side of the plot are strong  $\text{NO}_2$  generators upon thermolysis, while those on the left side either do not produce  $\text{NO}_2$  or do so in strong competition with other nitrogen containing products. Compound identities are given in Refs 36 and 37.

plausible that the length of the N-N bond in secondary nitramines might be an important factor in the tendency of the N-N bond to homolyze and liberate  $\text{NO}_2$  upon fast thermolysis. Because of the reactivity of  $\text{NO}_2$ , it is necessary to draw these conclusions from rapidly heated samples and to employ near real-time detection (IR spectra recorded at 50–100 msec intervals) of the initial gas products. Otherwise, secondary reactions of  $\text{NO}_2$  disguise any relationship of its concentration to the structure of the parent molecule. Of course, it must be emphasized that even simple homolysis of the N-N bond in the condensed phase is, overall, a complicated process. Intermolecular activity is possibly present. At the very least, some of the  $\text{NO}_2$  must diffuse through and desorb from the heterogeneous environment before it is detected. The most severe complication would be for N-N bond homolysis to follow or to compete with another decomposition route, such that the initial N-N bond distance would no longer be the controlling factor. If this were the case, then any general structure-decomposition relationship involving  $\text{NO}_2$  could be disguised.

The crystal structures of many nitramines are needed for this comparison. Fortunately many are available. Figure 9<sup>36,37</sup> shows a plot of the average N-N bond distance versus the average asymmetric  $\text{NO}_2$  stretching frequency from the infrared spectrum of a series of secondary nitramines,  $\text{R}_2\text{NNO}_2$ . The compound identities are given elsewhere.<sup>36,37</sup> A reasonably good relationship exists between these two parameters, suggesting that the force constant of  $-\text{NO}_2$  stretching depends markedly on the amount of electron density that the  $-\text{NO}_2$  group shares with the adjacent N-N bond. From fast thermolysis it was found that  $\text{NO}_2$  is the dominant, initially detected

product for compounds on the right side of this plot.  $\text{NO}_2$  was either not detected or was detected as a lesser abundant product from compounds on the left side. Thus, long N-N bonds favor N-N scission during fast thermolysis. Hence, with reasonable confidence one can predict the amount of  $\text{NO}_2$  that is likely to be generated by fast thermolysis of a given secondary nitramine compound from its IR spectrum or its crystal structure.

Although some exceptions exist to the  $\text{NO}_2$  structure/reactivity relationship mentioned above,<sup>38</sup> it is encouraging that most secondary nitramines thermolize in the condensed phase in a systematically predictable way. Thermal reactions in the neat condensed phase are complex, but the correlation above gives hope for uncovering and refining patterns that can be applied in practice to propellant ignition and explosives initiation.

#### 5.4.2. Tendency to form $\text{HONO(g)}$

Closely related to  $\text{NO}_2$  is the formation of  $\text{HONO}$ . At least one additional process, that of  $\text{H}^\cdot$  transfer, is required before  $\text{HONO(g)}$  is detected from nitramine decomposition. Kinetic modeling indicates that  $\text{HONO}$  formation plays a key role in the N-N bond fission process.<sup>39</sup> The formation of  $\text{HONO}$  has been used in many previous studies of nitramines to rationalize the appearance of other products, but  $\text{HONO}$  itself was very rarely detected prior to fast thermolysis/FTIR spectroscopy studies.<sup>40</sup>  $\text{HONO}$  is a reactive and, thus, transient molecule which is not observed without rapid heating and near real-time product detection. However, both the *cis* and *trans*- $\text{HONO}$  isomers can now be routinely observed from the thermolysis of nitramines.<sup>40</sup>

After examining a large number of nitramines heated at 145–180°C/sec under 15 psi Ar, it was discovered that the initial relative percent composition of  $\text{HONO}$  depends strongly on the parent secondary nitramine.<sup>40</sup> In one instance,  $\text{HONO}$  represented nearly 60% of the first detected gas products. A broad relationship was discovered between the ratio of the number of H atoms to  $\text{NO}_2$  groups in the parent molecule and the initial percentage of  $\text{HONO}$  in the gas products. The relationship is shown in Fig. 10. The leveling off at the higher percent values is attributable to dilution of the  $\text{HONO}$  by other gases. Qualitative insight into the processes by which  $\text{HONO}$  is formed from the condensed phase is contained in the pattern of Fig. 10. The concentration of  $\text{HONO}$  must depend on the adventitious encounter of  $\text{H}^\cdot$  (or an H source) and  $\text{NO}_2$  (or an  $\text{NO}_2$  source) in the condensed phase. Statistically increasing this chance for contact enhances the  $\text{HONO}$  concentration. The molecularity, the nature of the transition state and any other aspects of the reaction mechanism are beyond the extension of these condensed phase results. Many species could liberate  $\text{H}^\cdot$ , but it is interesting to note

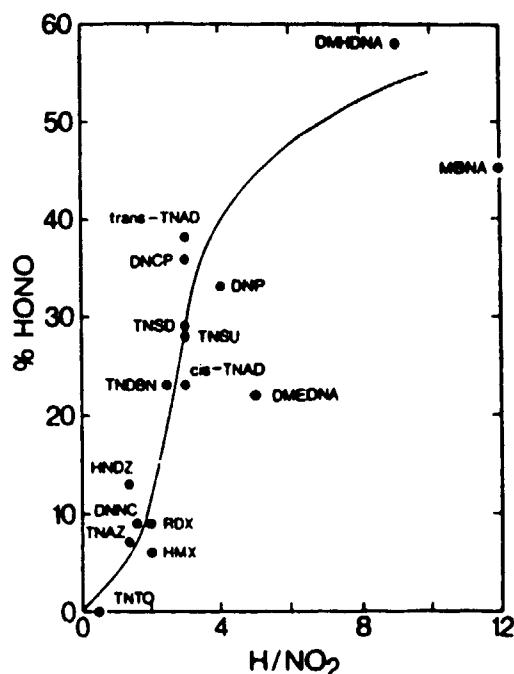
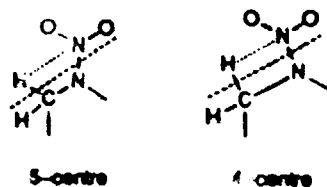


FIG. 10. A plot of the initial relative percent concentrations of HONO vs the  $H/NO_2$  ratio for a series of nitramine compounds. The identities of the compounds are given in Ref. 40.

that C-H bond fission has been proposed to be rate-determining in nitramine decomposition<sup>41,42</sup> and combustion.<sup>43</sup>  $H_2O$  assists in HONO formation in the condensed phase,<sup>44</sup> but the pattern in Fig. 10 would still need to be accommodated if this were the case. Compounds producing the largest amounts of HONO are not the ones expected to produce the largest amounts of  $H_2O$  because of their low oxygen content. Also, the four- and five-center concerted reactions whose connectivities are shown below and that could be important in the gas phase,<sup>45</sup> do not appear to dominate in the condensed phase. If they did, only a  $-CH_2-$  fragment adjacent to the nitramine would be required to produce HONO. All nitramines having this linkage should produce the same amount of HONO, which they do not.



The most plausible explanation for HONO formation in the condensed phase remains the chance contact between H and  $NO_2$ , possibly with  $H_2O$  as a catalyst. In keeping with this notion, steric crowding of H and  $NO_2$  groups in a molecule enhances the initial HONO concentration.<sup>46</sup> It is interesting to note that when the  $H/NO_2$  ratio is calculated using only the H atoms from secondary carbon atoms ( $-CH_2-$ ), the

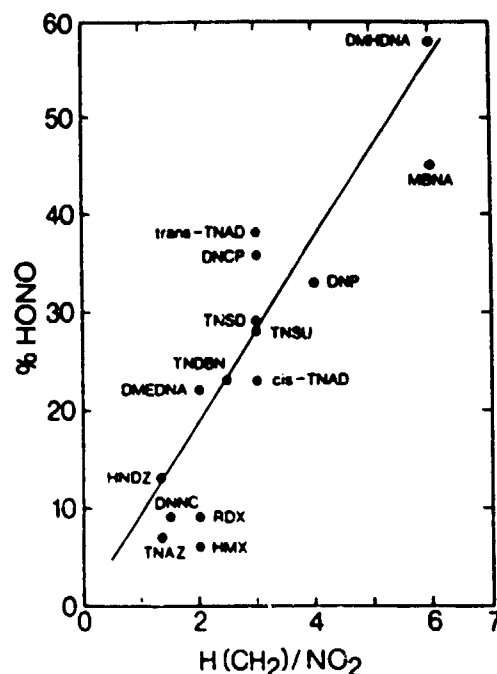


FIG. 11. A plot resembling Fig. 10 in which only the H atoms in the  $CH_2$  groups are counted in determining the  $H/NO_2$  ratio.

fit is slightly more linear as shown in Fig. 11. This suggests that  $-CH_2-$  groups may be somewhat more efficient H' sources than primary carbon atoms ( $-CH_3$ ). Nitramines having only tertiary carbon atoms ( $=CH$ ) are found not to produce HONO.<sup>46,47</sup>

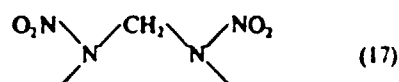
#### 5.4.3. Tendency to form $N_2O(g)$

It is not immediately obvious what governs the  $N_2O/NO_2$  branching ratio (reaction (16)) during the thermal decomposition of nitramines in the heterogeneous reaction state at high heating rates. A few secondary nitramines liberate a high amount of  $N_2O$  compared to  $NO_2$  (HONO).<sup>48-50</sup> Conversely, other nitramines generate  $N_2O$  as only a few percent of the total gases liberated,<sup>48,51-53</sup> while still others produce no  $N_2O$  at all.<sup>57,58</sup>

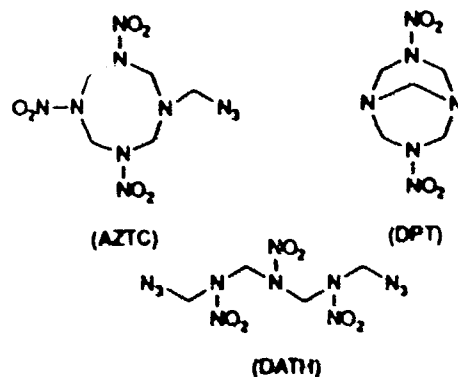
From RSFTIR work on the thermal decomposition of a wide variety of nitramines in the condensed phase where the decomposition temperatures range from 100°C to 300°C, there is rarely a correlation of the temperature with the  $N_2O/NO_2$  ratio from compound to compound. A notable exception to this pattern exists when the fast thermolysis of HMX (see Section 5 for the structure) is compared to that of RDX (Section 5.3). HMX and RDX have the same empirical formula and are simply isomers of methylene nitramine,  $CH_2=NNO_2$ . Upon fast heating RDX produces relatively more  $NO_2$  than  $N_2O$  initially, whereas HMX produces more  $N_2O$  than  $NO_2$  initially.<sup>6</sup> This difference might be attributed to the higher melting temperature of HMX which causes

more of the decomposition chemistry to take place in the condensed phase for HMX than is the case for RDX.<sup>6</sup> Although the  $N_2O/NO_2$  branching ratio could be partly phase dependent, the physical state of the compound is not likely to be the sole determining factor. Temperature may play a role for a given compound. For example, the  $N_2O/NO_2$  branching ratio for the gas phase decomposition of RDX is temperature dependent and has been said to reach unity at about 375°C.<sup>34</sup> The  $N_2O/NO_2$  ratio is found to be temperature dependent when condensed phase HMX is rapidly heated (Section 8). In general and considering all of the data at hand, our studies suggest that several reactions of nitramines may lead to  $N_2O$  and  $NO_2$  in the condensed phase and that the gas phase mechanisms do not necessarily generalize to the condensed phase behavior.

All of the compounds liberating  $N_2O$  have in common a  $-CH_2-$  group straddled by two nitrogen atoms as shown by unit (17). This feature appears to be the only structural requirement for  $N_2O$  formation by a secondary nitramine.



Three secondary nitramines that liberate virtually all of their nitramine nitrogen atoms as  $N_2O$  are AZTC,<sup>40</sup> DPT<sup>47</sup> and DATH.<sup>48</sup> The N-N bond distances in these compounds (1.355–1.375 Å) suggest that  $NO_2$  and  $N_2O$  should be competitive thermolysis products<sup>44,47</sup> based on the observations in Section

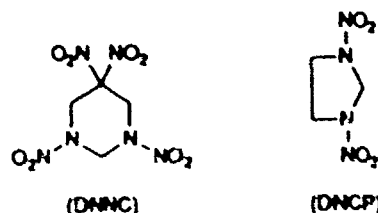


5.4.1 DATH produces this result at temperatures slightly above its decomposition point, but  $N_2O$  dominates around the decomposition point. Why these molecules produce little or no  $NO_2$  (although DATH produces  $NO_2$  at high temperature) emphasizes the importance of realizing that the balance among the multiple decomposition pathways is easily shifted in nitramines by the temperature conditions and structure. Both DATH and AZTC produce  $HN$ , (and no doubt  $N_2$ ) initially. Thus, the azide group begins the thermolysis reaction. By either radical or electron pair migration, the backbone tends to depolymerize in preference to N-N bond homolysis. During

the depolymerization process, oxygen is obviously transferred, but the data do not indicate how. Possibly the same type of reaction in DPT is initiated by the homolysis of a C-N bond in the  $-CH_2-$  bridging the non-nitrated amine atoms.

#### 5.4.4. Tendency to form $CH_2O(g)$

Formaldehyde is an important fuel in the primary flame of nitramines. Having just introduced the fact that a  $-CH_2-$  group straddled by two nitrogen atoms (unit (17)) appears to be important, if not required, to produce  $N_2O$  from a pure secondary nitramine compound, a logical implication is that the transfer of an oxygen atom from the  $NO_2$  group, perhaps to the adjacent  $-CH_2-$  group, liberates  $CH_2O$  along with  $N_2O$ .  $H$ ,  $H'$ ,  $OH$ , or  $H_2O$  could assist in lowering the barrier to this transfer reaction. While DPT, AZTC and DATH do indeed have this unit and liberate a large amount of  $CH_2O$  along with  $N_2O$ , several compounds do not follow this simple pattern with respect to  $CH_2O$  formation. DNNC,<sup>49</sup> DNCP and most bicyclonitramines<sup>50</sup> have unit (17) but liberate no  $CH_2O$ . DNNC also has a gem-dinitromethyl group (a carbon atom with two  $NO_2$  groups attached) whose thermolysis appears to initiate the decomposition.<sup>51</sup> The ring may open before the nitramine group has had a chance to react. The bicyclonitramines are strong HONO generators. Loss of  $NO_2$  and the removal of an excessive number of H atoms in the early reaction sequences could interfere with the tendency to form  $CH_2O$ .



In fact, the long held notion that  $CH_2O$  and  $N_2O$  form from a coupled process in the condensed phase decomposition of nitramines should be taken with some caution. Recent work on HMX using fast-heat-and-hold thermolysis techniques coupled with FTIR diagnostics in Section 8,<sup>52</sup> and simultaneous thermogravimetry coupled with modulated beam mass spectrometry<sup>53</sup> reveal that  $N_2O$  (and  $NO_2$ ) reach the gas phase distinctly ahead of  $CH_2O$  and  $HCN$ .  $CH_2O$  is retained in the condensed phase by its reaction with water.<sup>54</sup> Figure 12 shows the gas sequencing from HMX under isothermal conditions following rapid heating. At the temperatures used,  $N_2O$  and  $CH_2O$  should appear in the IR beam simultaneously if they are being released in the condensed phase from the same reaction at the same rate. The difference in their time of detection suggests a somewhat more complex reaction scheme than a simple oxygen transfer process is taking place under these experimental conditions.

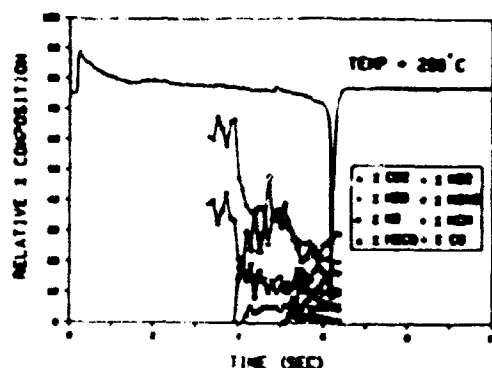


FIG. 12. The gas products from HMX superimposed on the difference voltage controlling the temperature of the filament. This voltage reflects the endothermic and exothermic chemistry of the sample. The sample was heated at 2000°C/sec to 296°C and held there while observing the gas products (Section 5). Melting (upward voltage deflection) is observed in the initial 1 sec. The sharp decomposition exotherm (downward deflection) occurs after 6 sec.

#### 5.4.5. Other studies of energetic compounds

Similar less extensive studies of structure-decomposition relationships have been conducted on primary nitramines,<sup>30</sup> metal-nitramine salts,<sup>31,32</sup> aliphatic C-NO<sub>2</sub> compounds,<sup>33,34,35</sup> nitrate esters,<sup>36</sup> azidomethyl compounds,<sup>37,38</sup> alkylammonium nitrate salts,<sup>39,40,41</sup> fluorodinitromethyl,<sup>42,43</sup> chlorodinitromethyl<sup>44</sup> and azidodinitromethyl compounds,<sup>45</sup> nitrosamines,<sup>46</sup> furazans,<sup>47,48</sup> furazans,<sup>49</sup> alkynes,<sup>50,51</sup> nitroxides,<sup>52</sup> tetrazoles,<sup>53,54</sup> and triazoles,<sup>55</sup> and metal complexes of furazans<sup>56</sup> and diaminoglyoximes.<sup>57</sup> An interesting result selected from these studies is the observation that the tendency for alkylammonium nitrate salts to release HNO<sub>3</sub>(g) (often the primary oxidant in the flame of an alkylammonium nitrate salt) upon fast thermolysis appears to be controlled by the basicity of the parent alkylamine.<sup>58,59</sup> HNO<sub>3</sub>(g) forms by proton transfer followed by desorption. As shown in Fig. 13, the gas phase basicity (proton affinity) of the parent alkylamine correlates with the first detected gas products from fast thermolysis of the alkylammonium nitrate salt. As the basicity increases, the proton transfer reaction leading to HNO<sub>3</sub> is less favored and HNO<sub>3</sub>(g) is not released. Instead, the NO<sub>2</sub> is retained in the condensed phase where it reacts and forms nitrogen oxides and other redox products. It is also interesting to note that the gas products from hydroxylammonium nitrate (HAN) appear to oscillate in concentration when HAN is heated at 130°C/sec at > 100 psi of Ar.<sup>60</sup>

#### 5.5. The Use of Decomposition Product Data in Combustion Modeling

An important application of the gas product data from fast thermolysis is to connect the composition and structure of the condensed phase to the flame zone characteristics. For example, in the case of alkyl-

ammonium nitrate salts, fast thermolysis suggests that the earliest flame zone should be dominated by the reaction of HNO<sub>3</sub> and NH<sub>3</sub>. Their reaction strongly influences the burn rate.<sup>61</sup>

The gas product ratios ascertained from fast thermolysis experiments are a guide to the choice of reactants in a flame model of a propellant that incorporates detailed chemistry.<sup>62</sup> While it would be unrealistic to expect that there is a perfect match between the gas products from fast thermolysis and those in the preparation zone of Fig. 1 during combustion, the data provide an experimentally based starting point for modelling the flame chemistry of a propellant. The thermolysis data also suggest some of the species that might be catalyzed to affect the burn rate.<sup>63</sup>

Another direct application of the gas product data from fast thermolysis studies is to understand the effect of additives on the burn rate of a propellant. For instance, diaminofurazan (DAF), diaminoglyoxime (DAG) and dicyandiamide (DCD) are all known to retard the burn rate of ammonium perchlorate-based composite propellant.<sup>64,65</sup> Fast thermolysis/FTIR studies of these materials<sup>66</sup> reveal that the cyclic azines melon and melamine are high temperature-stable end products that form among the decomposition gases. Reactions (12) and (13) show the products. The presence of NH<sub>4</sub>ClO<sub>4</sub> was not found to affect the tendency of DAG, DAF, and DCD to form cyclic azines. For example, melamine is observed along with decomposition products of NH<sub>4</sub>ClO<sub>4</sub> when intimate physical mixtures of NH<sub>4</sub>ClO<sub>4</sub> and DCD are rapidly heated at pressures above 500 psi Ar. This behavior would be expected to contribute to combustion modification of composite propellants. On the burning surface of the propellant, some of the DCD, DAG, and DAF thermolyses to thermally stable cyclic azines having a comparatively high molecular weight. Melon is reported to be thermally stable up to 747°C, which approaches or exceeds the surface temperature believed to be present in AP/H<sub>2</sub>O<sub>2</sub> composite propellants.<sup>67</sup> Melamine and melon would be expected to retard the heat and mass transfer rates at the surface when compared to the unmodified propellant. Hence, the burn-rate and pressure exponent at high pressure would be expected to be reduced. The identification of these azine products is an example of how the experimental study of fast thermal decomposition of materials provides insight into complex processes that would not be uncovered by theoretical analysis alone.

#### 6. TEMPERATURE PROFILING/FTIR SPECTROSCOPY

In the above fast thermolysis/FTIR methods, as in SMATCH/FTIR the final temperature and heating rate of the filament were established by spot-welding a thermocouple to the filament. In this way the endothermic and exothermic events of the condensed phase can also be tracked simultaneously with detection of the gas products. Figure 14 shows a block



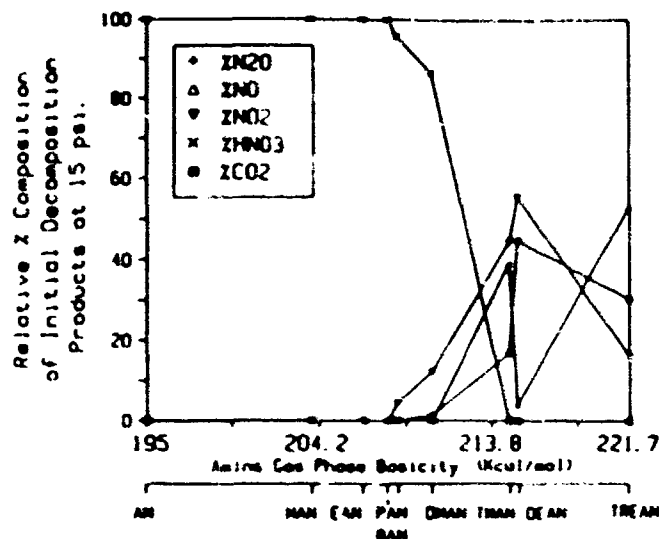


FIG. 13 A plot of the initially detected gas products from fast thermolysis under 15 psi Ar of various alkylammonium nitrate salts versus the gas phase basicity of the parent alkylamine: AN = ammonium nitrate; MAN = methylammonium nitrate; EAN = ethylammonium nitrate; DMAN = dimethylammonium nitrate; TMAN = trimethylammonium nitrate; DEAN = diethylammonium nitrate; TREAN = triethylammonium nitrate.

diagram of the constant voltage-variable current control circuit used for recording the temperature. The 60 Hz noise on the filament was removed by a low pass filter, and the signal was amplified by about 100  $\times$  with a differential amplifier. The analog output was processed through a Metrabyte DAS-16 AD converter to an IBM-PC. The 'take data' cycle of the interferometer triggered the heating of the filament so that there is a direct correlation between the time, temperature and interferogram. Four hundred temperature points were collected in the ten-second measurement when a sample filament was used. As many as 100 data points/sec were used in the SMATCH/FTIR method.

Figure 15 for ethylenediammonium dihydrate (EDD) shows a reference thermal trace (filament with no sample present) and a sample thermal trace (filament with 2 mg of EDD evenly and thinly spread on the center portion) superimposed on the amplified difference trace (sample trace minus reference trace). Most of the endotherms and exotherms are evident in

the sample thermal trace, but the difference trace clearly shows an endotherm preceding an exotherm in the 300–350°C range.<sup>10</sup>

The temperature signature in Fig. 15 needs to be explained for EDD, but, before doing so, it is worthwhile to mention several sources of endotherms and exotherms in the fast heating conditions used. Common origins of endotherms are melting, sublimation or evaporation, decomposition off-gassing, and endothermic chemical reactions in the condensed phase. Sources of exotherms are exothermic chemistry in the condensed phase and filament 'catch up'. Exothermic gas phase chemistry makes a negligible contribution to the filament temperature in this experiment. Filament 'catch up' arises from the fact that the

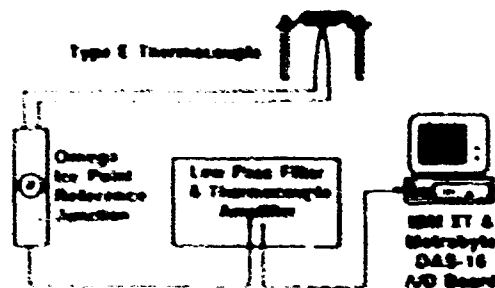


FIG. 14 A block diagram of the circuit used for real-time filament temperature measurement in temperature profiling/FTIR spectroscopy.

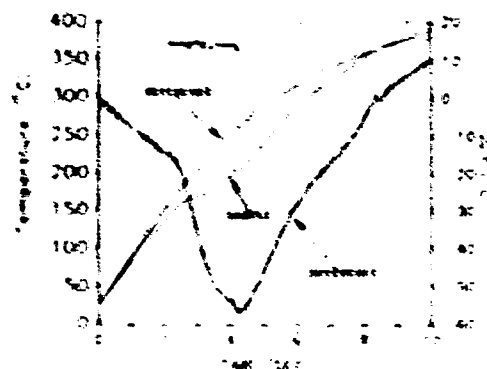


FIG. 15 The filament temperature trace without sample (reference), the filament trace with 2 mg of ethylenediammonium dihydrate (EDD) spread on it (sample), and the amplified difference thermal trace (sample trace minus reference trace). The initial heating rate is about 60–70°C/sec and the atmosphere is 15 psi Ar.

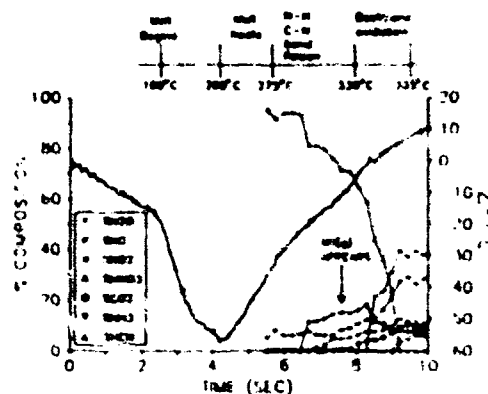


FIG. 16. The difference thermal trace superimposed on the quantified gas products from EDD.  $\text{H}_2\text{O}$ ,  $\text{NH}_3$ ,  $\text{NO}$ ,  $\text{AN}$  aerosol and IR inactive gases are excluded.

portion of the filament in contact with the sample and thermocouple can have a lower temperature than regions away from the sample. This is because the sample may leave the filament by endothermic decomposition off-gassing, evaporation or sublimation. Toward the end of this process heat can flow rapidly from the hotter regions of the filament toward the cooler thermocouple area resulting in a rapid temperature rise. Therefore, an apparent exotherm is sensed which may not be connected to an exothermic chemical event in the sample. A true sample exotherm is a temperature rise that drives the sample thermal trace above that of the reference trace. An apparent exotherm that leaves the filament temperature below the reference trace may or may not be due to exothermic chemistry, because a chemical event cannot be readily distinguished from 'catch up' by a single thermocouple measurement in this case. At this stage, detailed quantitation of the thermal trace, as is done in DSC and DTA measurements, is difficult because of the complexity of the heat transfer phenomena at these high heating rates. However, the qualitative information produced is great, especially when it is combined with the RSFTIR data.

Returning to the description of the thermal decomposition of EDD, Fig. 16 shows the quantified gas products from EDD superimposed on the difference thermal trace (sample trace minus reference trace).<sup>10</sup> This permits chemical and physical events to be attached to the temperature deflections. The initially negative slope of the difference thermal trace results from the additional heat capacity of the filament when the sample is present. The melting endotherm occurs at about 175–180°C. At about 200°C, melting is complete (not isothermal because of the rapid heating rate) and the liquid phase continues to heat to about 275°C without evidence of decomposition off-gassing. At 275°C, the first gas products are detected. These are  $\text{HNO}_3(\text{g})$  formed by proton transfer and desorption, and a small quantity of  $\text{NO}(\text{g})$ , probably from thermal decomposition of

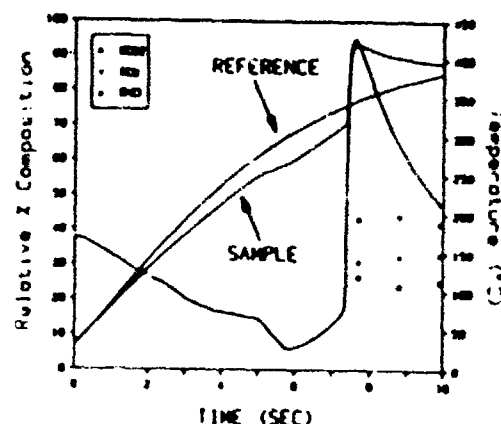


FIG. 17. The filament temperature traces superimposed on the amplified difference thermal trace when 1 mg of PDP is heated rapidly in Ar.

$\text{HNO}_3$ ,  $\text{NH}_3(\text{g})$  then appears perhaps from C–N bond heterolysis. The lag in the thermal trace shows that this stage of decomposition is, as might be expected, overall endothermic. However, above 330°C,  $\text{CO}_2$  from backbone oxidation and the more reduced nitrogen oxide products,  $\text{NO}$  and  $\text{N}_2\text{O}$  appear. The appearance of these products is accompanied by exothermic events in the condensed phase as evidenced by the increased heating rate of the filament. Thus, the combination of a real-time temperature record and near real-time observation of the gas products by RSFTIR provides a guide to the overall reaction sequence during the fast decomposition of a complex material.

An indication of the sensitivity of this technique to the thermal changes in the condensed phase can be obtained from the thermal trace of solid 1,3-propanediammonium perchlorate (PDP).<sup>10</sup> As shown in Fig. 17, the amplified difference thermal trace reveals the endothermic deflection of a solid–solid phase transition beginning at about 175°C prior to the decomposition of the salt. An independent measurement by DSC shows  $\Delta H = 47 \text{ kJ/mol}$  for this phase transition. Thus, about 47 kJ/mol is the approximate lower limit of enthalpy change that can be detected using this temperature profiling technique.

In practice, many energetic materials are used in heterogeneous mixtures containing oxidizers, fuels, modifiers, stabilizers, etc. The opportunity afforded by FTIR/temperature profiling to detect the gas products and the thermochemical deflections simultaneously makes it possible to learn about the decomposition processes of heterogeneous mixtures. This application is illustrated by the results for the 44/44/8 by weight mixture of EDD/ammonium nitrate (AN)/potassium nitrate (KN).<sup>10</sup> Such a eutectic mixture has a melting point low enough for safe melt-casting. It has been used as an insensitive explosive since before World War I in military and civilian applications. Figure 18 shows the thermal trace and gas products under 2 psi Ar. Melting is

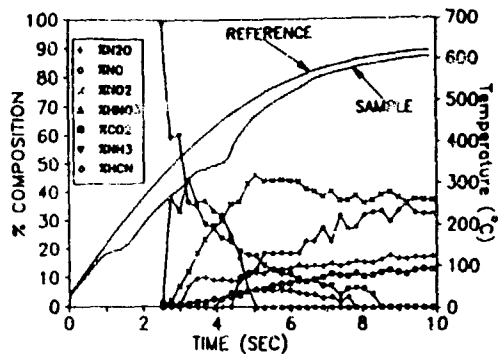


FIG. 18 The temperature trace and gas products from a 46/46/8 mixture of EDD/AN/KN demonstrating that the decomposition of individual components can be distinguished in a mixture.

observed at about 110°C, but the first gas products do not appear until about 200°C. These gases are predominantly from the decomposition of AN by comparison with an authentic sample. Note that an endotherm occurs during this step. The second endotherm occurs at about 280°C which corresponds to that of pure EDD. Finally, a third endotherm at 325°C corresponds to that found with pure AN. The decomposition of the mixture bears a strong resemblance to the sum of the endothermic and products of the pure components.

#### 7. THE EFFECT OF PRESSURE ON THE FIRST DETECTED PRODUCTS

Pressure is such a profoundly important variable in propellant and explosive applications that attempts have been made not only to understand its effects, but also to use pressure differences to uncover relationships between the parent molecular structure and decomposition, and to probe physico-chemical processes. Because the temporal resolution of the IR beam precludes observation of products other than the most thermally stable ones when the pressure is above 1000 psi, most studies of the effect of static pressure on thermolysis have been conducted in the 1-1000 psi range.

Two general types of behavior emerge when the relative percentage of the first detected gas products from many energetic compounds are plotted against the applied Ar pressure.<sup>92</sup> The first category, which contains various nitramines, aliphatic nitro compounds and nitrate esters, displays a strong pressure dependence in several or all of the gas products. Compounds in this category tend to release highly reactive gases, such as NO<sub>2</sub>, HONO, and CH<sub>2</sub>O, in the lower pressure range. Figure 19 illustrates this behavior for RDX. In the midrange pressure range of 40-200 psi, a different set of products dominates. These products are those of intermediate stability, such as NO and HCN, and result, in part, from further reactions of the gases that dominate at lower

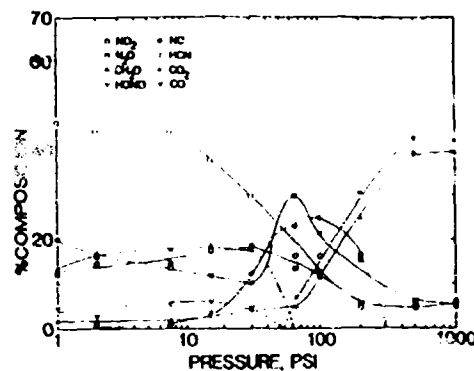


FIG. 19 The effect of the Ar pressure of the initially detected gas products from RDX heated at approximately the same rate at each pressure. Note the three-zone behavior of the dominant gas products.

pressure. At pressures above 200 psi combustion-like products, CO, CO<sub>2</sub>, H<sub>2</sub>O and (probably) N<sub>2</sub> dominate because of still more extensive reaction chemistry.

The second general category contains compounds that produce gases exhibiting only a minor dependence on pressure.<sup>92</sup> As with the first category, more than one type of energetic functional group is represented: nitramines, aliphatic nitro compounds, and azides. Thus, the behavior of compounds in this category results from a general process rather than the particular reaction mechanism of a functional group. Present are compounds that produce a reactive gas, such as NO<sub>2</sub>, but that do not also liberate another product with which NO<sub>2</sub> can react. Also present are compounds that liberate relatively unreactive products initially, such as N<sub>2</sub> or N<sub>2</sub>O, and compounds in which extensive condensed phase chemistry appears to have occurred before the gases reach the IR beam. Condensed phase chemistry is not especially dependent on pressure in the range used. Figure 20 for nitroguanidine,<sup>93</sup> shown below, illustrates the gas composition dependence on pressure for this category

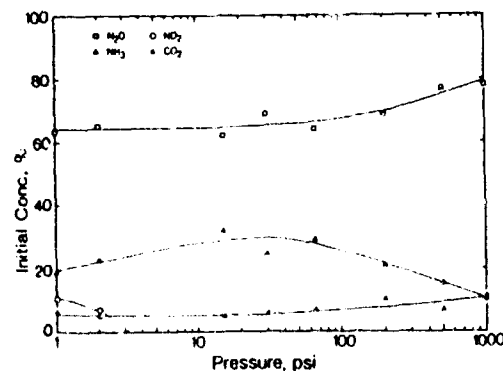
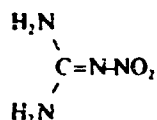


FIG. 20 The effect of the Ar pressure on the initially detected gas products from nitroguanidine. Note the relative independence of the gas products on pressure in this range in contrast to the data for RDX in Fig. 19.

of compounds.



The source of the strong effect of pressure on the first category of compounds has been demonstrated to result from the difference in the diffusion rates of the gases (and, thus, their residence time with the condensed phase) as a function of the applied pressure.<sup>17</sup> The gases must percolate through the condensed phase. As the pressure is raised, the extent of the heterogeneous gas phase/condensed phase reactions increases because the time of percolation and residence increases. Thus, the yield of increasingly stable gas products increases with pressure. The three-zone behavior shown in Fig. 19 simply reflects the natural progression in the nitrogen chemistry ( $\text{NO}_2(\text{HONO}) \rightarrow \text{NO} \rightarrow \text{N}_2$ ) and carbon chemistry ( $\text{CH}_2\text{O} \rightarrow \text{CO}, \text{CO}_2$ ) toward the more thermodynamically stable products at higher pressure and longer residence time in the reaction zone. There is no implication of a change in the decomposition mechanism as a function of pressure for these compounds in the 1–1000 psi range, although a change in the relative importance of the various reaction branches may result. It is interesting to note that this broad pattern of product dependence on pressure resembles the theoretical<sup>18</sup> derived<sup>19</sup> and experimentally measured<sup>20</sup> product distribution of the nitramine flame as a function of distance from the surface.

The above explanation for the source of the pressure dependence of the first-detected gases implies that initial pressure differences can be used to advantage. Recall that fast thermolysis/FTIR data mostly reflect condensed phase processes.<sup>2</sup> In the temperature profiling/FTIR method, the temperature deflections caused by the condensed phase processes are measured simultaneously with the gas products.<sup>7</sup> Thus, the pressure dependence of the gas product distribution and the temperature deflection can be used to distinguish decomposition processes involving the heterogeneous gas/condensed phase from those that are solely associated with the condensed phase. For example, the gas products of alkylammonium nitrate salt thermolysis depend on pressure. Therefore, heterogeneous gas/condensed phase processes are important during the fast thermal decomposition. On the other hand, the temperature deflections of trinitromethyl compounds are mostly caused by reactions of the condensed phase alone without participation of the gas products,<sup>64</sup> because the deflection is independent of pressure.

#### 8. ISOTHERMAL DECOMPOSITION AT HIGH TEMPERATURE

A variation on the temperature profiling/FTIR technique described in Section 6 is a technique we

have labeled fast-heat-and-hold/FTIR or T-jump/FTIR spectroscopy.<sup>10,55</sup> It permits isothermal decomposition studies to be performed on a thin slab of sample about 300  $\mu\text{m}$  thick at temperatures up to 200°C above the onset of the conventionally accepted thermal decomposition temperature. This gives a simulation of the conditions that are present in the condensed phase in the vicinity of the burning surface. Such studies require heating at a very high rate (e.g. 2000°C/sec.) to a high final filament temperature,  $T_f$ , and then carefully holding at  $T_f$  for some period of time while following the chemistry. The chemistry is followed by monitoring the near-surface gas products by RSFTIR spectroscopy throughout the heat-and-hold process. In this way insight is gained into the induction chemistry and the thermochemical processes that might take place at a burning surface.

In experiments involving fast heating to a high temperature, the efficiency of heat transfer from the heat source to the sample is important, as is the ability of the heater circuit to respond to the endothermic and exothermic events taking place in the sample. The times of the thermal changes and the spectra are then matched to reveal the sequence of events that take place during decomposition at  $T_f$ . Because much of the slower 'cooking' chemistry is bypassed by rapid heating, the products and their relative concentrations indicate how the various decomposition reaction branches of a compound depend on the sample temperature.

A small thin filament on which 200–300  $\mu\text{g}$  of sample is thinly spread helps to optimize the heat transfer and the responsiveness of the filament to temperature changes. A thermocouple can be used to sense the temperature change. Such a cell has been described.<sup>55</sup> Alternatively, a commercial pyroprobe controller (such as manufactured by CDS Instruments) and a platinum foil ribbon filament can be used to give excellent heating control.<sup>10</sup>  $dT/dt$  and  $T_f$  of the Pt filament can be controlled independently. Furthermore, the endothermic and exothermic events can be sensed by observing the control voltage of the Pt heater circuit. These facts were used to develop the fast-heat-and-hold/FTIR spectroscopy technique shown in Fig. 21.

The fast-heat-and-hold/FTIR technique can be used to simulate time-to-explosion tests of explosives.<sup>10</sup> Hence, fast thermolysis/FTIR is directly extendable to the study of the explosion hazard of materials. Engineering tests, such as Henkin<sup>66</sup> and one-dimensional time-to-explosion (ODTX),<sup>65</sup> measure the time-to-explosion as a function of the sample temperature. As shown in Fig. 22 for HMX, a similar measurement, the time-to-exotherm,  $t_{\text{exo}}$ , can be made with the fast-heat-and-hold experiment.<sup>10</sup> An apparent activation energy can be calculated from  $\ln(t_{\text{exo}})$  vs  $1/T$ . In addition, however, the IR spectra of the gas products are obtained simultaneously making the cell a spectroscopically instrumental thermal explosion test. Figure 12 showed the relative percent

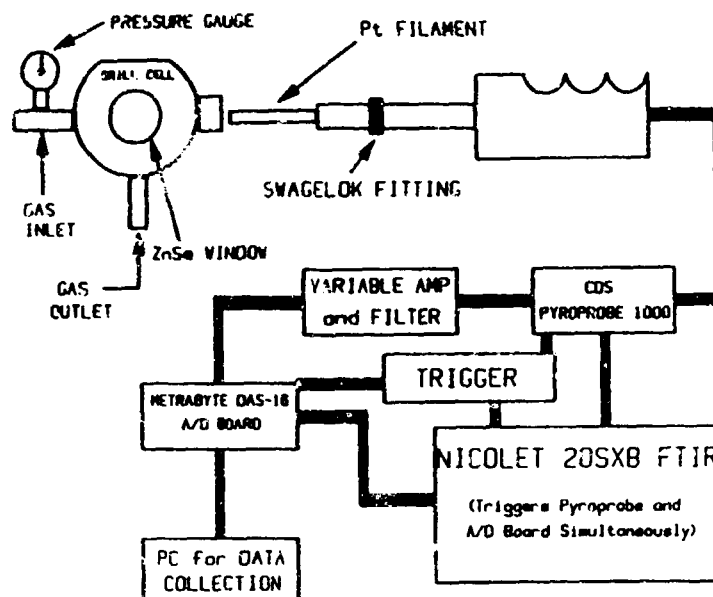


FIG. 21. A schematic design for a fast-heat-and-hold/FTIR technique based on the CDS 1000 (or 2000) pyroprobe.

concentrations of the gases from HMX measured in this way. First, it is important to note that thermal decomposition gases appear in advance of the exotherm indicating that autocatalysis occurs to achieve the exotherm. Second,  $N_2O$  and  $NO_2$  are the first detected gases and their appearance precedes the appearance of  $CH_2O$ . The formation of  $N_2O$  and  $CH_2O$  from HMX has frequently been considered to be a coupled process\* (Section 5.4). Figure 12 suggests that their formation is not necessarily coupled or at least that the evolution of  $CH_2O$  and HCN are retarded relative to  $N_2O$  and  $NO_2$ . Third, the  $N_2O/NO_2$  branching ratio as a function of temperature can be calculated from the relative concentrations of the final gas products. Figure 23 shows that the  $N_2O$  channel is favored at lower temperature

while the  $NO_2$  channel is favored at higher temperature (reaction (16)). The highest temperatures shown in Fig. 23 are above those believed to exist on a burning surface of an HMX propellant and thus Fig. 23 gives an indication of the ratio of the gas product concentrations that should be used in modeling the early flame zone of the propellant as a function of temperature. Given the complexity of the condensed phase reactions under these conditions, the branching ratios may be the most that a combustion modeller can expect to receive from the experimentalist at the present time regarding the nature of reactions in the condensed phase during combustion. These data might be used to model how the gas product ratios are affected by temperature fluctuations during combustion.

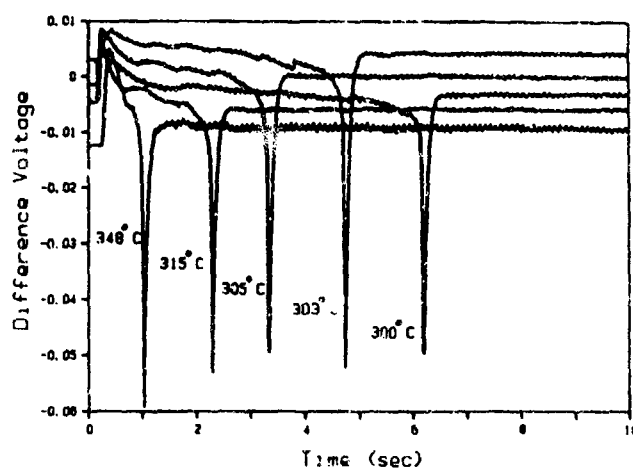


FIG. 22. The exotherms for 200 µg samples of HMX heated at 2000°C/sec and held isothermally at a predetermined temperature.

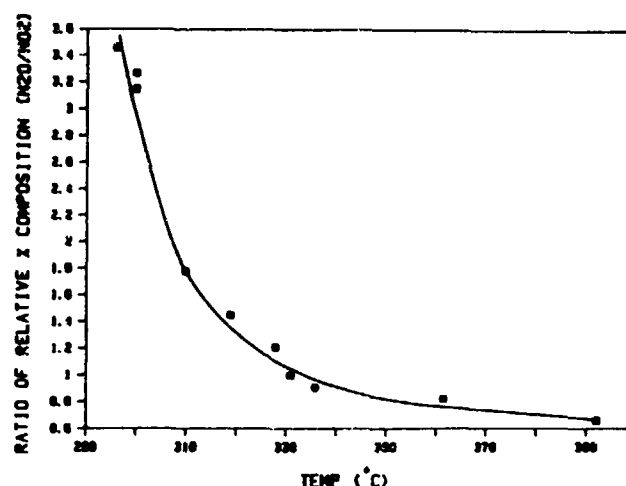


FIG. 23. The  $N_2O/NO_2$  ratio (reaction (16)) for isothermal decomposition of HMX as a function of temperature.

#### 3. STUDIES OF THE SUBMICROSECOND TIMESCALE

An interesting frontier lies in the possibility of directly studying the decomposition of energetic materials in the condensed phase. Such studies require the application of very rapid infrared spectroscopy techniques. The development of time-resolved infrared spectral photography (TRISP)<sup>17</sup> affords the opportunity to record 5 nsec snapshots of thin films of energetic materials heated to 1000°C at rates up to  $10^6$ °C/sec.<sup>18</sup> TRISP is as sensitive as conventional IR absorption spectroscopy and the probe beam is weak enough to prevent undesirable heating of the sample.

Figure 24 shows the experimental arrangement for

TRISP measurements on pulsed-laser heated thin-film samples. The 308 nm output of an XeCl laser is used to pump two dye lasers. The output of the broadband dye laser is mildly focused into a heatpipe containing alkali metal vapor (HP1) to generate broadband IR radiation having a 5 nsec pulse duration. The IR beam is reflected off the substrate in contact with the thin film. The IR beam containing the sample absorbance is then focused on a second heatpipe (HP2) where it spatially and temporally overlaps the output of the narrow band dye laser. Four-wave mixing in this heatpipe converts the IR radiation to visible wavelengths for photodetection.

Figure 25 illustrates a result from the study of an

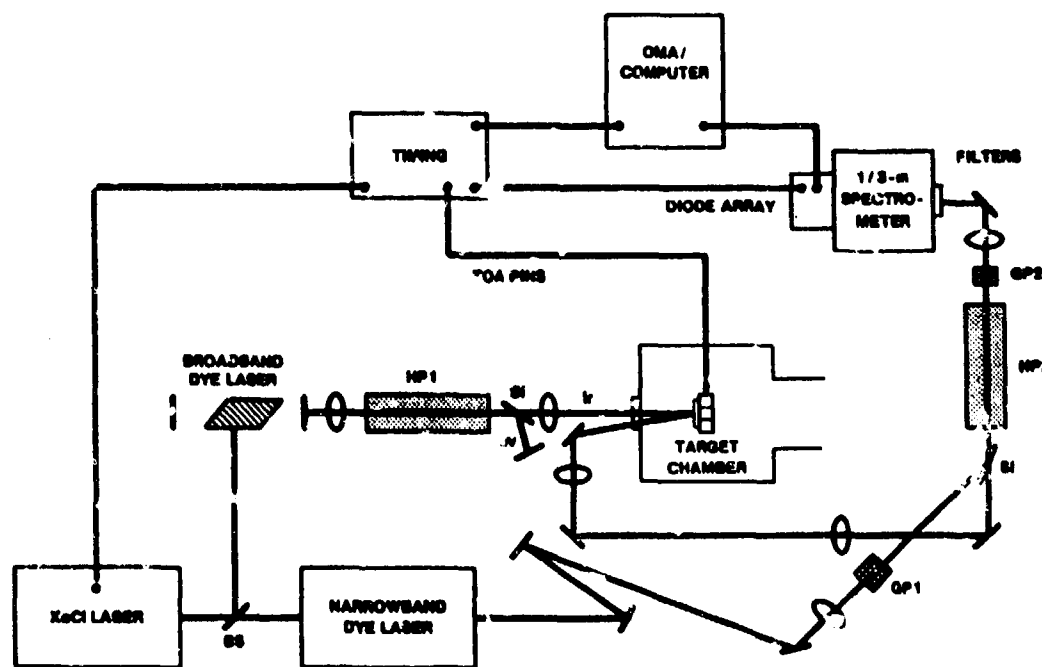


FIG. 24. The experimental design of the TRISP experiment (used with permission).

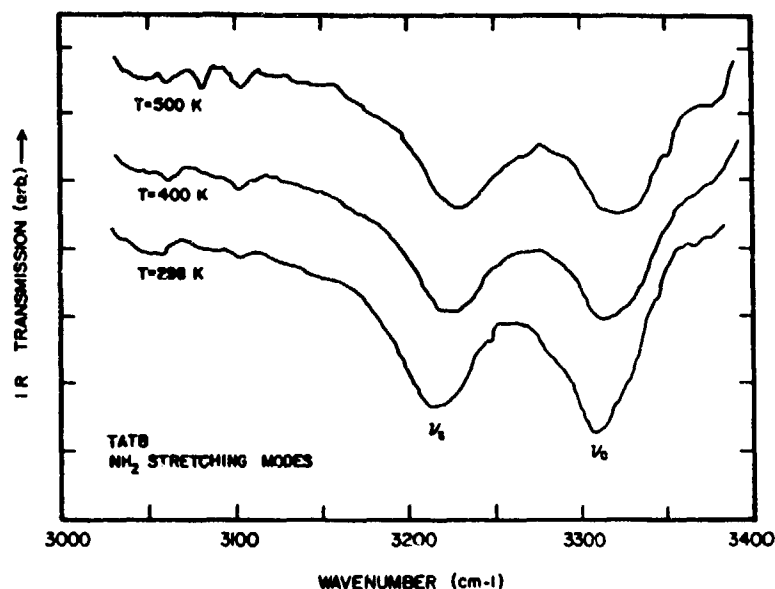


FIG. 25. The  $\text{NH}_2$  stretching region of TATB at three temperatures as measured by TRISP (used with permission).

insensitive energetic material triaminotrinitrobenzene (TATB) by TRISP.<sup>16</sup> Shown are the  $\nu_4$  and  $\nu_6$  ( $\text{NH}_2$ ) modes of a 2 mm thick sample of TATB. The sample was slowly heated to achieve the three temperatures shown. However, in principle, the sample could have been heated very rapidly. The broadening and shift to lower frequency at higher temperature is indicative of a weakening of the hydrogen bonding and an increase in the lattice disorder at higher temperature.

Picosecond and femtosecond IR studies of reactions in the condensed phase of energetic materials may be successful with the use of a liquid  $\text{N}_2$ -cooled single model CO laser.<sup>99</sup> This source can provide tunable radiation in the 1600–3000  $\text{cm}^{-1}$  range.

The results of these fast diagnostics studies could be quite exciting and useful for developing the picture at the reacting surface during combustion. They are much more demanding experiments than the fast thermolysis methods described in this article and, as a result, will not provide data at the same rate as the FTIR technique.

#### 10. FTIR MEASUREMENTS OF FLAMES

All of the experiments described above involve *simulations* of the condensed phase and surface processes during combustion. As a concluding section to this article, it is valuable to know that IR spectroscopy studies can be extended to study the stand-off flame zone during combustion of the propellant or a material that resembles a propellant.

Reactive two-phase flows, especially in flames, are usually produced when propellant formulations burn. This is because many solid rocket propellants contain fuels, such as Al or B, that burn to the solid oxide.

Inert particles, such as  $\text{ZrC}$ , are sometimes added to help dampen combustion oscillations. The solid particles appear as smoke. A similar particle laden flow can exist in hydrocarbon and coal combustion where the combustion gases might be mixed with soot, fly ash and char.

In recent years several techniques have been developed based on FTIR emission/transmission spectroscopy (FTIR E/T) that enable measurements to be made of particle and gas concentrations and temperatures in hot flows.<sup>100–104</sup> Specifically, (1) the temperature and concentration of the particle and soot phases have been measured separately in an ethylene-air diffusion flame;<sup>101</sup> (2) measurements have been made in densely loaded particle streams,<sup>101</sup> and (3) particle sizes have been measured.<sup>102</sup> Although most measurements have been line-of-sight, it has been recently shown that Fourier image reconstruction can be used to obtain absorbance and emittance spectra spatially resolved in about  $1 \times 1 \times 4$  mm volumes.<sup>104</sup>

The FTIR E/T method offers promise for studying propellant flames in which the number of scattering particles is not unusually large. However, an additional experimental complication to propellant combustion studies is that the surface burns as a regressing front. Therefore, a moving stage is needed to maintain the position of the propellant flame relative to the IR beam. This requirement contrasts with the simpler flow reactor designs that can be used to study premixed gas flames and coal particle-gas flames. Recently, FTIR emission spectra have been recorded on flames of ammonium perchlorate and HTPB.<sup>105</sup> A moving stage with servo feedback control was used to maintain the position of the propellant in the IR beam. Figure 26 shows the IR emission spectrum of the gas products:  $\text{CO}_2$ ,  $\text{CO}$ ,  $\text{H}_2\text{O}$ ,  $\text{HCl}$

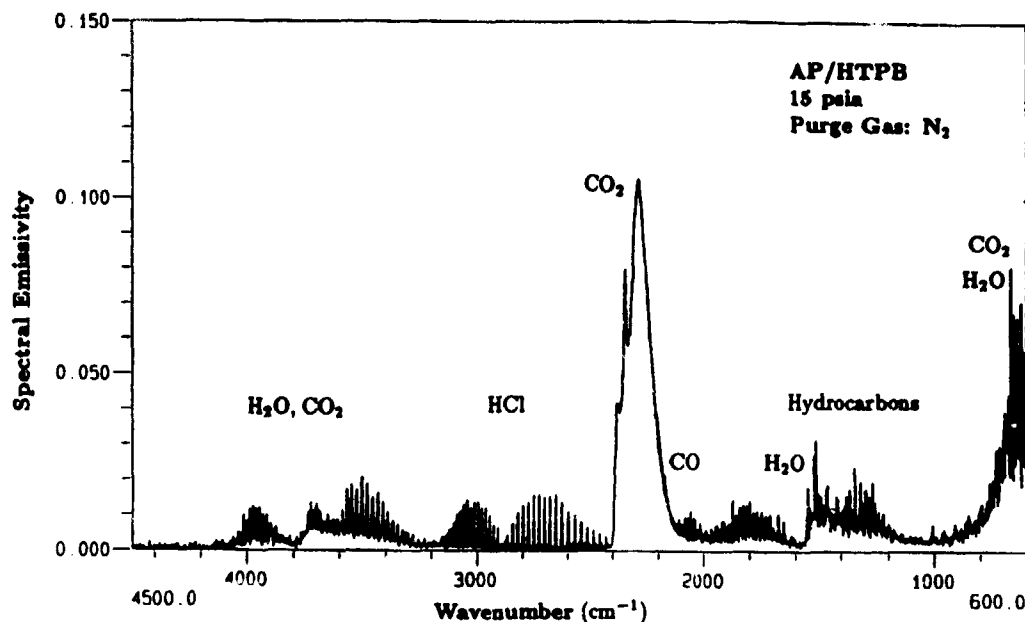


FIG. 26. Sixteen co-added emission IR spectra of the AP-HTPB flame zone assuming a temperature of 1500 K (used with permission).

and fragments of HTPB are detected. In addition,  $\text{NH}_3$  and  $\text{HClO}_4$  were also detected indicating that AP sublimates to some extent under combustion conditions.

FTIR spectroscopy has been used to obtain high resolution absorption spectra of the major steady-state species in premixed  $\text{C}_2\text{H}_2\text{-NO}_2^{106}$  and  $\text{HCN-NO}_2^{107}$  burner flames. Reactions involving these gases are believed to be among the more important ones in certain rocket and gun propellant flames produced by nitramines (see Section 5). The high temperature of these flames required modifications to be made to the IR spectrometer. For example, temperature gradients in various parts of the optical bench were caused by the flame and led to an interference pattern superimposed on the spectrum (channel spectra). Plane windows were, therefore, replaced by wedge windows to reduce this problem. The high infrared emissivity of the flame required the use of a long-pass IR filter and a high intensity globar to obtain quality spectra. With these modifications detailed studies have been made of the species concentration profiles and temperature as a function of distance above the burner surface. The temperature was extracted from the rotational band intensities of CO in various parts of the flame. When coupled with simulations of the kinetics, it could be concluded that the flame chemistry is dominated by oxygen atoms.<sup>107</sup> The production of oxygen atoms increases the burn rate while their consumption decreases the burn rate.

In place of the FTIR spectrometer, a tunable infrared laser source might be used to study species in homogeneous flames on a much shorter time scale.<sup>108-110</sup> The resolution and spectral detail are lost at high pressure and temperature so the tunable

infrared laser may be most suited to low pressure and low temperature flames.

## 11. SUMMARY

The objective of much of the research into the combustion of rocket propellants and the explosion of energetic materials is to gain control of the process. At the same time there is a strong need to develop predictive models that enable at least some of the expensive full-scale tests in this field to be avoided. Achievement of both of these goals requires a detailed knowledge of the chemistry and physics as input to the models. In addition to providing input to flame models, and understanding of catalysis and burn rate modification as described in this article, fast thermolysis/FTIR can be applied to other important problems. For instance, we know that the combustion characteristics of a propellant are influenced by its initial temperature (temperature sensitivity). We now can examine the chemical effects of temperature sensitivity. We can move into the area of combustion instability. Pressure oscillations brought on by instability cause temperature oscillations near the burning surface. Hence the fuel-oxidizer ratios can oscillate which affects the stability of the flame. We can examine the chemical oscillations during combustion by the use of fast thermolysis techniques. Details of these kinds of problems are extremely difficult to obtain and I hope that I have conveyed that experimental simulations are moving toward some of the required information.

**Acknowledgments**—In gaining the understanding of combustion in this article, the financial support of the Air Force Office of Scientific Research, the Army Research Office, the Air Force Armament Laboratory and Thiokol



Corporation is most appreciated. The hard work and contributions of my graduate student and post-doctoral coworkers, whose names appear in the references, made these advances possible.

## REFERENCES

- MILLER, J. A. and FINK, G. A., *Chem. Eng. News*, 22 (August 31, 1987).
- TIMKEN, M. D., CHEN, J. K. and BRILL, T. B., *Appl. Spectrosc.* 44, 701 (1990).
- CHEN, J. K. and BRILL, T. B., *Combust. Flame* 85, 479 (1991).
- CHEN, J. K. and BRILL, T. B., *Combust. Flame* 87, 157 (1991).
- CHEN, J. K. and BRILL, T. B., *Combust. Flame* 87, 217 (1991).
- OYUMI, Y. and BRILL, T. B., *Combust. Flame* 62, 213 (1985).
- CRONIN, J. T. and BRILL, T. B., *Appl. Spectrosc.* 41, 1147.
- CRONIN, J. T. and BRILL, T. B., *Appl. Spectrosc.* 43, 650 (1989).
- CRONIN, J. T. and BRILL, T. B., *Combust. Flame* 74, 81 (1988).
- BRUSH, P. J. and BRILL, T. B., to be published.
- DECKER, L. J., WARD, J. P. and FREEDMAN, E., *Thermochim. Acta* 8, 177 (1974).
- DOBRAZ, B. M., *LLNL Explosives Handbook*, pp. 19-95, UCRL-52997, Lawrence Livermore National Laboratory (March 1981).
- PATIL, D. G. and BRILL, T. B., to be published.
- GRIFFITHS, P. R. and DE HASETH, J. A., *Fourier Transform Infrared Spectroscopy*, John Wiley, New York (1986).
- PALMER, R. A., MANNING, C. J., RZEPIELA, J. A., WIDDER, J. M. and CHAO, J. L., *Appl. Spectrosc.* 43, 193 (1989).
- TROTT, W. M. and REHLUND, A. M., *Proc. 9th Symp. Deton.*, Vol. 1, p. 153, Portland, OR (1989).
- FLANGAN, D. A. and STOKES, B. B., AFRPL-TR-72-94, Air Force Rocket Propulsion Laboratory (October, 1980).
- LIEBMAN, S. A., AHLSTROM, D. H. and GRIFFITHS, P. R., *Appl. Spectrosc.* 30, 355 (1976).
- KARPOWICZ, R. J., PhD Dissertation University of Delaware, U.S.A. (1984).
- PALOPOLI, S. F. and BRILL, T. B., *Combust. Flame* 87, 45 (1991).
- (a) GAO, A., OYUMI, Y. and BRILL, T. B., *Combust. Flame* 83, 345 (1991); (b) DOWS, D. A. and PIMENTEL, G. C., *J. Chem. Phys.* 23, 1258 (1955).
- WAGNER, G. D. and WAGNER, E. L., *J. Phys. Chem.* 64, 1480 (1960).
- TAKIMOTO, M., *Nippon Kagaku Zasshi* 85, 168 (1964).
- SIMKINA, L. A., FINKEL'STEIN, A. I. and GAL'PERIN, V. A., *Zavod. Lab.* 39, 287 (1973).
- FINKEL'STEIN, A. I. and SPIRIDONOVA, N. V., *Russ. Chem. Rev.* 33, 400 (1964).
- FINKEL'STEIN, A. I. and SPIRIDONOVA, N. V., *J. Org. Chem. (Russ.)* 10, 602 (1964).
- SHURUKHIN, YU. V., KLYUYE, N. A. and GRANDBERG, I. I., *Kim. Get. Sardin.* 6, 723 (1985).
- SAWODNEY, W., NIEDENZU, K. and DAWSON, J. W., *J. Chem. Phys.* 45, 3155 (1966).
- KHEMEL'NITSKH, L. I., SHLYAPOCHNIKOV, V. A., CHERSKAYA, N. O., LEBEDEV, O. V., EPIMINA, L. V. and KIROTKOVA, G. V., *Izv. Akad. Nauk SSR, Ser. Khim.* 33, 174 (1984).
- SHERMAN, W. F. and SARULOVITCH, P. P., *J. Chem. Phys.* 52, 5187 (1970).
- DOWS, D. A., WHITTLE, E. and PIMENTEL, G. C., *J. Chem. Phys.* 23, 1475 (1955).
- BRILL, T. B., *Chemistry and Physics of Energetic Materials*, p. 277, S. Bulusu, (Ed.), Kluwer Press, Boston (1990).
- KOROSHEVICH, O. P., KUBIDA, L. V., ORLOV, V. N., TERESHCHENKO, A. G., KUTSENOK, K. P., MAVLEV, R. A., ERMOLIN, N. E., FOMIN, V. M. and EMEL'YANOV, I. D., *Mass Spec. Chem. Kinet.* 73, (1985).
- PARR, T. P. and HANSON-PARR, D. M., *CPIA Publ.* 457(1), 249 (1986).
- MELIUS, C. F., *J. Phys.* 48, C4-341 (1987).
- BRILL, T. B. and OYUMI, Y., *J. Phys. Chem.* 90, 2679 (1986).
- OYUMI, Y., RHEINGOLD, A. L. and BRILL, T. B., *Prop. Explos. Pyrotech.* 12, 1 (1987).
- OYUMI, Y., and BRILL, T. B., *Prop. Explos. Pyrotech.* 13, 69 (1988).
- MELIUS, C. F. and BINKLEY, J. S., *Proc. 21st Symp. (Int.) Combust.* 1453 (1986).
- BRILL, T. B. and OYUMI, Y., *J. Phys. Chem.* 90, 6848 (1986).
- SHACKELFORD, S. A., COOLIDGE, M. B., GOSHCARIAN, B. B., LOVING, B. A., ROGERS, R. N., JANNEY, J. L. and EBINGER, M. H., *J. Phys. Chem.* 89, 3118 (1985).
- BULUSU, S., WEINSTEIN, D. I., AUTERA, J. R. and VELICKY, R. W., *J. Phys. Chem.* 90, 4121 (1986).
- SHACKELFORD, S. A., *J. Phys.* 48, C4-193 (1987).
- MELIUS, C. F., BERGEN, N. and SHEPHERD, J. E., *Proc. 23rd Symp. (Int.) Combust.* Orleans, France, in press (1990).
- SHAW, R. and WALKER, F. E., *J. Phys. Chem.* 81, 2572 (1977).
- BRILL, T. B., KARPOWICZ, R. J., HALLER, T. M. and RHEINGOLD, A. L., *J. Phys. Chem.* 88, 4138 (1984).
- OYUMI, Y., BRILL, T. B. and RHEINGOLD, A. L., *J. Phys. Chem.* 90, 2526 (1986).
- OYUMI, Y., RHEINGOLD, A. L. and BRILL, T. B., *J. Phys. Chem.* 91, 920 (1987).
- OYUMI, Y., BRILL, T. B. and RHEINGOLD, A. L., *Thermochim. Acta* 114, 209 (1987).
- OYUMI, Y. and BRILL, T. B., *Combust. Flame* 62, 213 (1985).
- OYUMI, Y. and BRILL, T. B., *Combust. Flame* 62, 225 (1985).
- OYUMI, Y., BRILL, T. B. and RHEINGOLD, A. L., *J. Phys. Chem.* 89, 4824 (1985).
- OYUMI, Y., RHEINGOLD, A. L. and BRILL, T. B., *J. Phys. Chem.* 90, 4686 (1986).
- MELIUS, C. F., *CPIA Publ.* 476(1), 359 (1987).
- BRILL, T. B. and BRUSH, P. J., *Proc. 9th Symp. (Int.) Deton.*, Vol. 1, p. 218, Portland, OR, (1989).
- BEHRENS, R., *CPIA Publ.* 476(1), 333 (1987).
- BEHRENS, R., *J. Phys. Chem.* 94, 6706 (1990).
- OYUMI, Y. and BRILL, T. B., *Combust. Flame* 67, 121 (1987).
- PALOPOLI, S. F., GEIS, S. J., RHEINGOLD, A. L. and BRILL, T. B., *Inorg. Chem.* 27, 2963 (1988).
- PALOPOLI, S. F. and BRILL, T. B., *Inorg. Chem.* 27, 2971 (1988).
- OYUMI, Y. and BRILL, T. B., *J. Phys. Chem.* 91, 3657 (1987).
- OYUMI, Y. and BRILL, T. B., *Combust. Flame* 65, 103 (1986).
- OYUMI, Y. and BRILL, T. B., *Prop. Explos. Pyrotech.* 11, 35 (1986).
- BRILL, T. B. and SUBRAMANIAN, R., *Combust. Flame* 80, 150 (1990).
- OYUMI, Y. and BRILL, T. B., *Combust. Flame* 65, 9 (1986).
- OYUMI, Y. and BRILL, T. B., *Combust. Flame* 65, 127 (1986).

67. KRAUSE, H. and FREIL, A., *Proc. 21st Int. Conf. of ICT*, 8-1, Karlsruhe, Germany (1990).
68. OYUMI, Y., BRILL, T. B., RHEINGOLD, A. L. and LOWE-MA, C., *J. Phys. Chem.* 89, 2309 (1985).
69. RUSSELL, T. P. and BRILL, T. B., *Combust. Flame* 76, 393 (1989).
70. RUSSELL, T. P. and BRILL, T. B., *Prop. Explos. Pyrotech.* 15, 66 (1990).
71. RUSSELL, T. P. and BRILL, T. B., *Prop. Explos. Pyrotech.* 15, 77 (1990).
72. RUSSELL, T. P. and BRILL, T. B., *Prop. Explos. Pyrotech.* 15, 81 (1990).
73. RUSSELL, T. P. and BRILL, T. B., *Prop. Explos. Pyrotech.* 15, 123 (1990).
74. RUSSELL, T. P. and BRILL, T. B., *Prop. Explos. Pyrotech.* 16, 27 (1991).
75. PATIL, D. G., JAIN, S. R. and BRILL, T. B., *Prop. Explos. Pyrotech.*, in press.
76. BRILL, T. B. and SUBRAMANIAN, R., *Prop. Explos. Pyrotech.* 15, 137 (1990).
77. OYUMI, Y. and BRILL, T. B., *Combust. Flame* 62, 233 (1986).
78. STONER, C. E. and BRILL, T. B., *Combust. Flame* 83, 302 (1991).
79. OYUMI, Y. and BRILL, T. B., *Combust. Flame* 65, 313 (1986).
80. STONER, C. E. and BRILL, T. B., *Inorg. Chem.* 28, 4500 (1989).
81. MILLER, J. S., GLATZHOFFER, D. T., LAVERSANNE, R., CHITTIPEDDI, S., VACA, P., BRILL, T. B., TIMKEN, M. D., O'CONNER, C. J., ZHENG, J. H., CALABRESE, J. C. and EPSTEIN, A. J., *Chem. Mat.* 2, 60 (1990).
82. GAO, A., RHEINGOLD, A. L. and BRILL, T. B., *Prop. Explos. Pyrotech.* 16, 97 (1991).
83. STONER, C. E., RHEINGOLD, A. L. and BRILL, T. B., *Inorg. Chem.* 30, 360 (1991).
84. STONER, C. E., HAGGERTY, B. S., RHEINGOLD, A. L. and BRILL, T. B., *Prop. Explos. Pyrotech.*, in press.
85. CRONIN, J. T. and BRILL, T. B., *J. Phys. Chem.* 90, 178 (1986).
86. MELIUS, C. F., *Chemistry and Physics of Energetic Materials*, p. 51, S. Bulusu, (Ed.), Kluwer Press, Boston (1990).
87. ROBERTS, J. A. and MANGUM, M. G., Air Force Rocket Propulsion Laboratory, AFRPL-TR-84-038 (September, 1984).
88. CHI, M., GLEESON, B., HILL, J. and WILLER, R., (Thiokol Corp.) patent pending.
89. LIPERI, M., PhD Dissertation, Polytechnic of Milan (December, 1986).
90. CHEN, R., RUSSELL, T. P., RHEINGOLD, A. L. and BRILL, T. B., *J. Crystallogr. Spectrosc. Res.* 21, 167 (1991).
91. BRILL, T. B. and RUSSELL, T. P., AFATL-TR-89-55, Eglin AFB, FL (September, 1989).
92. OYUMI, Y. and BRILL, T. B., *Combust. Flame* 68, 209 (1987).
93. OYUMI, Y., RHEINGOLD, A. L. and BRILL, T. B., *Prop. Explos. Pyrotech.* 12, 46 (1987).
94. HENKIN, H. and MCGILL, R., *Ind. Eng. Chem.* 44, 1391 (1952).
95. MCGUIRE, R. R. and TARVER, C. M., *Proc. 7th Symp (Int.) Deton.* p. 56, Annapolis, MD (1981).
96. SCHROEDER, M. A., *CPIA Publ.* 308, 17 (1989; *CPIA Publ.* 347, 395 (1981)).
97. BETHUNE, D. S., LANKARD, J. R., LOY, M. M. T. and SOROKIN, P. P., *IBM J. Res. Dev.* 23, 556 (1979).
98. SKOCYPEC, R. D., ERICKSON, K. L., RENLUND, A. M. and TROTT, W. M., *Proc. 26th JANNAF Combustion Mtg*, JPL, Pasadena, CA (October, 1989).
99. ST. M. and HARRIS, C. B., *J. Amer. Chem. Soc.* 111, 8963 (1989).
100. BEST, P. E., CARANGELO, R. M., MARKHAM, J. R. and SOLOMON, P. R., *Combust. Flame* 66, 47 (1986).
101. SOLOMON, P. R., BEST, P. E., CARANGELO, R. M., MARKHAM, J. R., CHIEN, P.-L., SANTORO, R. J. and SEMERJIAN, H. G., *Proc. 21st Symp. (Int.) Combust.*, p. 1763 (1986).
102. SOLOMON, P. R., CARANGELO, R. M., HAMBLIN, D. G. and BEST, P. E., *Appl. Spectrosc.* 40, 746 (1986).
103. SOLOMON, P. R., CHIEN, P.-L., CARANGELO, R. M., BEST, P. E. and MARKHAM, J. R., *Proc. 22nd Symp. (Int.) Combust.*, p. 211 (1988).
104. MARKHAM, J. R., SHANG, Y. P., CARANGELO, R. M. and SOLOMON, P. R., *Proc. 23rd Symp. (Int.) Combust.*, in press.
105. KLOTZ, S., THYNELL, S. T., HUANG, I. T. and Kuo, K. K., AIAA-90-1850, American Institute of Aeronautics and Astronautics, Orlando, FL (July, 1990).
106. THORNE, L. R. and SMITH, O. I., *CPIA Publ.* 481 (II), p. 143 (1988).
107. THORNE, L. R. and MELIUS, C. F., *Proc. 23rd Symp (Int.) Combust.*, in press.
108. ZENG, Y. P., SHARPE, A. W., REIFSCHNEIDER, D., WITTIG, C. and BEAUDET, R. A., *J. Chem. Phys.* 93, 183 (1990).
109. BALLA, R. J. and PASTERNAK, L., *J. Phys. Chem.* 91, 73 (1987).
110. KANAMORI, H., BUTLER, J. E., KAWAGUCHI, K., YAMADA, L. and HIROTA, E., *J. Chem. Phys.* 83, 611 (1985).

# Condensed phase chemistry of explosives and propellants at high temperature: HMX, RDX and BAMO

BY T. B. BRILL AND P. J. BRUSH

*Department of Chemistry, University of Delaware, Newark, Delaware 19716, U.S.A.*

By studying the behaviour of a thin film of an explosive or propellant it is possible to produce a snapshot of the surface reaction zone that exists during combustion of such explosives as cyclotrimethylene trinitramine (RDX) and cyclotetramethylene tetranitramine (HMX). Rapid heating ( $2000\text{ K s}^{-1}$ ) and fast monitoring of the mass and heat-balance are performed simultaneously with fast Fourier transform infrared spectroscopic analysis of gaseous products.

Initially, HMX and RDX yield mainly  $\text{N}_2\text{O}$  at low temperatures or  $\text{NO}_2$  at higher temperatures; the former is quickly followed by  $\text{CH}_2\text{O}$  and the latter by HCN: these species are formed from the primary residue. These concurrent pathways compensate for one another thermochemically to make this a roughly thermoneutral 'initial' stage. Subsequently, a highly exothermic reaction between  $\text{CH}_2\text{O}$  and  $\text{NO}_2$  leads to  $\text{CO}$ ,  $\text{NO}$  and  $\text{H}_2\text{O}$  and constitutes the main source of heat for the condensed phase.

The azide polymer bis(azedomethyl)oxetane has also been studied as a prototype of rather different behaviour. For it, ratios of gaseous products are not very dependent on temperature in the range  $275$  to  $390^\circ\text{C}$ .

---

## 1. Introduction

As physical details are developed about the initiation and ignition of propellants and explosives, determination of the chemical processes under conditions of high heating rates, temperatures, and pressures is increasingly needed. Unfortunately, ignition and initiation of bulk solids involve heterogeneous phases at high pressure and temperature under dynamic, non-equilibrium conditions. The chemical details are very difficult to extract. Hence, the experimentalist is challenged to develop microscale methods that incorporate relevant conditions, but enable direct chemical studies to be made. The most convincing indication of a successful simulation is the reproduction of some key observable of a macroscale engineering test by the microscale experiment. In this way microscale chemical details can be learned about macroscale phenomena.

The quest for relevant experimental simulations has been a motivation of our laboratory. A breakthrough was recently made (Chen & Brill 1991*a, b, c*) with the SMATCH/FTIR (simultaneous mass and temperature change/Fourier transform infrared spectroscopy) method. The kinetics of fast weight loss of a thin film of material measured by this method predicted the linear burn rate of the bulk material measured at the same temperature and pressure. Hence, SMATCH/FTIR is a microscale laboratory simulation of the surface reaction zone of a burning material. The near-surface gas products are quenched and analysed in near real-time by rapid-scan IR

*Phil. Trans. R. Soc. Lond. A* (1992) **339**, 377–385  
Printed in Great Britain

© 1992 The Royal Society and the authors

377

Table 1. Comparison of calculated and measured burn rates ( $\text{mm s}^{-1}$ )

compound	SMATCH/FTIR	combustion measurement
NC	0.3	0.4
GAP	1.35	1.7
RDX	0.27	0.3
HTPB	0.21	0.19

spectroscopy. These gas products are the main reactants in the first stage of the flame zone were a flame to be present. These earliest reactants have resisted identification during actual combustion. Equally important is the discovery that the products identified by SMATCH/FTIR closely resemble those measured with our filament thermolysis methods (Oyumi & Brill 1985; Cronin & Brill 1987; Brush & Brill 1989) which are much easier to use. The connection between SMATCH/FTIR and the filament pyrolysis methods is the basis for using fast-thermolysis/FTIR spectroscopy to establish the high-temperature and high-pressure decomposition processes of bulk explosive and propellants at burning surface temperatures.

This paper describes the high temperature decomposition processes of cyclo-tetramethylene tetranitramine (HMX), cyclotrimethylene trinitramine (RDX) and bis(azidomethyl)oxetane polymer (BAMO) determined by the T-jump/FTIR method (Brill *et al.* 1992). However, as a backdrop, selected studies using SMATCH/FTIR are presented to support the premise that a carefully designed laboratory experiment can elucidate the chemistry that leads to ignition and the onset of explosion of an energetic material.

## 2. Connecting fast thermolysis to combustion

SMATCH/FTIR spectroscopy provides the dynamic weight loss, temperature change, and near-surface gas products when a 20–60  $\mu\text{m}$ -thick film (0.5–1 mg) of sample is heated at a chosen rate between 100 and 350  $^{\circ}\text{C s}^{-1}$  under 1 atm† of Ar (Timken *et al.* 1990; Chen & Brill 1991*a, b*). Polymers, such as 13% N nitrocellulose (Chen & Brill 1991*a*), glycidylazide polymer (GAP) (Chen & Brill 1991*b*), urethane cross-linked hydroxyl-terminated polybutadiene (HTPB) (Chen & Brill 1991*c*), and crystalline monopropellants, such as HMX and RDX, have been studied. The Arrhenius parameters for the weight loss enable the regression (burn) rate of the film to be calculated from a version of the pyrolysis law. The burn rates of these materials have been measured at or extrapolated to the same temperature and pressure as the SMATCH data. The results are compared in table 1. The remarkable similarity of the data implies that SMATCH/FTIR gives a 'snapshot' of the surface reaction zone as it exists during combustion. The successful simulation of the burn rate by a microscale fast thermolysis method is central to confidence in the use of these methods to determine the heterogeneous chemistry of combusting solids.

The gas products that evolve from the film into the Ar atmosphere are detected and quantified 3 mm above the surface by rapid-scan FTIR spectroscopy. Because they are formed thermally at the same rate and temperature as combustion, the products closely relate to the reactants for the first stage of the flame zone.

It is found that simply heating a thin film of sample on a filament at a high rate

† 1 atm  $\approx 10^5$  Pa.

as in SMATCH/FTIR gives the same product distribution. Moreover, these simpler filament pyrolysis methods can be optimized to give information about the sequence and temperature and pressure dependence of the products. This information helps unravel the dominant chemistry of heterogeneous decomposition of the bulk material. The remainder of this article describes results of high temperature, isothermal decomposition obtained from the filament pyrolysis technique of T-jump/FTIR spectroscopy (Brill *et al.* 1992).

### 3. The T-jump/FTIR method

During ignition, combustion and thermal explosion of a material, the temperature at the reacting interface rises rapidly to a high temperature. Hence, thermal decomposition takes place in a temperature range considerably above that of 'slow' decomposition. The gas product distribution can be strongly affected by temperature leading to an erroneous description if the temperature factor is unknown. To establish the high-temperature chemistry, rapid heating conditions and appropriate high temperatures must be created in a microscale experiment that also enables the species to be detected.

T-jump/FTIR is a variation of the fast thermolysis/FTIR method (Oyumi & Brill 1985). A 20  $\mu\text{m}$  thick Pt ribbon filament supports a thin film of material. Heating occurs at a chosen high rate up to 20000  $^{\circ}\text{C s}^{-1}$  to a chosen temperature ( $T_f$ ).  $T_f$  can be maintained while the decomposition gases are analysed by rapid-scan FTIR spectroscopy. The high heating rate reduces the 'cooking' chemistry that takes place at a low heating rate. The fact that  $T_f$  is adjustable enables the products to be determined at selected temperatures including the expected burning surface temperature.

The Pt filament is an element of a very rapidly responding and sensitive bridge circuit. The control voltage of the circuit linearly responds to the Pt resistance during the programmed heating step and maintains a constant resistance once  $T_f$  is reached. The temperature of the filament is calibrated and is determined by the resistance as in a Pt thermometer. The control voltage increases or decreases very rapidly to maintain  $T_f$  in response to endothermic or exothermic events of the sample. Therefore, monitoring the control voltage as a function of time uncovers these sequential events.

A useful form of the control voltage is the difference trace (voltage without sample minus voltage with sample present) as shown in figure 1 for 200  $\mu\text{g}$  of HMX. After heating at 2000  $^{\circ}\text{C s}^{-1}$  to  $T_f = 298^{\circ}\text{C}$ , an initial endotherm (positive deflection) occurs in the first second corresponding to melting and the higher heat capacity when sample is present. Later a sharp negative spike appears due to runaway exothermic decomposition. A heating rate of 2000  $^{\circ}\text{C s}^{-1}$  is the highest value that does not overshoot  $T_f$ . The thermal trace in figure 1 resembles a DSC thermogram, but the slope and area cannot be quantitated to obtain the reaction rate and total heat as in DSC because the rate of heat transfer between the filament and sample is not sufficiently fast. Hence the slope and area do not solely reflect the chemistry taking place. Despite this unavoidable heat transfer problem, the technique provides quasi-isothermal conditions at chosen temperatures and enables sequential thermal events and gas products to be detected at a high rate.

T-jump/FTIR has two important uses. First, the time-to-exotherm (runaway reaction, ignition, or explosion) can be determined as a function of temperature. Such

*Phil. Trans. R. Soc. Lond. A (1992)*

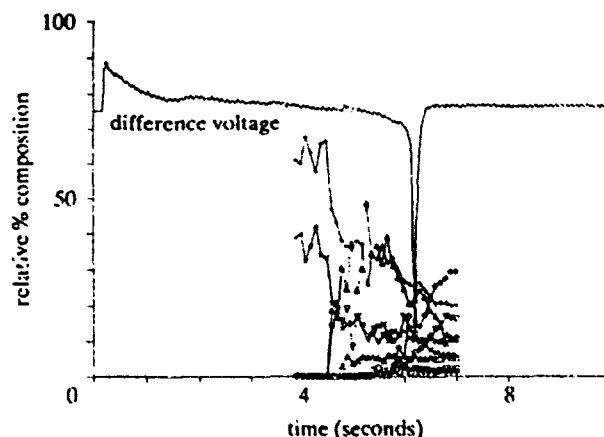


Figure 1. The thermal response trace and gas products from 200  $\mu\text{g}$  of HMX heated at  $2000\text{ }^{\circ}\text{C s}^{-1}$  to  $298\text{ }^{\circ}\text{C}$  and then held at  $298\text{ }^{\circ}\text{C}$  under 2.7 atm Ar.  $\Delta$ , %  $\text{CO}_2$ ; +, %  $\text{N}_2\text{O}$ ;  $\blacklozenge$ , %  $\text{NO}$ ;  $\diamond$ , %  $\text{CO}$ ;  $\times$ , %  $\text{NO}_2$ ;  $\nabla$ , %  $\text{HONO}$ ;  $\triangledown$ , %  $\text{HCN}$ ;  $\blacktriangle$ , %  $\text{H}_2\text{CO}$ ;  $\square$ , %  $\text{HNCO}$ .

data are important for thermal explosion studies and have been acquired in other ways such as the Henkin (1952), Wenograd (1961), and ODTX (McGuire & Tarver 1981) tests. This application is briefly described in §4. Second, the IR spectra recorded simultaneously give the gas evolution sequence and relative product concentrations. These data provide insight into the decomposition mechanisms and show how the main reaction branches shift with temperature.

#### 4. High-temperature chemistry of HMX, RDX and BAMO

##### (a) HMX and RDX

Time-to-exotherm data at several temperatures for 200  $\mu\text{g}$  of HMX under 2.7 atm Ar are shown in figure 2. The slope yields the apparent activation energy,  $E$ .  $E$  is the barrier to total energy transfer rather than a particular molecular process. At lower temperatures  $E$  resembles the global decomposition  $E$  measured by DSC and TGA suggesting that the chemical processes dominate. At higher temperatures,  $E$  has a small value probably because a gas layer develops between the sample and the filament. Hence, diffusion terms as well as chemistry contribute to  $E$ . An attempt is underway to develop a heat-transfer-chemistry model for this region.

High-temperature chemistry that can be learned about explosives and propellants is the most powerful application of T-jump/FTIR spectroscopy. Insight is obtained from plots such as figure 1 determined at various temperatures. Before describing the chemistry, we note that no IR inactive products ( $\text{O}_2$ ,  $\text{N}_2$ ,  $\text{H}_2$ ) are shown.  $\text{H}_2\text{O}$  was not quantified because of its complicated rotation-vibration fine structure. The absolute absorbance of HNCO was estimated to be half-way between that of  $\text{CO}_2$  and  $\text{N}_2\text{O}$ . Absorbances from evaporated HMX are evident at less than 2.7 atm and for RDX at less than 4 atm. The product concentrations in figure 1 are choppy because of turbulence, incomplete mixing, and bubble bursting as the products are released. Smoothing the raw data (figure 3) is helpful. The product concentrations differ somewhat from non-isothermal high-rate decomposition (Oyumi & Brill 1985; Palopoli & Brill 1991), but the interpretations given before remain valid. The isothermal studies described here define the details more specifically over the temperature range of  $290\text{--}390\text{ }^{\circ}\text{C}$  for HMX and  $260\text{--}375\text{ }^{\circ}\text{C}$  for RDX.

*Phil. Trans. R. Soc. Lond. A* (1992)

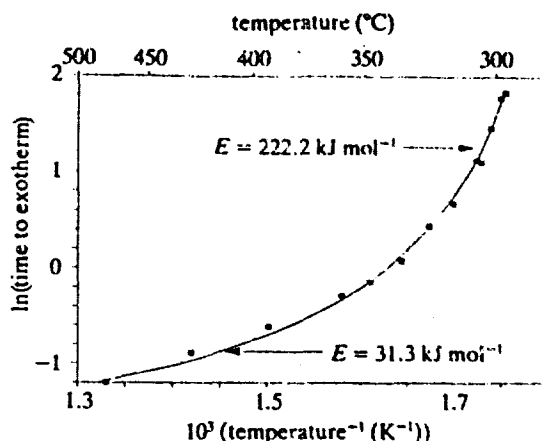


Figure 2. Time-to-exotherm for 200  $\mu\text{g}$  of HMX heated at  $2000\text{ }^{\circ}\text{C s}^{-1}$  under 2.7 atm Ar.

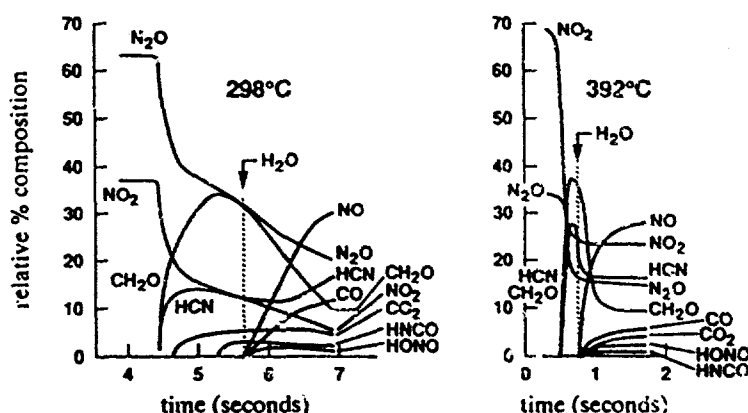
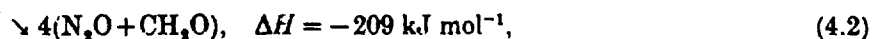
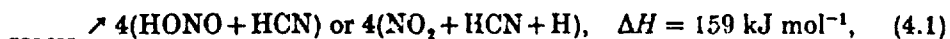


Figure 3. Smoothed gas product profiles for HMX at  $298\text{ }^{\circ}\text{C}$  (figure 1) and  $392\text{ }^{\circ}\text{C}$ .

Two global decomposition branches (4.1) and (4.2) occur for bulk RDX and HMX (Melius 1990).  $\Delta H$  for the products  $4(\text{HONO} + \text{HCN})$  rather than  $4(\text{NO}_2 + \text{HCN} + \text{H})$  is given for (4.1) because a residue rather than  $\text{H} + \text{HCN}$  forms when  $\text{NO}_2$  is released. In accordance with the sum of the  $\Delta H$  for (4.1) and (4.2), the control voltage trace in figure 1 shows only slight exothermicity



between 4 and 5.5 s where (4.1) and (4.2) dominate. Thus, these reactions release little energy in the condensed phase. The total IR absorbance of the products accelerates from 4 to 6 s despite the constant heat flow from the filament, which implies that autocatalysis occurs.

Reactions (4.1) and (4.2) imply that  $\text{N}_2\text{O}$  and  $\text{NO}_2$  should form simultaneously with  $\text{CH}_2\text{O}$  and  $\text{HCN}$ . This is not found at any temperature studied (e.g. figure 3). Rather,  $\text{N}_2\text{O}$  and  $\text{NO}_2$  appear before  $\text{CH}_2\text{O}$  and  $\text{HCN}$ , which form from the residue left by elimination of  $\text{N}_2\text{O}$  and  $\text{NO}_2$ . Behrens (1990) found that  $\text{N}_2\text{O}$  forms faster than

*Phil. Trans. R. Soc. Lond. A* (1992)

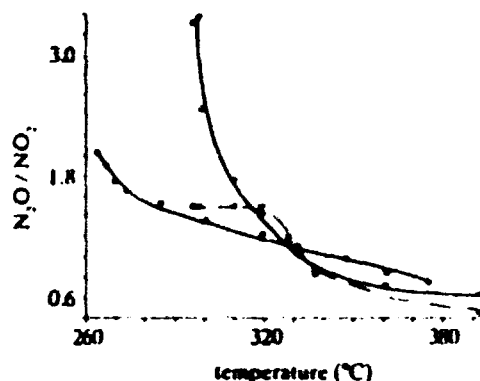


Figure 4. The temperature dependence of (4.1) and (4.2) reaction branches as measured by the  $N_2O/NO_2$  ratio for HMX ( $\square$ , initial,  $\blacksquare$ , final) and RDX (+).

$CH_2O$  in slow heating experiments on HMX. The residue of HMX decomposition includes products like hydroxymethylformamide (HMFA) and acetamide (Cosgrove & Owen 1974; Kimura & Kubota 1980; Karpowicz & Brill 1984; Behrens 1990). These products decompose leading to delayed release of  $CH_2O$ , HCN and  $HNCO$  by (4.3) and (4.4) (Behrens 1990; Palopoli & Brill 1991).



At 298 °C in figure 3, the concentrations of  $CH_2O$  and HCN in the 4.5–5.5 s range match those of  $N_2O$  and  $NO_2$  as dictated by (4.1) and (4.2).

In the vicinity of the runaway exotherm, the secondary reaction (4.5) occurs as evidenced by the fact that  $CH_2O$  and  $NO_2$  are consumed as  $NO$ ,  $CO$  and  $H_2O$  form.

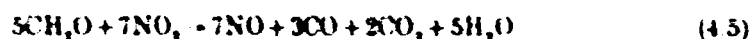


Figure 3 shows that more  $NO$  than  $CO$  forms in accordance with (4.5). Reaction (4.5) is highly exothermic with  $\Delta H = -1350 \text{ kJ mol}^{-1}$  and, by the large exotherm in figure 1, it is the main source of heat in the heterogeneous condensed phase. The time delay in the occurrence of (4.5) may stem from the fact that the residue and  $CH_2O$  are autocatalytic (Behrens 1990; Batten 1971). Hence, as the concentration of the residue grows, the rate of decomposition accelerates.  $HONO$  forms as  $CH_2O$  is consumed and  $H_2O$  appears suggesting that  $H$  atoms are especially free at this time in the reaction and combine with  $NO_2$  by adventitious contact (Brill & Oyumi 1986). These conclusions also apply at 392 °C (figure 3) except that the timescale is compressed. Hence, the above decomposition process of HMX and RDX describes the 300 °C range as well as the surface reaction zone (350–400 °C) during combustion. In accordance, Shackelford *et al.* (1989) found the same kinetic isotope effect with HMX for slow decomposition and combustion.

The main change in the chemistry of HMX and RDX at different temperatures is the branching ratio of (4.1) and (4.2). Figure 4 shows the final  $N_2O/NO_2$  concentration ratio for HMX and RDX and the initial  $N_2O/NO_2$  ratio for HMX against temperature. The initial  $N_2O/NO_2$  ratio is less accurate because of the low  $S/N$  ratio in the IR spectra. Clearly (4.1) is favoured at higher temperature, while (4.2) is favoured at lower temperature. At the surface temperature of burning HMX and RDX (350–400 °C), (4.1) and (4.2) are competitive. This finding is in line with

*Phil Trans R Soc Lond A* (1997)



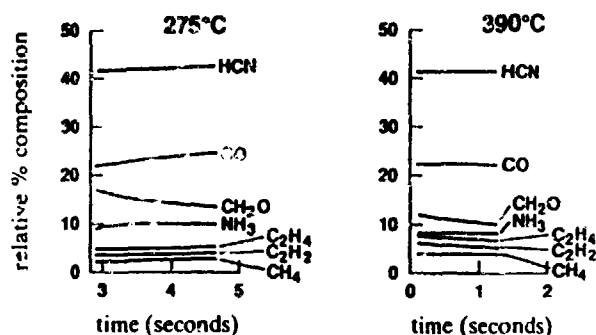
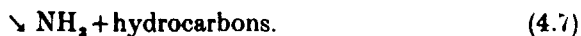
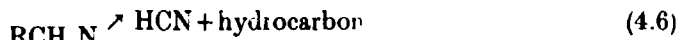


Figure 5. The gas products from BAMO at 275 °C and 390 °C showing the temperature independence of the decomposition products.

microprobe mass spectrum (MS) data of the gas ratios from burning HMX (Fetherolf *et al.* 1992). For combustion modelling the final steady state products shown in figure 3 are representative of the surface reactants for the first stage of the flame zone during combustion.

(b) BAMO

The large time and temperature dependence of the decomposition gases of HMX and RDX is not found for all energetic materials. The gas product concentrations for BAMO shown in figure 5 have little time or temperature dependence between 275 and 390 °C.  $N_2$  is released first by the azide group, but is not detected by IR spectroscopy. The products observed come from the residual nitrene,  $RCH_2N$ .  $RCH_2N$  has two decomposition branches based on the appearance of HCN (retention of C-N bond) and  $NH_3$  (cleavage of C-N bond). The high concentration of HCN indicates that (4.6) is favoured.



However, according to figure 5 the branching ratio and overall reactions are independent of temperature in the range studied.

## 5. The effect of pressure

The pressure dependence of the final gas product concentrations from isothermal decomposition of HMX at 300 °C and 360 °C was determined. Figure 6 gives the 360 °C data under 1–27 atm Ar. Similar studies under non-isothermal conditions are confirmed by figure 6 (Oyumi & Brill 1987). At 1 atm the most reactive gases ( $NO_2$ ,  $CH_2O$  and  $HONO$ ) have their highest residual concentration. At 2.7 atm,  $NO_2$  and  $HONO$  react to a greater extent with  $CH_2O$  yielding  $CO$  and  $NO$ . Under 6.7 atm these conversions are sufficiently complete that no  $NO$  is detected in the timescale of the experiment.  $N_2$  is the main nitrogen containing product. This pattern results from increased heterogeneous gas phase-condensed phase chemistry at higher pressure, because the diffusion of gas products away from the filament-sample zone is suppressed. The longer residence time in this high temperature zone advances the reaction scheme. Hence, the global nitrogen and carbon schemes of  $NO_2 \rightarrow NO \rightarrow N_2$  and  $CH_2O \rightarrow CO(CO_2)$  shift to the right at higher pressure. There is no evidence of a change in the decomposition mechanism in this pressure range.

*Phil Trans R Soc Lond A* (1992)

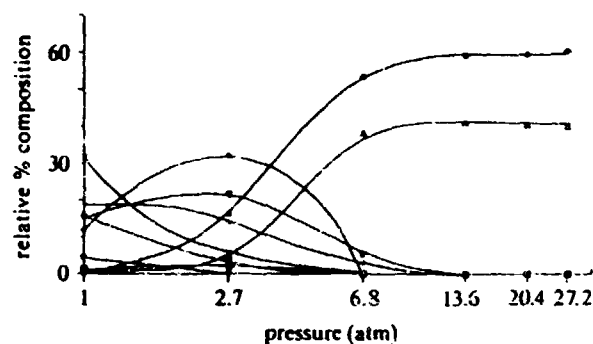


Figure 6. The dependence on the static Ar pressure of the final gas product concentrations from HMX heated at  $2000\text{ }^{\circ}\text{C s}^{-1}$  to  $360\text{ }^{\circ}\text{C}$ . See figure 1 for key to symbols.

We are grateful to the U.S. Air Force Office of Scientific Research, Aerospace Sciences for support of this work.

### References

- Batten, J. J. 1971 The thermal decomposition of RDX at temperatures below the melting point. *Aust. J. Chem.* **24**, 2025-2029.
- Behrens, R. Jr. 1990 Thermal decomposition of energetic materials. Temporal behaviors of the rates of formation of the gaseous pyrolysis products of HMX. *J. Phys. Chem.* **94**, 6706-6718.
- Brill, T. B. & Oyumi, Y. 1986 Thermal decomposition of energetic materials 17. A relationship of molecular composition to HONO formation. *J. phys. Chem.* **90**, 6848-6853.
- Brill, T. B., Brush, P. J., James, K. J., Shepherd, J. E. & Pfeiffer, K. J. 1992 *Appl. Spectrosc.* (In the press.)
- Brush, P. J. & Brill, T. B. 1989 Chemical phenomena associated with the initiation of thermal explosions. In *Proc. Ninth Symp. (Int.) on Detonation*, pp. 228-234. Office of Naval Research, U.S.A.
- Chen, J. K. & Brill, T. B. 1991a Thermal decomposition of energetic materials 50. Kinetics and mechanism of nitrate ester polymers at high heating rates by SMATCH/FTIR spectroscopy. *Combust. Flame* **85**, 479-488.
- Chen, J. K. & Brill, T. B. 1991b Thermal decomposition of energetic materials 54. Kinetics and near-surface products of AMMO, BAMO and GAP in simulated combustion. *Combust. Flame* **87**, 157-168.
- Chen, J. K. & Brill, T. B. 1991c Chemistry and kinetics of hydroxyl-terminated polybutadiene (HTPB) and diisocyanate-HTPB polymers during slow decomposition and combustion. *Combust. Flame* **87**, 217-232.
- Cosgrove, J. D. & Owen, A. J. 1974 The thermal decomposition of 1,3,5 trinitrohexahydro 1,3,5 triazine (RDX) - Part I. The products and physical parameters. *Combust. Flame* **22**, 13-18.
- Cronin, J. T. & Brill, T. B. 1987 Thermal decomposition of energetic materials 26. Simultaneous temperature measurements of the condensed phase and rapid-scan FTIR spectroscopy of the gas phase at high heating rates. *Appl. Spectrosc.* **41**, 1147-1151.
- Fetherolf, B. L., Liiva, P. M., Litzinger, T. A. & Kuo, K. K. 1992 Thermal and chemical structure of the preparation and reaction zones for RDX and RDX composite propellants. In *Proc. 28th JANNAF Combust. Meeting*. Chemical Propulsion Information Agency.
- Henkin, H. & McGill, R. 1952 Rates of explosive decomposition of explosives. *Ind. Eng. Chem.* **44**, 1391-1395.
- Karpowicz, R. J. & Brill, T. B. 1984 *in situ* characterization of the "melt" phase of RDX and HMX by rapid-scan FTIR spectroscopy. *Combust. Flame* **56**, 317-325.
- Kimura, J. & Kubota, N. 1980 Thermal decomposition process of HMX. *Prop. Explos.* **5**, 1-5.
- Melius, C. V. 1990 *Chemistry and physics of energetic materials* (ed. S. Bulusu), pp. 21-50. Dordrecht: Kluwer.

*Phil. Trans. R. Soc. Lond. A* (1992)

- McGuire, R. R. & Tarver, C. M. 1981 Chemical decomposition models for the thermal expansion of confined HMX, TATB, RDX and TNT explosives. In *Proc. Seventh Symp. (Int.) on Detonation*, pp. 56-64.
- Oyumi, Y. & Brill, T. B. 1985 Thermal decomposition of energetic materials 3. A high-rate, *in situ* FTIR study of the thermolysis of HMX and RDX with pressure and temperature as variables. *Combust. Flame* 62, 213-224.
- Oyumi, Y. & Brill, T. B. 1987 Thermal decomposition of energetic materials 22. The contrasting effects of pressure on the high-rate thermolysis of 34 energetic compounds. *Combust. Flame* 68, 209-216.
- Palopoli, S. F. & Brill, T. B. 1991 Thermal decomposition of energetic materials 52. On the foam zone and surface chemistry of rapidly decomposing HMX. *Combust. Flame* 87, 45-60.
- Shackelford, S. A., Goshgarian, B. B., Chapman, R. D., Askins, R. E., Flanigan, D. A. & Rogers, R. N. 1989 Deuterium isotope effects during HMX combustion: Chemical kinetic burn rate control mechanism verified. *Prop. Explos. Pyrotech.* 14, 93-102.
- Timken, M. D., Chen, J. K. & Brill, T. B. 1990 Thermal decomposition of energetic materials 37. SMATCH/FTIR spectroscopy. *Appl. Spectrosc.* 44, 701-706.
- Wenograd, J. 1961 The behaviour of explosives at very high temperatures. *Trans. Faraday Soc.* 57, 1612-1620.

### Discussion

P. GRAY (*Cambridge University, U.K.*). These novel techniques permit much greater assurance about probable pathways. I would like to suggest that although the  $\text{NO}_2$  and perhaps the  $\text{N}_2\text{O}$  are primary products, these atomic groupings being present in the reactants, the  $\text{CH}_2\text{O}$  and  $\text{HCN}$  follow them in time. The exothermic reaction between  $\text{CH}_2\text{O}$  and  $\text{NO}_2$  goes back many years, and I believe that it offers, via  $\text{HONO}$ , the main route to  $\text{NO}$ .

In the BAMO case the mono- and di-nitrenes are the plausible precursors and these species are not only notoriously reactive but may offer routes to reaction-chain branching (autocatalysis). Interestingly, that first step:



is not a source of great energy. The subsequent reactions of the nitrenes, however, will release much heat.

S. A. KINLOCH (*RMCS, Shrivenham, U.K.*). You stated that the first stage of the decomposition process in these experiments, in which production of  $\text{NO}_2$  and  $\text{N}_2\text{O}$  is witnessed, is thermally neutral because the two reaction pathways are thermodynamically opposite in character and approximately cancel each other. You later showed that the dominance ratio of the two reaction pathways could vary between approximately 0.6 and 3.5. Is the net endothermic or exothermic behaviour produced by this variation of sufficient magnitude to be reflected in the control voltage signal?

T. B. BRILL. The control voltage traces in the first stage are, indeed, somewhat more exothermic at lower temperature than at higher temperature. However, the differences are close to the limit of the sensitivity of the control voltage circuit.

# T-Jump/FT-IR Spectroscopy: A New Entry into the Rapid, Isothermal Pyrolysis Chemistry of Solids and Liquids

T. B. BRILL,\* P. J. BRUSH, K. J. JAMES, J. E. SHEPHERD, and K. J. PFEIFFER†

*Department of Chemistry, University of Delaware, Newark, Delaware 19716 (T.B.B., P.J.B., K.J.J.); Department of Mechanical Engineering, Rensselaer Polytechnic Institute, Troy, New York 12180-3590 (J.E.S.); and CDS Analytical, 7000 Limestone Road, Oxford, Pennsylvania 19363 (K.J.P.)*

The interface of a Pt filament pyrolysis control unit and a rapid-scan FT-IR spectrometer is described that enables the thermal decomposition of a thin film of material to be studied isothermally after heating at 2000°C/s. A model of the heat transfer of the Pt filament as a function of gas atmosphere and pressure is developed to help understand the instrument response. The control voltage of the Pt filament is highly sensitive to the thermochemistry of the thin film of sample. By simultaneously recording the control voltage and the rapid-scan IR spectra of the near-surface gas products, one learns considerable detail about chemical mechanisms relevant to combustion of a bulk material. The application of T-jump/FT-IR spectroscopy is illustrated with rapid thermolysis data for the energetic organoazide polymers azidomethyl-methyloxetane (AMMO), bis(azidomethyl)oxetane (BAMO), and glycidylazide polymer (GAP); the cyclic nitramine, octahydro-1,3,5,7-tetranitro-1,3,5,7-tetraazacine (HMX); and the nitroaromatic 1,3,5-triamino-2,4,6-trinitrobenzene (TATB).

Index Headings: FT-IR; Infrared; Thermal analysis; Analytical methods; Explosives; Combustion.

## INTRODUCTION

In recent years the development of fast thermolysis/FT-IR spectroscopy has enabled a material to be pyrolyzed at a heating rate exceeding 100°C/s, while the gas products are determined several millimeters above the surface in real-time by rapid-scan FT-IR spectroscopy.<sup>1</sup> Thermochemical events in the condensed phase are recorded simultaneously with the IR spectra. Much new information about rapid thermal decomposition mechanisms has been gained.

By the use of appropriately designed cells and circuitry,<sup>2-4</sup> fast thermolysis/FT-IR is the rapid-heating complement to conventional thermal analysis techniques, such as TGA and DSC. Of course, the quantitative aspects of DSC and TGA depend on maintaining quasi-equilibrium heat transfer that is difficult to achieve at a high heating rate. Hence, fast thermolysis/FT-IR is

not intended to be a quantitative analytical tool. It is, instead, intended to provide insight into chemical and physical processes where a high heating rate exists, as during ignition, combustion, or explosion of a bulk material. This chemistry cannot be extracted by slowly heating the material, because "cooking" frequently leads to side reactions and products that have little or no importance in the combustion scheme. The chemistry of combustion can only be learned from rapid heating diagnostics.

The recently developed fast thermolysis/FT-IR technique of Simultaneous Mass and Temperature Change (SMATCH)/FT-IR spectroscopy<sup>4</sup> has clearly established the connection between the microscale fast thermolysis approach and steady-state combustion of the bulk material.<sup>5-7</sup> However, a drawback of SMATCH/FT-IR and the other fast thermolysis techniques<sup>2-4</sup> is that the sample decomposes under nonisothermal conditions. Despite this complication, much information about chemical mechanisms has been gained, such as the relationship of the parent molecular structure to the decomposition gases,<sup>8</sup> the effect of pressure<sup>9</sup> and atmosphere<sup>10</sup> on the gas products, and a mechanism of burn-rate modification.<sup>11</sup> It would be especially advantageous to be able to heat the sample at a chosen high rate to a chosen constant temperature so that the decomposition process could be studied under essentially isothermal conditions. The technique of T-jump/FT-IR spectroscopy has been developed for this purpose and is described in this paper.

T-jump/FT-IR spectroscopy is the interface of a modified, commercial, filament pyrolysis control unit and an FT-IR spectrometer. The required control and triggering circuits are discussed. Although the chemical data obtained are not especially difficult to interpret, confidence about the origin of subtle differences caused by changes in the experimental conditions is heightened by the fact that the main characteristics of the technique are reproduced by a physical model of the Pt filament and the surrounding gas. It is found that T-jump/FT-IR provides sub-global thermochemical and reaction mechanism information during rapid thermal decomposition of bulk

Received 10 February 1992.

\* Author to whom correspondence should be sent.

† Present address: Tekmar Company, P.O. Box 429576, Cincinnati, OH 45224-9576.

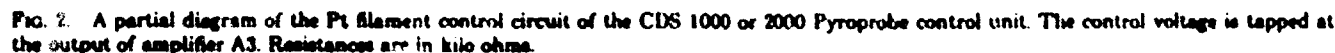


## OVERVIEW OF T-JUMP/FT-IR SPECTROSCOPY

Independent, highly responsive control of the heating rate ( $dT/dt \leq 20,000^\circ\text{C/s}$ ) and final filament temperature ( $T_f \leq 1200^\circ\text{C}$ ) of a Pt ribbon filament is provided by a CDS Analytical 1000 or 2000 Pyroprobe control unit. The circuit responds to the integrated resistance of the Pt filament. However, for a given value of the resistance, the temperature is nonuniform along the filament length

The control voltage that is applied to the filament to achieve the desired heating rate and to maintain  $T_f$  was digitized and recorded with an IBM PC. The filtering and amplification circuit is described along with considerations about the choice of  $dT/dt$  for T-jump/FTIR studies. If the sample exhibits an endotherm or exotherm while being held at  $T_f$ , the control voltage rapidly increases or decreases, accordingly, to maintain  $T_f$ . By recording the control voltage under the same conditions with and without sample present, and then subtracting the two traces, one obtains a difference voltage trace in which an endotherm and exotherm correspond to a positive and negative voltage deflection, respectively. These traces are illustrated in the next section.

The circuit is described for simultaneously triggering the FT-IR spectrometer and the filament control unit. When triggered together, the gas products detected by the IR spectrometer can be correlated with the endothermic and exothermic events of the sample. These gases are a historical record to the rapid decomposition reactions that occur in the condensed phase. A rapid-scan FT-IR spectrometer ( $\geq 5$  scans/s) is advantageous for characterizing vigorously reacting materials, such as explosives and propellants. Slower scan rates are acceptable for less vigorously decomposing materials. T-jump/FT-IR spectroscopy is found to provide sufficient control over the conditions to allow mechanistic detail to be obtained about the chemistry of the condensed phase during simulated combustion and explosion events.



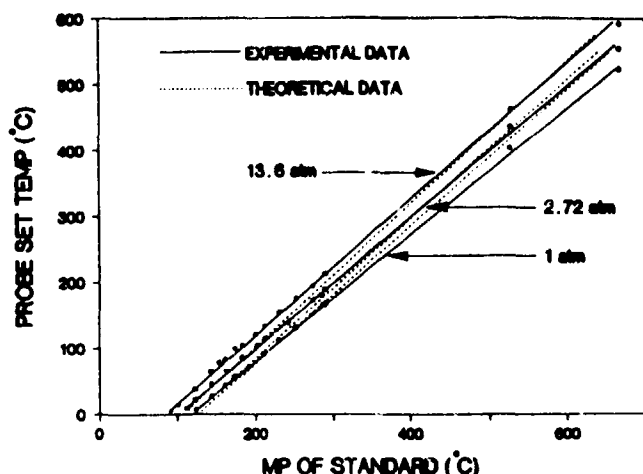


FIG. 3. The effect of Ar gas pressure in the cell on the probe set temperature as determined by visual observation of the melting points of standard samples. The dashed lines are calculated from the thermophysics model in this paper.

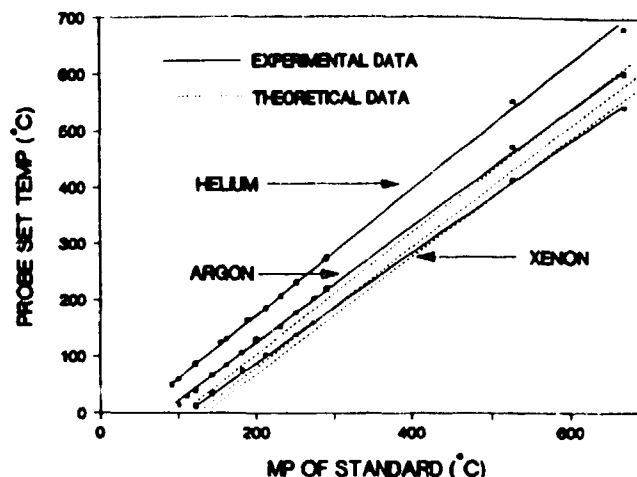


FIG. 4. The effect of the type of atmosphere at 1 atm in the cell on the probe set temperature as determined by visual observation of the melting points of standard samples. The dashed lines are calculated for each gas from the thermophysics model described in this paper.

## INSTRUMENT DETAILS

High-rate decomposition processes of bulk materials are chemically and physically complex. An understanding of the instrument design and physical details of T-jump/FT-IR spectroscopy is important in the interpretation of the information obtained.

**Temperature Control of the Platinum Filament.** A major requirement of the T-jump/FT-IR method is fast, sensitive registration of the heat flow to and from the sample. This was achieved by adapting the CDS Analytical 1000 or 2000 Pyroprobe control unit for this experiment. The control circuit for the Pt filament is shown in Fig. 2.

The desired temperature,  $T_f$ , is determined by the overall resistance of the Pt filament. The application of an electric current through the filament causes  $i^2R$  heating and subsequent resistivity changes. Control of this current provides fast and reasonably precise control of the filament resistance. The overall resistance of the filament is measured by passing the heating current through a fixed, temperature-stable resistance of  $0.1 \Omega$ , providing a voltage,  $V_R$ , that is proportional to the heating current, while simultaneously obtaining the voltage drop across the Pt filament,  $V_P$ . The two voltages are scaled in amplifiers A1 and A2, respectively, and then divided as  $V_P/V_R$  in an analog divider. An offset into the  $V_R$  input of the divider ensures that its output remains at 0.0 V when no current is being applied to the filament.

The divider output voltage is closely related to the overall resistance of the filament. This is compared to a voltage produced by a microprocessor through a digital-to-analog (DA) converter. The difference between these voltages, produced by amplifier A3, feeds a set of Darlington connected transistors providing the heating current through the filament. Due to the high gain of the amplifier A3, this output voltage is able to respond much faster ( $<0.1$  ms) than the characteristic time scale (50–100 ms) of the sample phase change or decomposition. Hence, the desired temperature ramp and  $T_f$  are easily maintained. The output voltage of A3 is that which is measured and termed the control voltage in this paper.

The chosen temperature ramp,  $dT/dt$ , is produced by setting the DA converter voltage to the appropriate voltages over the duration of the ramp.

To relate temperature of the Pt filament to its resistance, one derives the voltage produced by the microprocessor through the DA converter from a calibration curve stored in the processor memory. This curve is designed to produce a current through the Pt filament that yields the overall resistance that has been experimentally found to correspond to a particular filament temperature. This step includes accounting for the  $V_R$  offset, the need for some voltage difference across A3 in order to produce a heating current, and the fact that a temperature profile exists along the length of the Pt filament (see the later section, "Thermal Characteristics of the Platinum Filament") that stabilizes in several milliseconds, depending on the temperature ramp selected. The internal calibration curve is designed for a filament experiencing a 40 mL/min He gas flow at 350°C and 1 atm.

In practice, the T-jump/FT-IR method is likely to be used with atmospheres and pressures that are different from those described above to establish the internal calibration curve of the instrument. Therefore, the set temperature of the instrument and the actual temperature at the center of the Pt filament where the sample rests are not the same. A straightforward method for determining the actual temperature of the filament where the sample rests under various pressures and atmospheres is to compare the control unit set temperature to the melting temperature of Aldrich Chemical Co. standards. A mock IR pyrolysis cell, whose internal dimensions matched the real IR cell, was constructed for this calibration. The pressure and atmosphere in this cell are adjustable as desired. Melting of the sample was observed through a Kevlar window bolted onto a port cut through the top of the cell. Figure 3 shows the effect of the Ar pressure on the set temperature of the control unit that is required to melt a given standard compound. This type of calibration curve was used to relate the set temperature to the true temperature of the filament where the sample rests. Figure 4 shows the effect of different

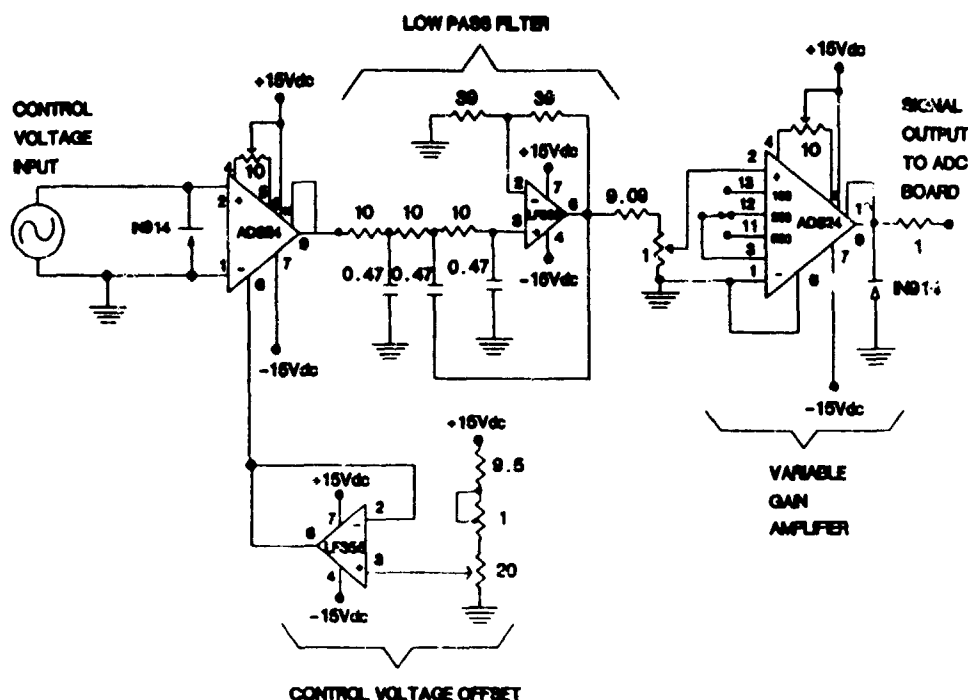


FIG. 5. The filter and amplifier circuit for processing the Pt filament control voltage. Resistances are in kilo ohms and capacitances are in microfarads.

noble gases at 1 atm on the control unit set temperature. The patterns in Figs. 3 and 4 can be understood by considering the mechanisms of heat transfer from the Pt filament to its surroundings. Such an analysis is described in the section on thermal characteristics of the platinum filament that appears later in this paper.

**The Control Voltage.** Extracting the control voltage that heats the filament and maintains the filament at constant resistance at  $T_f$  is a valuable part of gaining thermochemical insight into the rapid decomposition process. The control voltage (that is, the output of amplifier A3 in Fig. 2) is a 2.0–3.0 V signal. It was tapped and processed by the circuit shown in Fig. 5. With this circuit the signal was first reduced to 0.2–0.4 V by the signal offset stage and then low-pass filtered at 34 Hz. The output was then amplified  $31.25\times$  by a variable-gain amplifier and sent through one channel of a Metrabyte DAS-16 AD converter board for storage in the IBM PC.

Figure 6 shows the control voltage traces in the initial 0.4 s of heating at three rates to  $T_f = 375^\circ\text{C}$ . The circuit clearly controls the heat and hold steps responsibly at  $2000^\circ\text{C/s}$ , but for  $5000^\circ\text{C/s}$  and  $10,000^\circ\text{C/s}$  there are complicating factors in the Pt ribbon behavior until  $T_f$  is achieved. For this reason, a maximum heating rate of  $2000^\circ\text{C/s}$  was chosen so that the approach to  $T_f$  was smooth.

The control voltage responds rapidly to endothermic and exothermic events of the sample in order to maintain  $T_f$ . Figure 7 shows the control voltage trace with and without  $200\text{ }\mu\text{g}$  of a reacting sample thinly spread on the center of the filament. The decrease in the control voltage with time after  $T_f$  is reached in the initial 0.2 s results from the decreasing loss of heat to the gas surrounding the filament as the gas warms. The control voltage of the filament with sample present is higher (an endotherm) at 1–3 s because the sample melts, while at 10.5 s an

exotherm occurs. These events are more prominent when the sample trace is subtracted from the bare filament trace to produce a difference trace. The difference trace resembles a DSC thermogram, but neither the areas nor the slopes of the endotherm and exotherm quantitatively reflect the global reaction rate or enthalpy change, as in DSC,<sup>11</sup> because heat transfer between reacting sample and the filament is slow in comparison to the reaction rate.

**T-Jump/FT-IR Interface.** The IR cell employed in T-jump/FT-IR spectroscopy differs from previous designs<sup>12</sup> mainly in that the Pt filament is perpendicular

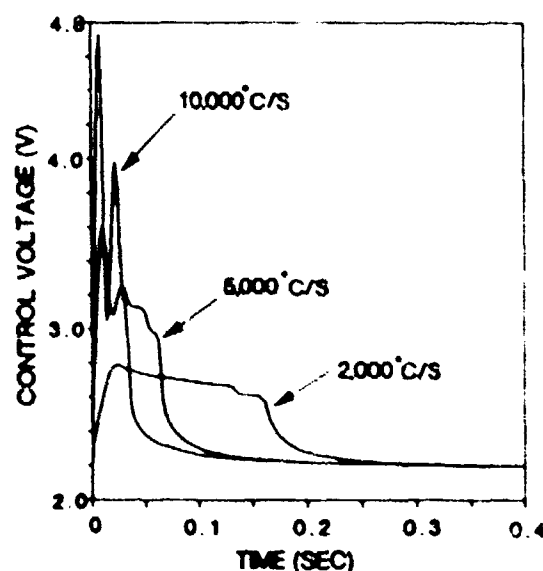


FIG. 6. The control voltage of the Pt filament heated to  $T_f = 375^\circ\text{C}$  at the three rates shown. The circuit is able to heat to this temperature without complicated behavior for heating rates  $\leq 2000^\circ\text{C/s}$ .

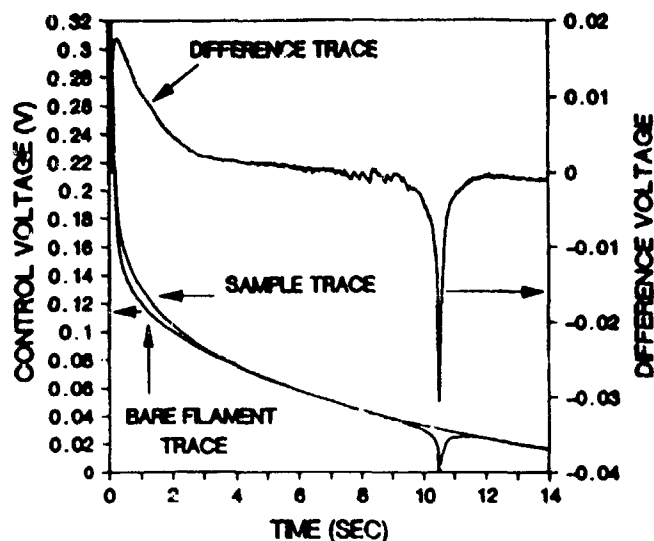


FIG. 7. The control voltage trace of the bare Pt filament and the filament with 200  $\mu$ g of a reacting sample thinly spread on the center. The difference trace (sample trace minus bare filament trace) clearly reveals an endotherm in the initial 3 s followed by bubbling disruptions in the 7–9 s range and final a strongly exothermic reaction at 10.5 s.

to the IR beam axis rather than parallel to it, as in the nichrome ribbon filament design.<sup>23</sup> The Pt filament forms the end of a removable Pyroprobe holder that is inserted and anchored to the cell wall by a Swagelok coupling. The cell can be purged and pressurized as desired in the 0.1–25 atm range. The sample compartment of a Nicolet 20SXB FT-IR spectrometer was expanded to accept the cell and probe handle.

Simultaneous measurement of the gas products of de-

composition and the thermal trace required synchronization of the start time of the Pyroprobe, control voltage acquisition, and IR spectra collection. Figure 8 is a schematic diagram of the circuit that senses the onset of data collection by the 20SXB and triggers the Pyroprobe. Because the 20SXB digitizer pulse rate changes frequency when data collection by the spectrometer begins, this circuit acts as a frequency discriminator. The circuit resets itself for low-frequency signals. If a high-frequency signal corresponding to data collection is detected, the circuit creates a 4–5 V pulse of about 1 s in duration. This pulse triggers a mechanical relay in the Pyroprobe. The 1-s dwell time eliminates electrical noise from the relay. At the end of this dwell time, the filament fires. A voltage marker from the trigger circuit and the control voltage from the filter-amplifier circuit (Fig. 5) are multiplexed to the DAS-16 AD board. The voltage marker identifies the interferogram that coincides with the onset of heating. The control voltage that coincides with the onset of heating. The control voltage is collected at the rate of 50 AD conversions/s by a Lotus Measure macro in the PC. Shielding of all circuits and connection cables reduced extraneous electrical interference.

The circuit in Fig. 8 is suitable for interferometers where a frequency change of the digitizer indicates data acquisition. For other interferometers (e.g., the Nicolet 60SX and 800), the height of the digitizer pulse changes during data acquisition. A different trigger circuit is required for these spectrometers.

#### THERMAL CHARACTERISTICS OF THE PLATINUM FILAMENT

The Pt ribbon filament serves as both the heat source and the sensor of the temperature and thermochemical

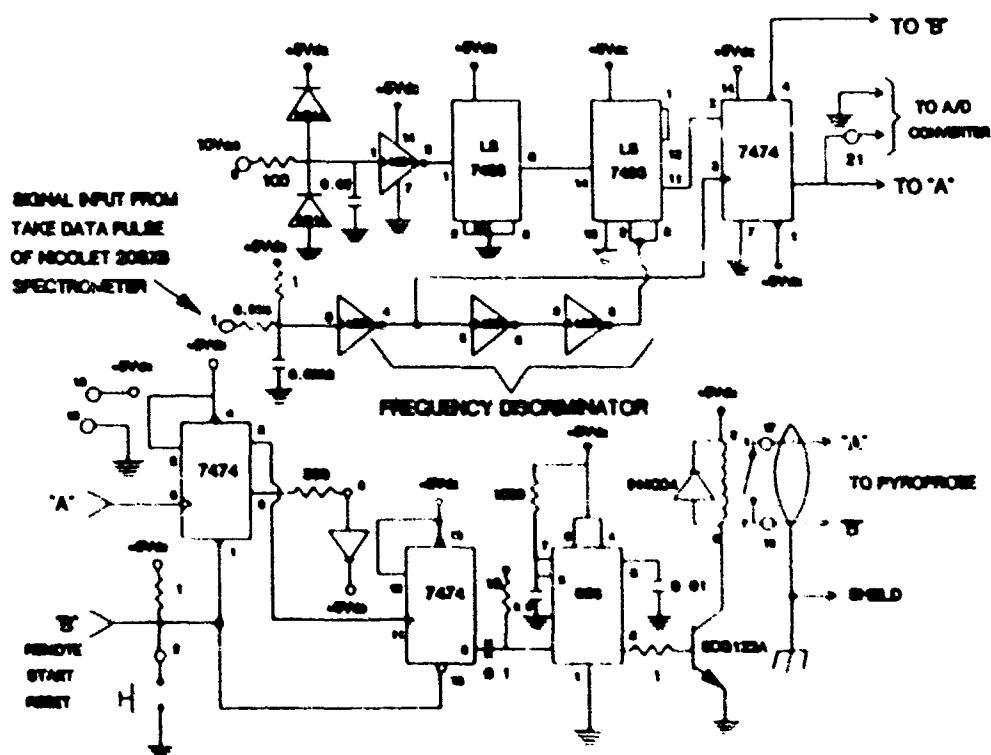


FIG. 8. The circuit that senses the onset of data collection by the Nicolet 20SXB interferometer and triggers the Pyroprobe. Resistances are in kilo ohms and capacitances are in microfarads.



changes of the sample. A heat transfer model described below helps clarify many of the observations about the instrument response during the development of T-jump/FT-IR spectroscopy.

**Thermal Analysis.** The steady-state calibration and the transient response of the Pt filament depend on the transfer of energy from the hot filament to the cold surroundings. Since the ends of the filament are cool, energy will be transferred by conduction from the center of the filament towards the end. This will produce a nonuniform temperature distribution, and the filament will be hotter in the center than at the ends. The temperature distribution depends on the competing effects of energy loss due to conduction, convection, and thermal radiation and energy addition due to Joule heating from the current passing through the filament.

Estimates of the order of magnitude of the energy loss mechanisms indicate that conduction, convection, and radiation must all be treated simultaneously. A reasonable model for the temperature distribution within the filament can be arrived at by assuming that only axial variations are present; that is, the filament is so thin ( $\leq 20 \mu\text{m}$ ) that the temperature at any cross section is uniform. Under this one-dimensional assumption, the transient energy balance for an axial element of the filament can be written as

$$A\rho c_p \frac{\partial T}{\partial t} = Ak_f \frac{\partial^2 T}{\partial x^2} - wh(T - T_g) - 2\epsilon\sigma(T^4 - T_g^4) + i^2 \frac{\rho_e}{A} + q_s \quad (1)$$

The symbols are:  $T$ , temperature of the filament at axial location  $x$  and time  $t$ ;  $A$ , cross-sectional area of the filament;  $\rho$ , mass density of the filament;  $c_p$ , specific heat of the filament;  $k_f$ , thermal conductivity of the filament;  $w$ , width of filament,  $h$ , natural convection coefficient;  $T_g$ , temperature of the gas and the cell;  $\epsilon$ , filament emissivity;  $\sigma$ , Stefan-Boltzmann constant ( $5.67 \times 10^{-8} \text{ W m}^{-2} \text{ K}^{-4}$ );  $i$ , current through the wire at time  $t$ ;  $\rho_e$ , electrical resistivity of the filament;  $q_s$ , thermal energy transferred from the sample into the filament. Nominal values of these parameters and others required subsequently are given in Table I for a representative platinum filament 38 mm long, 2 mm wide, and  $6.3 \mu\text{m}$  thick.

This energy equation applies along the length of the filament  $0 < x < L$ . At the ends  $x = 0$  and  $x = L$ , a supplementary boundary condition must be applied. For simplicity, we have chosen to fix the temperature of the ends as being equal to the ambient temperature of the cell.

$$T(x = L, t) = T(x = 0, t) = T_g \quad (2)$$

This is equivalent to assuming that the filament supports are massive and that their thermal resistance is very low. This simplifying assumption is probably one of the sources of error in the present analysis. However, in order to treat the end condition properly, a much more detailed model is required. The present model permits the thermal behavior of the Pt filament to be explored without excessive complexity.

The electrical resistivity is a function of temperature and for the purposes of the present study can be ap-

TABLE I. Parameter values used in filament thermal model.

$T_g$	Gas and cell temperature	298.15	K
$w$	Width of heater	2.0	mm
$\alpha$	Platinum temperature coefficient of resistivity	0.003927	K <sup>-1</sup>
$k_f$	Platinum thermal conductivity	73.0	W m <sup>-1</sup> K <sup>-1</sup>
$A$	Filament cross-sectional area	$6.3 \times 10^{-4}$	m <sup>2</sup>
$L$	Length of filament	38.0	mm
$\rho_e$	Reference resistivity of platinum	$1 \times 10^{-7}$	$\Omega \text{ m}$
$R$	External resistance of probe circuit	0.038	$\Omega$
$\epsilon$	Emissivity of filament	0.15	
$\alpha_f$	Thermal diffusivity of platinum	$2.58 \times 10^{-4}$	m <sup>2</sup> s <sup>-1</sup>
$\rho$	Mass density of platinum	$2.145 \times 10^4$	kg m <sup>-3</sup>
$c_p$	Specific heat of platinum	132.0	J kg <sup>-1</sup> K <sup>-1</sup>

proximated with a linear dependence, where  $\alpha$  is the temperature coefficient and  $T^0$  is the reference temperature (0°C) of Pt resistivity.

$$\rho_e = \rho_e^0(1 + \alpha(T - T^0)) \quad (3)$$

The natural convection coefficient  $h$  is a function of the temperature of the filament, the temperature and composition of the gas, and the width of the filament. In practice, the convection coefficient is computed from the Nusselt number  $Nu$  as

$$h = \frac{k_g/Nu}{w} \quad (4)$$

where  $k_g$  is the gas thermal conductivity. The Nusselt number is usually expressed in terms of the Rayleigh number as a correlation  $Nu(Ra)$ . For long, flat ribbons, a correlation<sup>13</sup> is

$$Nu = 0.16Ra^{0.25} + 0.58Ra^{0.2} \quad (5)$$

The Rayleigh number is defined as

$$Ra = \frac{g\beta(T - T_g)w^3}{\nu\alpha} \quad (6)$$

where  $g$  is acceleration of gravity ( $9.81 \text{ ms}^{-2}$ );  $\beta$  is the coefficient of thermal expansion,  $1/T$ , for an ideal gas;  $\nu$  is the gas kinematic viscosity,  $\nu = \mu/\rho$ , where  $\mu$  is the absolute viscosity; and  $\alpha$  is the gas thermal diffusivity,  $\alpha = k/\rho c_p$ , where  $k$  is the thermal conductivity. The properties  $\beta$ ,  $\nu$ , and  $\alpha$  of the gas are evaluated at sample temperature  $T_s = (T + T_g)/2$ . The Rayleigh number is a weak function of the filament temperature, but depends strongly on the gas pressure  $P$  and molar mass  $M$ . For a given temperature and filament width, the Rayleigh number will vary according to

$$Ra \sim P^2 W \quad (7)$$

For an argon atmosphere, the Rayleigh number is between 10 and 20 for typical filament operating conditions.

**Numerical Solution.** The energy balance equation (Eq 1) is solved numerically by the standard explicit finite difference method. The filament was divided into axial elements of length  $\Delta x$ , and time was divided into increments  $\Delta t$ . The temperature was defined at locations  $x_i$  and times  $t_n$  to be

$$T_{i,n} = T(x_i, t_n) \quad (8)$$

and the forward-time, centered-space approximation to the derivatives was used

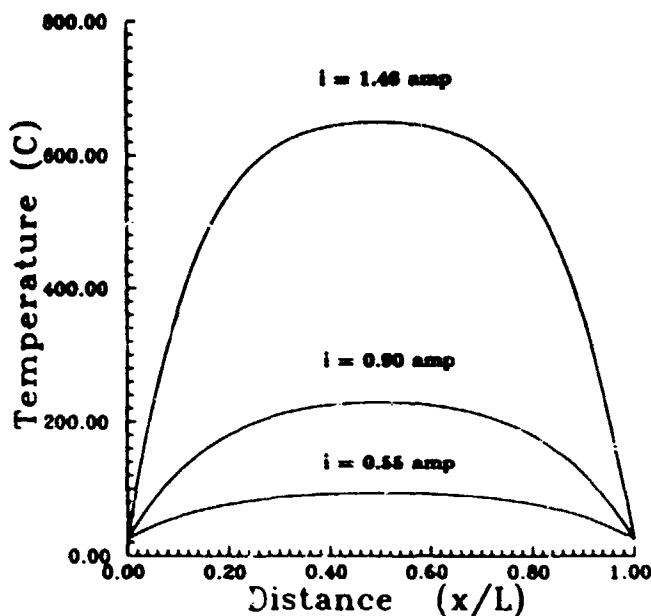


FIG. 9. The calculated temperature distribution along the Pt filament in an Ar atmosphere at 1 atm pressure. The results at three different currents are shown and reveal the large end effects at higher temperature.

$$\frac{\partial T}{\partial t} \approx \frac{T_{k+1}^n - T_k^n}{\Delta t} \quad (9)$$

and

$$\frac{\partial^2 T}{\partial x^2} \approx \frac{T_{k+1}^n + T_{k-1}^n - 2T_k^n}{(\Delta x)^2} \quad (10)$$

The usual stability restriction on the time step

$$\Delta t < \frac{\epsilon_f}{2(\Delta x)^2} \quad \epsilon_f = \frac{k_f}{\rho c_p} \quad (11)$$

results in a maximum time step size of 11 ms if the 38-mm-long filament is divided into 50 node points.

**Steady-State Solutions.** The energy balance equation can be integrated until a steady-state solution is reached for the case of no sample; i.e.,  $q_s = 0$ . This is relevant to the problem of calibrating the probe mentioned above. For a given current, the steady-state solution yields the temperature distribution along the filament. Steady state was determined by monitoring the temperature at several locations and determining when the time rate of change was less than 10 K/s.

Examples of three solutions for currents of 0.55, 0.90, and 1.46 amperes are shown in Fig. 9. These solutions are for an argon atmosphere at a pressure of 1 atm. For each case, the spatial average temperature  $\bar{T}$  of the filament is computed from the temperature distribution

$$\bar{T} = \frac{1}{L} \int_0^L T(x) dx \quad (12)$$

Since our assumed resistivity-temperature relation is linear, the total resistance  $R$  of the filament is the bulk resistance evaluated at the average temperature

$$R = R(\bar{T}) = \frac{\rho_0 L}{A} (1 + \alpha(\bar{T} - T_0)) \quad (13)$$

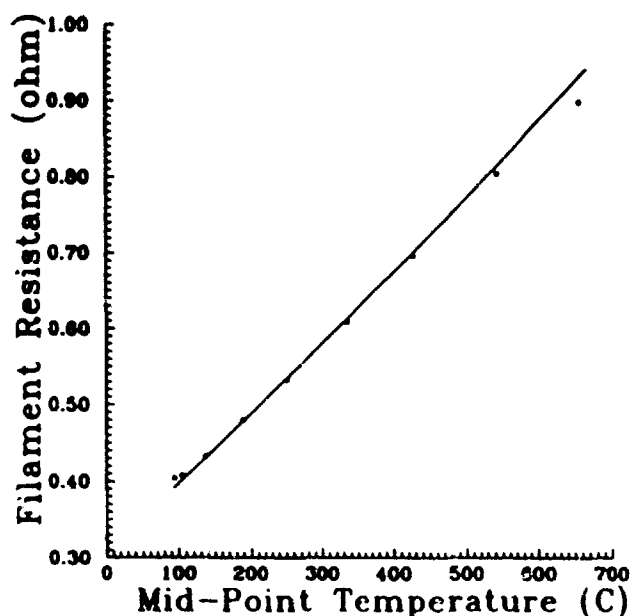


FIG. 10. Comparison of the computed and measured total filament resistance as a function of the midpoint temperature of the filament. An Ar atmosphere at 1 atm pressure was used.

As described in previous sections, the control circuit will maintain a constant value of  $R$  or equivalently  $\bar{T}$  after the initial heat up transient. The problem of calibration can now be seen to be the determination of the relationship of the average temperature  $\bar{T}$  of the filament (reflected by  $R$ ) to the temperature  $T_m$  where the sample rests at the axial midpoint of the filament  $x = L/2$ .  $T_m$  is, in effect,  $T_f$  by our melting point calibration method.

The numerical results of our model were compared against calibration experiments carried out for this purpose. Current, voltage, center temperature, and probe resistance were measured at 11 probe settings corresponding to temperature  $T_m$  between 95 and 845°C. The steady-state temperature distribution was then numerically computed for each of these cases. The comparison of  $R$  vs.  $T_m$  between the data (points) and calculation (line) is shown in Fig. 10. There are three parameters ( $R_0$ ,  $R_e$ , and  $\epsilon$ ) that have been varied in order to obtain this fit between data and analysis. The parameter  $R_0$  is the cold filament resistance, and  $R_e$  is the external resistance of the wiring and connections between the filament and the control circuit. If the cold probe resistance is  $R_p$ , then

$$R_p = R_0 + R_e \quad (14)$$

The value of  $R_p$  can be determined by extrapolating the data of Fig. 10 to  $T = T_0$ . For the example of Fig. 10,  $R_p = 0.33 \Omega$  and  $R_e = 0.03 \Omega$ . The value of  $R_0$  fixes the average cross-sectional area of the filament. The value of external resistance is determined *post facto* by examining the comparison between data and computation and choosing a value that minimizes the residuals. The value of  $\epsilon$  is found by trial and error and by examining the trends in  $\bar{R}$  as a function of  $T_m$ . Since thermal radiation is a significant source of losses at the higher temperature, numerical solutions will show appreciable departure from agreement with the data at higher temperature with incorrect values of  $\epsilon$ . A value of  $\epsilon = 0.15$

was found in this fashion. This value is reasonable given the surface condition of a typical filament.

Without any further adjustment of the model parameters, the effect of gas composition and pressure was examined. Steady-state solutions for atmospheres of helium and xenon were calculated, and the results are shown in Fig. 4. The calculated trends are the same as observed in the experiments. Note that the average temperature is proportional to the actual probe resistance, which is linearly proportional to the set point temperature. These results clearly show that it is the nonuniform temperature distribution and the effect of the convection heat transfer on this distribution that cause the calibration to change with the gas composition.

A simple explanation is possible for the results of Fig. 4. The convection losses are greatest with helium and lowest with xenon for a given average temperature. When the convection losses are larger, the temperature profile is flatter; i.e., the center temperature will be lower for a given average temperature. This is exactly what is shown by the data and the computations. The principal reason for this behavior is that the convection coefficient is directly proportional to the gas thermal conductivity and the gas thermal conductivity is inversely proportional to the square root of the molar mass,  $k_g \sim 1/\sqrt{W}$ . Convection losses are therefore greatest in helium and lowest in xenon. A secondary effect which slightly mitigates the thermal conductivity effect is the dependence of Rayleigh number on molar mass that was discussed above. The Rayleigh number is actually largest for xenon and smallest for helium. However, the dependence on the Rayleigh number is weak, and the thermal conductivity effect dominates.

The effect of increasing the initial pressure is to also increase the convection coefficient. The thermal conductivity of an ideal gas is independent of temperature so the effect is exclusively due to the dependence of Rayleigh number on pressure that was mentioned earlier. Steady-state solutions were computed for argon atmospheres of 1, 2.72, and 13.6 atm for comparison with the experimental data. The results are shown in Fig. 3. Note that the trends are qualitatively predicted by the model.

Careful comparison of the numerical model with experiment indicates that there are some problems with our choice of constants. With the choices used in the present paper, the dependence of the midpoint temperature on gas composition is not as strong as observed in the experiments. Apparently the emissivity of the filament is not as large as supposed and the convection losses are higher than the handbook values. With some adjustment of the parameters, the model may be more useful as a quantitative tool. A more careful treatment of the end effects may also be required.

**Transient Response.** The transient response of probe is important in understanding the control voltage change generated by sample phase change or decomposition, as shown in Fig. 7. The difference voltage in Fig. 7 is proportional to the perturbation  $\delta i$  to the filament current produced by the sample.

How is the perturbation  $\delta i$  related to the heat flux  $q$ , into the filament from the sample? In general, this problem requires investigating the solutions to the energy equation (Eq. 1) together with a model for the control

circuit for small perturbations about the steady-state solution. This leads to a linear partial differential equation for the temperature perturbation  $\delta T$ . However, the solution to this problem is simplified by the following circumstances:

- (1) The control system has a very high gain, so that the probe resistance can be taken as fixed during the sample decomposition.
- (2) Even though the temperature distribution of the filament is slightly altered by the sample, the power dissipation is essentially constant since the average temperature remains the same. This means that power changes in the filament are exclusively made to compensate for the energy added or removed by the sample, so that the net energy transfer rate, electrical and thermal, into the filament remains constant.

As a consequence, the power input change to the filament due to the sample energy flux  $Q$ , can be computed as

$$(i_0 + \delta i)^2 R + Q = i_0^2 R \quad Q = \int q \cdot dx \quad (15)$$

where  $i_0$  is the steady-state current and  $R$  is the (fixed) filament resistance. Expanding Eq. 15 for small perturbations in current  $\delta i \ll i_0$ , we obtain the approximate relation, Eq. 16:

$$\delta i = -\frac{Q}{2i_0 R} \quad (16)$$

Note that, as observed in Fig. 7, the current increases for endothermic processes  $Q < 0$  and decreases for exothermic processes. This very simple formula has also been obtained by carrying out the full transient thermal-electrical analysis and applying the simplifying approximations listed previously.

Although this result allows us to interpret the origin of the signal in Fig. 7, the relation of the  $Q$ , to the events within the sample is less straightforward. There is a thermal resistance between the sample and the filament so that the sample temperature is not necessarily equal to the filament temperature and is, in general, unknown. The sample is transferring energy to the surrounding gas as well as the filament. The sample can also evaporate and produce gaseous products, causing the mass to vary with time. This means that it is very difficult to use the observed control voltage variations in Fig. 7 to infer reaction rates or enthalpy changes. On the other hand, there is a wealth of new mechanistic information about combustion/explosion phenomena that can be extracted by combining the control voltage traces at various temperatures with the IR spectra of the near-surface gas products.

## T-JUMP/FT-IR DETERMINATION OF COMBUSTION-LIKE PYROLYSIS CHEMISTRY

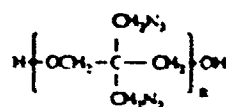
T-Jump/FT-IR spectroscopy was designed to elucidate some of the microscopic details of the rapid thermal decomposition mechanism of solids and liquids. For example, 200  $\mu\text{g}$  of sample thinly spread on the center of the Pt ribbon filament and rapidly heated is a microscale "snapshot" simulation of a burning surface. The tem-

TABLE II. Enthalpy of decomposition of the azidomethyl polymers measured by DSC.

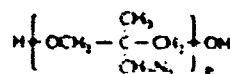
Polymer	$T_{\text{max}}(^{\circ}\text{C})$	$\Delta H$ (J/g)	% N
AMMO	233	-1550	33
GAP	221	-2080	42
BAMO	224	-2670	50

poral variation of the relative concentrations of the gas products combined with the control voltage data yields mechanistic detail about the chemistry of a burning surface. To provide additional variables, one can set the atmosphere and pressure in the cell as desired. An Ar atmosphere was employed in most of our studies. A positive pressure up to 30 atm minimized evaporation that was occasionally observed at 1 atm pressure. The gas products were quantified by a procedure that incorporates the absolute IR intensity values.<sup>14</sup>

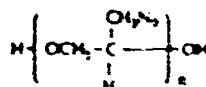
The three organoazide polymers AMMO, BAMO, and GAP, the cyclic nitramine HMX, and the nitroaromatic compound, TATB, illustrate a variety of behaviors of the T-jump/FT-IR technique as applied to determine the chemistry of fast pyrolysis. Table II gives the enthalpy of decomposition determined by DSC for AMMO, BAMO, and GAP.<sup>6</sup> The different  $\Delta H$  values for these compounds provide the opportunity to isolate the effect of the amount of heat released on the control voltage for an otherwise closely related set of compounds. HMX, an important explosive and propellant material, was chosen because it illustrates the large amount of chemical detail that can be extracted for certain compounds. TATB illustrates the behavior when a compound ignites and burns, starting at several sites in the sample.



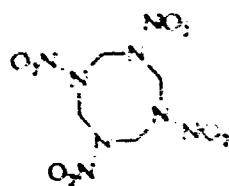
BAMO



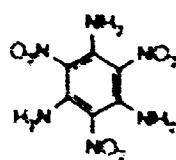
AMMO



GAP



HMX



TATB

In all cases except TATB, the times to exotherm as a function of  $T_j$  and the gas products are quite reproducible. However, as mentioned above in the section on tran-

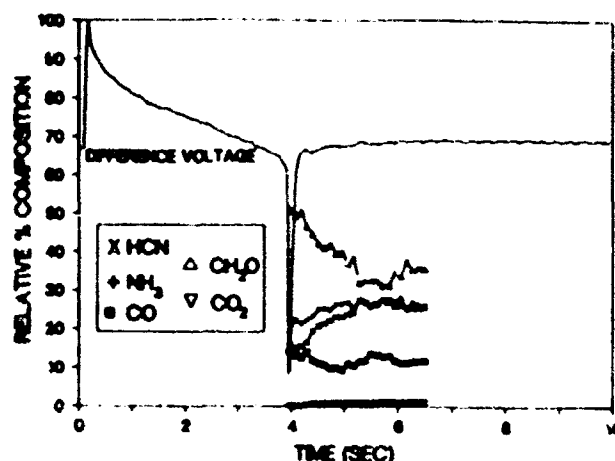
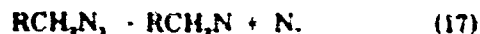


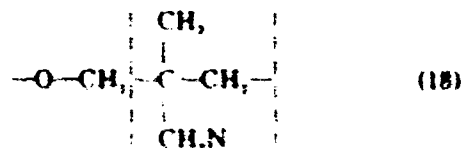
FIG. 11. T-jump/FT-IR data for 200  $\mu\text{g}$  of AMMO polymer heated at 2000 $^{\circ}\text{C}/2\text{ s}$  to  $T_j = 308^{\circ}\text{C}$  under 2.7 atm pressure of Ar.

sient response, the detailed rate of slope change and the total area of the exotherm are not sufficiently reproducible to be used to determine reaction rate or heat of reaction as a function of  $T_j$ .

AMMO, GAP, and BAMO. AMMO has the smallest  $\Delta H_{\text{decomp}}$  of the three azide polymers in Table II. The difference control voltage trace in Fig. 11 reveals an initial endotherm corresponding to energy consumed by liquefaction and the higher heat capacity when sample is present on the filament. Liquefaction of AMMO is sluggish, as indicated by the gradual decrease in the control voltage until about 4 s. At about 4 s, rapid exothermic decomposition is triggered by reaction 17, which releases  $\text{N}_2$  (IR inactive) and leaves the reactive nitrene. Products of the exothermic decomposition of the nitrene are detected at the exotherm.



Initially, more  $\text{CH}_2\text{O}$  is formed than other products. Not shown in the quantified products are absorbances resulting from the 2-methylallyl group [probably  $(\text{CH}_2\text{C}(\text{CH}_3)\text{CH}_2)_n\text{NH}_2^+$  which appear simultaneously with  $\text{CH}_2\text{O}$ . Bis(2-methylallyl)amine is a recombination product of the backbone fragment between the dashed lines in the polymer unit:



A certain percentage of the nitrene fragments (Fig. 18) also decompose to low molecular weight products. It is interesting to note that products of C-N bond retention ( $\text{HCN}$ ) and C-N bond fission ( $\text{NH}_3$ ) form from the nitrene in this process. The  $\text{HCN}/\text{NH}_3$  ratio (Fig. 12) increases from  $T_j = 288^{\circ}\text{C}$  to  $T_j = 377^{\circ}\text{C}$ , indicating that C-N bond retention is favored at higher temperature. This observation is consistent with the fact that fewer atom rearrangements are preferred at higher temperature (a faster reaction rate and greater importance of entropy). After the exotherm is complete, a milky solid residue remains on the filament and decomposes to  $\text{C}_7\text{H}_8$ ,  $\text{CH}_4$ ,  $\text{CO}$ ,  $\text{CO}_2$ , and  $\text{HCN}$  when heated above  $500^{\circ}\text{C}$ .

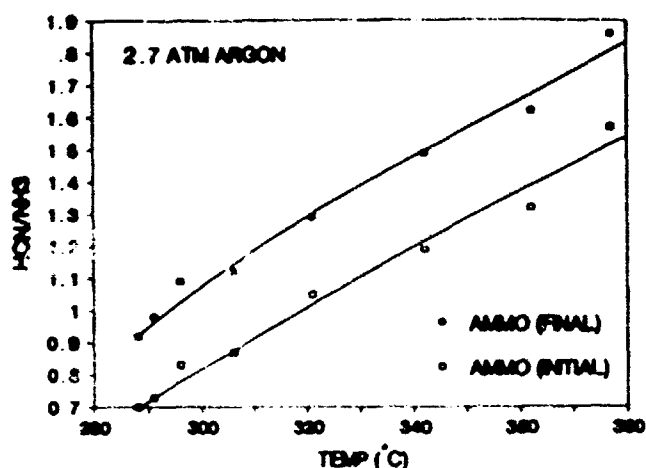


FIG. 12. The initially detected and final HCN/NH<sub>3</sub> concentration ratio from AMMO as a function of  $T$ , showing that the decomposition branching ratio of the nitrene product is temperature dependent.

GAP releases more heat upon decomposition than AMMO (Table II).<sup>6</sup> Figure 13 shows that the gas products that form at the exotherm are stable, low-molecular-weight molecules derived from the polymer backbone. Unlike the case for AMMO, no large molecules form upon fast thermolysis, probably because of the higher heat of decomposition. As with AMMO, the HCN/NH<sub>3</sub> ratio increases with temperature for  $T$ , in the 270–370°C range.

BAMO is the most energetic of the three azidomethyl polymers and illustrates a complication with the Pt filament method when applied to the most rapid exothermic reactions. Figure 14 shows that at about 2 s the polymer exothermically decomposes sharply, yielding products that are fragments of the backbone. However, the reaction is so violent that propulsion causes the Pt filament to distort. This motion produces an oscillation in the control voltage for about 1 s. In this case the control voltage excursions are partly from chemical changes and partly from physical changes and should not be mistaken as indicating a purely chemical event. The gas products are not affected by the filament distortion. The concentrations of the gas products are independent of  $T$ , in the 280–390°C range, probably because of the very high re-

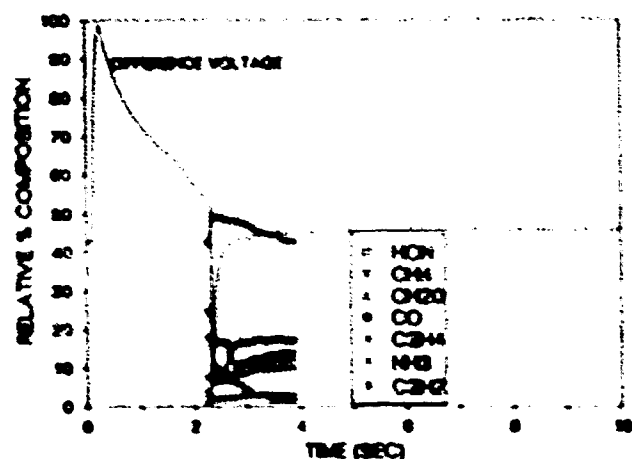


FIG. 13. T-jump/FT-IR data for 200  $\mu$ g of GAP polymer heated at 2000°C/s to  $T_f = 380^\circ\text{C}$  under 2.7 atm pressure of Ar.

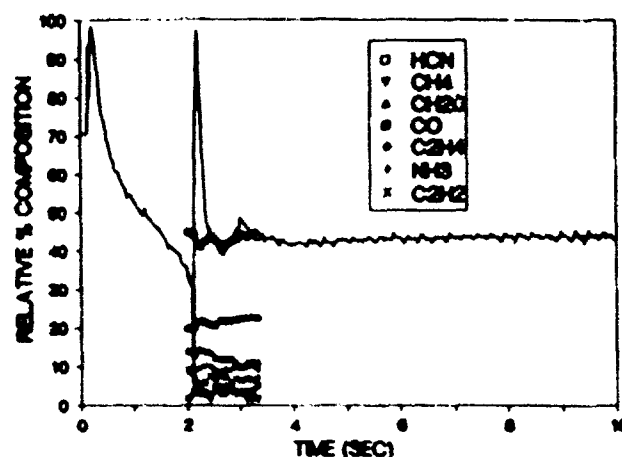


FIG. 14. T-jump/FT-IR data for 200  $\mu$ g of BAMO polymer heated at 2000°C/s to  $T_f = 290^\circ\text{C}$  under 2.7 atm pressure of Ar.

action rate. No residue or large molecule fragments are detected.<sup>15</sup>

The azidomethyl polymers demonstrate that major chemical differences are detected as the amount of heat released by a closely related series of compounds is changed. The only complication arises when the heat and gas release is so violent that the Pt filament is physically altered.

TATB. TATB is known to be an insensitive explosive with high thermal stability. Unlike the sharp exotherm found for each of the azide polymers, the control voltage trace for TATB in Fig. 15 reveals a broad exotherm having detailed structure that was different in each run. The time-to-exotherm value at a given  $T_f$  also changed by as much as several seconds from run to run. The origin of this unusual behavior was understood after visual observation of the sample on the filament. Under 10 atm pressure of Ar, TATB was observed to ignite at several spots, often at different times. Burning expanded out from these spots. The fact that the position of the ignition sites in the sample was random from run to run led to the erratic control voltage behavior observed. Hence, the control voltage traces for TATB, unlike the

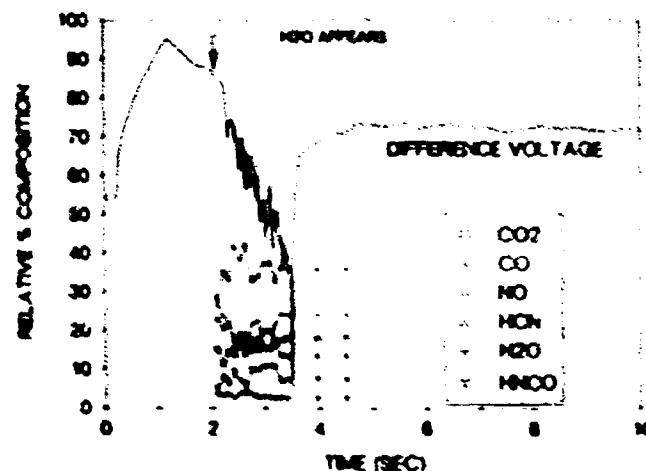


FIG. 15. The difference control voltage trace and gas products from 200  $\mu$ g of TATB T-jumped to  $T_f = 457^\circ\text{C}$  under 10 atm pressure of Ar. The position and appearance of the exotherm are highly nonreproducible for this compound.

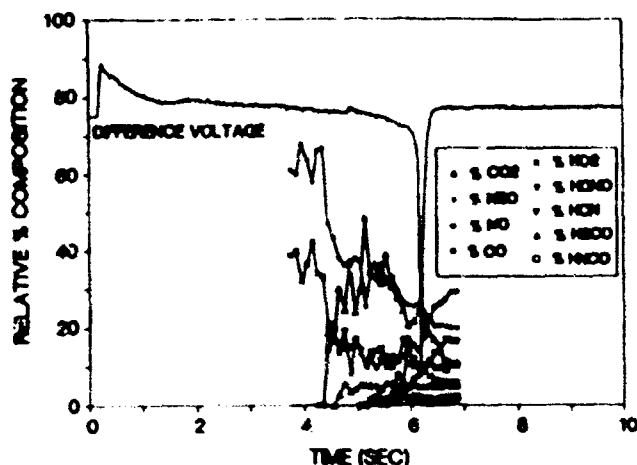
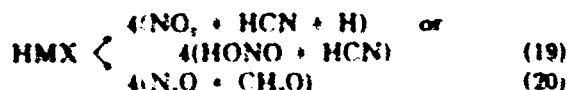


FIG. 16. T-jump/FT-IR data for 200 µg of HMX heated at 2000°C/s to  $T_j = 298^\circ\text{C}$  under 2.7 atm pressure of Ar.

other compounds mentioned in this paper, are highly nonreproducible.

A possible explanation for the multiple exotherms in the behavior of TATB is that furazan and furoxan compounds are found to form in thermally stressed samples.<sup>16</sup> These furazans and furoxans result from ring closure with elimination of  $\text{H}_2\text{O}$  and  $\text{H}_2$ . They are more sensitive and reactive than TATB itself, and their formation and ignition at various sites may be responsible for the multiple exotherms in the control voltage traces.

**HMX.** The power of T-jump/FT-IR spectroscopy for elucidating details of the decomposition mechanism is illustrated by the data for HMX (Fig. 16).<sup>17</sup> The sample melts in the initial 1.5 s. The control voltage is constant until about 4 s, when a small exothermic departure begins. Coinciding with this time,  $\text{NO}_2$  and  $\text{N}_2\text{O}$  are detected. At about 4.5 s the first traces of HCN and  $\text{CH}_2\text{O}$  are observed. A small amount of  $\text{CO}_2$  is also detected. The relative concentrations of these gases fluctuate somewhat because of bubble bursting in the molten HMX and mixing of the gases with the cool Ar atmosphere in the IR beam waist. Despite these fluctuations, the quantity of  $\text{CH}_2\text{O}$  and  $\text{N}_2\text{O}$  and the quantity of  $\text{NO}_2$  and HCN are approximately equal between 4.5 and 6 s. During this time, the control voltage reveals only slight exothermicity in the net reaction. The gas product data strongly indicate that two parallel decomposition reactions (19 and 20) occur during the pyrolysis of bulk HMX.



By measuring the  $\text{N}_2\text{O}/\text{NO}$  concentration ratio for samples at  $T_j$  in the 290–390°C range, one finds that reaction 19 is favored at high temperature, while reaction 20 is favored at low temperature.<sup>18</sup> However, the sequence of gas products in Fig. 15 reveals that  $\text{CH}_2\text{O}$  and HCN appear after  $\text{N}_2\text{O}$  and  $\text{NO}$ , and, therefore, do not come from the same reactions as implied by reactions 19 and 20. Instead,  $\text{N}_2\text{O}$  and  $\text{NO}$  evolve and leave a residue whose subsequent decomposition is the source of  $\text{CH}_2\text{O}$  and HCN. This residue is probably a mixture of amides.<sup>19</sup>  $\text{CH}_2\text{O}$ , HCN, and a third product from the residue,

HNCO, can be formed by thermolysis of amides.<sup>20</sup> Hence, reactions 19 and 20 involve multiple steps, but, from a practical point of view, the main events in the breakdown of bulk HMX are established. These are that (1) the gas product concentrations in Fig. 16 at 4.5–6.0 s match the stoichiometry dictated by nonelementary reactions 19 and 20, and (2) there is approximate thermoneutrality in the control voltage trace when reactions 19 and 20 dominate. Hess's law confirms that, for reaction 19,  $\Delta H = 159 \text{ kJ/mol}$  for the  $\text{HONO} + \text{HCN}$  products, while  $\Delta H$  for reaction 20 is  $-209 \text{ kJ/mol}$ . Taken together, the enthalpies of these two steps approximately cancel, providing little or no energy for the combustion or explosion of HMX.

The high-energy release from HMX comes in a later step beginning at about 6 s when  $T_j = 298^\circ\text{C}$ . At this time the control voltage trace shows that the reaction turns rapidly exothermic, and much  $\text{NO}_2$  and  $\text{CH}_2\text{O}$  are consumed, while  $\text{NO}$ ,  $\text{CO}$  and  $\text{H}_2\text{O}$  (not quantified) appear for the first time. The occurrence of reaction 21 is indicated by this result:



Note that the relative concentrations of  $\text{NO}$  and  $\text{CO}$  in Fig. 16 are correct for the stoichiometry of reaction 21 and, moreover,  $\Delta H = 1350 \text{ kJ/mol}$ . Hence, reaction 21 is the first large source of energy in the decomposition chain to drive the combustion and explosion process of bulk HMX. It comes after induction reactions 19 and 20 have built up sufficient  $\text{CH}_2\text{O}$  and  $\text{NO}_2$  for reaction 21 to take over as the dominant source of energy. Ignition or explosion takes place when reaction 21 occurs.

When HMX is T-jumped to  $T_j = 390^\circ\text{C}$ , which is approximately the temperature at the surface of bulk HMX burning at 1 atm, the mechanism described above remains valid.<sup>17</sup> However, the relative contribution of reactions 19 and 20 changes with temperature. As  $T_j$  increases, reaction 19 becomes increasingly important relative to reaction 20.<sup>18</sup>

## SUMMARY

The T-jump/FT-IR technique described herein was developed by interfacing a commercially available Pt filament control unit and a rapid-scan FT-IR spectrometer. The Pt filament was employed as both the heat source and the thermochemical sensor for the sample. However, it was found that the thermophysics of the Pt filament are strongly influenced by the surrounding atmosphere. Modeling of the heat transfer mechanisms revealed that convection heat loss differences produced this atmosphere and gas pressure dependence in the conditions employed. The true sample temperature was known only after calibration of the filament with melting point standards under each set of experimental conditions.

With the system and thermophysical model described in this paper, T-jump/FT-IR spectroscopy confidently provides new insight into the sub-global decomposition reaction mechanisms of bulk materials. Because the heating rate and temperature can be chosen to be high and are controlled, the surface reaction zone of a bulk material during combustion is experimentally simulated. This advance can be used profitably to understand the

behavior of bulk materials in practical combustion problems, such as in incineration, energy production, propulsion, and explosion.

#### ACKNOWLEDGMENTS

T.B.B. gratefully acknowledges the support of the Air Force Office of Scientific Research, Aerospace Sciences (AFOSR-87-0033 and AFOSR-89-0521), and the Air Force Armament Laboratory, Eglin AFB, FL (FO8635-90-C-0211), for support of this work. Charles Buzzard designed the circuits shown in Figs. 5 and 8.

1. T. B. Brill, *Anal. Chem.* **61**, 897A (1989).
2. Y. Oyumi and T. B. Brill, *Combust. Flame* **62**, 213 (1985).
3. J. T. Cronin and T. B. Brill, *Appl. Spectrosc.* **41**, 1147 (1987).
4. M. D. Timken, J. K. Chen, and T. B. Brill, *Appl. Spectrosc.* **44**, 701 (1990).
5. J. K. Chen and T. B. Brill, *Combust. Flame* **85**, 479 (1991).
6. J. K. Chen and T. B. Brill, *Combust. Flame* **87**, 157 (1991).
7. J. K. Chen and T. B. Brill, *Combust. Flame* **87**, 217 (1991).
8. T. B. Brill, in *Chemistry and Physics of Energetic Materials*, S. Bulusu, Ed. (Kluwer Publishing Co., Boston, 1990), p. 255.
9. Y. Oyumi and T. B. Brill, *Combust. Flame* **68**, 209 (1987).
10. S. F. Palopoli and T. B. Brill, *Combust. Flame* **87**, 45 (1991).
11. C. E. Stoner, Jr., and T. B. Brill, *Combust. Flame* **83**, 302 (1991).
12. W. W. Wendlandt, *Thermal Analysis* (John Wiley and Sons, New York, 1985), 3rd ed.
13. F. Kreith and M. S. Bohn, *Principles of Heat Transfer* (Harper and Row, New York, 1986), 4th ed., p. 276.
14. T. B. Brill, *Prog. Energy Comb. Sci.* **18**, 91 (1992).
15. T. B. Brill and P. J. Brush, *Phil. Trans. R. Soc. Lond. A*, in press.
16. J. Sharma and B. C. Beard, in *Chemistry and Physics of Energetic Materials*, S. Bulusu, Ed. (Kluwer Publishing Co., Boston, 1990), p. 587.
17. A. P. Snyder, J. H. Kremer, S. A. Liebman, M. A. Schroeder, and R. A. Fifer, *Org. Mass Spectrom.* **24**, 15 (1989).

# Thermal Decomposition of Energetic Materials 56. On the Fast Thermolysis Mechanism of Ammonium Nitrate and its Mixtures with Magnesium and Carbon

Dilip G. Patil, Sampat R. Jain<sup>(\*)</sup>, and Thomas B. Brill<sup>(\*\*)</sup>

University of Delaware, Department of Chemistry, Newark, DE 19716 (USA)

**Thermische Zersetzung von energiereichen Verbindungen 56. Der Mechanismus der schnellen Thermolyse bei Ammoniumnitrat und seinen Mischungen mit Magnesium und Kohlenstoff**

Untersuchungen über die schnelle Thermolyse von Ammoniumnitrat (AN) und seinen Mischungen mit Magnesium und Aktivkohle sind durchgeführt worden mittels Fourier-Transform-Infrarotspektroskopie/Temperaturprofil-Technik. Bei schnellem Erhitzen (ca. 80 °C/s) sublimiert/zersetzt sich AN bei etwa 300 °C. Die Sublimation dominiert bei Raumtemperatur. Die IR-aktiven Zersetzungsprodukte sind:  $\text{NH}_3$ ,  $\text{NO}_2$ ,  $\text{N}_2\text{O}$  und  $\text{H}_2\text{O}$ . Reaktionsmechanismen für die Zersetzungsprodukte werden vorgeschlagen einschließlich Protonenwanderung, die zu  $\text{NH}_3$ - und  $\text{HNO}_3$ -Bildung führt mit nachfolgender Oxidation von  $\text{NH}_3$  durch die Zersetzungsprodukte der  $\text{HNO}_3$ . Die Zersetzung von AN wird beträchtlich verstärkt, wenn AN mit Magnesiumpulver oder Holzkohle gemischt wird und tritt unterhalb 135 °C ein. Während  $\text{NH}_3$  das Hauptprodukt der Zersetzung von AN/Mg-Mischungen ist, wird bei AN/C-Mischungen kein  $\text{NH}_3$  beobachtet. Die Ergebnisse werden erklärt durch die Reaktion von  $\text{HNO}_3$  und  $\text{NH}_3$  mit Mg oder C.

**Décomposition thermique de composés énergétiques 56. Le mécanisme de la thermolyse rapide pour le nitrate d'ammonium et ses mélanges avec le magnésium et le carbone**

Des études sur la thermolyse rapide du nitrate d'ammonium et ses mélanges avec le magnésium et le charbon actif ont été réalisées au moyen de la spectroscopie infrarouge à transformation de Fourier et de la technique des profils de température. Lors d'un chauffage rapide (env. 80 °C/s), AN est sublimé/décomposé à environ 300 °C. La sublimation domine à pression ambiante. Les produits de décomposition actifs dans l'infrarouge sont  $\text{NH}_3$ ,  $\text{NO}_2$ ,  $\text{N}_2\text{O}$  et  $\text{H}_2\text{O}$ . On propose des mécanismes de réaction pour les produits de décomposition, impliquant un transfert de protons qui conduit à la formation de  $\text{NH}_3$  et  $\text{HNO}_3$  avec oxydation consécutive de  $\text{NH}_3$  par les produits de décomposition de  $\text{HNO}_3$ . La décomposition de AN est amplifiée considérablement lorsque AN est mélangé à de la poudre de magnésium ou du charbon de bois et elle se produit à des températures inférieures à 135 °C. Alors que  $\text{NH}_3$  est le produit principal de la décomposition de mélanges AN/Mg, on n'observe aucune trace de  $\text{NH}_3$  dans les mélanges AN/C. Ces résultats s'expliquent par les réactions de  $\text{HNO}_3$  et  $\text{NH}_3$  avec Mg ou C.

## Summary

Fast thermolysis studies of ammonium nitrate (AN) and its mixtures with magnesium and activated charcoal have been carried out by the Fourier transform infrared spectroscopy/temperature profiling technique. When subjected to rapid heating (ca. 80°C/s), AN sublimates/decomposes around 300°C. Sublimation dominates at ambient pressures. The IR-active products of decomposition are  $\text{NH}_3$ ,  $\text{NO}_2$ ,  $\text{N}_2\text{O}$  and  $\text{H}_2\text{O}$ . Reaction schemes accounting for the products are proposed which involve proton transfer leading to  $\text{NH}_3$  and  $\text{HNO}_3$  and the subsequent oxidation of  $\text{NH}_3$  by the decomposition products of  $\text{HNO}_3$ . The decomposition of AN is significantly enhanced when AN is mixed with magnesium powder or charcoal, and occurs at as low a temperature as 135°C. Whereas  $\text{NH}_3$  is the major product of decomposition of AN-Mg mixtures, no  $\text{NH}_3$  is observed from AN-C mixtures. The results are explained by the reactions of  $\text{HNO}_3$  and  $\text{NH}_3$  with Mg or C.

## 1. Introduction

Ammonium nitrate (AN) has been the main oxidizer in many compositions of propellants and explosives. Although it gives virtually smokeless products of combustion, its use in solid propellants has been limited because of its awkward phase transition involving a volume change around the room temperature, its low energy content, and its poor igni-

tability. With the availability of modified-phase transition AN in recent years, the phase transition problem is less of an issue. The addition of reactive metal fuels improves the burn rate and ignitability.

Owing to its availability and application as an explosive, the thermal decomposition of AN has been studied widely. It is generally agreed that thermal decomposition is initiated by proton transfer<sup>(1)</sup>. Further aspects have been more difficult to explain. In fact, Fedoroff<sup>(2)</sup> lists ten modes of decomposition of AN. Nitranide intermediates have been advocated more recently<sup>(3,4)</sup>. The many possible mechanisms arise because the thermolysis of AN greatly depends on the experimental conditions, including the pressure, temperature, sample size, state of confinement, rate of heating, time lapse in monitoring the gaseous products, and small amounts of impurities or additives. The dependence on these factors is so severe that an endotherm can be converted to an exotherm simply by changing the state of confinement, sample size or pressure. For combustion applications, conditions of high heating rate and elevated pressure are required for the most useful conclusions to be drawn.

Of late, highly metallized, fuel-rich compositions have found application in ramjet propulsion systems. While

<sup>(\*)</sup> Permanent address: Department of Aerospace Engineering, Indian Institute of Science, Bangalore - 560012, India

<sup>(\*\*)</sup> Correspondence author



examining the thermal ignition characteristics<sup>(5)</sup> and combustion<sup>(6)</sup> of fuel-rich AN-based systems, it was found that the behavior of AN is drastically modified by the presence of high loadings of magnesium powder<sup>(5,6)</sup> and also activated charcoal<sup>(5)</sup>. The process was sensitized to such an extent that the decomposition occurred at 135°C, i.e., even below the melting point of pure AN. While these results suggest enhancement of the ignitability of the AN compositions, the actual mechanism of the process is not known.

Rapid-scan FT-IR spectroscopy combined with fast thermolysis methods<sup>(7,8)</sup> enables the gaseous products to be monitored in near real time as they are formed. In the study described here the samples were decomposed at a controlled heating rate of about 80°C/s so as to resemble the rate of heating of the condensed phase at the onset of ignition. The rapid thermolysis data have been supplemented with the usual DSC and TG data in some cases. The additional insight from this work helps specify some of the features of the fast decomposition mechanism of AN and the effect of Mg and C on the process.

## 2. Experimental

The details of the rapid-scan FT-IR/temperature profiling technique, spectral procedures and methods of quantitation are reported elsewhere<sup>(7,8)</sup>. In the present case, the thermolysis was carried out by heating a thinly spread sample (1-2 mg) on a nichrome filament in an atmospheric pressure of Ar, employing an heating rate of 80°C/s and then holding the temperature at 450°C. This temperature was chosen since magnesium and its compositions react with the filament at high (600°C) temperatures. The FT-IR spectra were recorded at a scan rate of 10 scans/s and two spectra per file. The relative amounts of each detected species were obtained from the IR intensities. In doing so, however, the relative percentage of the AN aerosol, H<sub>2</sub>O, and IR inactive species could not be taken into account. The DSC and the TG runs were obtained on a Dupont Instruments 910 system at 10°C/min in open Al cups in an Ar atmosphere, unless otherwise stated.

Certified ACS grade ammonium nitrate having no organic coating was supplied by M/S Fisher Scientific Co. Other materials, magnesium powder (50 mesh, 99+ % purity), activated carbon and Mg(NO<sub>3</sub>)<sub>2</sub> · 6 H<sub>2</sub>O were obtained from the Aldrich Chemical Co. Various compositions by weight of AN were made keeping the amount of magnesium or carbon constant and varying the amount of AN. Fine powders of each were mixed by shaking them in a vial.

## 3. Results and Discussion

### 3.1 Pure AN

A typical thermal trace of pure AN given in Fig. 1 shows an endotherm at about 170°C due to the melting of AN, and another endotherm around 280°C. These observations are consistent with the DSC thermogram, wherein besides these endotherms, solid-solid phase-transition endotherms are

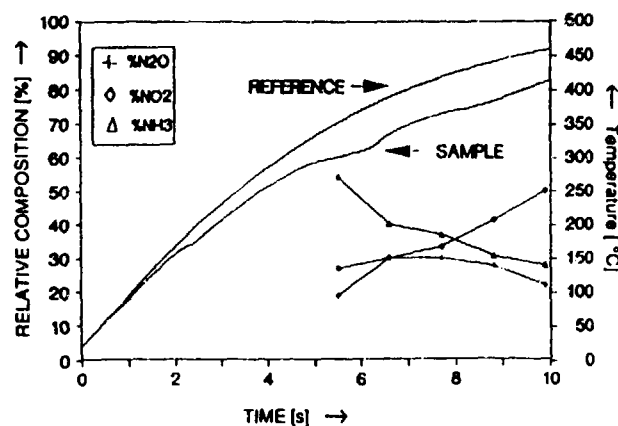


Figure 1. The relative percent composition of quantified gas products measured 2 mm above the surface when AN is heated at 80°C/s under 15 psi Ar. AN(aerosol), H<sub>2</sub>O and IR-inactive products are not quantified. Superposed is the temperature profile of the condensed phase (sample) and the reference filament temperature. The results are somewhat different from those reported in reference 9, largely because a lower heating rate is employed in this paper.

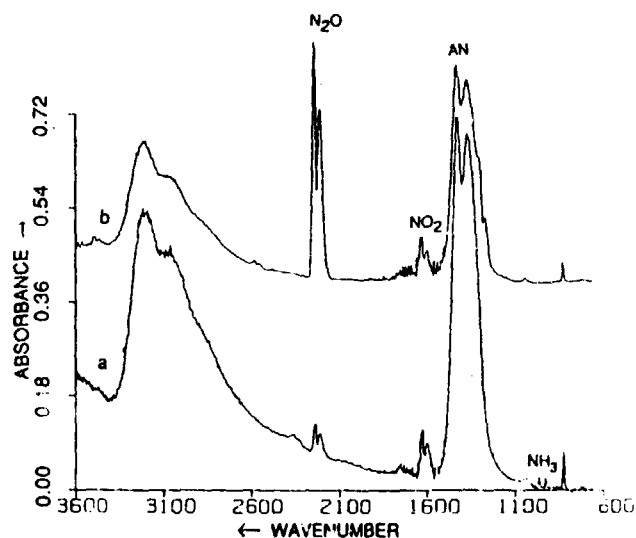
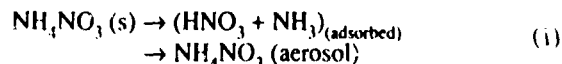


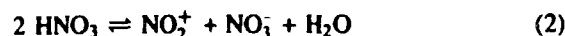
Figure 2. Rapid-scan FT-IR spectra of the products of decomposition of AN in the gas phase after 10 s at (a) 15 psi, (b) 280 psi of Ar. An increase in the N<sub>2</sub>O concentration is indicative of the extensive decomposition of AN at higher pressure.

also observed below 170°C. The endotherm at 280°C could be associated with the predominance of the evaporation process in the decomposition/dissociation<sup>(9)</sup> of AN, reaction (1).

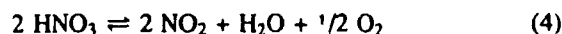


The detectable amounts of gas products, which appear in the IR spectrum after about 5 seconds (300°C), mainly consist of AN aerosol, NO<sub>2</sub>, N<sub>2</sub>O, NH<sub>3</sub>, and H<sub>2</sub>O (Fig. 2). A small amount of NO also appears soon after. Although the amount of AN aerosol cannot be quantitated, the absorbance values indicate that a significant amount of evaporation has taken place. The presence of N<sub>2</sub>O and H<sub>2</sub>O which are well established decomposition products<sup>(1,4)</sup> of AN, shows that both the dissociation (which leads to evaporation) and decomposition of AN occur simultaneously.

Most mechanisms proposed for the AN decomposition assume the subsequent oxidation of  $\text{NH}_3$  by the dissociation products of  $\text{HNO}_3$ . For example, Rosser, et al.<sup>(1)</sup> assumed the equilibrium reaction (2) for  $\text{HNO}_3$  that leads to the actual oxidizing species  $\text{NO}_2^+$  [reaction (3)].

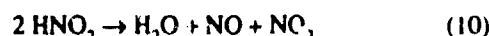


Essentially, the same species was assumed to be responsible, at least during low temperature decomposition, for the oxidation of  $\text{NH}_3$  by Koper, et al.<sup>(3)</sup> and Brower, et al.<sup>(4)</sup>. The dissociation equilibrium of 100 %  $\text{HNO}_3$  by reaction (2) is well known and occurs in the liquid state. Reaction (3) is based on the observation that  $\text{N}_2\text{O}$  and  $\text{H}_2\text{O}$  are the main products of decomposition. Brower, et al.<sup>(4)</sup> found no  $\text{NO}_2$  when AN was decomposed in a sealed capillary tube and the products examined subsequently. However,  $\text{NO}_2$  is known to form in other modes of decomposition<sup>(2)</sup>. *In situ* decomposition and immediate analysis of the products by FTIR spectroscopy<sup>(9)</sup> clearly reveals that  $\text{NO}_2$  forms besides  $\text{N}_2\text{O}$  and  $\text{H}_2\text{O}$ . It is, therefore, imperative that any decomposition scheme proposed should account for the formation of  $\text{NO}_2$ . Furthermore, in the decomposition of AN,  $\text{HNO}_3$  is produced only at high temperatures where it is likely to decompose quickly because the equilibrium constant for the decomposition of 100 %  $\text{HNO}_3$  by reaction (4) is  $8.5 \times 10^2$  at  $223^\circ\text{C}$ <sup>(10)</sup>.

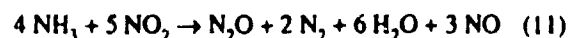


Therefore, in accounting for the decomposition products the oxidation of  $\text{NH}_3$  by  $\text{NO}_2$  and  $\text{O}_2$  near the surface needs to be considered. The present study examines this aspect. Such a reaction would obviate the need to include the formation of nitramide ( $\text{NH}_2\text{NO}_2$ ) by radical recombination at temperatures<sup>(7)</sup> above  $290^\circ\text{C}$  or by dehydration<sup>(11)</sup>.  $\text{NH}_2\text{NO}_2$  is described as an extremely unstable substance and is known to decompose rapidly<sup>(12)</sup> above  $70^\circ\text{C}$ . Alternately, we propose that the decomposition products of  $\text{HNO}_3$  (reaction 4) react with  $\text{NH}_3$  in the near surface giving the observed products.

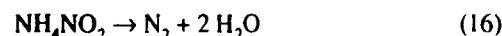
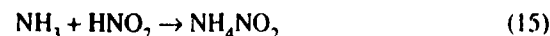
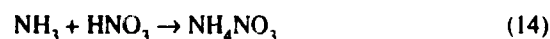
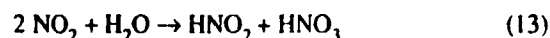
The reaction of  $\text{NO}_2$  with  $\text{NH}_3$  was described in terms of elementary reactions by Bedford and Thomas<sup>(13)</sup> in the temperature range  $342^\circ\text{C}$ - $387^\circ\text{C}$  (reactions 5-10).



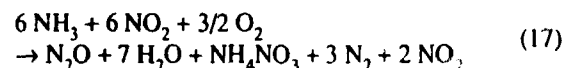
leading to the overall stoichiometry:



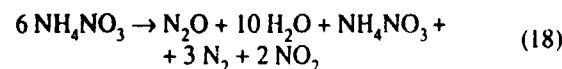
In addition to these products,  $\text{NH}_4\text{NO}_3$  is also formed<sup>(13-15)</sup>. In fact, below  $170^\circ\text{C}$  the products<sup>(14,15)</sup> are  $\text{N}_2$ ,  $\text{H}_2\text{O}$  and  $\text{NH}_4\text{NO}_3$ . Unlike  $\text{NO}_2$ , oxygen reacts slowly with  $\text{NH}_3$  in the temperature<sup>(16)</sup> range  $400^\circ\text{C}$ - $700^\circ\text{C}$ , but it reacts nearly instantaneously<sup>(17)</sup> with  $\text{NO}$ . It is likely, therefore, that the involvement of oxygen may be limited to the further oxidation of  $\text{NO}$  formed in the above reaction. The reformation of AN, on the other hand, may be related to the reactions involving  $\text{NH}_3$ ,  $\text{NO}_2$  and water<sup>(10)</sup>, in addition to reaction (1). These subsequent reactions are represented by reactions (12-16).



The overall reaction becomes

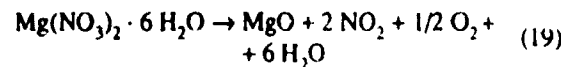


or

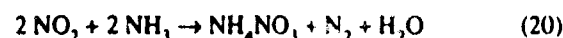


The above scheme of reactions represents the observed decomposition products of AN quite well. Note that  $\text{NO}_2$  is present in higher quantity than  $\text{N}_2\text{O}$  in Fig. 1. It also indicates that besides the AN aerosol formed due to the evaporation/sublimation process, some AN might form in the reaction of  $\text{NO}_2$  and  $\text{NH}_3$  in the gas phase.  $\text{H}_2\text{O}_2$  postulated in reactions (5) and (6) is not observed in the decomposition gases. Its transient presence in the decomposition gases of nitramines is well known<sup>(18)</sup>. The reason for its apparent absence here is not clear although it could be that it reacts as it forms in the highly ionic condensed phase of decomposing AN.

The feasibility of reaction (17) was evaluated by reacting  $\text{NH}_3$  with the products of thermally decomposed  $\text{Mg}(\text{NO}_3)_2 \cdot 6 \text{H}_2\text{O}$ . The thermolysis of  $\text{Mg}(\text{NO}_3)_2 \cdot 6 \text{H}_2\text{O}$  gives  $\text{NO}_2$ ,  $\text{H}_2\text{O}$  and (presumably)  $\text{O}_2$  by reaction (19) according to the IR spectrum (Fig. 3). Solid  $\text{MgO}$  is also formed.



Next,  $\text{Mg}(\text{NO}_3)_2 \cdot 6 \text{H}_2\text{O}$  was decomposed in an atmosphere of  $\text{NH}_3$ . The IR spectrum of the products shows that  $\text{NH}_3$  is oxidized to  $\text{N}_2\text{O}$  as indicated by the relative decrease in the absorbance of  $\text{NH}_3$  compared to the increase in the intensity of  $\text{N}_2\text{O}$  (Fig. 3). The spectra also show the presence of ammonium nitrate which forms<sup>(14)</sup> by reaction (20).



More insight into reaction (20) was gained by the pyrolysis of  $\text{Pb}(\text{NO}_3)_2$  which is known to give  $\text{NO}_2$  as the only

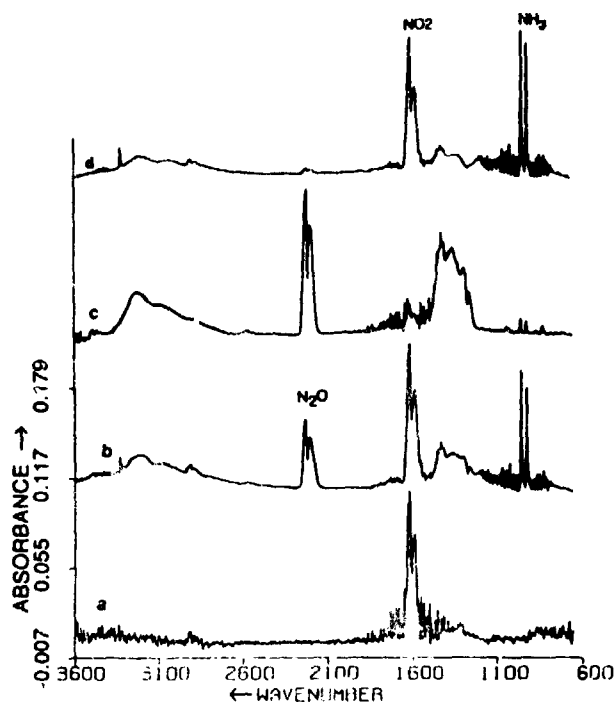
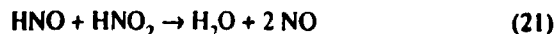


Figure 3. Rapid-scan FT-IR spectra of the decomposition products of  $\text{Mg}(\text{NO}_3)_2 \cdot 6 \text{H}_2\text{O}$  in Ar (a = 10 s), in  $\text{NH}_3$  (b = 2.4 s, c = 10 s); and  $\text{Pb}(\text{NO}_3)_2$  in  $\text{NH}_3$  (d = 10 s) following the onset of heating ( $t = 0$  s). The samples were heated at a rate of about  $120^\circ\text{C/s}$  and held at  $650^\circ\text{C}$ .

gaseous product of decomposition<sup>(19)</sup>. This was done in an  $\text{NH}_3$  atmosphere under essentially the same conditions as those used in the  $\text{Mg}(\text{NO}_3)_2 \cdot 6 \text{H}_2\text{O}$  study. No AN formed. The products contain  $\text{N}_2\text{O}$ , but only in a small amount, and some NO (Fig. 3). The absolute intensity of NO is very small, but the amount present is non-negligible.

The contrast between the decomposition products of  $\text{Pb}(\text{NO}_3)_2$  and  $\text{Mg}(\text{NO}_3)_2 \cdot 6 \text{H}_2\text{O}$  in  $\text{NH}_3$  could be attributed to the formation of  $\text{H}_2\text{O}$  and  $\text{O}_2$  *in-situ* in the latter case. AN and  $\text{N}_2\text{O}$  are known to form in the reaction between  $\text{NH}_3$  and  $\text{NO}_2$  at room temperature only when traces of water and air are present<sup>(20a)</sup>. The reaction leading to the formation of AN is known to be enhanced in the presence<sup>(21)</sup> of  $\text{H}_2\text{O}$ . It is likely, therefore, that the formation of AN occurs with the involvement of  $\text{H}_2\text{O}$  produced during the dehydration of  $\text{Mg}(\text{NO}_3)_2 \cdot 6 \text{H}_2\text{O}$  as in reactions (13) and (14). The fate of  $\text{HNO}_2$  may follow reactions (15) and (16) giving the net reaction (20). The formation of  $\text{N}_2\text{O}$ , on the other hand, could be related to the presence of  $\text{O}_2$ , which may facilitate reaction (7) by oxidizing NO to  $\text{NO}_2$ . Indeed, the absence and presence of NO in the decomposition products of  $\text{Mg}(\text{NO}_3)_2 \cdot 6 \text{H}_2\text{O}$  and  $\text{Pb}(\text{NO}_3)_2$  in  $\text{NH}_3$ , respectively support this view. Furthermore, it is interesting to note that while the formation of NO is invariably noticed in the reaction between  $\text{NH}_3$  and  $\text{NO}_2$ ,  $\text{N}_2\text{O}$  is produced either at high temperature<sup>(13)</sup> or in the presence of  $\text{O}_2/\text{H}_2\text{O}$ . The apparent difference in the reaction products may be understood in terms of the elementary reactions by assuming that at low temperatures, the  $\text{HNO}$  formed by reaction (7), instead of decomposing thermally by reaction (9), reacts<sup>(22)</sup> with  $\text{HNO}_2$  formed by reactions (5) and (6) giving NO and  $\text{H}_2\text{O}$ .



Thus, while the formation of NO would be feasible at relatively low temperatures, the  $\text{N}_2\text{O}$  formation, being dependent on the thermal decomposition of  $\text{HNO}$ , should form at relatively high temperatures. Similarly, in the presence of  $\text{O}_2$  the steep temperature rise resulting from the exothermic oxidation of NO to  $\text{NO}_2$  enhances the formation of  $\text{N}_2\text{O}$ .

The thermolysis experiments on  $\text{Mg}(\text{NO}_3)_2 \cdot 6 \text{H}_2\text{O}$  indicate that the same oxidizing species are produced as are formed by the thermal decomposition of  $\text{HNO}_3$ . Furthermore, upon reaction of these species with  $\text{NH}_3$  the products are the same as observed in the thermolysis of AN. It seems, therefore, that the reaction scheme (5-18) explains the products of AN without the need to involve the thermally unstable  $\text{NH}_2\text{NO}_2$  intermediate.

The decomposition products of AN under high pressure are consistent with the above mechanism. When AN was thermolysed under 280 psi of Ar (Fig. 2), as expected<sup>(9)</sup>, very little sublimation was observed. The gases  $\text{NH}_3$  and products of decomposed  $\text{HNO}_3$  react closer to the surface and as a result, enhance the decomposition process.  $\text{N}_2\text{O}$  and  $\text{H}_2\text{O}$  are predominant products.

### 3.2 AN-Mg Mixtures

The DSC thermograms of AN-Mg mixtures agree with previous DTA data<sup>(5)</sup>. It is evident that the decomposition of AN is drastically modified in the presence of Mg powder. While pure AN evaporates giving an endotherm around  $280^\circ\text{C}$ , AN-Mg mixtures decompose exothermically beginning at  $130^\circ\text{C}$ . After rapid decomposition near this temperature, the AN-Mg (3:1) mixture shows an endotherm around  $417^\circ\text{C}$ . Since these experiments were conducted in Ar, no ignition of the metal was noticed, as reported earlier when air was present<sup>(5)</sup>. The residue of the mixture after heating the sample in Ar to  $300^\circ\text{C}$  was found to contain  $\text{Mg}(\text{NO}_3)_2 \cdot x\text{H}_2\text{O}$ , according to the IR spectrum (Fig. 4). On the other hand, a sample heated to  $500^\circ\text{C}$  was found to be mostly MgO. Therefore, it seems that the decomposition of AN-

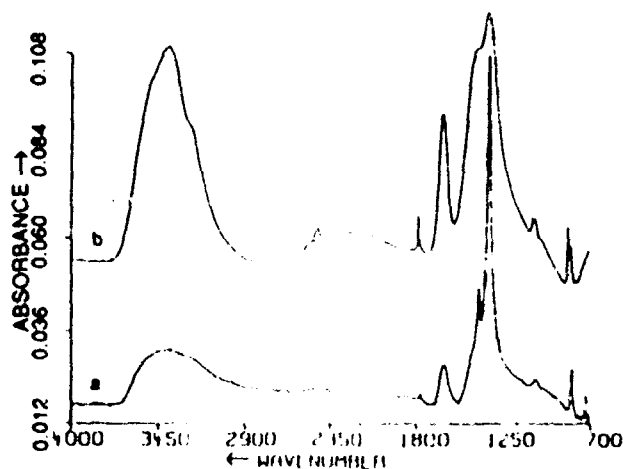


Figure 4. The FT-IR spectra of solid  $\text{Mg}(\text{NO}_3)_2 \cdot 6 \text{H}_2\text{O}$  at  $25^\circ\text{C}$  (a), and a decomposed AN-Mg (3:1) mixture at  $300^\circ\text{C}$  (b), showing the formation of  $\text{Mg}(\text{NO}_3)_2 \cdot x\text{H}_2\text{O}$ .

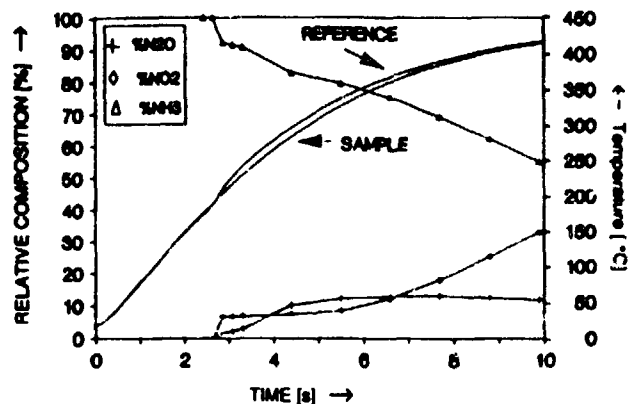


Figure 5. The relative concentrations of the gas products at several times after the onset of heating when an AN-Mg (3:1) mixture is heated at 80°C/s under 15 psi Ar. The reference and the sample thermal traces are superposed.

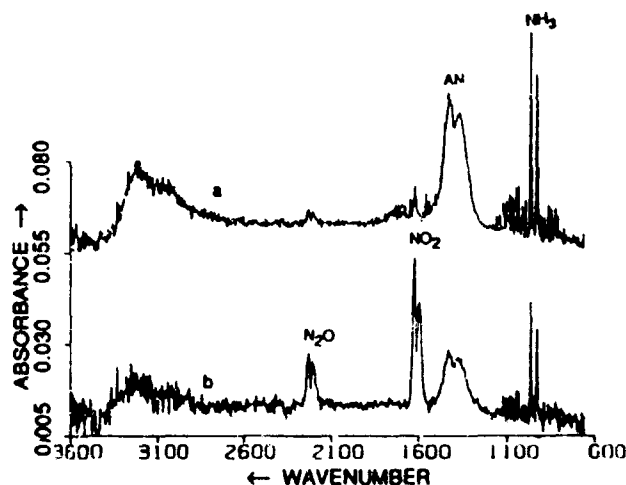


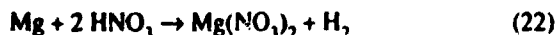
Figure 6. Rapid-scan FT-IR spectra of the gaseous decomposition products of an AN-Mg (3:1) mixture at 15 psi in Ar (a) 2.6 s after the onset of heating. (b) is the spectrum after 10 s showing the formation of  $\text{NO}_2$  and  $\text{N}_2\text{O}$  in the later stages of decomposition.

Mg mixtures proceeds via the formation of  $\text{Mg}(\text{NO}_3)_2$ , which subsequently decomposes to  $\text{MgO}$ . Apparently, an exothermic reaction between AN and Mg occurs in the solid state at about 130°C. Most of the AN is consumed in the formation of  $\text{Mg}(\text{NO}_3)_2$ . The heat evolved during this reaction decomposes and evaporates some of the AN.

Thermal trace of the rapidly heated AN-Mg (3:1) mixture shows that  $\text{NH}_3$  is evolved at about 150°C (Fig. 5). A rapid scan FT-IR spectrum of the gaseous products taken 2.6 s after the onset of heating shows AN aerosol (Fig. 6) and other products in minor amounts. Pure AN begins to evaporate and to decompose only after 5 s under similar experimental conditions. Monitoring of the gas atmosphere for 10 s shows that the relative concentration of  $\text{NH}_3$  decreases steadily while that of  $\text{NO}_2$  increases. From the gases produced and their temporal behavior, it is apparent that a portion of the AN in the AN-Mg mixture is evaporated/decomposed without interacting with Mg, but at a much lower temperature than occurs with pure AN. Fast thermolysis of the mixtures having a larger amount of AN (e.g. 6.6:1 and 10:1), gave similar thermal traces and identical

products as the 3:1 mixture. Here again,  $\text{NH}_3$  was the main product in the initial stage with  $\text{NO}_2$  and  $\text{N}_2\text{O}$  present in lesser amounts.

These results can be explained by the same mechanism envisaged for the decomposition of AN, with the proviso that proton transfer is facilitated by the Mg. The mechanism would be reaction (1) followed by reactions (22) and (23), followed in turn by reaction (17).



AN is reported<sup>(23)</sup> to lose weight beginning at 150°C, although not to a significant extent. Reaction (1) is the primary cause. In the presence of Mg powder, it is likely that reaction (1) is facilitated because the  $\text{HNO}_3$  is partly consumed by reaction (22).  $\text{NH}_3$  from reaction (1) escapes to the gas phase, and appears as the first product in the FT-IR spectrum. The Mg- $\text{HNO}_3$  reaction is highly exothermic, and the heat evolved in the condensed phase causes some AN to evaporate/decompose at a much lower thermocouple temperature than is found for pure AN.

The major difference between the thermal decomposition of the mixtures having a larger amount of AN and those of pure AN and AN-Mg (3:1) is that while the concentration of  $\text{N}_2\text{O}$  increased in the later stage with the AN-Mg 6.6:1 and 10:1 mixtures,  $\text{NO}_2$  prevails over  $\text{N}_2\text{O}$  in the latter cases. This is understandable by the reaction stoichiometry. All of the AN should be consumed in forming the  $\text{Mg}(\text{NO}_3)_2$  in the 3:1 (AN-Mg) mixture. Magnesium nitrate decomposes subsequently, but only above 400°C, with the production of  $\text{NO}_2$ , leading to the  $\text{NO}_2$  concentration increase in the later spectral scans. On the other hand, mixtures with higher amounts of AN, 6.6:1 and 10:1, have a stoichiometric or excess amount of AN than is required for reaction with Mg. These mixtures would, therefore, decompose to give  $\text{NH}_3$  and  $\text{Mg}(\text{NO}_3)_2$  followed by the evaporation/decomposition of the remaining unreacted AN. On increasing the temperature, the  $\text{Mg}(\text{NO}_3)_2$  decomposes giving  $\text{NO}_2$  and  $\text{O}_2$  which, in turn, reacts by reaction (17) with  $\text{NH}_3$  converting it to  $\text{N}_2\text{O}$  in the later stages of decomposition of these mixtures.

### 3.3 AN-C Mixtures

The DSC thermogram of an AN-C (3:1) mixture is essentially similar to that obtained<sup>(5)</sup> by the DTA showing several minor exotherms starting at about 135°C and a major exotherm peaking near the melting point of pure AN (170°C). In the TG analysis, the weight loss at 170°C corresponds to the stoichiometric oxidation of carbon to  $\text{CO}_2$  by AN. Since the mixture contains excess carbon, some carbon remains unaltered.

The FT-IR spectrum of the decomposition products of the rapidly heated sample shows, apart from AN aerosol, the presence of  $\text{CO}_2$ ,  $\text{N}_2\text{O}$ ,  $\text{NO}_2$  and  $\text{H}_2\text{O}$  as main products (Fig. 7). A trace amount of HCN and an absorption at 2268  $\text{cm}^{-1}$ , characteristic of  $\text{HNCO}$ , are also seen. Most of these species appear simultaneously at about 120°C (Fig. 8).

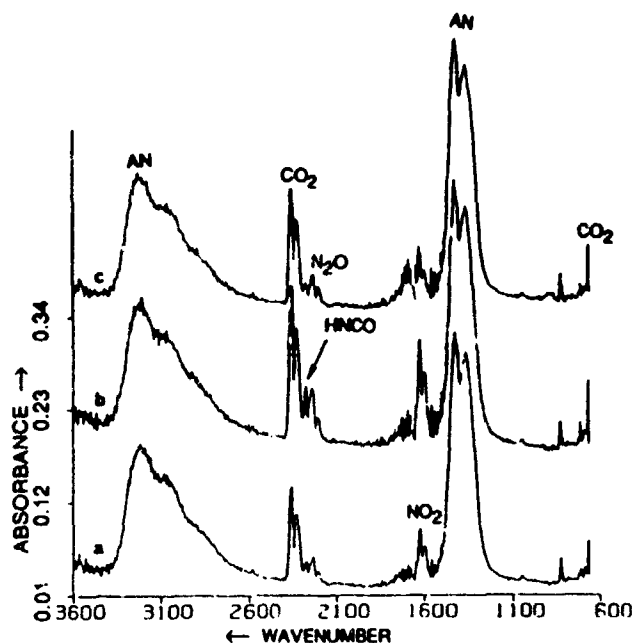


Figure 7. Rapid-scan FT-IR spectra of the decomposition products of AN-C (3:1) mixture showing the amount of HNCO at different times [(c) = 2.64 s, (b) = 3.2 s and (a) = 7.6 s] after the onset of heating.

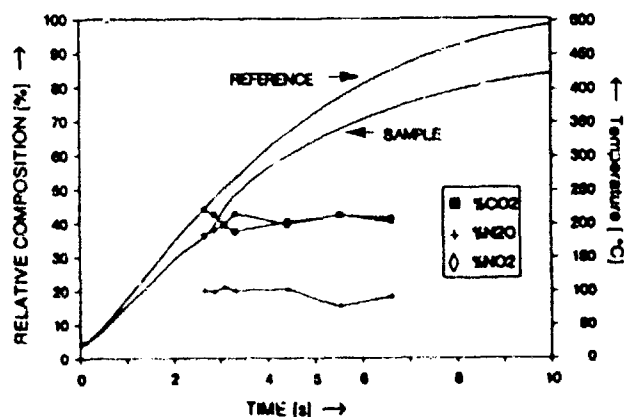


Figure 8. The relative concentration of the gas products when an AN-C (3:1) mixture is decomposed at 80°C/s under 15 psi Ar. The reference and the sample thermal traces are superposed.

Once formed, the relative concentrations of  $\text{NO}_2$ ,  $\text{N}_2\text{O}$  and  $\text{CO}_2$  remain unchanged. The intensity of the peak at  $2268\text{ cm}^{-1}$  grows and then decays, vanishing almost completely after 10 s. Unlike pure AN and AN-Mg mixtures, no  $\text{NH}_3$  is observed. This is despite the fact that a portion of the AN is sublimed/decomposed due to the exothermicity of the reaction between AN and C without undergoing any reaction with C. AN-C mixtures of 13.3:1 and 20:1 gave the same products of decomposition but the concentration ratios varied. Here again,  $\text{NH}_3$  was absent, although sublimed AN is prominently present in the products.

Based on reaction (1), it may be envisaged that carbon reacts with the  $\text{HNO}_3$  formed by the dissociation of AN. Although the oxidation of C by  $\text{HNO}_3$  to  $\text{CO}_2$  is known<sup>(24)</sup>, when  $\text{HNO}_3$  was reacted with C in a modified IR cell at room temperature,  $\text{NO}_2$  initially formed followed by  $\text{CO}_2$ . This observation suggests the involvement of  $\text{NO}_2$  in the

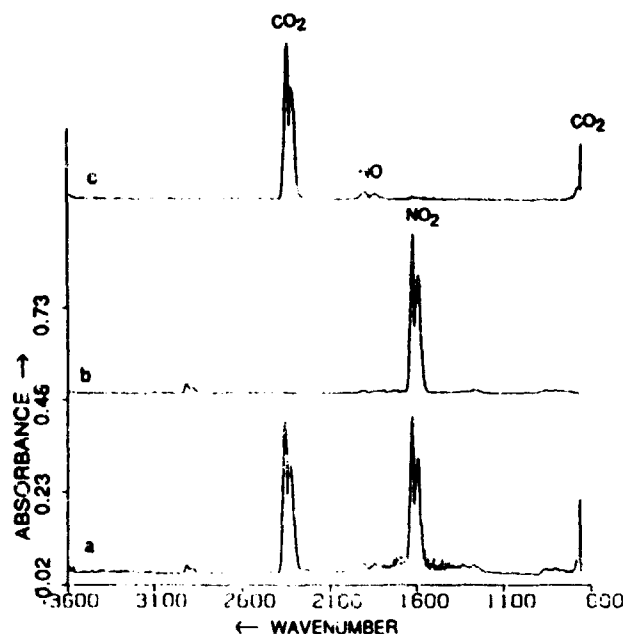
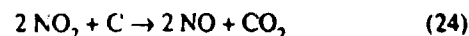
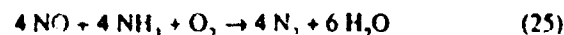


Figure 9. Rapid-scan FT-IR spectra of the decomposition products after 10 s of an  $\text{Mg}(\text{NO}_3)_2 \cdot 6\text{H}_2\text{O}$ -C (3:1) mixture (a);  $\text{Pb}(\text{NO}_3)_2$  (b); and a  $\text{Pb}(\text{NO}_3)_2$ -C (3:1) mixture (c) in Ar. The samples were heated at a rate of about  $120^\circ\text{C/s}$  and held at  $650^\circ\text{C}$ .

oxidation of C. To verify this, the mixtures of carbon with  $\text{Pb}(\text{NO}_3)_2$  and  $\text{Mg}(\text{NO}_3)_2 \cdot 6\text{H}_2\text{O}$  were thermolysed in the IR cell. The FT-IR spectra indeed show the formation of  $\text{CO}_2$ . In turn,  $\text{NO}_2$  is reduced to NO (Fig. 9) by reaction (24).



This observation is consistent with the fact that hot activated C can be used for pretreating the waste gases containing  $\text{NO}_2$  to convert<sup>(25)</sup>  $\text{NO}_2$  to NO. The NO can be removed by treating with activated charcoal<sup>(26)</sup> in the presence of  $\text{NH}_3$  at high temperature. In fact, NO from flue gases is usually removed by treating with  $\text{NH}_3$  in the presence of a catalyst<sup>(27,28)</sup> according to reaction (25).

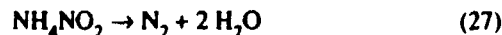
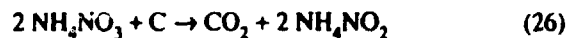


In the AN-C mixtures, charcoal may be involved in removing NO. Reaction (25) could explain the absence of  $\text{NH}_3$  in the decomposition products of AN-C mixtures. The oxidative decomposition products of  $\text{HNO}_3$  and  $\text{Mg}(\text{NO}_3)_2 \cdot 6\text{H}_2\text{O}$  (namely  $\text{NO}_2$  and  $\text{O}_2$ ) being common, it is highly likely that they would react in a similar manner with C and  $\text{NH}_3$  present in the system. The  $\text{NH}_3$  formed in the AN-C system due to the dissociation of AN might, therefore, have been consumed in the removal of  $\text{NO}_2$ .

Alternatively, it could be argued that the ammonia partly reacts with  $\text{CO}_2$  forming the carbamate and its decomposition product, urea, which could decompose further. Urea forms by the reaction<sup>(29)</sup> of  $\text{CO}_2$  with  $\text{NH}_3$  and might occur in the present instance at low ( $< 160^\circ\text{C}$ ) temperatures. Urea under certain conditions is known to decompose<sup>(29)</sup> to give HNCO, which could explain the presence of the IR absorption at  $2268\text{ cm}^{-1}$  in the products. While this alternative appears attractive, attempts to establish it were not success-

ful. For instance, in a DSC experiment the AN-C (3:1) mixture was decomposed at a controlled heating rate up to 175°C. The residue was examined. Its IR spectrum revealed no urea or decomposition products of urea, such as biuret and triuret<sup>(29)</sup>.

According to Glazkova, et al.<sup>(30)</sup> the decomposition of AN-C mixtures proceeds via the formation of  $\text{NH}_4\text{NO}_2$ , which subsequently decomposes to  $\text{N}_2$  and  $\text{H}_2\text{O}$  (reactions 26 and 27).



Identical burning rates of the mixtures of C with  $\text{NH}_4\text{NO}_3$  and C with  $\text{NH}_4\text{NO}_2$  and the assumption that decomposition of the  $\text{NH}_4\text{NO}_2$  determines the rate provide support to this mechanism. It involves no formation of ammonia and hence accounts for its absence, as found here for these mixtures. The mechanism, however, does not explain the formation of HCN or the absorption at  $2268 \text{ cm}^{-1}$  tentatively attributed to HNCO. On the other hand, the HCN could be accounted for if the formation of  $\text{HNO}_3$  is assumed, as  $\text{HNO}_3$  is known to react with C giving HCN, in some instances<sup>(20b)</sup>. Similarly,  $\text{NH}_3$  is known to react with C on heating<sup>(20b)</sup> giving  $\text{NH}_4\text{CN}$  which could be further oxidized to the cyanate<sup>(31)</sup>. Its subsequent dissociation could then lead to HCNO, which is actually seen as HNCO in the vapor phase<sup>(31)</sup> thereby accounting for the IR absorption band observed at  $2268 \text{ cm}^{-1}$ .

#### 4. References

- (1) W. A. Rosser, S. H. Inami, and H. Wise, *J. Phys. Chem.* 67, 1753 (1963).
- (2) B. T. Fedoroff, "Encyclopedia of Explosives and Related Items", Vol. 1, Picatinny Arsenal, NJ, 1960, pp. A311-379.
- (3) J. H. Koper, O. G. Jansen, and P. J. van den Berg, *Explosivstoffe* 8, 181 (1970).
- (4) K. R. Brower, J. C. Oxley, and M. Tiwan, *J. Phys. Chem.* 93, 4029 (1989).
- (5) S. R. Jain and C. Oommen, *J. Therm. Anal.* 35, 1119 (1989).
- (6) M. Q. Brewster and T. A. Sheridan, "Combustion Studies of Clean Burning Propellants", Final Report submitted to Thiokol Corporation (1990).
- W. H. Anderson, K. W. Bills, E. Mishuck, G. Moe, and R. D. Schultz, *Combust. Flame* 3, 301 (1959).
- (7) J. T. Cronin and T. B. Brill, *Appl. Spectrosc.* 41, 1147 (1987).
- (8) Y. Oyumi and T. B. Brill, *Combust. Flame* 62, 213 (1985).
- (9) T. P. Russell and T. B. Brill, *Combust. Flame* 76, 393 (1989).

- (10) M. C. Sneed and R. C. Brasted (eds.), "Comprehensive Inorganic Chemistry", Vol. V, Van Nostrand Co., Inc., New York, 1956, pp. 72, 91.
- (11) T. L. Davies and A. J. J. Abrams, *J. Am. Chem. Soc.* 47, 1043 (1925).
- (12) J. Thiele and A. Lachman, *Chem. Ber.* 27, 1909 (1894); H. S. Booth (ed.), *Inorganic Synthesis* 1, 73, (1939).
- (13) G. Bedford and J. H. Thomas, *J. Chem. Soc. Faraday Trans. 1*, 2163 (1972).
- (14) R. Falk and R. N. Pease, *J. Am. Chem. Soc.* 76, 4746 (1954).
- (15) M. Patry, R. Garlet, and S. Pupko, *C. R. Hebd. Seances Acad. Sci.* 225, 941 (1947).
- (16) P. W. M. Jacobs and H. M. Whitehead, *Chem. Rev.* 69, 551 (1969).
- (17) F. A. Cotton and G. Wilkinson, "Advanced Inorganic Chemistry", 3rd Ed., Interscience Publishers, John Wiley and Sons, New York, 1972, p. 355.
- (18) T. B. Brill and Y. Oyumi, *J. Phys. Chem.* 90, 6848 (1986).
- (19) G. Brauer (ed.), "Handbook of Preparative Inorganic Chemistry", Vol. 1, 2nd Edition, Academic Press, New York, 1963, p. 488.
- (20) (a) J. W. Mellor, "A Comprehensive Treatise on Inorganic and Theoretical Chemistry" Vol. VIII, Longmans, Green & Co., London, 1928, p. 219;  
(b) Vol. V, 1924, pp. 827-828.
- (21) A. M. Mearns and K. Ofozu-Ardeu, *J. Chem. Technol. Biotechnol., Chem. Technol.* 34A, 350 (1984).
- (22) C. F. Melius, "Chemistry and Physics of Energetic Materials", S. N. Bulusu (ed.), Kluwer Academic Publishers, Boston, 1990, p. 72.
- (23) L. Erdey, S. Gal, and G. Liptay, *Talanta* 11, 913 (1964).
- (24) J. B. Donnet and J. Lahaye, *Bull. Soc. Chim. (Fr.)*, 1282 (1966).
- (25) K. Kaneburi, M. Seki, M. Kataumoto, and H. Sakurai, *Japan Kokai Tokyo Koho* 79, 83698 (1977), CA, 92, 98827.
- (26) K. Kawamura and T. Matsuo, *Japan Kokai Tokyo Koho* 77, 72376 (1975), CA, 87, 122494.
- (27) W. C. Wong and K. Nobe, *Ind. Eng. Chem. Prod. Res. Dev.* 25, 179, 186 (1986).
- (28) In-Sik Nam, J. W. Eldridge, and J. R. Kittrell, *Ind. Eng. Chem. Prod. Res. Dev.* 25, 186, 192 (1986).
- (29) Kirk-Othmer, "Encyclopedia of Chemical Technology", Vol. 21, 2nd Ed., Interscience, N.Y. (1970) p. 41.
- (30) A. P. Glazkova, Yu. A. Kazarov, and A. V. Savelev, *Comb. Expl. Shock Waves* 19, 308 (1982), (Engl. Transl.).
- (31) S. Patai (ed.), "The Chemistry of Cyanates and Their Derivatives", Part 1, John Wiley and Sons, New York, 1977, pp. 509.

#### Acknowledgements

We are grateful to the Thiokol Corporation and the Air Force Office of Scientific Research for support of this work.

(Received April 4, 1991; Ms 18/91)

## CHEMICAL PATHWAYS AT A BURNING SURFACE

T. B. BRILL, P. J. BRUSH, D. G. PATIL, AND J. K. CHEN

Department of Chemistry  
University of Delaware  
Newark, DE 19716  
USA

The chemical origin of burning rate differences among bulk materials is analyzed by an experimental simulation of the surface reaction zone. The simulation involves high-rate heating of a thin film of compounds displaying low, intermediate and high burn-rates. The simulation is validated by the close match of the burn rates calculated from the Arrhenius constants determined by SMATCH/FTIR spectroscopy and burn-rates measured by combustion of the bulk material at 1 atm. A second microscale pyrolysis technique, T-jump/FTIR spectroscopy, is used to specify chemical details of the simulated burning surface isothermally at high temperature. High burn-rate materials, such as azide polymers, release a large amount of energy in very early reaction steps at the surface. Intermediate burn-rate materials, such as RDX and HMX, initially decompose by an approximately thermally neutral set of reactions. The high heat release occurs as the products of these initial steps concentrate and react. As a result, the heat release is delayed and divided between the heterogeneous condensed phase and the gas phase. Low regression rate materials, such as isocyanate-cross-linked hydroxyl-terminated polybutadiene, decompose into clipped fragments of the backbone and little heat is released. In this case, the regression rate is controlled mostly by the rate of desorption of the fragments and not the magnitude and time of the heat release.

### Introduction

The linear rate of burning is a vital practical combustion parameter of a bulk material. There are complex chemical and physical reasons for why some materials are slow burning while others are fast burning. Although the linear burn rate,  $\dot{r}$ , can be used to estimate a surface temperature or global decomposition activation energy at a given pressure,  $\dot{r}$  is a one-dimensional parameter in which all chemical reaction rates are lumped with the heat and mass transfer rates. Consequently, few fundamental details about combustion are learned from  $\dot{r}$  alone.

Advancement in understanding the different combustion characteristics of bulk materials requires knowledge about the chemistry and physics of the surface reaction zone that connects the bulk material to the gas phase. Unfortunately, this region is physically very thin. It also has a steep temperature gradient that produces a dynamically changing microstructure of heterogeneous phases and non-equilibrium chemistry. This complexity mitigates against direct measurement of the surface reactions during combustion.

Recently, chemical details of the surface reaction zone have been acquired by developing experiments that simulate the conditions of the surface

reaction zone. Over a very short time interval the burning surface is a thin film of reacting material. Hence, a simulation of this zone is achieved by rapid, programmed heating of a thin film. Chemistry is learned by simultaneously determining the heat flow and acquiring rapid-scan FTIR spectra of the near-surface gas products. The gases detected form the first stage of the flame zone were a flame to be present. One deficiency in this approach is that back-diffusion of H atoms from the flame to the surface is not included. Back-diffusion is likely to play an increasing role at higher pressure and is not the major influence on the chemistry at 1-3 atm where these experiments were performed.

Convincing evidence that the rapidly heated thin film is a surface simulation comes from the SMATCH/FTIR method<sup>1</sup> in which a film of uniform, chosen thickness (20-60  $\mu\text{m}$ ) is heated at  $\geq 150^\circ \text{C/s}$  while the dynamic mass change, temperature change, and gas products are all measured simultaneously. The  $\dot{r}$  calculated from SMATCH/FTIR kinetics matches  $\dot{r}$  from bulk combustion measurements at the same pressure.<sup>2-4</sup> Hence, the heat flow conditions are similar to those of the surface reaction zone during bulk combustion. By inference, other techniques designed for fast, controlled heating of a thin film, such as T-jump/FTIR,<sup>5</sup> that are specifically designed for chemical studies, give ex-

tensive details of the surface reaction zone for the first time. The chemical basis for the behavior of fast-burning (azide polymers), medium-burning (nitramines) and slow-burning (polybutadiene) materials come into light.

### Experimental

Details of SMATCH/FTIR<sup>1-4</sup> and T-jump/FTIR<sup>5</sup> spectroscopy are given elsewhere, but are briefly summarized here. SMATCH/FTIR employs a cantilevered quartz tube whose vibrational frequency depends on the sample mass. Typically, 0.2–0.5 mg of sample was painted onto a metal tip attached to the tube giving a uniform film of 16–64  $\mu\text{m}$  thickness. If the film thickness is not uniform, then the experiment fails. The metal end-tip was heated by RF induction at a chosen rate in the 100–200° C/s range. The sample atmosphere was 1 atm of Ar. The heating rate and film thickness are matched so that the heat transfer is fast enough to give a reasonably uniform temperature throughout the film.<sup>2</sup> The dynamic weight change of the sample was measured by the change in the vibrational frequency of the tube. Data were recorded at 160 Hz which provides enough points on the weight-loss curve to be confident of fitting the shape by (E1).  $\alpha$  is

$$1 - \alpha = \sum_{i=1}^3 a_i t^i \quad (\text{E1})$$

the degree of conversion and  $t$  is time. Typically, (E1) was applied for the initial 50% of weight loss. The temperature was measured by a type E thermocouple spot-welded to the metal end-tip and in contact with the sample film. Infrared spectra of the decomposition gases were measured about 3 mm above the metal end-tip by using a Nicolet 60SX rapid-scan FTIR spectrometer (10 scan/s, 4  $\text{cm}^{-1}$  resolution). The IR spectra were converted to the relative percent composition scale by integrating the absorption bands and converting them to a relative concentration scale by using their absolute intensities.<sup>6</sup> IR inactive species, such as  $\text{N}_2$  and  $\text{H}_2$ , are not detected, and, therefore, are not included in the quantitation procedure.  $\text{H}_2\text{O}$  was not quantified because of its complicated rotational-vibrational fine-structure. The absolute absorbance of  $\text{HNCO}$  was estimated to be half-way between that of  $\text{CO}_2$  and  $\text{N}_2\text{O}$ . These gas products evolve into a cool Ar atmosphere where they are identified, rather than into a high temperature flame zone, as in actual combustion, where they would be instantly consumed.

The reduction of SMATCH/FTIR temperature and weight change data is afforded by (E1) and its derivative, which are related to Arrhenius parameters by (E2).

$$\frac{d\alpha}{dt} = A e^{-E/RT} (1 - \alpha)^n \quad (\text{E2})$$

Rearrangement of (E2) yields (E3), which is a straight line by the appropriate choice of  $n$ .  $n = 2$  linearizes most SMATCH/FTIR

$$\log \left[ \frac{d\alpha}{dt} \left( \frac{1}{1 - \alpha} \right)^2 \right] = \log A - \frac{E}{2.3RT} \quad (\text{E3})$$

data and has been rationalized elsewhere.<sup>3</sup> A version of the pyrolysis law, (E4), where  $h$  is the experimental film thickness, can be used to calculate the burn rate,  $\dot{r}$ , in mm/s from the

$$\dot{r} = h A e^{-E/RT} \quad (\text{E4})$$

SMATCH/FTIR Arrhenius constants at the pressure and temperature of the experiment.  $T$  is the average temperature during the initial 50% of the weight loss. (E4) applies provided  $h$  approximates the surface reaction zone thickness at 1 atm. A value of  $h = 20 - 60 \mu\text{m}$  is reasonable<sup>7</sup> at 1 atm.

While  $\dot{r}$  can be calculated from SMATCH/FTIR, the chemical processes that are witnessed from the gas products are somewhat confused by the fact that decomposition occurs non-isothermally. To gain the chemical details more clearly, the T-jump/FTIR technique was developed.<sup>5</sup> In T-jump/FTIR, a thin film of material is deposited on a 20  $\mu\text{m}$  thick Pt ribbon filament. Heating occurs at a chosen high rate up to 20000° C/s to a chosen temperature ( $T_f$ ). 2000° C/s is normally used because this is the highest heating rate that does not overshoot  $T_f$ .  $T_f$  can be maintained while the decomposition gases are analyzed by rapid-scan FTIR spectroscopy. The high heating rate reduces the "cooking" chemistry that takes place at a low heating rate. The fact that  $T_f$  is adjustable enables the products to be determined isothermally at selected temperatures including the expected burning surface temperature.

The Pt filament is an element of a very rapidly responding and sensitive bridge circuit. The control voltage of the circuit linearly responds to the Pt resistance during the programmed heating step and maintains a constant resistance once  $T_f$  is reached. The temperature of the filament is determined by the resistance as with a Pt thermometer. The control voltage increases or decreases very rapidly to maintain  $T_f$  in response to endothermic or exothermic events of the sample. Therefore, monitoring the control voltage as a function of time uncovers these sequential events.

A useful form of the control voltage is the difference trace (voltage with sample minus voltage without sample present) as illustrated in Fig. 1 for 200  $\mu\text{g}$  of RDX. After heating at 2000° C/s to  $T_f = 263^\circ \text{C}$ , an initial endotherm (positive deflection)



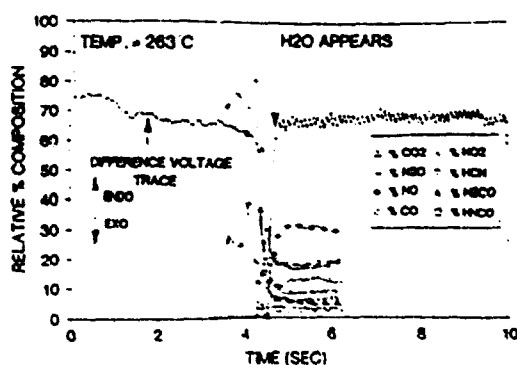
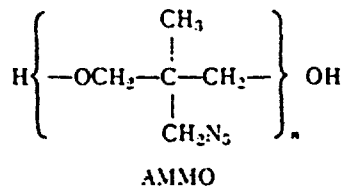
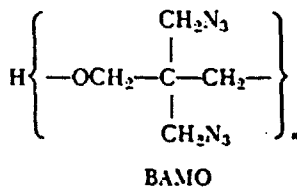
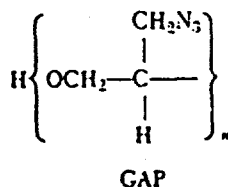


FIG. 1. T-jump/FTIR data for 200  $\mu\text{g}$  of RDX in 5 atm of Ar heated at 2000° C/s to 263° C and held at 263° C. The difference control voltage trace is superimposed on the relative concentrations of the gas products detected in real time 3 mm above the surface. Endothermic melting occurs in the first second followed by an exotherm at about 4.5 sec. Gas products first appear at about 3.5 sec, but the sum of the reactions is close to thermal neutrality until the exotherm.

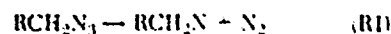
occurs in the first second corresponding to melting and the higher heat capacity when sample is present. Later a sharp negative spike appears due to runaway exothermic decomposition. These data for RDX will be discussed in a later section.

Strand burner tests on azide polymers, such as glycidyl azide polymer (GAP),<sup>5</sup> reveal a high burn rate (Table II). Other azide polymers, such as BAMO and AMMO, behave similarly.



As shown in Table I,  $\dot{r}$  calculated from the SMATCH/FTIR kinetics for GAP resembles  $\dot{r}$  measured in a strand burner at higher pressures and extrapolated to 1 atm. Hence, the microscale SMATCH/FTIR technique simulates the surface reaction zone during bulk combustion and can be used to establish details of the surface reaction zone.

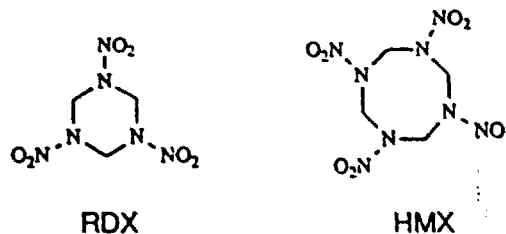
T-jump/FTIR was used to gain insight into the decomposition process. Smoothed gas product data for GAP are shown in Fig. 2 at two temperatures. The gases are recognizable, stabilized fragments of the GAP polymer backbone and appear simultaneously at the exotherm. The initial decomposition reaction of GAP is (R1). Decomposition of the unstable nitrene,  $\text{RCH}_2\text{N}$ , for example



by (R2), is highly exothermic ( $\Delta H = 600 - 700$  kJ/mol). In accordance, the control voltage trace turns sharply exothermic. In reality,  $\text{RCH}_2\text{N}$  decomposes by two branches as evidenced by the fact that HCN and  $\text{NH}_3$  form. When the C—N bond is retained, HCN is the product. When the C—N bond cleaves and H migration occurs,  $\text{NH}_3$  forms. The branching ratio (Fig. 3) is temperature dependent with C—N retention being preferred at higher temperature. The high heat release from rapid nitrene decomposition that occurs in the earliest stages of the decomposition process is dumped in the surface reaction zone and is responsible for the high burn rates displayed by these azide polymers.

#### Medium Burn-Rate Materials: RDX and HMX

Burn rates for the pure bulk nitramines, RDX and HMX, measured in a strand burner at higher



pressure and extrapolated to 1 atm are in the 0.3–0.5 mm/s range. Values of  $\dot{r}$  from SMATCH/FTIR (Table I) resemble these strand burner data showing that the microscale SMATCH/FTIR technique simulates macroscale combustion of these nitramines. Therefore, fast thermolysis methods can be used to provide chemical details of the surface reaction zone during combustion. These details reveal why nitramines have a lower burn rate at 1 atm than GAP. The behavior of RDX described here is similar to that of HMX.<sup>9</sup>

Figure 1 showed T-jump/FTIR data for a thin film of RDX heated at 2000° C/s to 263° C and then held isothermally while IR spectra of the near-surface gas products are recorded. The behavior of gas

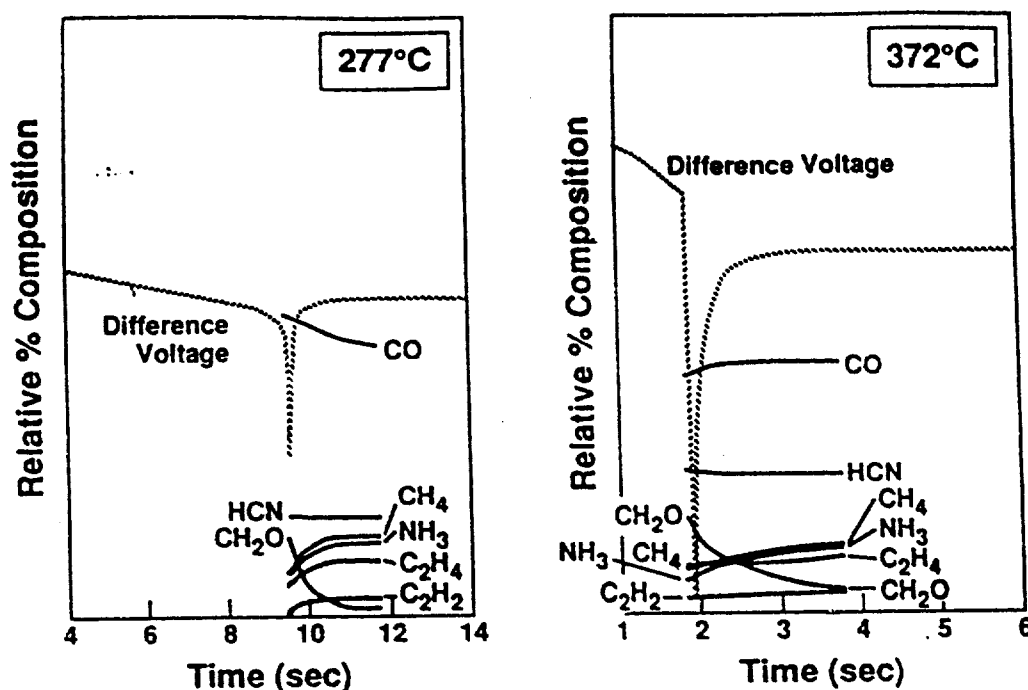


FIG. 2. The relative gas product concentrations (excluding  $N_2$ ) from GAP T-jumped at  $2000^\circ/\text{s}$  in 1 atm of Ar to  $277^\circ\text{C}$  and  $372^\circ\text{C}$  and then held at those temperatures. Note that the gas products appear at the exotherm. Secondary reaction of  $\text{CH}_2\text{O}$  appears to occur.

products is more easily discussed with the smoothed profiles shown at two temperatures in Fig. 4.

The global decomposition branches (R3) and (R4) occur for bulk RDX and HMX. (R3) and (R4) imply that  $\text{N}_2\text{O}$  and  $\text{NO}_2$  should

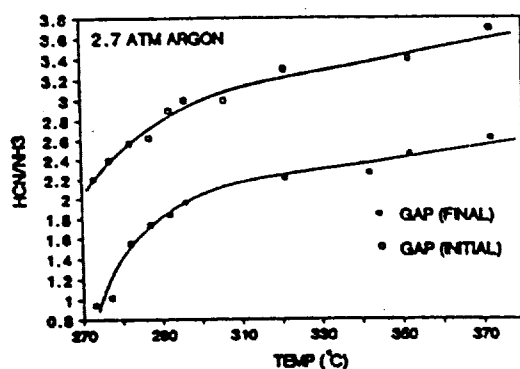
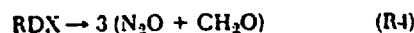


FIG. 3. The temperature dependence of the  $\text{HCN}/\text{NH}_3$  ratio of GAP showing that retention of the C-N bond is favored at higher temperature.

form simultaneously with  $\text{CH}_2\text{O}$  and  $\text{HCN}$ . This is not found at any temperature studied. Rather,  $\text{N}_2\text{O}$  and  $\text{NO}_2$  appear before  $\text{CH}_2\text{O}$  and  $\text{HCN}$ , which form from the residue left by elimination of  $\text{N}_2\text{O}$  and  $\text{NO}_2$ . This residue is a mixture of products like hydroxymethylformamide and acetamide,<sup>10-13</sup> which decompose leading to the delayed release of  $\text{CH}_2\text{O}$ ,  $\text{HCN}$  and  $\text{HNCO}$ .<sup>13,14</sup>

The total IR absorbance of the products accelerates between 3.5 and 4.5 s despite the constant heat flow from the filament, which implies that autocatalysis occurs in this stage of decomposition of RDX. Moreover, the control voltage trace in Fig. 1 reveals only mild exothermicity between 3 and 4 sec when (R3) and (R4) dominate. Thus, these reactions release little energy in the condensed phase.

A runaway exotherm develops at 4.5 s. The secondary reaction resembling (R5) appears to be responsible as evidenced by the fact that  $\text{CH}_2\text{O}$  and  $\text{NO}_2$  are consumed as  $\text{NO}$ ,  $\text{CO}$ , and  $\text{H}_2\text{O}$  appear.

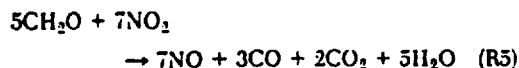


Figure 4 shows that more  $\text{NO}$  than  $\text{CO}$  forms in accordance with (R5). (R5) is highly exothermic as written ( $\Delta H = -1350 \text{ kJ}$ ) and, by the large exo-

TABLE I  
Kinetic constants and calculated burn rates,  $\bar{r}$ , from SMATCH/FTIR compared to strand burner  $\bar{r}$  values for the bulk material

Compound	SMATCH/FTIR					Strand Burner
	$E^a$	$\log A^b$	$h^c$	$T, ^\circ\text{C}^d$	$\bar{r}^e$	$\bar{r}^f$
GAP	42.3	19.0	30	260	1.35	1.7 <sup>g</sup>
HMX	36.5	14.8	50	303	0.37	0.5 <sup>g</sup>
RDX	29.0	13.6	45	191	0.38	0.3 <sup>h</sup>
HTPB/IPDI	11.3	4.5	60	350	0.21	0.19 <sup>g</sup>

<sup>a</sup>kcal/mol  
<sup>b</sup>s<sup>-1</sup>

<sup>c</sup>Experimental film thickness in  $\mu\text{m}$ .

<sup>d</sup>Average temperature during the initial 50% of the weight loss.

<sup>e</sup>mm/s at 1 atm.

<sup>f</sup>Extrapolated from reference 8.

<sup>g</sup>Boggs, T. L.: Progress in Astronautics and Aeronautics (K. K. Kuo and M. Summerfield, Eds.), Vol. 90, p. 121, 1984.

<sup>h</sup>Aleksandrov, V. V. Tukhtaev, R. K., Boldyrev, V. V. and Boldyrev, A. V.: Comb. Flame 35, 1, 1979.

<sup>i</sup>Extrapolated from Stacer, R. G., Eisele, S. and Eisenreich, N.: Twenty-first International Conference of the ICT, paper 80, Karlsruhe, FRG, July, 1990.

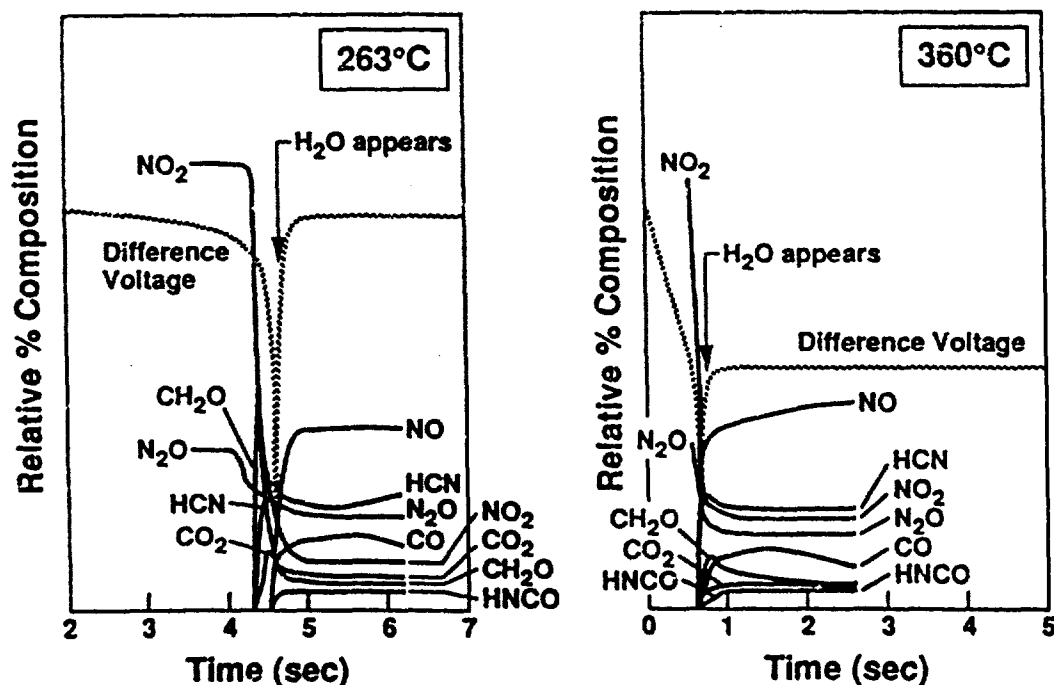


FIG. 4. Smoothed relative concentrations of the gas products from plots of RDX of the type shown in Fig. 1. Unlike Fig. 2 for GAP, there is a strong time dependence in the appearance of the gas products. The temperature dependence of the gas products is not large although the relative concentrations of  $\text{N}_2\text{O}$  and  $\text{NO}_2$  are reversed (see ref. 9 for further discussion).

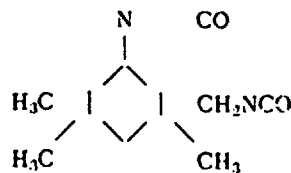
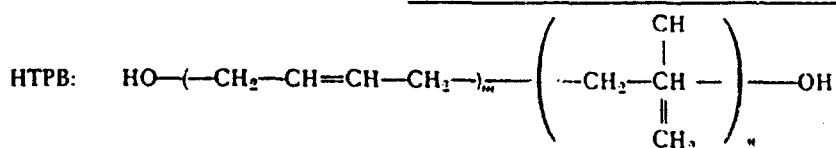
therm in Fig. 1, it is the main source of heat in the heterogeneous condensed phase. These conclusions also apply at 360° C (Fig. 4) except that the time-scale is compressed. Hence, this description of the decomposition of RDX at 263° C applies as well at the surface reaction zone temperature (350–400° C) during combustion. However, the branching ratio of (R3) and (R4) depends on temperature and favors (R3) at higher temperature.<sup>9</sup>

The fact that an approximately thermally balanced preparation stage (R3 and R4) occurs for RDX and HMX in order to produce the reactants for the later stage exothermic reaction (R5) causes a division of the heat release by R5 between the heterogeneous surface reaction zone (a mixture of solid, liquid and gas phases) and the gas phase. This later stage heat release makes the nitramines described here burn more slowly than the organoazides where a large heat release occurs in the very early reaction steps at the surface.

The different rate of heat release identified for GAP and the nitramines has practical ramifications. When a composite propellant containing GAP and HMX is burned, GAP burns vigorously and spews off many unburned HMX particles.<sup>15</sup> This is because (R1) and (R2) enable GAP to release energy very rapidly while the heat release reaction of HMX (R5) is delayed until (R3) and (R4) have occurred to a sufficient extent.

#### Low Regression-Rate Materials: Urethane Cross-linked HTPB

An example of a low regression-rate material is hydroxyl-terminated polybutadiene (HTPB) cross-linked by isophorone diisocyanate (IPDI) to form urethane bonds (R6).



IPDI:

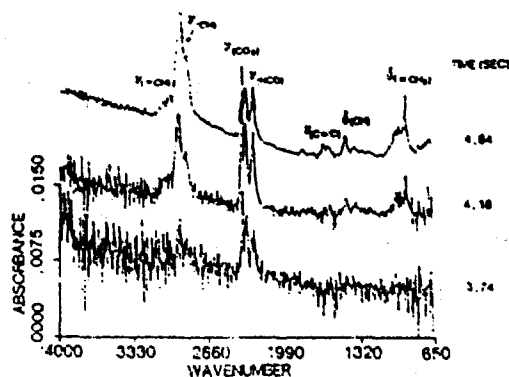
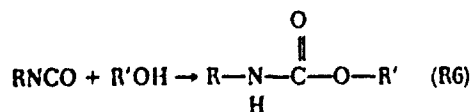
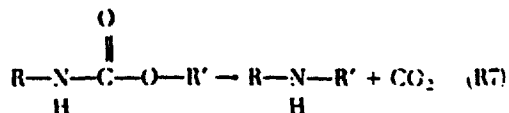


FIG. 5. Rapid-scan FTIR spectra recorded at the time shown 3 mm above the surface of HTPB-IPDI heated at 150° C/s in 1 atm of Ar. The  $\text{NCO}$  and  $\text{CO}_2$  absorbances appear before the butadiene and 4-vinylcyclohexene absorbances. The thermocouple trace of the condensed phase recorded simultaneously (not shown) reveals no exothermicity during the formation of these products.

Table I gives the regression-rate data. As before, the SMATCH/FTIR kinetic measurements at 1 atm faithfully match  $\bar{r}$  determined from combustion measurements on the bulk polymer at higher pressure and extrapolated to 1 atm. Therefore, the degradation of the condensed phase to form smaller molecules for the flame zone can be determined from the IR spectra upon thermolysis in 1 atm of Ar at 150° C/s<sup>1</sup>.

Figure 5 shows that the first detected gas products (3.7 sec after the onset of heating) above the surface of HTPB-IPDI are  $\text{CO}_2$  and a compound containing the isocyanate ( $\text{NCO}$ ) group. The isocyanate is most likely IPDI formed by reversal of

(R6). IPDI evaporates.  $\text{CO}_2$  probably comes from another decomposition reaction of the urethane linkage, (R7). Following the appearance of  $\text{CO}_2$  and IPDI are absorbances matching those of butadiene



the stabilized dimer of butadiene, 4-vinylcyclohexane (4.2 sec). All of these products would enter the flame zone and, except for  $\text{CO}_2$ , be reactants, were a flame to be present. However, the formation of these products is, at most, mildly exothermic and, therefore,  $\dot{r}$  for HTPB/IPDI is mainly controlled by the rate of volatilization of the fragments of the polymer. Hence, a low regression rate results. This behavior contrasts with the nitramines and organoazides discussed above, where the rate, amount, and time of the energy release control the burn rate.

### Conclusions

SMATCH/FTIR spectroscopy is a remarkable microscale laboratory simulation in which the kinetics of weight loss from a thin film match the burn rate of the bulk material during combustion at the same pressure. This technique validates the use of fast thermolysis methods on a thin film to determine chemical details of the heterogeneous surface reaction zone during combustion. High-temperature isothermal decomposition studies by T-jump/FTIR spectroscopy give the desired information. The main factor that controls the burn rate of bulk materials at 1 atm is the amount of heat available at the surface. This amount of heat depends not only on the magnitude of  $\Delta H$  but also the time location of main heat release reaction in the overall reaction scheme. The lowest regression rates result mainly from diffusion control as opposed to heat release control.

### Acknowledgement

We are grateful to the Air Force Office of Scientific Research, Aerospace Sciences, for support of this work.

### REFERENCES

1. TIMKEN, M. D., CHEN, J. K. AND BRILL, T. B.: *Appl. Spectrosc.* 44, 701 (1990).
2. CHEN, J. K. AND BRILL, T. B.: *Combust. Flame* 83, 479 (1991).
3. CHEN, J. K. AND BRILL, T. B.: *Combust. Flame* 87, 157 (1991).
4. CHEN, J. K. AND BRILL, T. B.: *Combust. Flame* 87, 217 (1991).
5. BRILL, T. B., BRUSH, P. J., JAMES, K. J., SHEPHERD, J. E. AND PFEIFFER, K. J.: *Appl. Spectrosc.* 46, 990 (1992).
6. BRILL, T. B.: *Prog. Energy Combust. Sci.*, 18, 91 (1992).
7. KUBOTA, N. AND SAKAMOTO, S.: *Prop. Explos. Pyrotech.* 14, 6 (1989).
8. KUBOTA, N. AND SONOBE, T.: *Prop. Explos. Pyrotech.* 13, 172 (1988).
9. BRILL, T. B. AND BRUSH, P. J.: *Phil. Trans. Royal Soc., London A*, 339, 377 (1992).
10. COSGROVE, J. D. AND OWEN, A. J.: *Combust. Flame* 22, 13 (1974).
11. KIMURA, J. AND KUBOTA, N.: *Prop. Explos.* 5, 1 (1980).
12. KARPOWICZ, R. J. AND BRILL, T. B.: *Combust. Flame*, 56, 317, 1984.
13. BEHRENS, R.: *J. Phys. Chem.* 94, 6706 (1990).
14. PALOPOLI, S. F. AND BRILL, T. B.: *Combust. Flame* 87, 45 (1991).
15. WOOLERY, D. O.: Rocketdyne, personal communication, 1992.

### COMMENTS

*Tam Nguyen, DSTO, Australia.* 1. In your experiment on HTPB/IPDI, do you have any idea about the thickness of the heterogeneous reaction zone?

2. In your experiment on the same type of sample, you mentioned the heat release is divided between the gas phase and condensed phase. Have you estimated how much heat release goes to the gas and how much goes to the condensed phase, i.e., in what proportion?

3. Finally, one question about vibrational spectroscopy. What band was attributed to  $\text{C}_2\text{H}_2$  in the BAMO decomposition? The  $\nu_{\text{as}}$  ( $\text{C} \equiv \text{C}$ ) is IR inactive in the gas phase molecule.

*Author's Reply.* 1. At the 1 atm pressure and 625K temperature of the HTPB experiment, the heterogeneous reaction zone is about 60  $\mu\text{m}$  thick.

2. HMX and RDX behave this way. We have not tried to proportion the heat release. Your question is difficult to answer in general terms because the thickness and lifetime of the active surface zone depends on the pressure and temperature. The most exothermic early reaction ( $\text{CH}_2\text{O} + \text{NO}_2$ ) is nominally a gas phase reaction but can occur in voids in the liquid surface which is part of the condensed phase. A combustion model that includes detailed surface features is the best hope for specifying the partitioning of energy release.

3. We used the HCC bending mode ( $\Pi_2$ ) at  $729\text{ cm}^{-1}$ .

*F. A. Williams, University of California at San Diego, USA.* I agree that the chemical mechanism is important in propellant deflagration, and I like your observations on mechanisms in your high-heating-rate experiments. However, I think that the mechanisms are likely to be different for typical high-pressure propellant combustion. For example, I think it unlikely that an energetically neutral zone exists in nitramine deflagration. What do you think?

*Author's Reply.* Our experience has been that pressure up to 65 atm mostly shifts the balance of the existing processes rather than introduces new

processes. That is, mechanism differences with pressure are a matter of degree rather than kind. For example, a decrease in diffusion with increasing pressure may simply push a complex reaction scheme farther to completion in a given volume element. Also, in a complex reaction scheme there is a greater role of bimolecular steps involving the heterogeneous condensed phase compared to unimolecular steps as the pressure is raised.

The simulation experiments of nitramine decomposition indicate that thermally neutral set-up chemistry occurs before the energy is released. However, in practice this chemistry spatially and temporally overlaps the highly exothermic  $\text{CH}_2\text{O} + \text{NO}_2$  reaction; so I agree with you that separate zones would be difficult to distinguish during deflagration.

# Burning surfaces

The details of the heterogeneous reaction zone at the surface of a burning material are elusive. However, insights into this complex zone are now emerging from laboratory techniques designed to simulate some of the key conditions of combustion.

A wide range of processes involve combustion—eg incineration, energy production, propulsion, and flammability.<sup>1</sup> The fundamental details of these processes are complex, involving rapid, heterogeneous, non-equilibrium reactions at high temperature and pressure. The direct determination and measurement of the chemistry at the interface of the bulk condensed phase (parent material) and the gas phase flame zone during combustion often exceeds the capability of modern diagnostics. However, without this knowledge, prediction and control is purely speculative.

Progress is now being made towards understanding burning surface chemistry by developing laboratory techniques that simulate some of the key conditions of combustion. For example, a 'snapshot' of a burning surface shows a thin film reaction zone with a sizable temperature gradient where a rapid phase change is occurring, driven by chemical reactions and heat transfer. This zone could therefore be simulated by a thin film of material which is heated rapidly. The heating rate, temperature, and pressure are controllable and the configuration of the film can be constructed to allow real-time spectroscopic measurements.<sup>2</sup> An example of this technique is T-jump/FTIR spectroscopy<sup>3</sup> in which a film of material is heated on a Pt filament at 2000 °C s<sup>-1</sup> to a chosen temperature, which is maintained while recording the infrared spectrum of the surface gas products at 50 scans s<sup>-1</sup>. These gases are the reactants from the earliest stages of the flame zone and are indicative of rapid decomposition reactions in the film. The gases are normally quenched by

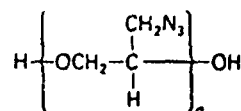
evolving them into a cool atmosphere of argon. By monitoring the control voltage of the Pt filament, the infrared spectra can be connected to the endothermic and exothermic events of the parent material film. These techniques and approaches are applicable to any heterogeneous combustion problem, although this article looks mainly at energetic materials.

An important question is 'how well does the laboratory simulation of the burning surface represent the combustion of the bulk material?' For energetic materials and organic polymers studied to date in our laboratory at the University of Delaware, the answer is 'quite well'. This is seen from the close match of the regression (burn) rate,  $\dot{r}$ , of the thin film calculated from the Arrhenius kinetics of rapid weight loss in another simulation experiment, simultaneous mass and temperature change SMATCH/FTIR,<sup>4</sup> to the linear burn rate of the combusting bulk material (Table 1).<sup>5-7</sup> The important point is that the heat flow to the thin film and to the burning surface have been adequately matched.

Knowing something about the chemical reactions at the burning surface means that combustion events are better understood and can potentially be controlled. For example, explanations are emerging for why some materials burn rapidly while others burn slowly.<sup>8</sup> The mode of action of certain combustion modifiers can also be rationalised.

## Fast burn rate

The linear rate of burning ( $\dot{r}$ ) of a particular material is frequently measured by using a strand burner, whereby the mate-



(1) GAP

rial is cast in the shape of a soda straw and ignited. The distance that the regressing front travels in a fixed amount of time is the linear burning rate.

Strand burner tests on the azide polymer poly(glycidyl azide) (GAP, 1),<sup>8</sup> show a high burn rate (Table 1). Kinetic measurements by using SMATCH/FTIR spectroscopy on a thin film of GAP at 1 atm match the burn rate of bulk GAP quite well.<sup>6</sup> Therefore, rapid thermolysis of a thin film can be used to establish details of the surface reaction zone. The initial decomposition reaction (a) is mildly exothermic. Conversely, the decomposition of the resultant nitrene, RCH<sub>2</sub>N, is highly exothermic. For example, reaction (b) has  $\Delta H = 600\text{--}700 \text{ kJ mol}^{-1}$ .

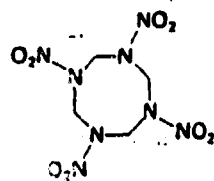


This is shown by the control voltage trace from T-jump/FTIR spectroscopy<sup>3</sup> which reveals violent exothermicity during the release of the decomposition gases. Many reactions of RCH<sub>2</sub>N occur, giving recognisable, stabilised fragments of the GAP polymer backbone<sup>9</sup>—ie CO, CH<sub>2</sub>O, HCN, NH<sub>3</sub>, CH<sub>4</sub>, C<sub>2</sub>H<sub>2</sub>, C<sub>2</sub>H<sub>4</sub>. (N<sub>2</sub> and possibly H<sub>2</sub> are present but are not infrared active.) The appearance of both HCN and NH<sub>3</sub> suggests that the CH<sub>2</sub>N portion of RCH<sub>2</sub>N decomposes by two branches, rather than by reaction (b) alone. When the C–N bond is retained,

Table 1. Burn rates ( $\dot{r}$ ) at 1 atm calculated from the kinetic constants of the microscale laboratory technique SMATCH/FTIR spectroscopy with the macroscale strand burner value extrapolated to 1 atm.

Compound	Burn-rates ( $\dot{r}$ )/mm s <sup>-1</sup>	
	SMATCH/FTIR	Strand burner
GAP	1.35	1.70
HMX	0.37	0.5
HTPB-IPDI	0.19	0.21

<sup>3</sup>SMATCH/FTIR spectroscopy permits simultaneous measurement of the dynamic mass change, temperature change and near-surface gas products of a thin film of material heated at 100–350 °C s<sup>-1</sup>.



(2) HMX

HCN is produced, however when the C-N bond cleaves and H migration occurs,  $\text{NH}_3$  forms. (HCN formation is favoured at higher temperatures.) The infrared active gas products from GAP are the reactants for the first stage of the luminous flame zone when the bulk material is burned.

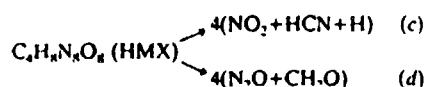
Because strongly exothermic reactions occur very early in the decomposition process, much heat is released at the surface. This high surface heat release is responsible for the high GAP burn rate and suggests that this will be difficult to modify because the decomposition pathway of  $\text{RCH}_2\text{N}$  may not be easy to alter.

### Medium burn rate

The cyclic nitramine, HMX (2), has a lower burn rate than GAP. The burn rate of bulk HMX in a strand burner is about  $0.5\text{ mm s}^{-1}$  at 1 atm.<sup>9</sup> Values of  $\dot{r}$  from SMATCH/FTIR (Table 1) correspond with the strand burner rate, showing that the microscale SMATCH/FTIR technique accurately simulates the amount of heat flow at the surface during macroscale combustion of HMX. The chemistry

learned from T-jump/FTIR spectroscopy reveals why HMX has a lower burn rate at 1 atm than GAP.

Figure 1 shows T-jump/FTIR data for a thin film of HMX heated at  $2000^\circ\text{C s}^{-1}$  to  $298^\circ\text{C}$  and then held at  $298^\circ\text{C}$  while infrared spectra of the near-surface gas products are recorded.<sup>10</sup> Two main stages are apparent during the decomposition. The first stage at 4.0–5.5 s is approximately thermally neutral according to the control voltage trace and yields mainly  $\text{N}_2\text{O}$ ,  $\text{NO}_2$ ,  $\text{CH}_2\text{O}$  and HCN. However,  $\text{N}_2\text{O}$  and  $\text{NO}_2$  are liberated first and leave a residue comprising a complex mixture of various amides and other compounds.<sup>11–15</sup> This residue decomposes primarily to HCN and  $\text{CH}_2\text{O}$ . Interestingly, the relative concentrations of  $\text{NO}_2$  and HCN match one another while  $\text{N}_2\text{O}$  and  $\text{CH}_2\text{O}$  match one another at about 5.5 s. Two stoichiometric reactions, (c) and (d), are consistent with this observation, although they do not fully describe the decomposition process of bulk HMX.



The second stage begins at about 5.5 s where decomposition becomes sharply exothermic according to the control voltage trace. Reaction (e) is probably occurring because  $\text{CH}_2\text{O}$  and  $\text{NO}_2$  are consumed while NO, CO and  $\text{H}_2\text{O}$  appear.

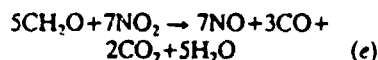


Fig. 1. The relative concentrations of the near surface infrared active gas products quantified from FTIR spectra of a  $200\text{ }\mu\text{g}$  film of HMX heated at  $2000^\circ\text{C s}^{-1}$  to  $298^\circ\text{C}$  and held at  $298^\circ\text{C}$ .

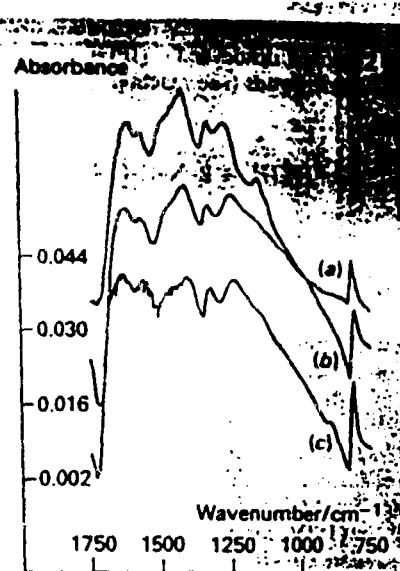
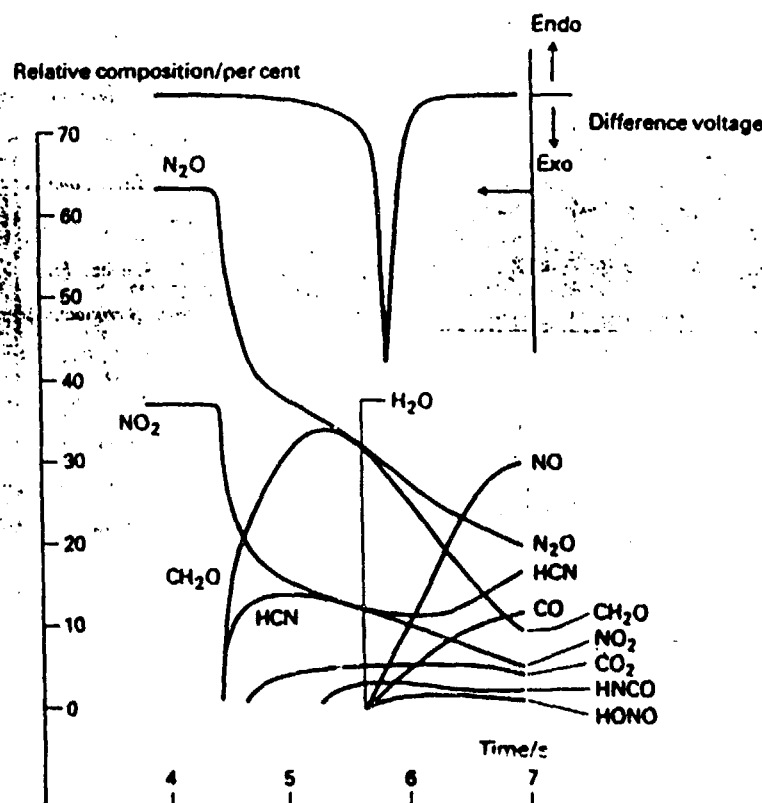


Fig. 2. The transmission infrared spectra of (a) the solid residue from DAG and (b) from DAF; and (c) a sample of melon obtained by heating melamine to  $530^\circ\text{C}$ .

Figure 1 agrees with reaction (e), showing that more NO forms than CO; the large exotherm ( $\Delta H = -1350\text{ kJ mol}^{-1}$ ) makes this reaction the main source of heat in the heterogeneous condensed phase. The time delay in the occurrence of reaction (e) is consistent with autocatalysis; a sufficient concentration of  $\text{CH}_2\text{O}$  and  $\text{NO}_2$  must develop before runaway heat release occurs.

The decomposition of HMX for the  $300^\circ\text{C}$  range also applies at the surface reaction zone temperature of HMX ( $350\text{--}400^\circ\text{C}$ ) during combustion at 1–5 atm. However, the relative importance of reactions (c) and (d) shifts with temperature.<sup>10</sup> The infrared spectra of the product gas ratio ( $\text{N}_2\text{O}/\text{NO}_2$ ) as a function of the filament temperature shows the relative contribution of (c) and (d) at each temperature. Thus the (c):(d) ratio is about 5:7 at  $350\text{--}400^\circ\text{C}$ , matching the stoichiometry of  $\text{CH}_2\text{O}/\text{NO}_2$  in (e). It is at least provocative that the burning surface temperature of HMX is the same temperature at which the first large heat producing reaction (e) is stoichiometrically optimised.

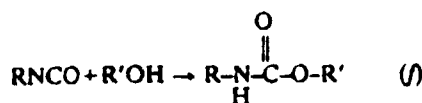
The need for a thermally neutral preparation stage for reactions (c) and (d) to produce the reactants for the later exothermic reaction (e) means that the heat released by reaction (e) is divided between the heterogeneous surface reaction zone (a mixture of solid, liquid and gas phases) and the gas phase flame zone. This late stage heat release gives HMX a lower burn rate than GAP where a very large heat release occurs in the first reaction steps at the surface. Both reaction (c) and reaction (d) need to be altered to increase the concentrations of the reactants for the exothermic reaction (e), explaining why it is difficult to change the burn rate of HMX.

### Slow burn rate

An example of a low burn-rate material is the organic polymer, hydroxyl terminated



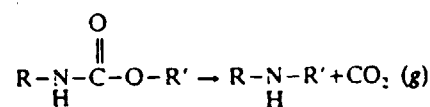
polybutadiene (HTPB) cross-linked by isophorone diisocyanate (IPDI) to form urethane bonds (see reaction f). As



before the SMATCH/FTIR kinetic<sup>2</sup> measurements at 1 atm give a burn rate that agrees well with  $\bar{r}$ , determined during combustion of the bulk polymer<sup>16</sup> (Table 1). Therefore, the degradation of the condensed phase to form smaller molecules for the flame zone can be determined from microscale fast thermolysis.

The first detected gas products above the surface of HTPB-IPDI are  $\text{CO}_2$  and an isocyanate. The isocyanate is most likely to be IPDI formed by the reversal of reaction (f)—IPDI evaporates. The  $\text{CO}_2$  probably comes from another decomposition reaction of the urethane linkage, reaction (g).

Later in the spectra, there are absorbances consistent with butadiene and the



stabilised dimer of butadiene, 4-vinyl-cyclohexane.<sup>7</sup> With the exception of  $\text{CO}$ , all of these products enter the flame zone and become reactants in the presence of a flame. However, the formation of these products is, at most, mildly exothermic and, therefore,  $\bar{r}$  for HTPB-IPDI is controlled mainly by the rate of volatilisation of the fragments from the surface. This is effectively diffusion control and for this particular compound results in a low regression rate. Diffusion control contrasts with HMX and GAP, where the rate and amount of the energy release and the position of the reaction in the time sequence control the burn rate. The burn rate of HTPB could be accelerated with an

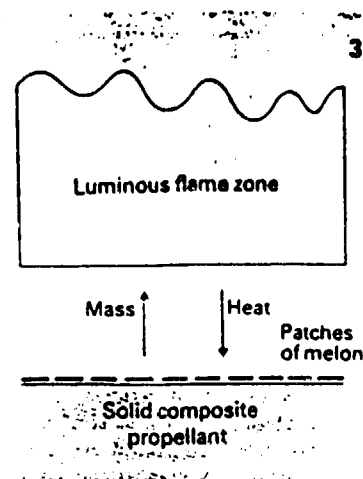
Fig. 3. DAG, DAF and DCD suppress the burn rate of a composite propellant by forming patches of melon and melon on the surface that retard the heat and mass transfer rates.

additive that releases heat in the condensed phase and increases the rate of desorption.

### Combustion controls

Chemical details about the surface reaction zone during combustion indicate ways of modifying the process. An example of how fast thermolysis data have helped in this area is illustrated by studies of diacyandiamide (DCD, 3), diaminoglyoxime (DAG, 4) and diaminofurazan (DAF, 5).<sup>17</sup> These molecules suppress the burn rate of rocket propellants composed of  $\text{NH}_4\text{ClO}_4$ , Al and HTPB (a composite propellant).<sup>18,19</sup> When DCD, DAF and DAG are subjected to high rate thermolysis, they form solid cyclic azines, such as melamine (6), melem (7) and melon (8) (Scheme 1), in addition to low molecular weight gas products. These cyclic azines have a high thermal stability, and the presence of  $\text{NH}_4\text{ClO}_4$  did not affect their formation.<sup>17</sup> In fact, melon is thermally stable in the temperature range at the surface of a burning composite propellant (700°C). Hence, these cyclic azines can accumulate as patches on the surface where they retard the heat and mass transfer between the condensed phase and the gas phase during combustion (Fig. 3). This results in suppression of the burn-rate compared to that of the unmodified propellant.

The suppression of heat and mass transfer by the formation of thermally stable polymeric patches on the surface is predicted with other additives that decompose to DCD, or its monomer, cyanamide ( $\text{NH}_2\text{CN}$ ). A potential burn-rate modifier



is 5-aminotetrazole (5-ATZ, 9), which produces melamine upon fast thermolysis.<sup>20</sup> (The  $\text{NH}_2\text{CN}$  linkage is evident in 5-ATZ).

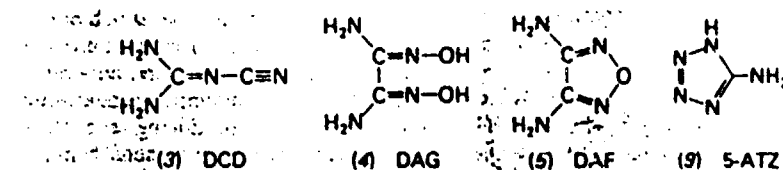
### Conclusions

Despite its importance, the chemistry of the heterogeneous reaction zone at the surface of a combusting solid has proved elusive. However, much information is now emerging from microscale simulation experiments that are designed to mimic the key conditions of combustion. Fast thermolysis studies on thin films reveal the nature of the chemical controls on the burning rate of solids, and sometimes even the mechanism of this reaction. From this information, there appears to be an increasingly bright future for altering and controlling the combustion characteristics of solids.

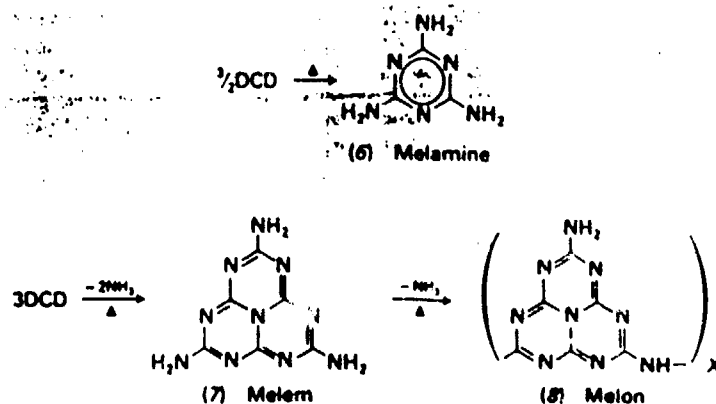
Thomas Brill is professor of chemistry in the department of chemistry, University of Delaware, Newark, Delaware 19716, US.

### References

1. J. A. Miller and G. A. Fisk, *Chem. Eng. News*, August 31, 1987, p. 22.
2. T. B. Brill, *Anal. Chem.*, 1989, 61, 897A.
3. T. B. Brill et al., *Appl. Spectrosc.*, 1992, 46, 900.
4. M. D. Timken, J. K. Chen and T. B. Brill, *ibid.*, 1990, 44, 703.
5. J. K. Chen and T. B. Brill, *Combust. Flame*, 1991, 85, 479.
6. *Idem*, 1991, 87, 157.
7. *Idem*, 1991, 87, 217.
8. N. Kubota and T. Sonobe, *Prop. Explos. Pyrotech.*, 1988, 13, 172.
9. T. L. Boggs, *Prog. Astronaut. Aeronaut.*, 1984, 90, 121.
10. T. B. Brill and P. J. Brush, *Philos. Trans. R. Soc. London, A*, 1992, 339, 377.
11. J. D. Cosgrove and A. J. Owen, *Combust. Flame*, 1974, 22, 13.
12. J. Kimura and N. Kubota, *Prop. Explos.*, 1990, 5, 1.
13. R. J. Karpowicz and T. B. Brill, *Combust. Flame*, 1984, 56, 317.
14. R. J. Behrens, *J. Phys. Chem.*, 1990, 94, 6706.
15. S. F. Palopoli and T. B. Brill, *Combust. Flame*, 1991, 87, 45.
16. R. G. Stacer, S. Eisele and N. Eisenreich, *21st Int. Conf. ICT, Karlsruhe, FRG*, paper no. 80, 1990.
17. C. E. Stoner, Jr and T. B. Brill, *Combust. Flame*, 1991, 83, 302.
18. J. A. Roberts and M. G. Mangum, AFRPL-TR-84-038, California: Air Force Rocket Propulsion Laboratory, Edwards AFB, 1984.
19. M. Chu et al., *US Patent 5071495*, December, 1991.
20. A. Gao, Y. Oyumi and T. B. Brill, *Combust. Flame*, 1991, 83, 345.



Scheme 1. The high rate thermolysis of DCD.



## Thermal Decomposition of Energetic Materials 60. Major Reaction Stages of a Simulated Burning Surface of $\text{NH}_4\text{ClO}_4$

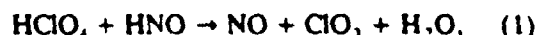
T. B. BRILL,\* P. J. BRUSH, and D. G. PATIL

*Department of Chemistry, University of Delaware, Newark, DE 19716*

Major stages of pyrolysis that occur in a heterogeneous gas-condensed phase layer of  $\text{NH}_4\text{ClO}_4$  (AP) representative of the burning surface are described. T-Jump/FTIR spectroscopy provides the sequence of appearance of the gas products and the corresponding energy balance of a thin layer of AP heated at  $2000^\circ\text{C/s}$  to  $440^\circ\text{C}$  under 13 atm Ar. Some  $\text{HClO}_4$ , but no  $\text{NH}_3$ , escapes the reaction zone before significant heat is released.  $\text{NH}_3$  is oxidized to  $\text{NO}$ ,  $\text{N}_2\text{O}$ , and  $\text{H}_2\text{O}$ . At least some of the  $\text{N}_2\text{O}$  may result from  $2\text{HNO} \rightarrow \text{N}_2\text{O} + \text{H}_2\text{O}$ . As the decomposition rapidly accelerates and becomes strongly exothermic,  $\text{NO}$  and  $\text{H}_2\text{O}$  are formed in large amounts and no more  $\text{HClO}_4$  is evolved. In agreement with previous kinetic schemes, these observations are consistent with the large influence of  $\text{HClO}_4 + \text{HNO} \rightarrow \text{NO} + \text{ClO}_3 + \text{H}_2\text{O}$  in the overall rate. The acceleration of the process may result from growth in the  $\text{HNO}$  concentration. The final product concentrations qualitatively resemble the product profiles determined by microprobe-mass spectrometry of the AP flame. Dynamic weight loss of an AP film determined by SMATCH/FTIR spectroscopy extrapolates reasonably well to the burn rate of AP measured with a combustion bomb.

### INTRODUCTION

In excess of 1000 reactions may be involved in the decomposition and combustion of ammonium perchlorate (AP),  $\text{NH}_4\text{ClO}_4$ , [1] because of the presence of four elements and the full range of oxidation states utilized by nitrogen and chlorine. A limited chain reaction scheme of 10 reactions employed by Guirao and Williams [2] to model AP combustion was expanded to 80 reactions by Ermolin et al. [1], to simulate the gas products in the flame zone measured by microprobe-mass spectrometry [3]. Of the many reactions, Guirao and Williams [2] and Ermolin et al. [1] both emphasize the important role that reaction 1,



plays in controlling the rate of the gas-phase scheme.

Although insight is obtained by using laser pyrolysis-mass spectrometry [4], it would be valuable to have additional experimental evidence of the major steps given the complexity of the reaction scheme. T-Jump/FTIR spectroscopy [5] has the potential to provide evi-

dence of reaction 1 as well as other aspects of the rapid decomposition mechanism of AP. This is because T-jump/FTIR gives the sequence of gas products formed in the heterogeneous gas-condensed phase and correlates this simultaneously with the overall energy balance [6, 7]. For example, during the rapid decomposition of bulk AP, a drop in the  $\text{HClO}_4(\text{g})$  production accompanied by a sharp rise in the  $\text{NO}$  and  $\text{H}_2\text{O}$  concentrations during the stage of rapid heat release would be good evidence for reaction 1 in the heterogeneous gas-condensed phase.

In this article a filmlike sample of AP representative of the reacting surface was heated at about  $2000^\circ\text{C/s}$  to a temperature resembling that during burning, while the gas products were followed in near real-time by rapid-scan FTIR spectroscopy. The results support the important role of reaction 1, as well as indicate other details of the rapid decomposition mechanism of AP.

### EXPERIMENTAL

Finely powdered AP was dried in vacuum for 24 h prior to use. T-Jump/FTIR spectroscopy has been described elsewhere [5]. Approximately 200  $\mu\text{g}$  of sample was thinly spread on

\* Corresponding author.

a Pt ribbon filament that is housed in a gas-tight IR cell having about 25 cm<sup>3</sup> internal volume. The cell was flushed with Ar and pressurized to 13 atm. The filament was heated by a power control unit at about 2000°C/s (the T-jump) to a known constant temperature in the 440–540°C range. Control over the filament was achieved by rapidly sensing its resistance. Endothermicity and exothermicity of the sample is detected by monitoring the control voltage required to maintain constant resistance. The difference control voltage is obtained by subtracting the voltage of the filament without sample from the voltage when the sample is present. A negative slope represents an exotherm of the sample.

Because of the small mass of the sample, its temperature is relatively uniform. However, the interfacial heat transfer is complex [8]. The sample and the filament form a reaction zone that contains the gas and condensed phase in close contact with the heat source. From the point of view of the chemistry of the heterophase surface, this condition qualitatively resembles a surface during combustion. Instead of forming a flame, the decomposition products are quenched by the cool Ar atmosphere. They rise by convection into the IR beam of a Nicolet 20SXB rapid-scan FTIR spectrometer. The beam is about 3 mm above the sample surface. Collection of complete IR spectra every 100 ms gives the identity, sequence of formation, and relative concentrations of the products.

The IR absorbances for each product were converted to concentrations by multiplying the absorbance of a characteristic vibrational mode by a factor derived from the absolute absorbance [9]. In this way the rate of evolution of the product is ascertained. Unfortunately, the IR inactive products O<sub>2</sub> and Cl<sub>2</sub> are not detected and exist in a substantial amount. H<sub>2</sub>O is also detected in large concentration but was not quantified. Two different concentration scaling factors for HCl have been given previously [9, 10] because of different interpretations of the original report [11]. For the work described in this article, the factor of 10.3 (relative to 1 for CO<sub>2</sub>) was used to scale the absorbance [9] and is regarded as the most reliable value because it is based on direct

measurement of the intensity of the HCl vibration-rotation mode at 2820 cm<sup>-1</sup> for known partial pressures of HCl and CO<sub>2</sub>.

The SMATCH/FTIR techniques and data reduction methods have been described elsewhere [12–15]. In SMATCH/FTIR spectroscopy, Simultaneous Mass and Temperature CHange measurements are made along with an FTIR spectroscopy determination of the gas products. Briefly, a film of AP having about 60 μm thickness and about 900 μg mass was coated onto the stainless steel end-tip of the quartz vibration element by repeatedly dipping the tube into an aqueous acetone solution and drying by evaporation. The rate of weight loss during heating at 250°C/s was determined by the change of the vibrational frequency of the tube. A thermocouple spot-welded to the metal end-tip provided a real-time temperature measurement. The initial 50% of weight loss was fit by the polynomial equation

$$1 - \alpha = \sum_{i=0}^3 a_i t^i. \quad (2)$$

This polynomial and its first derivative yield  $1 - \alpha$ , and  $d\alpha/dt$ , respectively for use in Eq. 3, where  $\alpha$  is the fraction of the sample decomposed [13–15]:

$$\ln \left[ \frac{d\alpha}{dt} \frac{1}{(1 - \alpha)^n} \right] = \ln A - \frac{E_a}{RT} \quad (3)$$

Equation 3 was found to be linear with  $n = 1$  and, by use of the temperature of 617 K at 25% of weight loss, was solved for the prefactor  $A$  ( $5.1 \times 10^3 \text{ s}^{-1}$ ) and the global activation energy  $E_a$  (9.0 kcal/mol). These kinetic constants apply only at the pressure and temperature conditions of the experiment. They do not reflect a chemical mechanism. The regression rate of the film,  $\bar{r}$ , was calculated by a modified version of the pyrolysis law,

$$\bar{r} = A^{1/2} h e^{-E_a/2RT} \quad (4)$$

where  $h$  is the film thickness given above. Equation 4 is valid if  $h$  is approximately the thickness of the surface reaction zone during combustion at 1 atm. A value of  $\bar{r} = 0.011 \text{ cm/s}$  was obtained.

### REGRESSION RATE OF AP

The burn rate of bulk nitramine monopropellants, such as HMX, RDX, and DNNC [6, 7], and energetic polymers, such as glycidyl azide polymer and nitrocellulose [13, 14], extrapolate reasonably well to the regression rate computed from the Arrhenius data for rapid weight loss determined by SMATCH/FTIR spectroscopy [7, 12-15]. Hence, the heat flow into the film and to the burning surface scale reasonably well to one another. All the forenamed materials decomposed from the same phase at the temperature and pressure conditions of both the SMATCH and the burn-rate tests. In each case, Eq. 3 could be linearized by the choice of  $n = 2$ .

AP is different. The surface temperature of burning AP is believed to be approximately the melting point of about 560°C, while the temperatures reached in the SMATCH/FTIR study are only 300°-400°C. Consequently, the SMATCH data and the combustion bomb data probably apply to AP decomposing from different phases. As a result, it is possible that the regression rates obtained in a combustion bomb at high pressure will not extrapolate to the SMATCH regression rate at 1 atm. Figure 1 shows that the AP burn rate data of Hightower and Price [16] on single crystals of AP predict approximately twice the burn rate than is measured by the SMATCH technique. The AP data are unusual in that a value of  $n = 1$  was needed to linearize the SMATCH data in Eq. 3. The form of Eq. 3, therefore, might

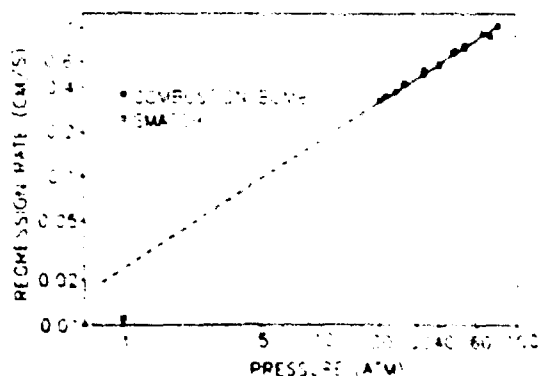


Fig. 1. A comparison of the extrapolated regression rate of single crystal AP measured in a combustion bomb (ref. 16) to that of a film calculated from SMATCH/FTIR data.

depend on the phase during decomposition. This detail was not examined further because the decomposition mechanism of AP is more the central issue.

### DECOMPOSITION PROCESSES

It is not universally agreed upon whether heat is released [2] or consumed [17] in the condensed phase of burning AP because the heat balance is sensitive to the pressure and temperature conditions [4]. It is widely accepted that significant chemistry can occur in the surface layer. Determination of the reactions is experimentally very difficult because the surface layer is specially thin and transient during combustion. However, an instantaneous simulation of the burning surface can be obtained by rapidly heating a thin film of material to the burning surface temperature. Some confidence in this simulation is gained by the fact that the burn rate of pure AP in a combustion bomb extrapolates reasonably well to the rate of weight loss of a rapidly heated thin film, as described in the preceding section.

The sequential chemistry of this heterogeneous gas-condensed phase layer can be stretched over several seconds and studied by T-jump/FTIR spectroscopy [5-7]. The endothermicity or exothermicity of the overall process at each time is obtained from the difference control voltage trace of the Pt filament. The gas products are liberated into a cool nonreactive atmosphere where they are quenched and detected. Although only the more stable products are observed, these products initiate much of the oxidizer flame chemistry and come from the pyrolysis process in the heterophase surface.

Several comments about the IR spectra will help clarify the discussion. Absorbances indicating the formation of a large amount of  $H_2O$  vapor grow during the decomposition of AP. We have difficulty specifying the exact amount of  $H_2O$  because the complex rotation-vibration fine structure is overlapped by other absorptions. However, the large concentration of  $H_2O$  vapor complicates the description of  $HClO_4$ ,  $HCl$ , and  $HNO_3$ , because both the anhydrous and hydrated forms of these acids are potentially present in the vapor phase.

Also, the concentrations of IR inactive products, such as  $\text{Cl}_2$  and  $\text{O}_2$ , are not determined in this article but are established elsewhere by mass spectrometry [1, 3]. Despite these difficulties the IR active gas products that are detected before, during, and after the major heat release stage are evidence of the dominant reactions that occur in the surface layer of burning bulk AP.

#### Pre-exotherm Processes

If, as is frequently thought [18], the surface temperature of burning AP at elevated pressure is  $\geq 560^\circ\text{C}$ , the decomposition reactions are likely to occur too quickly to detect sequential events by rapid-scan FTIR spectroscopy. However, justification exists for using a somewhat lower temperature to study the decomposition mechanism. The surface temperature is about  $330^\circ\text{C}$  at 1 atm [17]. The surface temperature of about  $560^\circ\text{C}$  occurs at the low-pressure deflagration limit of 20 atm

for AP having an initial temperature of  $25^\circ\text{C}$ . The surface temperatures measured by Seleznev et al. [19] at various pressures and extrapolated to 13 atm yield a surface temperatures of about  $440^\circ\text{C}$ . Therefore, the rapid thermal decomposition of AP was studied here at 13 atm Ar on a sample heated at  $2000^\circ\text{C/s}$  to  $440^\circ\text{C}$ . Even if this temperature is unrealistically low for practical combustion conditions, the final gas products from AP decomposition at different temperatures in the  $440^\circ\text{C}$ – $540^\circ\text{C}$  range are found to be quite similar. Consequently, the overall decomposition mechanism appears to be similar in this temperature range.

Figure 2 shows the change of concentration of the gas products from AP measured from the absorbances by rapid-scan FTIR spectroscopy, along with the heat balance that is sensed by the control voltage of the Pt filament. IR active gas products are first detected at about 5 s and consist of  $\text{HNO}_3$ ,  $\text{NO}_2$ ,  $\text{N}_2\text{O}$ ,  $\text{H}_2\text{O}$ ,  $\text{HClO}_4$ , and  $\text{HClO}_4(\text{aq})$ . The rise in gas product concentrations over the next few sec-

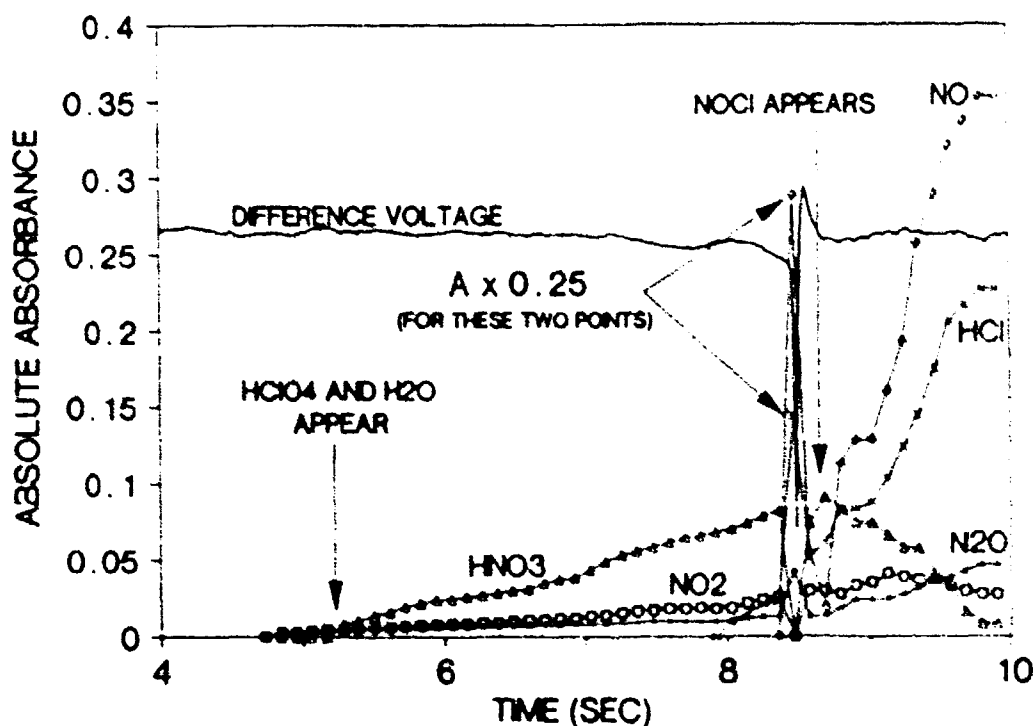
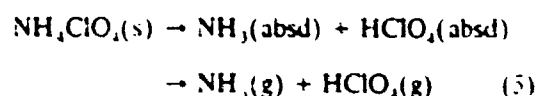


Fig. 2. T-Jump/FTIR data for 300  $\mu\text{g}$  of AP heated at  $2000^\circ\text{C/s}$  to  $440^\circ\text{C}$  under 13 atm Ar. Gradual decomposition occurs initially with slow growth in the IR active gas products and slight exothermicity (negative sloping of the control voltage). At the exotherm,  $\text{NO}$ ,  $\text{H}_2\text{O}$  (not shown), and  $\text{HCl}$  spike. Final concentrations are reached at 10 s after the gas disturbance in the cell settles down.

onds indicates that the amount of sample decomposing gradually increases. The overall process is exothermic because the control voltage acquires a slight negative slope during this time.

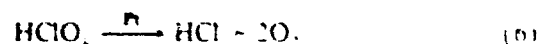
The initial decomposition reaction of AP is widely regarded to be dissociative evaporation:



Evidence of this reaction exists below 3 atm where the recombination of  $\text{NH}_3(\text{g})$  and  $\text{HClO}_4(\text{g})$  to form  $\text{NH}_4\text{ClO}_4$  (aerosol) is observed in the IR spectrum. Below 13 atm Ar, Fig. 3 shows that no  $\text{NH}_4\text{ClO}_4$  (aerosol) and  $\text{NH}_3$  (*vide infra*) are detected, but that  $\text{HClO}_4$  is present, mostly in the hydrated form. The fact that some  $\text{HClO}_4$  survives to reach the cool atmosphere, whereas  $\text{NH}_3$  does not, may simply result from the fact that AP is over oxidized. Not all of the  $\text{HClO}_4$  is needed to oxidize  $\text{NH}_3$ . Hydrated  $\text{HClO}_4$  from AP was confirmed by the match of the  $\text{ClO}_4^-$  asymmetric stretching mode with that of the gas

phase above a rapidly heated 70%  $\text{HClO}_4$  solution.

The complex multiplet from the asymmetric Cl-O stretching mode of anhydrous  $\text{HClO}_4$  overlaps a mode of  $\text{HNO}_3$ , but resembles the reported spectrum [20]. The absence of  $\text{NH}_4\text{ClO}_4$  (aerosol) is indicated by the fact that the  $\text{ClO}_4^-$  absorptions in Fig. 3 do not match  $\text{NH}_4\text{ClO}_4$  (solid). Figure 4 shows that the O-H stretching region of the gas products above decomposing AP before the exotherm closely resembles that of vaporized aqueous  $\text{HClO}_4$ .  $\text{HCl}(\text{g})$  and hydrated  $\text{HCl}$ , discussed in the next section, are absent or present in an undetectable amount. The observation of  $\text{HClO}_4$  and absence of  $\text{HCl}$  in this stage of the experiment alleviates concerns that the Pt filament is chemically involved in the gas products observed. Platinum is known to catalyze as [21]



but apparently does not do so significantly under the conditions of these experiments. Even the gas phase above 70%  $\text{HClO}_4$  that has been heated on the Pt filament contains no  $\text{HCl}$  (Fig. 5).

The  $\text{NH}_3$  from reaction 5 is oxidized very rapidly in the hot heterogeneous gas-condensed phase zone by  $\text{HClO}_4$ . No  $\text{NH}_3$  survives to reach the IR beam because the inversion doublet at 968 and 932  $\text{cm}^{-1}$  is absent in Fig. 3. The reduction product of  $\text{HClO}_4$  is  $\text{Cl}_2$

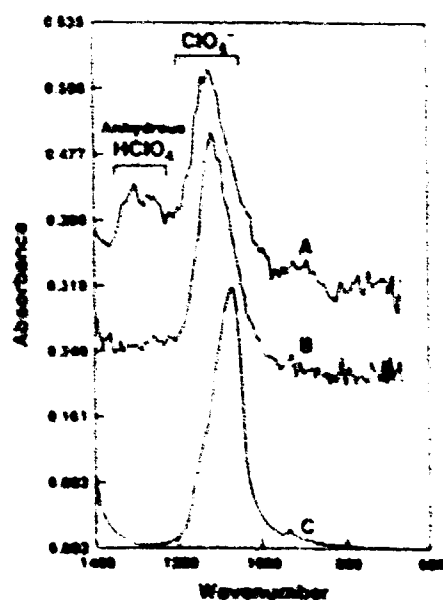


Fig. 3 IR spectra of the  $\text{ClO}_4^-$  asymmetric stretching region. Gas phase over (A) AP before exotherm showing hydrated and anhydrous  $\text{HClO}_4$ ; (B) A 70%  $\text{HClO}_4$  solution heated on the filament; (C) Solid AP showing that little or no  $\text{NH}_4\text{ClO}_4$  aerosol forms in A.

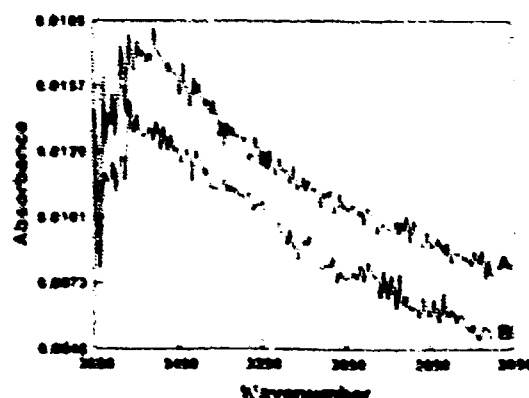


Fig. 4 IR spectra of the OH stretching region of the gas phase over (A) AP before the exotherm; (B) 70%  $\text{HClO}_4$  heated on the filament. Only hydrated  $\text{HClO}_4$  is present before the exotherm.

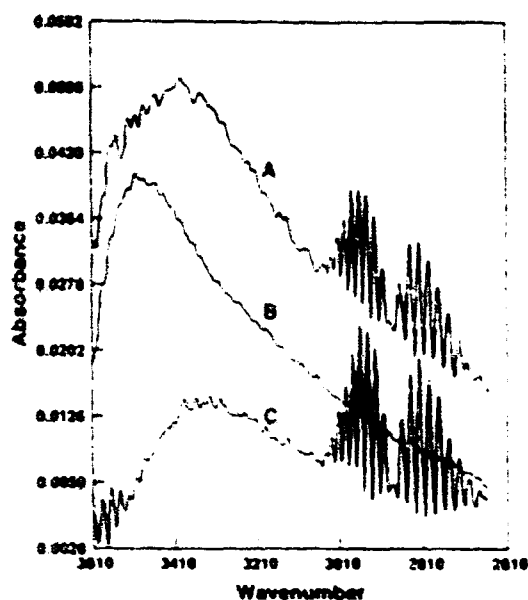


Fig. 5. The OH and HCl IR stretching region. The gas phase over: (A) AP after the exotherm showing that anhydrous HCl, hydrated HCl, and hydrated HClO<sub>4</sub> are all present. (B) Aqueous 70% HClO<sub>4</sub> vaporized from the filament. (C) Aqueous 40% HCl vaporized from the filament.

because no HCl (g), hydrated HCl, or NH<sub>4</sub>Cl (aerosol) is observed in this stage of decomposition. NO<sub>2</sub>, N<sub>2</sub>O, HNO<sub>3</sub>, and H<sub>2</sub>O are products of ammonia oxidation. HNO<sub>3</sub> may simply result from hydrolysis of NO<sub>2</sub> and, as such, would not be an important product were a flame present. N<sub>2</sub>O can form by [1]



Preventing the buildup of HNO (see *infra*) by reaction (7) would be one of the chemical ways that AP is able to decompose slowly at lower temperature without developing a runaway release of heat.

#### Exotherm and Post-Exotherm Processes

The development and growth of exotherm of the AP in Fig. 2 is a sharp event. The gas product concentrations during the exotherm are unusual in the occurrence of the large pulse of NO, HCl, and H<sub>2</sub>O. The HClO<sub>4</sub> concentration remains at or below the pre-exotherm level. The behavior of HClO<sub>4</sub>, NO, and

H<sub>2</sub>O are fully consistent with a major role of reaction 1 in the acceleratory exothermic phase of AP decomposition. Reaction 1 increases in importance and ultimately controls the overall rate because HNO accumulates with time [1]. At the time when reaction 1 dominates the rate, reaction 7 is largely bypassed as evidenced by the fact that the final concentration of N<sub>2</sub>O is only approximately double the pre-exotherm value. Because of their reactivity and short-life time at the temperature of the experiment, HNO and ClO<sub>2</sub> are not detected. In fact, for the same reason, no chlorine oxides or HClO are observed here, but they are by mass spectrometry [1, 3]. HNO has also been detected by mass spectrometry in the decomposition of AP [22].

After the exotherm, nonuniform turbulent mixing and deflection of the IR beam caused by the change of refractive index of the gases both perturb the concentration profiles. The steady-state concentrations are reached about 2 s after the exotherm, but are affected by several secondary reactions. The particular reactions may not be important in the flame zone where the temperature rises steeply in the gas phase. An illustration of how care is needed in interpreting the IR spectra of the gas products is shown in Fig. 5. Following the exotherm, the O-H stretching region of the gas phase is the composite of hydrated HClO<sub>4</sub> vapor, hydrated HCl vapor, and anhydrous HCl. Figure 5 contrasts with Fig. 4 of this region before the exotherm where only hydrated HClO<sub>4</sub> is detected.

An indication of the role of perturbing secondary reactions and the universality of the chemical mechanisms is obtained by comparing the final concentrations in Fig. 2 to those measured by microprobe-mass spectrometry of the AP flame at 1 atm [4]. Table I gives the relative concentrations of the measured products in common in these two studies. In the broad sense the pattern is the same, which is gratifying given the very different experimental conditions. The flame zone and fast thermolysis methods agree that NO<sub>2</sub> and N<sub>2</sub>O have relatively low and about equal concentration. Also, both methods indicate that the HCl and NO concentrations are considerably higher than N<sub>2</sub>O and NO<sub>2</sub>, but disagree on the mag-

TABLE I

Gas Products from Rapid Pyrolysis of AP ( $\geq 440^\circ\text{C}$ )  
Quantified by Two Methods

	Mass Fraction (mass spectrometry) <sup>a</sup>	Relative Absorbance (IR spectroscopy) <sup>b</sup>
HCl	0.12	0.24 <sup>c</sup>
NO	0.10	0.35
NO <sub>2</sub>	0.04	0.03
N <sub>2</sub> O	0.03	0.04

<sup>a</sup> 1.5 cm above surface in flame zone at 1 atm (ref. 1).

<sup>b</sup>  $440^\circ\text{C}$  under 13 atm Ar (this work).

<sup>c</sup> Anhydrous HCl.

nitude of the difference. In reality, the true NO concentration is underestimated to some extent in the fast thermolysis data because an absorbance at  $1800\text{ cm}^{-1}$  indicates the presence of NOCl. NOCl forms by



but cannot be quantified for the lack of absolute absorbance data. The HCl concentration is also somewhat underestimated in the fast thermolysis data because the quantified amount shown is only from HCl(g). Aqueous HCl vapor is also present as shown in Fig. 5. Although the mass spectral and IR analysis do not agree quantitatively, the similar trends give confidence that these two techniques describe the same chemistry.

The importance of Cl-O homolysis of  $\text{HClO}_4$  in initiating and perhaps controlling rapid decomposition of AP has been repeatedly emphasized in many studies. In the present study a case can also be made for a fundamental role for HNO in the same sense that products of both the early stage and exothermic stage are consistent with reactions of involving HNO.

*We are grateful to the Air Force Office of Scientific Research, Aerospace Sciences, for support of this work on AFOSR-89-0521.*

## REFERENCES

1. Ermolin, N. E., Korobeinichev, O. P., Tereshenko, A. G., and Fomin, V. M., *Combust. Explos. Shock Waves* 18:180-189 (1982).
2. Guirao, C., and Williams, F. A., *AIAA J.* 9:1345-1356 (1971).
3. Korobeinichev, O. P., and Tereshenko, A. G., *Tenth Materials Research Symposium Churct. High Temperature Vapors and Gases*, NBS publ. 561, Gaithersburg, MD, 1978, pp. 479-490.
4. Pellett, G. L., *Fourteenth Symp. (International) Combustion*, The Combustion Institute, Pittsburgh, 1973, pp. 1317-1330.
5. Brill, T. B., Brush, P. J., James, K. J., Shepherd, J. E., and Pfeiffer, K. J., *Appl. Spectrosc.* 46:900-911 (1992).
6. Brill, T. B., and Brush, P. J., *Philos. Trans. R. Soc. (Lond.) A*, 339:377-385 (1992).
7. Brill, T. B., Patil, D. G., Duterque, J., and Lengellé, G., *Combust. Flame*, submitted.
8. Shepherd, J. E., Brill, T. B., and Brush, P. J., in press.
9. Brill, T. B., *Prog. Energy Combust. Sci.* 18:91-116 (1992).
10. Chen, R. M., Russell, T. P., Rheingold, A. L., and Brill, T. B., *J. Crystallogr. Spectrosc. Res.* 21:167-171 (1991).
11. Szczepanik K., and Person, W. B., *J. Mol. Struct.* 80:309-316 (1982).
12. Timken, M. D., Chen, J. K., and Brill, T. B., *Appl. Spectrosc.* 44:701-706 (1990).
13. Chen, J. K., and Brill, T. B., *Combust. Flame* 85:479-488 (1991).
14. Chen, J. K., and Brill, T. B., *Combust. Flame* 87:157-168 (1991).
15. Chen, J. K., and Brill, T. B., *Combust. Flame* 87:217-232 (1991).
16. Hightower, J. D., and Price, E. W., *Eleventh Symposium (International) Combustion*, The Combustion Institute, Pittsburgh, 1967, pp. 463-472.
17. Yano, Y., Miyata, K., Kubota, N., and Sakamoto, S., *Prop. Explos. Pyrotech.*, 12:137-140 (1987).
18. Beckstead, M. W., *Twenty-Sixth JANNAF Combustion Meeting*, CPIA Publication 529, 4:255-268 (1989).
19. Seleznev, V. A., Pokhil, P. F., Maltsev, V. M., and Bavykin, I. B., *Combust. Flame* 13:139-142 (1969).
20. Karelin, A. I., Grigorovich, Z. I., and Rosolovskii, V. Ya., *Spectrochim. Acta* 31A:765-771 (1975).
21. Heath, G. A., and Majer, J. R., *Trans. Farad. Soc.* 60:1783-1791 (1964).
22. Hackman, E. E., Hesser, H. H., and Beachell, H. C., *J. Phys. Chem.* 76:3545-3554 (1972).

Received 12 October 1992; revised 2 February 1993



## FTIR SPECTROSCOPY FOR SURFACE PYROLYSIS PHENOMENA AND FLAME DIAGNOSTICS

Thomas B. Brill

Department of Chemistry  
University of Delaware  
Newark, DE 19716 USA

### INTRODUCTION

Chemical description of the combustion and explosion of bulk energetic materials continues to be one of the greatest challenges to the energetics community. Laser diagnostic and microprobe mass spectrometry are established techniques for characterizing the homogeneous flame zone in terms of the species, concentrations and the temperature profile [1]. A particularly daunting problem has been the chemical description of the heterophase reaction zone at the surface of a burning propellant. The chemistry of this region is important because it connects the flame characteristics to the formulation of the propellant. During combustion, this condensed phase-to-gas phase transition zone is specially thin, has a steep temperature gradient and has a microstructure of mixed phases that

are shown in Figure 1. No experimentally-based description of the chemical details of this reaction zone has been possible while the flame is present. An alternate approach to gain the required information is to simulate the conditions of the surface zone in a manner that enables spectroscopic diagnostics to be conducted. Hence, the larger part of this article is devoted to the use of FTIR spectroscopy to characterize dynamically the simulated surface reaction zone of a burning propellant. The applications of FTIR spectroscopy to characterize the flame zone conclude the article. The use of FTIR spectroscopy to characterize recovered samples or with time-delayed analysis is not covered because of space limitations.

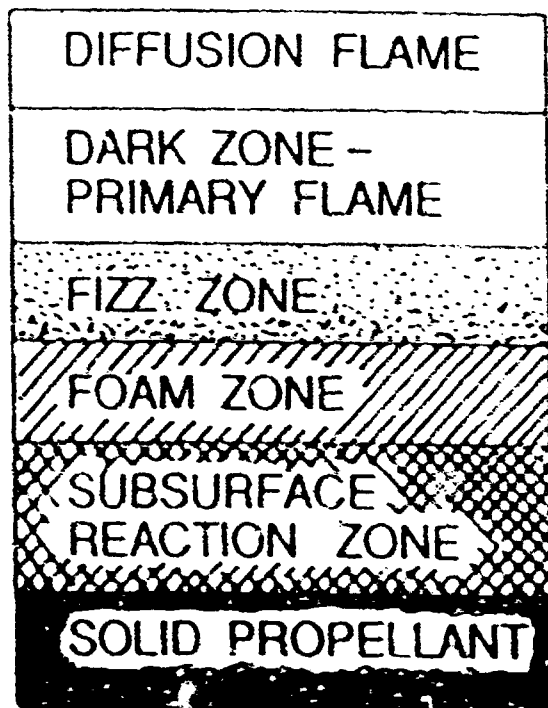


Figure 1. The generalized 1-D surface reaction zone of a burning propellant

FTIR spectroscopy has the advantage over dispersive IR methods when high energy throughput, rapid data acquisition and broad band IR spectra are required. For real or near real-time data acquisition, a research grade rapid-scanning FTIR spectrometer (RSFTIR) is invaluable. Fortunately, commercial instrumentation is available so that little space needs to be devoted to the theory and practice of FTIR spectrometry [2].

The RSFTIR spectrometer takes advantage of the fact that both the forward and reverse motions of the moving mirror of a Michelson interferometer can generate all of the spectral information. This fact, coupled with a high mirror velocity and a very stable interferometer, allows mid-IR spectra to be collected at 60-80 scans per second with 16-32  $\text{cm}^{-1}$  resolution. A mercury-cadmium-telluride (MCT) detector and digital signal processing provide a low noise signal in which absorbances from all IR active species are clearly evident in a single-scan spectrum. The interferograms acquired in this way are stored independently by fast analog-digital transfer with the time attached to each interferogram. At a later time, the interferograms are transformed to spectra. The operator can manipulate many of the parameters of the data collection and Fourier transformation to optimize the scan speed, resolution and spectra details. We settled on a scan speed of ten scans/sec at 4  $\text{cm}^{-1}$  resolution as optimal for our research. However, a faster scan speed could have been chosen while sacrificing resolution. Modifications of the sample compartment may also be required to be compatible with the conditions of the experiment. For example, a high temperature flame can heat the optics and create interference patterns. This can be eliminated by the use of wedged windows.

Perhaps the most important consideration in the solution of combustion and explosion problems by FTIR spectroscopy is the design of sample cells that simulate the conditions appropriate for the event being sought. Most of our effort has gone into this area and is described next.

#### ANALYSIS OF SURFACE PYROLYSIS PROCESSES BY FTIR SPECTROSCOPY

FTIR spectroscopy is an effective method to identify and quantify gases produced by fast reactions of solids and liquids, such as burning energetic materials [3]. When studying ignition, combustion and explosion phenomena, the sample must be heated rapidly. To capture the important events, the FTIR analysis must be performed with minimal time delay between the event and analysis. Hence, the IR beam should be focused as close to the reacting surface as possible and the data collected by RSFTIR. If the gases are evolved into a cool non-reactive atmosphere, they will quench and be detected. Since the time-delay between the reaction and the analysis is minimal, many relatively reactive species are observed with concentrations more close to the original than when longer time-delays exist. Of course, the time delay is still large relative to the rates of the elementary reactions. Nevertheless, the instantaneous relative concentrations of the gases are observed that feed the flame zone, if a flame were present. Analysis of the gas products can be made if the flame is present, but the flame zone products tend to dominate the reactive, near-surface products in this case.

## FTIR SPECTROSCOPY

FTIR spectroscopy has the advantage over dispersive IR methods where high energy throughput, rapid data acquisition and broad band IR spectra are required. For real or near real-time data acquisition, a research grade rapid-scanning FTIR spectrometer (RSFTIR) is invaluable. Fortunately, commercial instrumentation is available so that little space needs to be devoted to the theory and practice of FTIR spectrometry [2].

The RSFTIR spectrometer takes advantage of the fact that both the forward and reverse motions of the moving mirror of a Michelson interferometer can generate all of the spectral information. This fact, coupled with a high mirror velocity and a very stable interferometer, allows mid-IR spectra to be collected at 60-80 scans per second with 16-32  $\text{cm}^{-1}$  resolution. A mercury-cadmium-telluride (MCT) detector and digital signal processing provide a low noise signal in which absorbances from all IR active species are clearly evident in a single-scan spectrum. The interferograms acquired in this way are stored independently by fast analog-digital transfer with the time attached to each interferogram. At a later time, the interferograms are transformed to spectra. The operator can manipulate many of the parameters of the data collection and Fourier transformation to optimize the scan speed, resolution and spectra details. We settled on a scan speed of ten scans/sec at 4  $\text{cm}^{-1}$  resolution as optimal for our research. However, a faster scan speed could have been chosen while sacrificing resolution. Modifications of the sample compartment may also be required to be compatible with the conditions of the experiment. For example, a high temperature flame can heat the optics and create interference patterns. This can be eliminated by the use of wedged windows.

Perhaps the most important consideration in the solution of combustion and explosion problems by FTIR spectroscopy is the design of sample cells that simulate the conditions appropriate for the event being sought. Most of our effort has gone into this area and is described next.

### ANALYSIS OF SURFACE PYROLYSIS PROCESSES BY FTIR SPECTROSCOPY

FTIR spectroscopy is an effective method to identify and quantify gases produced by fast reactions of solids and liquids, such as burning energetic materials [3]. When studying ignition, combustion and explosion phenomena, the sample must be heated rapidly. To capture the important events, the FTIR analysis must be performed with minimal time delay between the event and analysis. Hence, the IR beam should be focused as close to the reacting surface as possible and the data collected by RSFTIR. If the gases are evolved into a cool non-reactive atmosphere, they will quench and be detected. Since the time-delay between the reaction and the analysis is minimal, many relatively reactive species are observed with concentrations more close to the original than when longer time-delays exist. Of course, the time delay is still large relative to the rates of the elementary reactions. Nevertheless, the instantaneous relative concentrations of the gases are observed that feed the flame zone, if a flame were present. Analysis of the gas products can be made if the flame is present, but the flame zone products tend to dominate the reactive, near-surface products in this case.

The most powerful laser-based technique for determining the chemical processes in the burning surface reaction zone is T-jump/FTIR spectroscopy [4]. The technique is based on recreating a "snap shot" view of the reaction zone of a burning surface (Figure 1), which is a thin layer of rapidly heated material. This scenario is produced by T-jump/FTIR spectroscopy in which a thin film of material is heated at 20000°C/sec to a constant chosen temperature while simultaneously monitoring the heat flow to the film and determining the gaseous products released in near real-time. Figure 2 shows the essential details of this experiment.

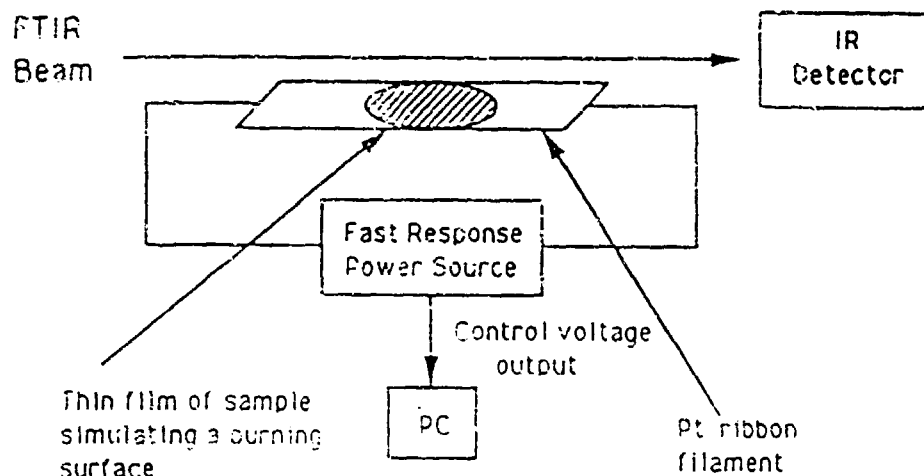


Figure 2. The T-jump/FTIR experiment

Typically, approximately 200  $\mu\text{g}$  of polycrystalline sample is spread on a Pt ribbon filament that is housed in a gas-tight IR cell having about 25  $\text{cm}^3$  internal volume. The cell is flushed with Ar and pressurized as desired. The filament is heated by a power control unit at about 2000°C/sec to a constant temperature in the 240-500°C range depending on the sample. Control is achieved by rapidly sensing the Pt resistance. Endothermicity and exothermicity of the sample is detected by monitoring the control voltage required to maintain constant resistance. The difference control voltage is obtained by subtracting the voltage of the filament without sample from the voltage when the sample is present. A negative excursion represents an exotherm of the sample.

Because of the small mass, the sample temperature is relatively uniform. However, the interfacial heat transfer is complex. The sample and the filament form a reaction zone that contains the gas and condensed phase in close contact with the heat source. From the point of view of the chemistry of the heterophase surface, this condition qualitatively resembles a surface during combustion. Instead of forming a flame, the decomposition products rise into and are quenched by the cool Ar atmosphere. The beam of the RSFTIR spectrometer is positioned about 3 mm above the sample surface. Collection of complete IR spectra every 100 msec gives the identity, sequence of formation, and relative concentrations of the products.

The IR absorbances of each product are converted to concentrations by multiplying the absorbance of a characteristic vibrational mode

Table 1  
The Multiplicative Factor F used in Relative  
Percent Concentration Calculations

Gas	Absorbance, cm <sup>-1</sup>	F
CO <sub>2</sub>	2349 (R)	1 <sup>a</sup>
HNCO	2274 (R)	1.5 <sup>b</sup>
N <sub>2</sub> O	2224 (R)	2
CO	2143 (P)	25
NO	1876 (R)	32
CH <sub>2</sub> O	1744 (R)	15
HNO <sub>3</sub>	1709	8
NO <sub>2</sub>	1621	2
HCOOH	1103	3.7
NH <sub>3</sub>	968 (Q)	5
HONO (cis)	856 (Q)	3.2 <sup>c</sup>
HONO (trans)	794 (Q)	
HCN	713 (Q)	3
CH <sub>4</sub>	3020 (Q)	11
C <sub>2</sub> H <sub>4</sub>	949	7.5
C <sub>2</sub> H <sub>2</sub>	729	3.4
HCl	2974 (R)	10.3

<sup>a</sup>reference compound  
<sup>b</sup>estimated  
<sup>c</sup>sum of cis and trans intensity

by a factor F derived from the absolute absorbance [5]. Table 1 gives the values of F used. In this way the rate of evolution of the product is ascertained. IR inactive products are not detected. H<sub>2</sub>O is frequently detected but was not quantified.

### Surface Chemistry of Nitramines

Nitramines, such as HMX and RDX, are especially important as minimum smoke, high energy explosive and propellant ingredients. The decomposition of HMX [6] and RDX [7] is similar and so only RDX will be described.

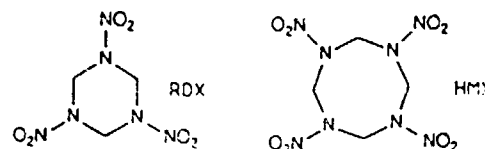
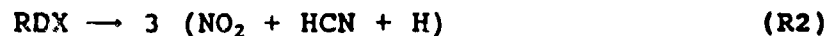


Figure 3 shows T-jump/FTIR data for a thin film of RDX heated at 2000°C/sec to 263°C and then held isothermally while IR spectra of the near-surface gas products are recorded. The global decomposition branches, R1 and R2 occur for bulk RDX and HMX. R1 and R2 imply that N<sub>2</sub>O

and NO<sub>2</sub> should form simultaneously with CH<sub>2</sub>O and HCN. This is not found at any temperature studied. Rather, N<sub>2</sub>O and NO<sub>2</sub> appear before

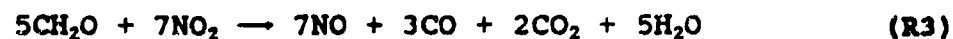


CH<sub>2</sub>O and HCN, which form from the residue left by elimination of N<sub>2</sub>O and NO<sub>2</sub>. This residue is a mixture of products like hydroxymethylformamide and acetamide [8-11], which decompose and delay the release of CH<sub>2</sub>O, HCN and HNCO [11,12].

The total IR absorbance of the products accelerates between 3.5 and 5.0 sec despite the constant heat flow from the filament, which implies that autocatalysis occurs in this stage of decomposition of HMX and RDX. Moreover, the control voltage trace in Figure 3 reveals only mild exothermicity between 3.5 and 4.5 sec when R1 and R2 dominate. Thus, these reactions release little energy in the condensed phase.

A runaway exotherm develops at 4.5 sec. The secondary reaction R3 appears to be responsible because CH<sub>2</sub>O and NO<sub>2</sub> are consumed as NO,

CO, and H<sub>2</sub>O appear. Figure 3 shows that more NO than CO forms in



accordance with R3. R3 is highly exothermic as written ( $\Delta H = -320$  kcal) and, by the large exotherm in Figure 3, it is the main source of heat in the heterogeneous condensed phase. These conclusions also apply at 360°C (Figure 3) except that the time-scale is compressed. Hence, this description of the decomposition of RDX at 263°C applies as well at the surface reaction zone temperature (350 - 400°C) during combustion. However, the branching ratio of R1 and R2 depends on temperature and favors R2 at higher temperature [6]. This finding is illustrated by Figure 4, where the final

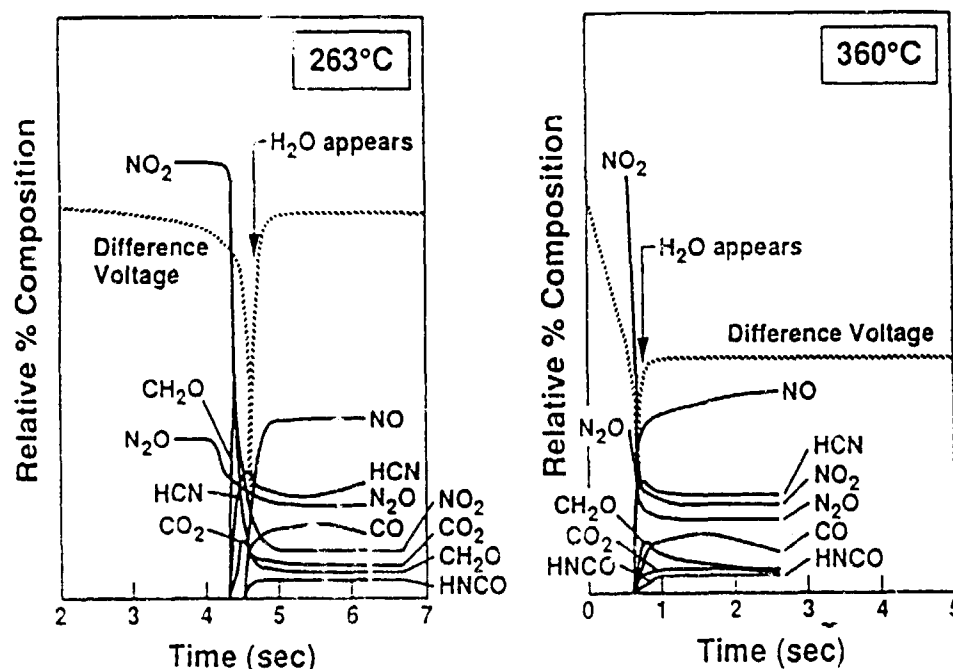


Figure 3. The gas products and heat change of RDX at 263°C and 360°C under 4 atm Ar

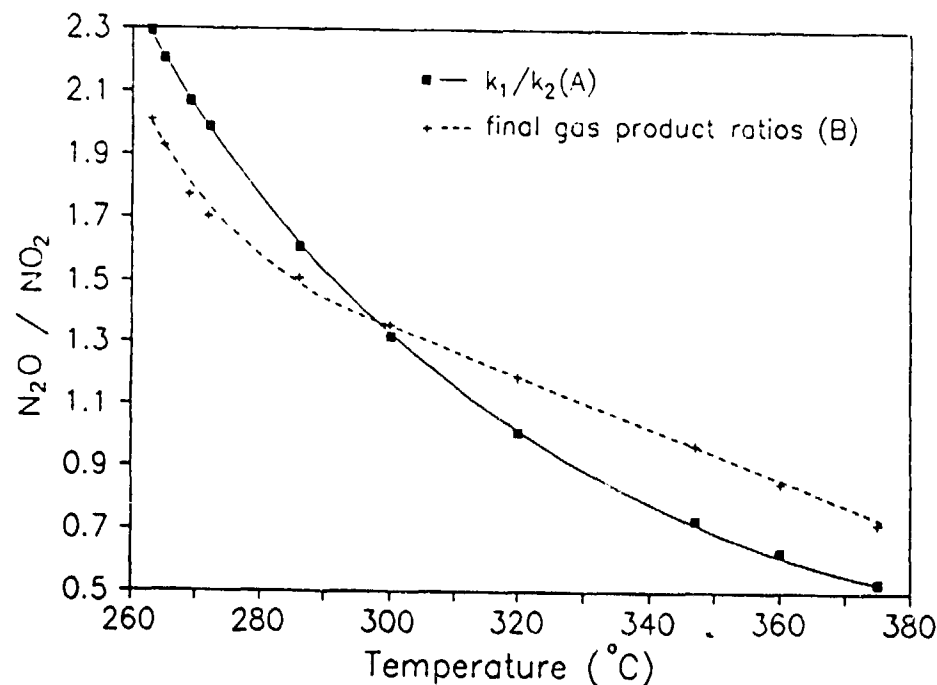


Figure 4. The calculated and experimental temperature dependence of the R1/R2

$\text{N}_2\text{O}/\text{NO}_2$  product concentration ratio is plotted vs. the temperature to which the sample was T-jumped. Also shown is the ratio of the rate constants  $k_1$  and  $k_2$  representative of R1 and R2, respectively, given by Melius [13]. The agreement in the trends is reasonably good indicating that the rates of the semi-global decomposition branches R1 and R2 can be experimentally verified.

$$k_1 = 10^{13} \exp(-36000/RT) \text{ sec}$$

$$k_2 = 2 \times 10^{16} \exp(-45000/RT) \text{ sec}$$

#### Surface Chemistry of $\text{NH}_4\text{ClO}_4$

In excess of 1000 reactions may be involved in the decomposition and combustion of ammonium perchlorate (AP),  $\text{NH}_4\text{ClO}_4$ , [14] because of the presence of four elements and the full range of oxidation states utilized by nitrogen and chlorine. A limited chain reaction scheme of 10 reactions employed by Guirao and Williams [15] to model AP combustion was expanded to 80 reactions by Ermolin, et al., [14] to simulate the gas products in the flame zone measured by microprobe-mass spectrometry [16]. Of the many reactions, Guirao and Williams and Ermolin, et al., both emphasize the important role that R4 plays in controlling the rate of the gas phase scheme.



T-Jump/FTIR spectroscopy [4] has the potential to provide evidence of R4 as well as other aspects of the rapid decomposition mechanism of AP. For example, during the rapid decomposition of bulk AP, a drop in the  $\text{HClO}_4(\text{g})$  production accompanied by a sharp rise in the  $\text{NO}$  and  $\text{H}_2\text{O}$  concentrations during the stage of rapid heat release would be good evidence for R4 in the heterogeneous gas-condensed phase. Figure 5 shows the change of concentration of the gas products from AP measured from the absorbances by RSFTIR, along

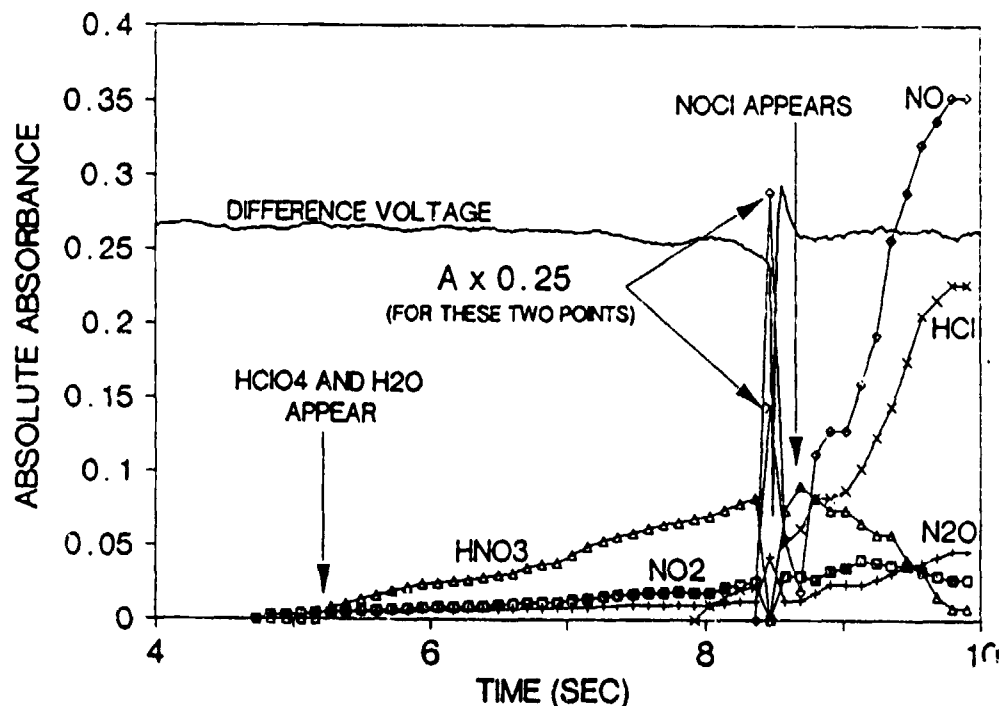
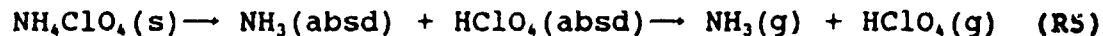


Figure 5. Gas products and the heat change of  $\text{NH}_4\text{ClO}_4$  at  $440^\circ\text{C}$  under 13 atm Ar

with the heat balance sensed by the Pt control voltage [17]. Before the exotherm, IR active gas products are first detected at about 5 sec and consist of  $\text{HNO}_3$ ,  $\text{NO}_2$ ,  $\text{N}_2\text{O}$ ,  $\text{H}_2\text{O}$ ,  $\text{HClO}_4$ , and  $\text{HClO}_4(\text{aq})$ . The rise in gas product concentrations over the next few seconds indicates that the amount of sample decomposing gradually increases. The overall process is exothermic because the control voltage acquires a slight negative slope during this time.

The initial decomposition reaction of AP is widely regarded to be dissociative evaporation R5. Evidence of this reaction exists



below 3 atm where recombination of  $\text{NH}_3(\text{g})$  and  $\text{HClO}_4(\text{g})$  to form  $\text{NH}_4\text{ClO}_4(\text{aerosol})$  is observed in the IR spectrum. Below 13 atm Ar, no  $\text{NH}_4\text{ClO}_4(\text{aerosol})$  and  $\text{NH}_3$  are detected, but  $\text{HClO}_4$  is present, mostly in the hydrated form. The fact that some  $\text{HClO}_4$  survives to reach the cool atmosphere, whereas  $\text{NH}_3$  does not, may simply result from the fact that AP is over oxidized. Not all of the  $\text{HClO}_4$  is needed to oxidize  $\text{NH}_3$ . Hydrated  $\text{HClO}_4$  from AP was confirmed by the match of the  $\text{ClO}_4^-$  asymmetric stretching mode with that of the gas phase above a rapidly heated 70%  $\text{HClO}_4$  solution [17].

The  $\text{NH}_3$  from R5 is oxidized very rapidly in the heterogeneous gas-condensed phase zone by  $\text{HClO}_4$ . No  $\text{NH}_3$  survives to reach the IR beam because the inversion doublet at 968 and 932  $\text{cm}^{-1}$  is absent. The reduction product of  $\text{HClO}_4$  is  $\text{Cl}_2$  because no  $\text{HCl}(\text{g})$ , hydrated  $\text{HCl}$ , or  $\text{NH}_4\text{Cl}(\text{aerosol})$  are observed in this stage of decomposition.  $\text{NO}_2$ ,  $\text{N}_2\text{O}$ ,  $\text{HNO}_3$  and  $\text{H}_2\text{O}$  are products of ammonia oxidation.  $\text{HNO}_3$  may simply result from hydrolysis of  $\text{NO}_2$  and, as such, would not be an important product were a flame present.  $\text{N}_2\text{O}$  can form by R6. Preventing the build-up of  $\text{HNO}$  (*vide infra*) by R6 would be one of the chemical ways that AP is able to decompose slowly at lower temperature without developing a runaway release of heat.



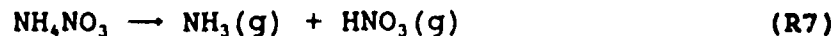
The development and growth of the exotherm of AP in Figure 5 is a sharp event. The gas product concentrations during the exotherm are unusual in the occurrence of the large pulse of  $\text{NO}$ ,  $\text{HCl}$  and  $\text{H}_2\text{O}$ . The  $\text{HClO}_4$  concentration remains at or below the pre-exotherm level. The behavior of  $\text{HClO}_4$ ,  $\text{NO}$  and  $\text{H}_2\text{O}$  is fully consistent with a major role of R4 in the acceleratory exothermic phase of AP decomposition. R4 increases in importance and ultimately controls the overall rate because  $\text{HNO}$  accumulates with time [14]. At the time when R4 dominates the rate, R6 is largely bypassed as evidenced by the fact that the final concentration of  $\text{N}_2\text{O}$  is only approximately double the pre-exotherm value. Because of their reactivity and short life-time at the temperature of the experiment,  $\text{HNO}$  and  $\text{ClO}_3$  are not detected. In fact, for the same reason, no chlorine oxides or  $\text{HClO}$  are observed, but they are by mass spectrometry [14,16].  $\text{HNO}$  has also been detected by mass spectrometry in the decomposition of AP in other work [18].

The importance of Cl-O homolysis of  $\text{HClO}_4$  in initiating and perhaps controlling rapid decomposition of AP has been repeatedly emphasized in many studies. It is highly likely that a fundamental role exists for  $\text{HNO}$  in the sense that products of both the early stage and exothermic stage are consistent with reactions of involving  $\text{HNO}$ . R4 plays a major role in the regression rate of AP.



## Surface Chemistry of Ammonium Nitrate and Ammonium Dinitramide

Interest is growing in oxidizers that might replace AP in solid propellants. Upon combustion, AP liberates HCl and H<sub>2</sub>O that form an environmentally undesirable plume of HCl(aq). Nucleation of H<sub>2</sub>O into droplets by HCl contributes to a prominently visible signature. These detracting features have rekindled interest in ammonium nitrate (AN). Unfortunately, AN has a low surface temperature and a low burn rate. The decomposition chemistry of AN is largely responsible for the low energy release. For example, two major decomposition reactions of AN, R7 and R8, are endothermic and mildly exothermic, respectively.



The decomposition of AN is compared to that of ammonium dinitramide (ADN),  $\text{NH}_4[\text{N}(\text{NO}_2)_2]$  [19]. Unlike AN, ADN decomposes very rapidly. Part of the additional energy release is attributable to the higher heat of formation of ADN (-35 kcal/mol [20]) compared to AN(-78 kcal/mol). Beyond this difference, the chemical reactions that cause ADN to decompose very exothermically are not obvious because the gas products from rapid thermolysis of ADN are similar to those of AN. Both compounds liberate HNO<sub>3</sub>, NH<sub>3</sub>, N<sub>2</sub>O, NO<sub>2</sub>, NO, H<sub>2</sub>O and N<sub>2</sub>, although the mole fractions differ somewhat. By T-jump/FTIR spectroscopy it seems likely that the reaction of NH<sub>3</sub> and NO<sub>2</sub> near the surface plays a major role in driving the regression of the surface [19].

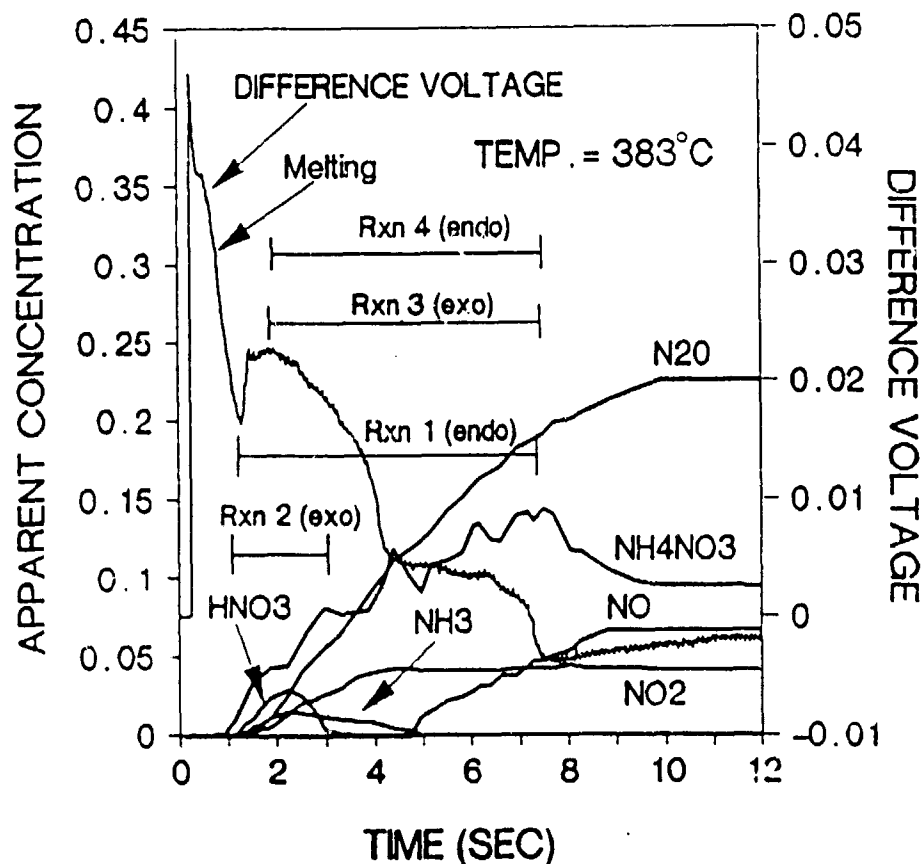
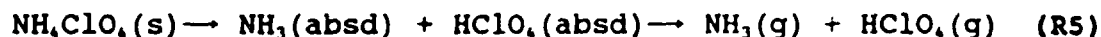


Figure 6. Gas products and the heat changes of  $\text{NH}_4\text{NO}_3$  at 383°C under 1 atm Ar. The reactions are shown in Scheme I.

with the heat balance sensed by the Pt control voltage [17]. Before the exotherm, IR active gas products are first detected at about 5 sec and consist of  $\text{HNO}_3$ ,  $\text{NO}_2$ ,  $\text{N}_2\text{O}$ ,  $\text{H}_2\text{O}$ ,  $\text{HClO}_4$ , and  $\text{HClO}_4(\text{aq})$ . The rise in gas product concentrations over the next few seconds indicates that the amount of sample decomposing gradually increases. The overall process is exothermic because the control voltage acquires a slight negative slope during this time.

The initial decomposition reaction of AP is widely regarded to be dissociative evaporation R5. Evidence of this reaction exists



below 3 atm where recombination of  $\text{NH}_3(\text{g})$  and  $\text{HClO}_4(\text{g})$  to form  $\text{NH}_4\text{ClO}_4(\text{aerosol})$  is observed in the IR spectrum. Below 13 atm Ar, no  $\text{NH}_4\text{ClO}_4(\text{aerosol})$  and  $\text{NH}_3$  are detected, but  $\text{HClO}_4$  is present, mostly in the hydrated form. The fact that some  $\text{HClO}_4$  survives to reach the cool atmosphere, whereas  $\text{NH}_3$  does not, may simply result from the fact that AP is over oxidized. Not all of the  $\text{HClO}_4$  is needed to oxidize  $\text{NH}_3$ . Hydrated  $\text{HClO}_4$  from AP was confirmed by the match of the  $\text{ClO}_4^-$  asymmetric stretching mode with that of the gas phase above a rapidly heated 70%  $\text{HClO}_4$  solution [17].

The  $\text{NH}_3$  from R5 is oxidized very rapidly in the heterogeneous gas-condensed phase zone by  $\text{HClO}_4$ . No  $\text{NH}_3$  survives to reach the IR beam because the inversion doublet at 968 and 932  $\text{cm}^{-1}$  is absent. The reduction product of  $\text{HClO}_4$  is  $\text{Cl}_2$  because no  $\text{HCl}(\text{g})$ , hydrated  $\text{HCl}$ , or  $\text{NH}_4\text{Cl}(\text{aerosol})$  are observed in this stage of decomposition.  $\text{NO}_2$ ,  $\text{N}_2\text{O}$ ,  $\text{HNO}_3$  and  $\text{H}_2\text{O}$  are products of ammonia oxidation.  $\text{HNO}_3$  may simply result from hydrolysis of  $\text{NO}_2$  and, as such, would not be an important product were a flame present.  $\text{N}_2\text{O}$  can form by R6. Preventing the build-up of  $\text{HNO}$  (*vide infra*) by R6 would be one of the chemical ways that AP is able to decompose slowly at lower temperature without developing a runaway release of heat.

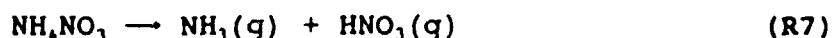


The development and growth of the exotherm of AP in Figure 5 is a sharp event. The gas product concentrations during the exotherm are unusual in the occurrence of the large pulse of  $\text{NO}$ ,  $\text{HCl}$  and  $\text{H}_2\text{O}$ . The  $\text{HClO}_4$  concentration remains at or below the pre-exotherm level. The behavior of  $\text{HClO}_4$ ,  $\text{NO}$  and  $\text{H}_2\text{O}$  is fully consistent with a major role of R4 in the acceleratory exothermic phase of AP decomposition. R4 increases in importance and ultimately controls the overall rate because  $\text{HNO}$  accumulates with time [14]. At the time when R4 dominates the rate, R6 is largely bypassed as evidenced by the fact that the final concentration of  $\text{N}_2\text{O}$  is only approximately double the pre-exotherm value. Because of their reactivity and short life-time at the temperature of the experiment,  $\text{HNO}$  and  $\text{ClO}_3$  are not detected. In fact, for the same reason, no chlorine oxides or  $\text{HClO}$  are observed, but they are by mass spectrometry [14,16].  $\text{HNO}$  has also been detected by mass spectrometry in the decomposition of AP in other work [18].

The importance of Cl-O homolysis of  $\text{HClO}_4$  in initiating and perhaps controlling rapid decomposition of AP has been repeatedly emphasized in many studies. It is highly likely that a fundamental role exists for  $\text{HNO}$  in the sense that products of both the early stage and exothermic stage are consistent with reactions of involving  $\text{HNO}$ . R4 plays a major role in the regression rate of AP.

## Surface Chemistry of Ammonium Nitrate and Ammonium Dinitramide

Interest is growing in oxidizers that might replace AP in solid propellants. Upon combustion, AP liberates HCl and H<sub>2</sub>O that form an environmentally undesirable plume of HCl(aq). Nucleation of H<sub>2</sub>O into droplets by HCl contributes to a prominently visible signature. These detracting features have rekindled interest in ammonium nitrate (AN). Unfortunately, AN has a low surface temperature and a low burn rate. The decomposition chemistry of AN is largely responsible for the low energy release. For example, two major decomposition reactions of AN, R7 and R8, are endothermic and mildly exothermic, respectively.



The decomposition of AN is compared to that of ammonium dinitramide (ADN),  $\text{NH}_4[\text{N}(\text{NO}_2)_2]$  [19]. Unlike AN, ADN decomposes very rapidly. Part of the additional energy release is attributable to the higher heat of formation of ADN (-35 kcal/mol [20]) compared to AN(-78 kcal/mol). Beyond this difference, the chemical reactions that cause ADN to decompose very exothermically are not obvious because the gas products from rapid thermolysis of ADN are similar to those of AN. Both compounds liberate HNO<sub>3</sub>, NH<sub>3</sub>, N<sub>2</sub>O, NO<sub>2</sub>, NO, H<sub>2</sub>O and N<sub>2</sub>, although the mole fractions differ somewhat. By T-jump/FTIR spectroscopy it seems likely that the reaction of NH<sub>3</sub> and NO<sub>2</sub> near the surface plays a major role in driving the regression of the surface [19].

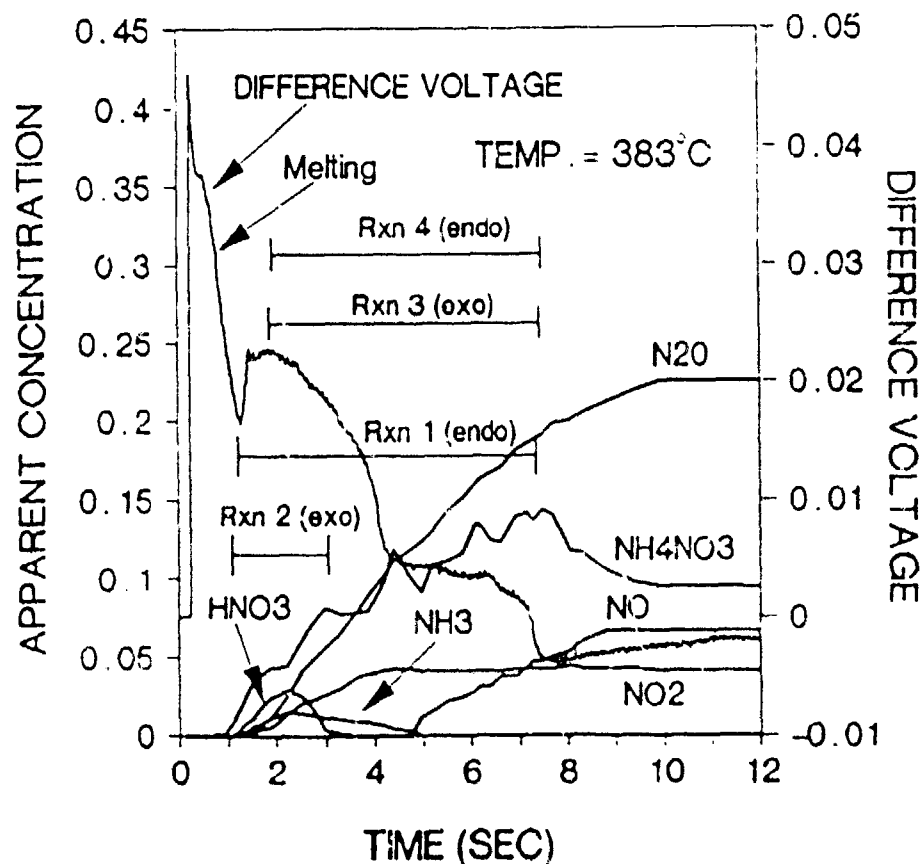


Figure 6. Gas products and the heat changes of  $\text{NH}_4\text{NO}_3$  at 383°C under 1 atm Ar. The reactions are shown in Scheme I.

Although pure AN will not burn at 1 atm, a sample can be driven by the T-jump method to a temperature that is at or above the measured surface temperature of AN burning at 25 atm or above (300-350°C [21]). Figure 6 shows the gas products and thermal response of a 200µg film of AN heated at 2000°C/sec to 383°C and held at 383°C. The concentration data in this plot are based on the scaled growth of the IR absorbance values for each product. The superposition of several stoichiometric reactions is indicated. Of course, many elementary steps are imbedded in each of these stoichiometric reactions, but they are not determinable by T-jump/FTIR spectroscopy.

The first event is rapid endothermic melting of AN as indicated by the upward deflection in the difference control voltage trace. The control voltage decreases upon completion of melting from 0.5 - 1 sec. The process turns markedly endothermic again at about 1 sec. This second endothermic event corresponds to the appearance and growth of AN aerosol. AN aerosol forms from the endothermic dissociation of AN and desorption to  $\text{HNO}_3(\text{g}) + \text{NH}_3(\text{g})$ , followed by recombination of  $\text{NH}_3$  and  $\text{HNO}_3$  in the gas phase (Scheme I, reaction

SCHEME I. PROPOSED REACTIONS THAT ACCOUNT FOR THE PRODUCTS OF HIGH TEMPERATURE DECOMPOSITION OF AN (see Figure 6).

	Approx $\Delta H$ , kcal
A. $4[\text{NH}_4\text{NO}_3(\text{l}) \rightarrow \text{HNO}_3(\text{g}) + \text{NH}_3(\text{g}) \rightarrow \text{NH}_4\text{NO}_3(\text{solid aerosol})]$	$4(44)^1$
B. $3[5\text{NH}_4\text{NO}_3(\text{l}) \rightarrow 2\text{HNO}_3 + 4\text{N}_2 + 9\text{H}_2\text{O}]$	$3(-35)$
C. $5[\text{NH}_4\text{NO}_3(\text{l}) \rightarrow \text{N}_2\text{O} + 2\text{H}_2\text{O}]$	$5(-13)$
D. $4\text{NH}_4\text{NO}_3(\text{l}) \rightarrow 2\text{NH}_3 + 3\text{NO}_2 + \text{NO} + \text{N}_2 + 5\text{H}_2\text{O}$	81
A-D <sup>2</sup> . $28\text{NH}_4\text{NO}_3(\text{l}) \rightarrow 6\text{HNO}_3 + 3\text{NO}_2 + \text{NO} + 2\text{NH}_3 + 5\text{N}_2\text{O} + 13\text{N}_2 + 42\text{H}_2\text{O} + 4\text{NH}_4\text{NO}_3(\text{aerosol})$	87

<sup>1</sup>  $\Delta H$  for the desorption step only (see text).

<sup>2</sup> Gives the approximate IR active gas product ratios at 2 sec at 383°C (Figure 6).

A). Only the endothermic first step of reaction A is included in  $\Delta H$  given for reaction A because the second step occurs in the cooler region of the cell away from the filament. Hence, the exothermic second step is not sensed by the filament. However, a white smoke of AN aerosol is visually observed.

Despite the continuation of reaction A throughout the decomposition process as evidenced by the growth of the AN (aerosol) concentration, the decomposition process becomes less endothermic again at about 2 sec.  $\text{H}_2\text{O}$  (not quantified) and excess  $\text{HNO}_3$  form at this time which is consistent with the occurrence reaction B. This reaction is known and its enthalpy has been deduced [22]. It is exothermic and would reduce the overall endothermicity of the decomposition process, as is found.

The process becomes still less endothermic from 2-4 sec as the amount of  $\text{HNO}_3$  diminishes. However,  $\text{N}_2\text{O}$  grows rapidly in concentration through this time suggesting that the exothermic reaction C plays an increasingly important role. However, there is evidence of yet another reaction that occurs in parallel as indicated by the appearance of  $\text{NO}_2$  and the eventual decrease in exothermicity again between 4-6 sec. Also,  $\text{NO}$ , whose IR absorbance

is very small, probably forms earlier than is indicated in Figure 6. Reaction D [23] accounts for these observations. Its endothermicity is superimposed on the exothermicity of reaction C and results in a leveling of the control voltage trace (heat flow is balanced) at 4-7 sec. Reaction D is also a source of  $\text{NH}_3$ , which appears as a product for a much longer time than  $\text{HNO}_3$ .

The multiplicative factors of the reactions in Scheme I were determined by the need to match the approximate relative concentrations of the gas products at a time when all of the reactions contribute. The concentrations at 2 sec were chosen. The stoichiometry of the net reaction in Scheme I approximates that found at 2 sec in Figure 6. Although the enthalpy of the net reaction is slightly exothermic as written, the relative contribution of reaction A need only be increased somewhat to produce a net endothermic process.

The formation of  $\text{NH}_3$  and  $\text{NO}_2$  by reaction D raises the possibility that the process could become exothermic when confined by pressure. The reaction of  $\text{NH}_3$  and  $\text{NO}_2$  becomes rapid and exothermic in the 330-530°C range [24,25]. However, significant generation of heat requires confinement to enhance the concentration of  $\text{NH}_3$  and  $\text{NO}_2$  in the hot zone around the condensed phase.

Figure 7 shows the decomposition process of a 200 $\mu\text{g}$  film of AN heated at 2000°C/sec to 415°C under 33 atm of Ar. The concentrations are shown as relative percents throughout so that the behavior early in the decomposition process can be clearly seen. The melting endotherm initially dominates. The heat of reactions A-D leading to the formation of AN aerosol,  $\text{N}_2\text{O}$ ,  $\text{HNO}_3$ ,  $\text{NH}_3$ , and  $\text{NO}_2$  are overall endothermic until 1.5 sec. At this time the concentrations of  $\text{NH}_3$  and  $\text{NO}_2$  formed by reaction D drop markedly and are accompanied by an exotherm which suggests that R9 occurs.  $\Delta H$  is about -148 kcal for this reaction as written. Under pressure, this nominally gas phase reaction could occur in the heterogeneous

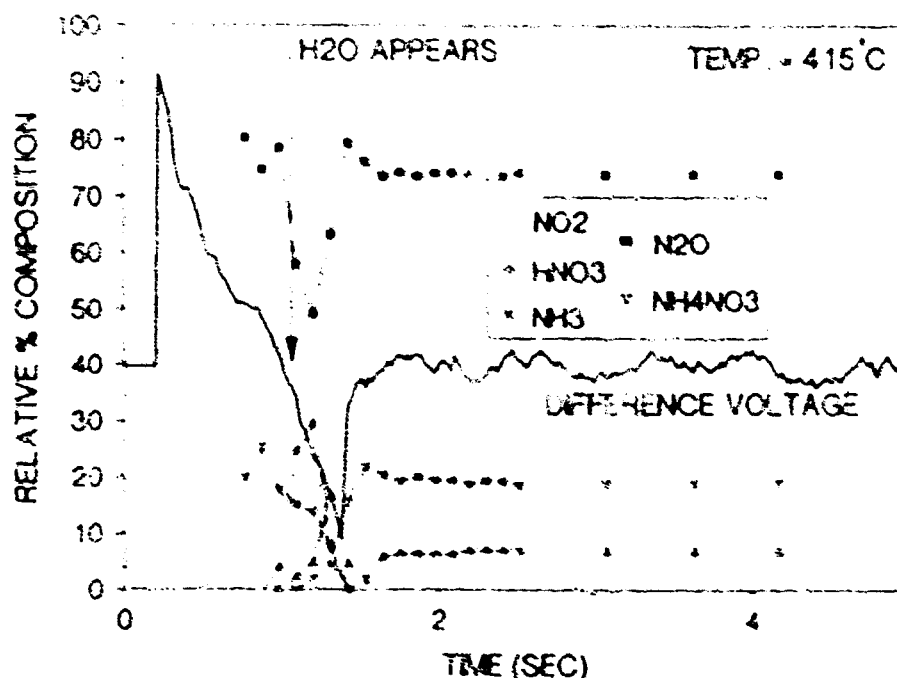


Figure 7. Gas products and the heat changes of  $\text{NH}_3$ ,  $\text{NO}_2$ , at 415°C under 33 atm of Ar

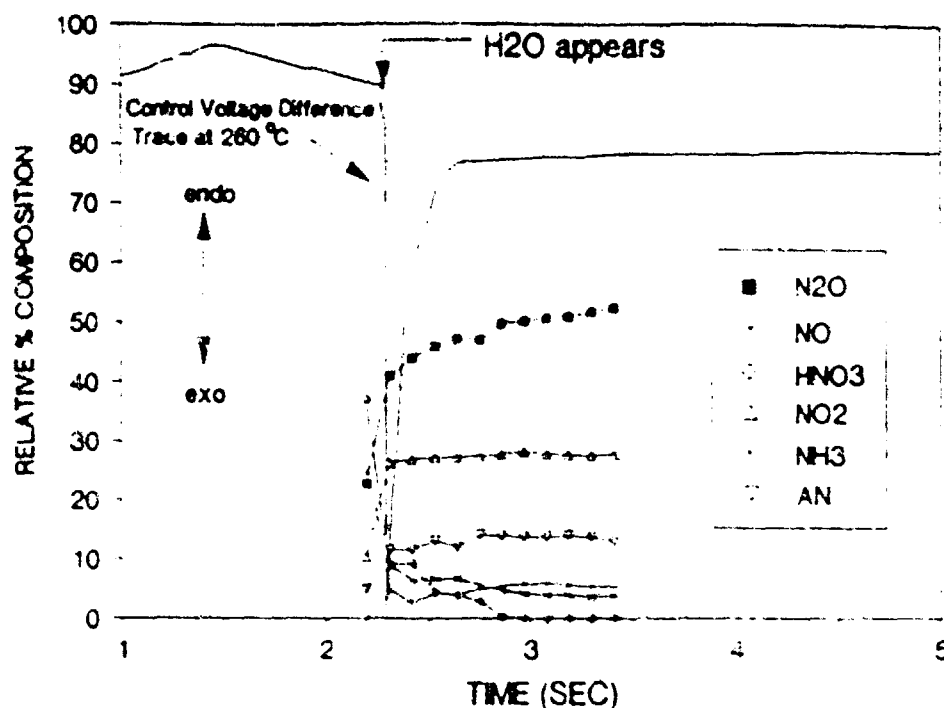


Figure 8. Gas products and the heat change of  $\text{NH}_4\text{N}(\text{NO}_2)_2$  (ADN) at 260°C under 1 atm Ar

SCHEME II: PROPOSED REACTIONS RESPONSIBLE FOR THE GASES RELEASED BY ADN DURING HIGH RATE PYROLYSIS

	Branch A <sup>1</sup>	Approx. $\Delta H$ , kcal
	$3[\text{ADN} \rightarrow \text{NH}_3 + \text{HNO}_3 + \text{N}_2\text{O}]$	$3(+11.5)$
	Branch B	
a	$9[\text{ADN} \rightarrow \text{NH}_3 + \text{HN}(\text{NO}_2)_2]$	
b	$9[\text{HN}(\text{NO}_2)_2 \rightarrow \text{NO}_2 + \text{HNNO}_2]$	
c	$6[\text{HNNO}_2 \rightarrow \text{N}_2\text{O} + \text{OH}]$	
d	$2[\text{HNNO}_2 + \text{OH} \rightarrow 2\text{NO} + \text{H}_2\text{O}]$	
e	$\text{HNNO}_2 + \text{NO} \rightarrow \text{NO}_2 + \text{HNNO}$	
f	$\text{HNNO} + \text{OH} \rightarrow \text{N}_2\text{O} + \text{H}_2\text{O}$	
g	$3[\text{NH}_3 + \text{OH} \rightarrow \text{H}_2\text{O} + \text{NH}_2]$	
h	$3[\text{NH}_2 + \text{NO} \rightarrow \text{N}_2 + \text{H}_2\text{O}]$	
j <sup>2</sup>	$9\text{ADN} \rightarrow 6\text{NH}_3 + 7\text{N}_2\text{O} + 10\text{NO}_2 + 9\text{H}_2\text{O} + 3\text{N}_2$	-49
j'	$12\text{ADN} \rightarrow 9\text{NH}_3 + 10\text{N}_2\text{O} + 10\text{NO}_2 + 9\text{H}_2\text{O} + 3\text{N}_2 + 3\text{HNO}_3$	-14
k	$4\text{NH}_3 + 4\text{NO}_2 \rightarrow 3\text{N}_2 + 2\text{NO} + 6\text{H}_2\text{O}$	-309
l <sup>3</sup>	$12\text{ADN} \rightarrow 5\text{NH}_3 + 10\text{N}_2\text{O} + 6\text{NO}_2 + 15\text{H}_2\text{O} + 2\text{NO} + 6\text{N}_2 + 3\text{HNO}_3$	-323
m <sup>4</sup>	$2\text{NH}_3 + 2\text{HNO}_3 \rightarrow 2\text{NH}_4\text{NO}_3$ (aerosol)	
n <sup>5</sup>	$12\text{ADN} \rightarrow 3\text{NH}_3 + 10\text{N}_2\text{O} + 6\text{NO}_2 + 15\text{H}_2\text{O} + 2\text{NO} + 6\text{N}_2 + \text{HNO}_3 + 2\text{NH}_4\text{NO}_3$	-323

<sup>1</sup> Assumes  $\Delta H_f$  (ADN) = -35 kcal/mol, and  $\Delta H$  (HNO<sub>3</sub>(g)) is -33 kcal/mol.  
<sup>2</sup> Sum of a-h.

<sup>3</sup> Sum of Branches A & B.

<sup>4</sup> Sum of reactions j+k.

<sup>5</sup> Occurs in gas phase away from surface so reaction m is not included in  $\Delta H$ .

<sup>6</sup> Sum of l and m gives the approximate gas phase stoichiometry at the end of the exotherm (Figure 8).

gas-condensed phase (eg. bubbles and voids) and contribute to the condensed phase heat balance under combustion conditions. The thermal decomposition behavior of bulk ADN is very different from that of AN despite the fact that similar gas products are formed upon rapid decomposition. Figure 8 shows T-jump/FTIR data for a 200 $\mu$ g film of ADN heated at 2000°C/sec to 260°C. This temperature compares with a preliminary surface temperature measurement of burning ADN of about 300°C [26], which is surprisingly similar to that of AN. At the onset of decomposition, gas products and, in contrast to AN, sharp exothermicity occur instantly. The first detected products are mostly HNO<sub>2</sub>, NH<sub>3</sub>, and N<sub>2</sub>O in roughly similar amounts. Minor quantities of NO<sub>2</sub>, AN and H<sub>2</sub>O are also present in the initial spectrum.

The formation of HNO<sub>2</sub>, NH<sub>3</sub>, and N<sub>2</sub>O in comparable amounts at the beginning suggests the presence of Branch A in Scheme II. This mildly endothermic reaction may have a role during slow decomposition at lower temperatures. It appears to be a minor branch during rapid heating, especially because it does not account for the major heat release that is experimentally observed.

Branch B of Scheme II is proposed to dominate under rapid thermolysis conditions [19]. Reaction a of Branch B is dissociation of ADN to produce NH<sub>3</sub> and HN(NO<sub>2</sub>)<sub>2</sub>. HN(NO<sub>2</sub>)<sub>2</sub> is not detected and probably homolyses in the condensed phase at high temperature by reaction b to NO<sub>2</sub> and HNNO<sub>2</sub>. Reactions a and b are endothermic. Because relatively large quantities of NH<sub>3</sub> and NO<sub>2</sub> occur early in Branch B, much heat can be generated by reaction k in the gas phase near the surface or even as part of the heterogeneous gas-liquid zone at the surface. The high exothermicity is evident in the large control voltage deflection at 2.3 sec, and provides the energy to complete the decomposition process very rapidly. Some of the NH<sub>3</sub> and NO<sub>2</sub> remains unreacted because it escapes to the cooler region of the atmosphere. Reactions g-h are plausible subsequent steps for decomposition of HNNO<sub>2</sub>, but they are not determined by T-jump/FTIR spectroscopy. They are simply proposed as reasonable sources of stable products in the quantities detected. The net reaction i of Branch B is mildly exothermic. Combining Branches A and B yields the exothermic reaction j. Adding some gas phase recombination of NH<sub>3</sub> and HNO<sub>2</sub> (reaction m) to account for the observed AN solid aerosol yields reaction n, whose stoichiometry approximates the experimentally observed gas product ratios observed at 2.5 sec in Figure 8. Reaction n is strongly exothermic largely because of reaction k, which is the reaction of NH<sub>3</sub> with NO<sub>2</sub>.

For both AN and ADN, the exothermic NH<sub>3</sub> + NO<sub>2</sub> reaction appears to dominate the heat release stage. In the case of AN the exotherm occurs only under a large applied pressure is accompanied by a drop in the amount of NH<sub>3</sub> and NO<sub>2</sub> that appear in the gas phase. Although the reaction of NH<sub>3</sub> and NO<sub>2</sub> appears to be responsible for this exotherm, the amount of NH<sub>3</sub> and NO<sub>2</sub> is smaller for AN than for ADN and, therefore much less heat is generated.

The rapid decomposition process of ADN is strongly exothermic early in the reaction scheme. This behavior is consistent with the ease of formation of a large amount of NH<sub>3</sub> and NO<sub>2</sub> in the early decomposition steps. Because the reaction of NH<sub>3</sub> and NO<sub>2</sub> can dominate early and produces a large amount of heat, the overall decomposition and gasification process is driven at a much higher rate for ADN than AN. Therefore, for both AN and ADN the reaction

of  $\text{NH}_3$  with  $\text{NO}_2$  is implicated as the main source of heat when the pure material is decomposed at high temperature. For AN this reaction only becomes important under confinement, such as by the application of pressure.

#### IS PYROLYSIS OF THIN FILMS RELATED TO THE BURNING SURFACE?

Good evidence that the rapidly heated thin film is a surface simulation comes from the SMATCH/FTIR method (SMATCH stands for simultaneous mass and temperature change) [27] in which a film of uniform, chosen thickness (20-60  $\mu\text{m}$ ) is heated at  $\geq 150^\circ\text{C}/\text{sec}$  while the dynamic mass change, temperature change, and gas products are all measured simultaneously. The burn rate  $r$  calculated from

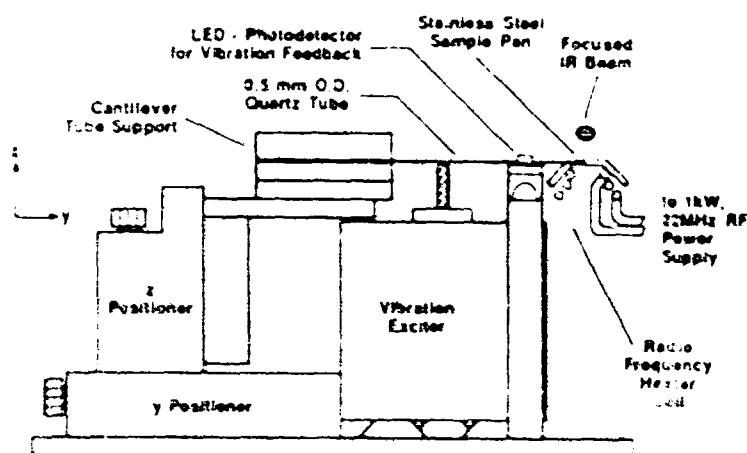


Figure 9. A side-view of the SMATCH/FTIR sampling device

SMATCH/FTIR kinetics matches  $\dot{r}$  from bulk combustion measurements at the same pressure [28-31]. Hence, the heat flow conditions are similar to those of the surface reaction zone during bulk combustion. By inference, other techniques designed for fast, controlled heating of a thin film, such as T-jump/FTIR [4], that are also specifically designed for chemical studies, give extensive details of the surface reaction zone.

Details of SMATCH/FTIR and spectroscopy are given elsewhere [27-30], but are briefly summarized here. As shown in Figure 9, SMATCH/FTIR employs a cantilevered quartz tube whose vibrational frequency depends on the sample mass. Typically, 0.2 - 0.8 mg of sample was painted onto a metal tip attached to the tube giving a uniform film of 16 - 54  $\mu\text{m}$  thickness. If the film thickness is not uniform, then the experiment fails. The metal end-tip was heated by RF induction at a chosen rate in the 100 - 200  $^\circ\text{C}/\text{sec}$  range. The sample atmosphere was 1 atm of Ar. The heating rate and film thickness are matched so that the heat transfer is fast enough to give a reasonably uniform temperature throughout the film [28]. The dynamic weight change of the sample was measured by the change in the vibrational frequency of the tube. Data were recorded at 160 Hz which provides enough points on the weight-loss curve to be confident of fitting the shape by Eq. 1.  $\alpha$  is the degree of

$$1 - \alpha = \sum_{i=0}^n a_i t^i \quad (E1)$$



conversion and  $t$  is time. Typically, E1 was applied for the initial 50% of weight loss. The temperature was measured by a type E thermocouple spot-welded to the metal end-tip and in contact with the sample film. Infrared spectra of the decomposition gases were measured about 3 mm above the metal end-tip by using RSFTIR (10 scan/sec, 4  $\text{cm}^{-1}$  resolution).

The reduction of SMATCH/FTIR temperature and weight change data from E1 and its derivative are related to Arrhenius parameters by E2.

$$\frac{da}{dt} = Ae^{-E/RT}(1-\alpha)^n \quad (\text{E2})$$

Rearrangement of E2 yields E3, which is a straight line by the appropriate choice of  $n$ .  $n=2$  linearizes most SMATCH/FTIR data and has been rationalized elsewhere [28]. Modified versions of the pyrolysis law, E4 and E5, where  $h$  is the experimental film

$$\log\left[\frac{dx}{dt}\left(\frac{1}{(1-\alpha)^n}\right)\right] = \log A - \frac{E}{2.3RT} \quad (\text{E3})$$

thickness, can be used to calculate the regression rate,  $\dot{r}$ , in mm/sec from the SMATCH/FTIR Arrhenius constants at the pressure and temperature of the experiment [28-31].  $T$  is the average temperature during the initial 50% of the weight loss. E4 and E5 apply provided  $h$  approximates the surface reaction zone thickness at 1 atm. A value of  $h = 20 - 60 \mu\text{m}$  is reasonable at 1 atm [32].

Table 2 Burn Rate Comparisons		
Compound	$\dot{r}$ , mm/sec (1 atm)	
	SMATCH	Strand burner
AP	0.11	0.25
HMX	0.37	0.5
RDX	0.38	0.38
DNNC	0.27	0.27
13%N NC	0.3	0.4
GAP	1.35	1.7

$$\dot{r} = hAe^{-E/RT} \quad (\text{E4})$$

$$\dot{r} = hA^{1/2}e^{-E/2RT} \quad (\text{E5})$$

Table 2 compares the regression rates of various energetic materials computed by E4 and E5 at 1 atm from SMATCH/FTIR data and the values measured at 1 atm or extrapolated from higher pressure to 1 atm from combustion bomb data. The reasonably good match suggests that the rate and characteristics of heat transfer to the thin film are equal to or scale to those at the surface during combustion.

#### FTIR Measurements of Flames

Reactive two-phase flows, especially in flames, are usually produced when propellant formulations burn. This is because many solid rocket propellants contain fuels, such as Al or B, that burn to the solid oxide. Inert solids, such as ZrC, are sometimes added to help dampen combustion oscillations. The solid particles appear as smoke. A similar particle laden flow can exist in hydrocarbon and coal combustion where the combustion gases might be mixed with soot, fly ash and char.

In recent years several techniques have been developed based on FTIR emission/transmission spectroscopy (FTIR E/T) that enable measurements to be made of particle and gas concentrations and temperatures in hot flows [33-37]. Specifically, 1) the temperature and concentration of the particle and soot phases have been measured separately in an ethylene-air diffusion flame [34]; 2) measurements have been made in densely loaded particle streams [34]; and 3) particle sizes have been measured [35]. Although most measurements have been line-of-sight, it has been recently shown that Fourier image reconstruction can be used to obtain absorbance and emittance spectra spatially resolved in about 1 x 1 x 4 mm volume [37].

The FTIR E/T method offers promise for studying propellant flames in which the number of scattering particles is not unusually large. However, an additional experimental complication to propellant combustion studies is that the surface burns as a regressing front. Therefore, a moving stage is needed to maintain the position of the propellant flame relative to the IR beam. This requirement contrasts with the simpler flow reactor designs that can be used to study premixed gas flames and coal particle-gas flames. Recently, FTIR emission spectra have been recorded on flames of AP and HTPB binder [38]. A moving stage with servo feedback control was used to maintain the position of the propellant in the IR beam. Figure 10 shows the IR emission spectrum of the gas products.  $\text{CO}_2$ ,  $\text{CO}$ ,  $\text{H}_2\text{O}$ ,  $\text{HCl}$  and fragments of HTPB are detected. In addition,  $\text{NH}_3$  and  $\text{HClO}_4$  were also detected indicating that AP sublimates to some extent under combustion conditions. Recently considerable advancement has been made by Thynell, Kuo and coworkers [39] toward understanding IR spectral emission variables of propellant combustion in a manner that provides species concentration and temperature profiles. Further studies are described in a paper by Huang, et al., in this Symposium.

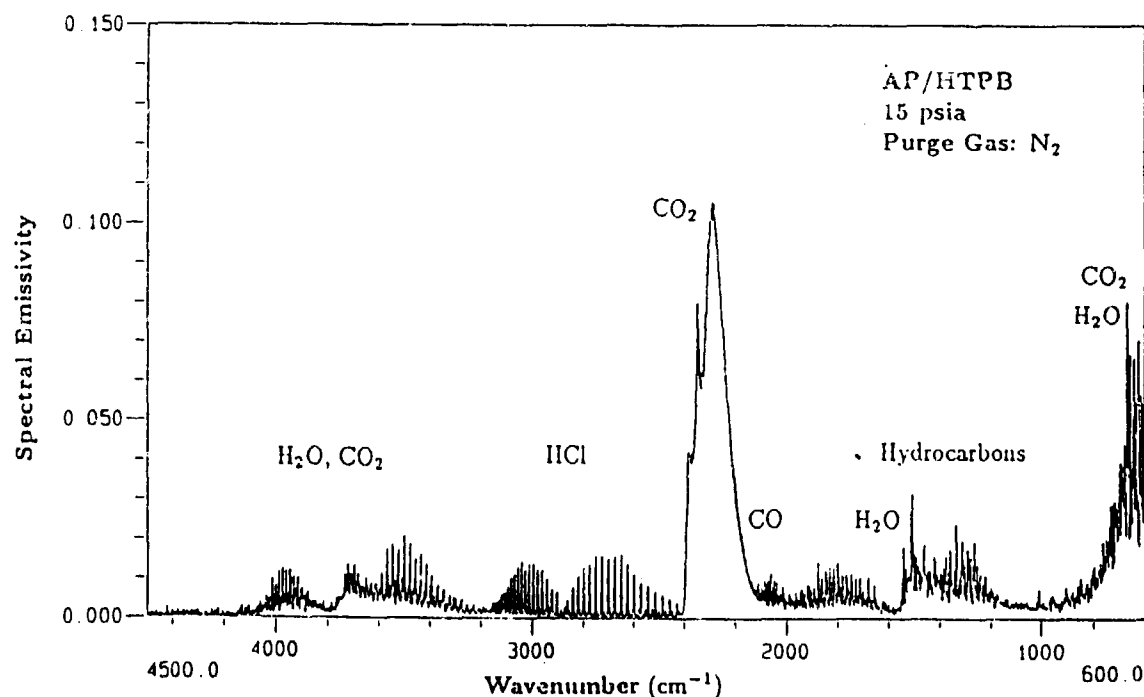


**Figure 10. Sixteen coadded emission spectra of the AP-HTPB flame zone assuming  $T = 1500 \text{ K}$  (ref. 38)**

Computed tomographic reconstruction has recently been used by McNesby and Fifer [40] to obtain species profiles from FTIR spectra

as a function height and lateral distribution above a  $\text{CH}_4/\text{N}_2\text{O}$  low pressure, premixed, flat flame burner. Discrimination of cold interferences from the hot gas distribution is made. FTIR spectroscopy has been used to obtain high resolution absorption spectra of the major steady-state species in premixed  $\text{C}_2\text{N}_2\text{-NO}_2$  [41] and  $\text{HCN-NO}_2$  [42] burner flames. Reactions involving these gases are believed to be among the more important ones in certain rocket and gun propellant flames produced by nitramines. The high temperature of these flames required modifications to be made to the IR spectrometer. For example, temperature gradients in various parts of the optical bench were caused by the flame and led to channel spectra. Plane windows were, therefore, replaced by wedge windows to reduce this problem. The high infrared emissivity of the flame required the use of a long-pass IR filter and a high intensity globar to obtain quality spectra. With these modifications detailed studies have been made of the species concentration profiles and temperature as a function of distance above the burner surface. The temperature was extracted from the rotational band intensities of CO in various parts of the flame. When coupled with simulations of the kinetics, it could be concluded that the flame chemistry is dominated by oxygen atoms [42]. The production of oxygen atoms increases the burn rate while their consumption decreases the burn rate.

#### ACKNOWLEDGMENTS

The support of the Air Force Office of Scientific Research, Aerospace Sciences, is gratefully acknowledged. Most of this overview is based on research of graduate and post-doctoral students Mark Timken, Peter Brush, Dilip Patil, and Jangqiang Chen, whose work is referenced below.

#### REFERENCES

1. M. H. Alexander, P. J. Dagdigian, M. E. Jacox, C. E. Kolb, C. F. Melius, H. Rabitz, M. D. Smooke and W. Tsang, *Prog. Energy Combust. Sci.* 17, 263 (1991).
2. P. R. Griffiths and J. A. deHaseth, *Fourier Transform Infrared Spectroscopy*, Wiley-Interscience, New York, 1986.
3. T. B. Brill in *Chemistry and Physics of Energetic Materials*, S. Bulusu, Ed. Kluwer Academic Press, Dordrecht, The Netherlands, 1990, p. 255.
4. T. B., Brill, P. J. Brush, K. J. James, J. E. Shepherd and K. J. Pfeiffer, *Appl. Spectrosc.*, 46, 900 (1992).
5. T. B. Brill, *Prog. Energy Combust. Sci.*, 18, 91 (1992).
6. T. B. Brill and P. J. Brush, *Phil. Trans. Royal Soc. (Lond.) A*, 339, 377 (1992).
7. T. B. Brill, P. J. Brush, D. P. Patil and J. K. Chen, *Proc. 28th Symp. (Int.) Combustion*, Sydney, Australia, July, 1992.
8. J. D. Cosgrove and A. J. Owen, *Combust. Flame*, 22, 13 (1974).
9. J. Kimura and N. Kubota, *Prop. Explos.*, 5, 1 (1980).
10. R. J. Karpowicz and T. B. Brill, *Combust. Flame*, 56, 317 (1984).

11. R. Behrens, J. Phys. Chem., 94, 6706 (1990).
12. S. F. Palopoli and T. B. Brill, Combust. Flame, 87, 45 (1991).
13. C. F. Melius in Chemistry and Physics of Energetic Materials, S. Bulusu, Ed. Kluwer Academic Publ., Dordrecht, The Netherlands, 1990, p. 51.
14. N. E. Ermolin, O. P. Korobeinichev, A. G. Tereshenko and V. M. Fomin, Comb. Explos. Shock Waves, 18, 180 (1992).
15. C. Guirao and F. A. Williams, AIAA J., 9, 1345 (1971).
16. O. P. Korobeinichev and A. G. Tereshenko, in Tenth Mat. Res. Symp. Charact. High Temp. Vapors and Gases, NBS publ. 561, Gaithersburg, MD, 1978, p. 479.
17. T. B. Brill, P. J. Brush and D. G. Patil, Combust. Flame, in press.
18. E. E. Hackman, H. J. Hesser and H. C. Beachell, J. Phys. Chem., 76, 3545 (1972).
19. T. B. Brill, P. J. Brush and D. G. Patil, Combustion Flame, 92, 178 (1993).
20. M. Swett, NWC, personal communication (1992).
21. A. G. Whittaker and D. C. Barham, J. Phys. Chem., 68, 196 (1964).
22. B. T. Federoff, Encyclopedia of Explosives and Related Items, Vol. I, Picatinny Arsenal, Dover, NJ, 1960, A3111.
23. R. Kaiser, Angew. Chem., 48, 149 (1935).
24. W. A. Rosser and H. Wise, J. Chem. Phys., 25, 1078 (1956).
25. G. Bedford and J. H. Thomas, J. Chem. Soc. Farad. Trans. I, 2163 (1972).
26. B. L. Fetherolf and T. A. Litzinger, Penn State Univ., personal communication (1992).
27. M. D. Timken, J. K. Chen and T. B. Brill, Appl. Spectrosc., 44, 701 (1990).
28. J. K. Chen and T. B. Brill, Combust. Flame, 85, 479 (1991).
29. J. K. Chen and T. B. Brill, Combust. Flame, 87, 157 (1991).
30. J. K. Chen and T. B. Brill, Combust. Flame, 87, 217 (1991).
31. T. B. Brill, D. P. Patil, J. Duterque and G. Lengelle, Combust. Flame, submitted.
32. N. Kubota and S. Sakamoto, Prop. Explos. Pyrotech., 14, 6 (1989).
33. P. E. Best, R. M. Carangelo, J. R. Markham and P. R. Solomon, Combust. Flame, 66, 47 (1986).

34. P. R. Solomon, P. E. Best, R. M. Carangelo, J. R. Markham, P-L. Chien, R.J. Santoro and H.G. Semerjian, Proc. 21st Symp. (Int.) Combustion, 1763 (1986).
35. P. R. Solomon, R. M. Carangelo, D. G. Hamblen and P. E. Best, Appl. Spectrosc., 40, 746 (1986).
36. P. R. Solomon, P-L. Chien, R. M. Carangelo, P. E. Best, and J. R. Markham, Proc. 22st Symp. (Int.) Combustion, 211 (1988).
37. J. R. Markham, Y. P. Zhang, R. M. Carangelo, and P. R. Solomon, Proc. 23rd Symp. (Int.) Combustion, 1869 (1990).
38. S. Klotz, S. T. Thynell, I. T. Huang, K. K. Kuo, J. Propuls. Power, 8, 537 (1992).
39. I. T. Huang, S. T. Thynell and K. K. Kuo, Appl. Spectrosc., 46, 1182 (1992).
40. K. L. McNesby and R. A. Fifer, BRL-TR-3333, Ballistic Research Laboratory, Aberdeen Proving Ground, MD, April 1992.
41. L. R. Thorne and O. I. Smith, CPIA Publ. 481, Vol II, 143 (1988).
42. L. R. Thorne and C. F. Melius, Proc. 23rd Symp. (Int.) Combustion, 397 (1990).

## Thermal Decomposition of Energetic Materials 58. Chemistry of Ammonium Nitrate and Ammonium Dinitramide Near the Burning Surface Temperature

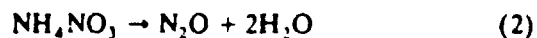
T. B. BRILL\*, P. J. BRUSH, and D. G. PATIL

*Department of Chemistry, University of Delaware, Newark, DE 19716*

The rapid pyrolysis chemistry of films of ammonium nitrate (AN),  $\text{NH}_4\text{NO}_3$ , and ammonium dinitramide (ADN),  $\text{NH}_4[\text{N}(\text{NO}_2)_2]$ , at temperatures approximating a burning surface is described by the use of T-jump/Fourier transform infrared (FTIR) spectroscopy. The sequence of appearance and amounts of each gas product combined with the net endothermicity and exothermicity of the process at each time enables consistent reaction schemes to be developed. The decomposition of the condensed phase of AN is net endothermic up to at least 33 atm. Although dissociative sublimation and the formation of  $\text{N}_2\text{O}$  and  $\text{H}_2\text{O}$  dominate the overall process, the superposition of two additional reactions is needed to account for all of the products observed from AN. ADN becomes highly exothermic very early in the decomposition process. The superposition of two stoichiometric reaction branches explains this behavior. The spectra and thermal responses are consistent with the reaction of  $\text{NH}_4^+$  with  $\text{NO}_2^-$  being the major source of heat released during the decomposition of AN above 33 atm and ADN at 1 atm and higher.

### INTRODUCTION

Interest is growing in oxidizers that might replace ammonium perchlorate (AP) in solid propellants. On combustion, AP liberates HCl and  $\text{H}_2\text{O}$ , which form an environmentally undesirable plume of hydrochloric acid. Nucleation of  $\text{H}_2\text{O}$  into droplets by HCl contributes to a prominently visible signature. These detracting features have rekindled interest in ammonium nitrate (AN) as a possible substitute oxidizer. Unfortunately, AN has a low surface temperature and a low burn rate. Although these problems are somewhat alleviated by formulating AN with a reactive metal, such as magnesium, the decomposition chemistry of AN is largely responsible for the low energy release. For example, two major decomposition reactions of AN (1 and 2) are endothermic and mildly exothermic, respectively.



\* Corresponding author

Many studies exist on the decomposition products and kinetics of AN [1-7]. Pyrolysis of AN under combustion conditions has led to the conclusion that reactions 1 and 2 dominate [8, 9]. To ground these conclusions firmly on experimental results, it is helpful to know the sequence of gas-product formulation at high temperature. Previous studies at high heating rates [6, 7] have given some information, but were obtained under nonisothermal conditions. To gain more detailed insight, AN decomposition is described in this article based on the gas products and thermal response of the sample at a high, relatively constant temperature following heating at a high rate. The objective is to understand the decomposition process as it might occur in propellant ignition and combustion. Hence, the product gases were allowed to remain in contact with the condensed phase.

The decomposition of AN is compared to that of ammonium dinitramide (ADN),  $\text{NH}_4[\text{N}(\text{NO}_2)_2]$  [10]. Unlike AN, ADN decomposes very rapidly. Part of the additional energy release is attributable to the higher heat of formation of ADN (-35 kcal/mol [11]) compared to AN(-78 kcal/mol). Beyond this

difference, the chemical reactions that cause ADN to decompose very exothermically are not obvious because the gas products from rapid thermolysis of ADN are similar to those of AN. Both compounds liberate  $\text{HNO}_3$ ,  $\text{NH}_3$ ,  $\text{N}_2\text{O}$ ,  $\text{NO}_2$ ,  $\text{NO}$ ,  $\text{H}_2\text{O}$ , and  $\text{N}_2$ , although the mole fractions differ somewhat.  $\text{NH}_3(g)$  and  $\text{HNO}_3(g)$  can recombine to form AN aerosol if a cool nonreactive atmosphere is present.

A study of AN and ADN was undertaken by T-jump/FTIR spectroscopy [12] to define the decomposition process more clearly at temperatures and heating rates that resemble the surface under ignition conditions. The surface can be thought of as a thin film that rapidly heats to a high temperature while decomposing [13]. T-Jump/FTIR spectroscopy determines the isothermal decomposition characteristics of a thin polycrystalline layer of sample on a Pt filament following heating of the Pt ribbon at  $2000^\circ\text{C}/\text{sec}$  to a chosen constant temperature. Simultaneous recording of the thermal response of this condensed heterophase layer and the IR spectra of the near-surface gas products helps define the semi-global decomposition chemistry that is representative of an igniting surface. The reaction schemes that are presented are consistent with the sequential formation of gas products and thermal response, and explain the slight increase in exothermicity of the condensed phase of AN with pressure. They also suggest why AN and ADN are thermochemically so different, yet liberate similar gas products. These reaction schemes contain elementary steps whose kinetics are largely unknown. The kinetic details are the vital information needed to test these proposals.

## EXPERIMENTAL

### Samples

$\text{NH}_4\text{NO}_3$  (CP grade) was obtained from Fisher Scientific Co., Fair Lawn, NJ. The AN was ground to a fine powder and dried at  $10^{-3}$  torr for 12 hr before use.  $\text{NH}_4[\text{N}(\text{NO}_2)_2]$  was obtained from T. P. Russell of the Naval Surface Warfare Center and was originally prepared at Stanford Research International. It was kept in

a sealed vial in a desiccator and ground to a fine powder before use.

### T-Jump / FTIR Spectroscopy

The T-jump/FTIR technique is described in detail elsewhere [12]. Briefly, approximately 200  $\mu\text{g}$  of powdered AN or ADN (hereafter referred to as the "film") was thinly spread on a Pt ribbon filament. The filament holder was inserted through the wall of the IR cell, the cell purged with Ar, and the static pressure in the cell adjusted as desired. The cell was placed in the sample compartment of a Nicolet 20 SXB rapid-scan FTIR spectrometer. The IR beam was positioned about 3 mm above the surface of the film. Triggering of the heater circuit and spectral data collection occurred simultaneously. The Pt ribbon was heated at  $2000^\circ\text{C}/\text{sec}$  to a chosen constant temperature ( $T_1$ ). Both AN and ADN melted giving a film on the center of the filament. The control voltage that maintains constant resistance of the Pt filament at the chosen value (temperature) was recorded on a personal computer (PC). The circuit is very responsive and sensitive to the thermal changes of the sample, but imperfections in the contact intimacy between the sample and filament affect the heat flow. Hence, the shape and area of the control voltage trace has little quantitative value. The temperatures quoted in this paper are the Pt filament temperatures. They approximate the sample temperature, but, because of imperfect thermal contact, the sample and the filament cannot be maintained at exactly the same temperature. By subtracting the control voltage trace with no sample present from the control voltage trace with the sample present, a difference voltage is obtained in which an upward excursion from the horizontal line corresponds to an endotherm of the sample and a downward excursion is an exotherm. Because of the small amount of sample, the heat transfer limitations are minimized as much as possible and the pressure change is very small during the decomposition process. The gases evolve into a cool Ar atmosphere where they are quenched and detected with 100 msec time resolution by the IR spectrometer. The rotational structure

indicates that the gases are in the ground vibrational states. The control voltage deflections are correlated in time with the IR spectra of the gas products.

The IR absorbances were converted to relative concentrations of the gas products in two ways. For AN at 1 atm, the time resolution of the experiment is sufficiently fast to see the growth rate of the product gases in a spectral series. Apparent relative concentrations can be obtained by measuring the absorbance of each gas and multiplying by a factor [13] that is based on the absolute absorbance of the vibrational mode. This procedure converts the absorbances to apparent concentrations and enables the rate of formation of each product to be examined. For AN at 33 atm and for ADN, the gas product concentrations are based on a 100% scale throughout. In effect, these are mole fractions that are independent of the amount of gas present at any particular time. With the first procedure all gas products start from zero concentration and grow to be related as mole fractions. In the second procedure the mole fraction relationship based on a 100% scale throughout makes it easy to see the sequential differences when the concentrations are low. However, the gas product ratios are the same in both procedures.

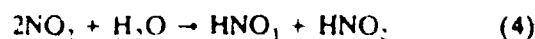
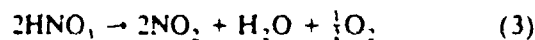
N<sub>2</sub>, O<sub>2</sub>, and H<sub>2</sub> are not IR active and are not included in the quantitation procedure. H<sub>2</sub>O is observed but is not included in the quantitation process because the rotation-vibration fine-structure makes the amount of H<sub>2</sub>O difficult to determine. No absolute IR intensity values exist for AN solid as an aerosol. Therefore, the AN aerosol was included in the quantitation process with a multiplicative factor of unity. This value does not arbitrarily weight AN more or less than the other products, and was chosen mainly so that the behavior of AN aerosol could be followed relative to the gas products.

The decomposition of AN was studied at 356°, 383°, 410°, 426°, and 447°C and several pressures from 1–33 atm. The relative amount of products is similar at all temperatures, but the amount of HNO<sub>3</sub> formed relative to sublimation is greater at higher temperatures. ADN was studied from 220°–300°C in 20° increments at 1 atm. Again, the results were similar at

each condition so that the 260°C data were chosen as representative.

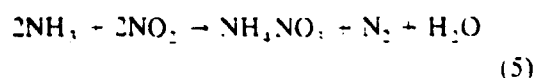
### AMMONIUM NITRATE

Thermal decomposition studies of bulk AN conducted over the past several hundred years suggest that the process can be surprisingly involved [1–7]. It is difficult to distinguish between reactions in the gas phase and reactions in the condensed phase when the decomposition is performed under practical conditions. Moreover, these reaction regimes contribute differently at each temperature and pressure. The balance of ionic and radical chemistry shifts toward radical chemistry at higher temperature [3], and the reaction rate is affected by the gases that contact the sample [4]. Fluctuations occur in the heat balance at different times and temperatures from the onset of melting to the end of gasification [7]. However, in the absence of secondary reactions between the gas and condensed phase the decomposition temperature is predicted not to rise above a particular value determined by the pressure [2, 14]. Such behavior is found in practice [7, 15]. It is interesting to note that the surface temperature of burning AN is in the 300°–350°C range [16, 17], which is similar to the limiting temperature range of decomposition of 280°–320°C [14]. Unfortunately, not only are the decomposition reactions numerous and intertwined, but the description of AN decomposition is complicated by insidious secondary reactions that may occur in a different part of the vessel or during analysis that regenerate primary products. For example, HNO<sub>3</sub> forms by reaction 1 in the primary degradation process, but HNO<sub>3</sub> can decompose by reaction 3 and then reappear later by reaction 4.



Consequently, the origin of all of the HNO<sub>3</sub> detected during AN decomposition might not be from reaction 1. Another example is AN aerosol. Most of the AN aerosol comes from recombination of NH<sub>3</sub> and HNO<sub>3</sub> that was formed by reaction 1. However, AN aerosol could also arise from reaction 5 [18].





Considering the experimental limitations, proof of the detailed reactions that are responsible for all of the decomposition products of bulk AN cannot be obtained. At high temperature the realities are that the various combinations of reactions of  $\text{NH}_4\text{NO}_3$ ,  $\text{HNO}_3$ ,  $\text{NH}_3$ , and  $\text{NO}_2$  in the presence of  $\text{H}_2\text{O}$  become almost impossible to distinguish. Nevertheless, the sequential appearance of the gas products combined with the corresponding thermochemical details enables a reaction scheme to be developed that matches the experimental findings.

#### Decomposition at 383°C: 1 atm

Although pure AN will not burn at 1 atm, a sample can be driven by the T-jump method to a temperature that is at or above the measured surface temperature of AN burning at 25 atm or above (300°–350°C [16, 17]). At 1 atm pressure the chemical sequences expand in time compared to those at higher pressure and are, therefore, easier to determine. Figure 1 shows the gas products and thermal response of a 20  $\mu\text{g}$  film of AN heated at 2000°C/sec to 383°C and then held at 383°C.

The concentration data in this plot are based on the scaled growth of the IR absorbance values for each product as described in the experimental section. Such a procedure indicates the amount of gas formed at each time as well as the relative concentration. The superposition of several stoichiometric reactions (Scheme I) is indicated. Of course, many elementary steps are imbedded in each of these

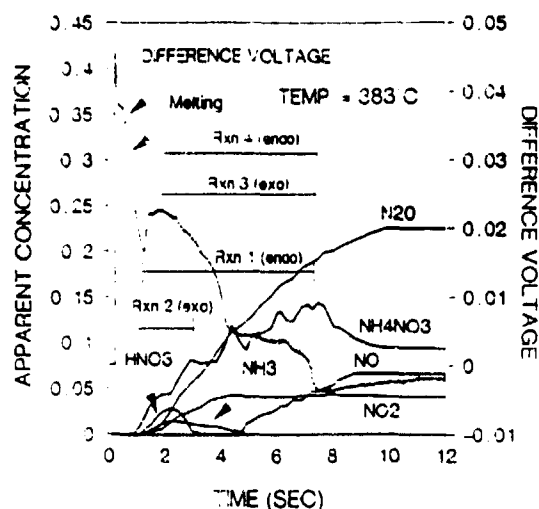


Fig. 1. T-Jump/FTIR data for AN heated at 2000°C/sec to 383°C and held isothermally at that temperature while under 1 atm Ar. The proposed reactions are given in Scheme I. The relative concentrations of the gas products are based on the IR absorbance values scaled by the absolute absorbance at each time. AN is solid aerosol and was given a multiplicative factor of unity in the quantitation process (see experimental section).

stoichiometric reactions, but they are not determinable by T-jump/FTIR spectroscopy.

The first event is rapid endothermic melting of AN as indicated by the upward deflection in the difference control voltage trace. The control voltage decreases on completion of melting from 0.5–1 sec. The process turns markedly endothermic again at about 1 sec. This second endothermic event corresponds to the appearance and growth of AN aerosol. AN aerosol forms from the endothermic dissociation of AN and desorption to  $\text{HNO}_3(\text{g}) + \text{NH}_3(\text{g})$ , followed by recombination of  $\text{NH}_3$  and  $\text{HNO}_3$  in the gas phase (Scheme I, reaction A). Only the

#### SCHEME I

Proposed Reactions that Account for the Products of High Temperature Decomposition of AN (see Figure 1)

	Approx $\Delta H$ , kcal
A. $4(\text{NH}_4\text{NO}_3(\text{l}) \rightarrow \text{HNO}_3(\text{g}) + \text{NH}_3(\text{g}) \rightarrow \text{NH}_4\text{NO}_3(\text{solid aerosol}))$	4(44) <sup>1</sup>
B. $3(\text{NH}_4\text{NO}_3(\text{l}) \rightarrow 2\text{HNO}_3 + 4\text{N}_2 + 9\text{H}_2\text{O})$	3(-35) <sup>2</sup>
C. $5(\text{NH}_4\text{NO}_3(\text{l}) \rightarrow \text{N}_2\text{O} + 2\text{H}_2\text{O})$	5(-13)
D. $4\text{NH}_4\text{NO}_3(\text{l}) \rightarrow 2\text{NH}_3 + 3\text{NO}_2 + \text{NO} + \text{N}_2 + 5\text{H}_2\text{O}$	81

A. D<sup>1</sup>  $28\text{NH}_4\text{NO}_3(\text{l}) \rightarrow 6\text{HNO}_3 + 3\text{NO}_2 + \text{NO} + 2\text{NH}_3 + 5\text{N}_2\text{O} + 13\text{N}_2 + 42\text{H}_2\text{O} + 4\text{NH}_4\text{NO}_3(\text{aerosol})$  87

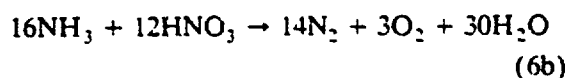
<sup>1</sup>  $\Delta H$  for the desorption step only (see text).  $\Delta H_f$  for  $\text{HNO}_3(\text{g})$  from ref. 27

<sup>2</sup> Ref. 1, p. A320

<sup>3</sup> Gives the approximate IR active gas product ratios at 2 sec for AN at 383°C (Fig. 1).

endothermic first step of reaction A is included in  $\Delta H$  given for reaction A because the second step occurs in the cooler region of the cell away from the filament. Hence, the exothermic second step is not sensed by the filament. However, a white smoke of AN aerosol is visually observed.

Despite the continuation of reaction A throughout the decomposition process as evidenced by the growth of the AN aerosol concentration, the decomposition process becomes less endothermic again at about 2 sec.  $H_2O$  (not quantified) and excess  $HNO_3$  form at this time, which is consistent with the occurrence in reaction B. This reaction is known and its enthalpy has been deduced [1]. Although the details of reaction B are debatable, previous studies also show that the concentration of  $HNO_3$  in the vapor exceeds that  $NH_3$  [2, 19, 20]. Reactions 6a and 6b, which are equivalent to reaction B, have been proposed to explain the buildup of  $HNO_3$  because they consume more  $NH_3$  than  $HNO_3$  [2, 21]. Reaction 6b was proposed to account for the presence of a



small amount of  $O_2$  in the product gases [2]. However, various other decomposition reactions of AN can produce  $O_2$ . As reactions 6a,b imply, reaction B of Scheme I can be thought of as a secondary reaction of the products of reaction A. Reaction B occurs because of the presence of a heat source, which is the filament in this case, but would be the flame, were gas-phase combustion occurring. Consistent with this is the fact that the amount of  $HNO_3(g)$  relative to the other products is greater as the filament is stepped to higher temperatures. Irrespective of the reaction detail, the control voltage trace reveals that decreased endothermicity of the overall process coincides with the appearance of excess  $HNO_3$ . Reactions B, 6a, and 6b are all exothermic and would reduce the overall endothermicity of the decomposition process, as is found.

The process becomes still less endothermic from 2–4 sec as the amount of  $HNO_3$  diminishes. However,  $N_2O$  grows rapidly in concen-

tration through this time suggesting that another exothermic reaction plays an increasingly important role. The exothermic reaction C accounts for these results and is a universally accepted decomposition reaction of AN [1–7]. However, there is evidence of yet another reaction that occurs in parallel as indicated by the appearance of  $NO_2$  and the eventual decrease in exothermicity again between 4–6 sec. Also,  $NO$ , whose IR absorbance is very small, probably forms earlier than is indicated in Figure 1. Reaction D [22] accounts for these observations. Its endothermicity is superimposed on the exothermicity of reaction C and results in a leveling of the control voltage trace (heat flow is balanced) at 4–7 sec. Reaction D is also a source of  $NH_3$ , which appears as a product for a much longer time than  $HNO_3$ . At 7 sec the sample has completely gasified.

The multiplicative factors of the reactions in Scheme I were determined by the need to match the approximate relative concentrations of the gas products at a time when all of the reactions contribute. The concentrations at 2 sec were chosen. The stoichiometry of the net reaction in Scheme I approximates that found at 2 sec in Figure 1. Although the enthalpy of the net reaction is slightly exothermic as written, the relative contribution of reaction A need only be increased somewhat to produce a net endothermic process. As mentioned in the experimental section, the relative amount of AN aerosol is not known because no IR absorbance value is available. Hence, we do not know exactly how much AN aerosol is present. As can be seen in Figure 1, the relative contributions of reactions A–D change with time so the multiplicative coefficients in Scheme I will be different at each time in the decomposition process. This will also affect the net amount of heat released at any particular time. Hence, the step behavior of the thermochemical trace of Figure 1 and in other work [7] is understandable.

Several other factors contribute to the final gas product concentrations in Figure 1. AN aerosol will deposit on the cooler surfaces in the cell resulting in a drop in the AN concentration at the end of the process. Also, the gas surrounding the filament becomes hotter with time. This can significantly increase the con-

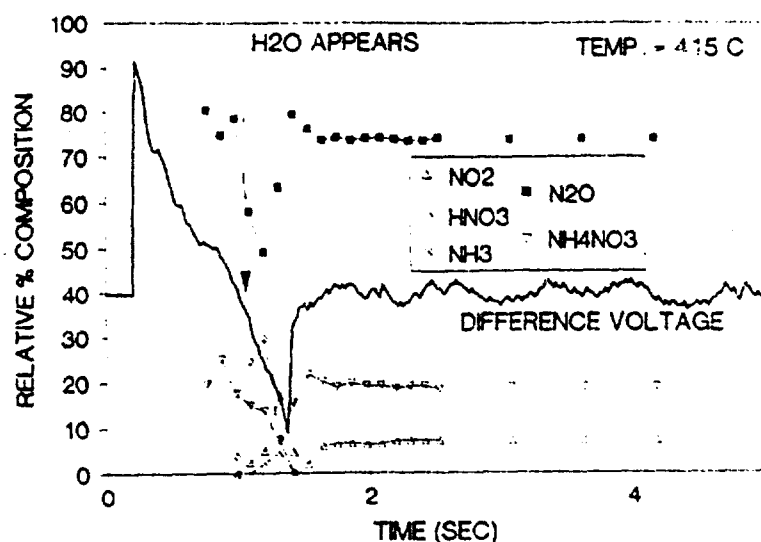


Fig. 2. T-Jump/FTIR data for AN heated at 2000°C/sec to 415°C and held while under 33 atm of Ar. The process only becomes exothermic in the late stage when the  $\text{NH}_3 + \text{NO}_2$  reaction occurs. The relative percentage of composition of the gas products based on a 100% scale throughout is given.

centration of NO relative to  $\text{NO}_2$  as a result of reaction 7. Assuming a value of  $K = 0.09$  M for reaction 7 at



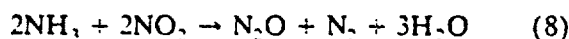
at 383°C, the NO/ $\text{NO}_2$  ratio is about 2/3. The concentration of NO at the end of the reaction is indeed greater than reaction D predicts, probably because of the contribution of reaction 7.

#### Decomposition at 415°C; 33 atm

The formation of  $\text{NH}_3$  and  $\text{NO}_2$  by reaction D raises the possibility that the process could be made exothermic when confined by pressure. The reaction of  $\text{NH}_3$  and  $\text{NO}_2$  becomes rapid and exothermic in the 330–530°C range [23, 24]. However, significant generation of heat requires confinement to enhance the concentration of  $\text{NH}_3$  and  $\text{NO}_2$  in the hot zone around the condensed phase. In fact, the application of pressure was previously observed to cause the late stage endotherm of AN to become an exotherm [7], but this could not be explained with the data available at the time.

Figure 2 shows the decomposition process of a 200  $\mu\text{g}$  film of AN heated at 2000°C/sec to 415°C under 33 atm of Ar. The concentrations are shown as relative percentages as described in the experimental section so that the behavior early in the decomposition process can be more clearly seen.

The melting endotherm initially dominates. The heat of reactions A–D leading to the formation of AN aerosol,  $\text{N}_2\text{O}$ ,  $\text{HNO}_3$ ,  $\text{NH}_3$ , and  $\text{NO}_2$  are overall endothermic until 1.5 sec. At this time the concentrations of  $\text{NH}_3$  and  $\text{NO}_2$  formed by reaction D drop markedly and are accompanied by an exotherm, which suggests that reaction 8 occurs [24].  $\Delta H$  is about –148 kcal for this reaction.



Under pressure, this nominally gas-phase reaction, which has been recognized as such for AN [25], could occur in the heterogenous gas-condensed phase (e.g. bubbles and voids) and contribute to the condensed phase heat balance under combustion conditions. However, despite this late stage exothermicity, the overall decomposition process in Fig. 2 is close to thermoneutral or mildly endothermic. The difficulty of making the condensed phase decomposition process of AN become exothermic even under a pressure of 33 atm Ar seems in line with the findings of Brewster et al., [16] that the condensed phase is endothermic by 200–400 cal/g when pure AN burns at 27 atm.

#### AMMONIUM DINITRAMIDE

The thermal decomposition behavior of bulk ADN is very different from that of AN despite the fact that similar gas products are formed

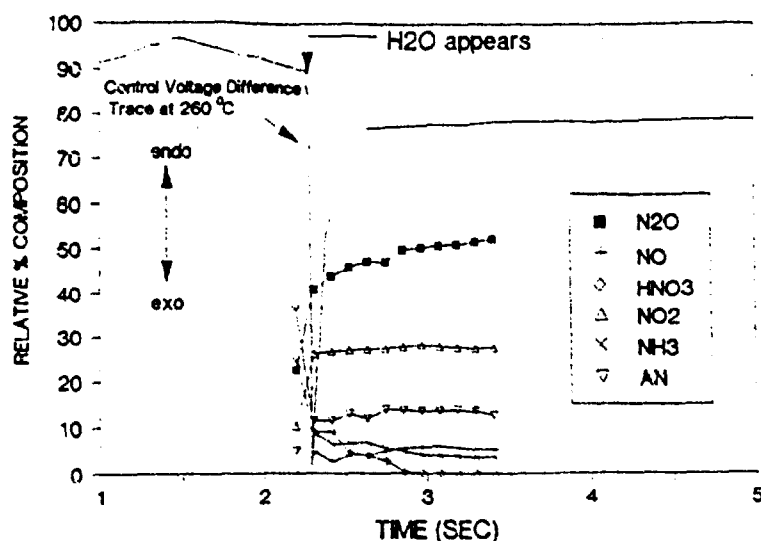


Fig. 3. T-Jump/FTIR data for ADN heated on a Pt filament at 2000°C/sec to 260°C under 1 atm Ar. Unlike Fig. 1, the relative concentrations of the gas products are shown. The decomposition process becomes strongly exothermic as the first gas products are detected.

on rapid decomposition. Figure 3 shows T-jump/FTIR data for a 200  $\mu\text{g}$  film of ADN heated at 2000°C/sec to 260°C. This temperature compares with a preliminary surface temperature measurement of burning ADN of

about 300°C [26], which is surprisingly similar to that of AN. According to Fig. 3, melting of ADN is centered at about 1.5 sec. At the onset of decomposition, gas products and, in contrast to AN, sharp exothermicity occur instantly. The

#### SCHEME II

The Proposed Reactions that are Responsible for the Gases Released by ADN During High Rate Pyrolysis

		Approx. $\Delta H_{rxn}$ , kcal
	<i>Branch A</i> <sup>1</sup>	
	$3[\text{ADN} \rightarrow \text{NH}_3 + \text{HNO}_3 + \text{N}_2\text{O}]$	$3(+11.5)$
	<i>Branch B</i>	
<i>a</i>	$9[\text{ADN} \rightarrow \text{NH}_3 + \text{HN}(\text{NO}_2)_2]$	
<i>b</i>	$9[\text{HN}(\text{NO}_2)_2 \rightarrow \text{NO}_2 + \text{HNNO}_2]$	
<i>c</i>	$6[\text{HNNO}_2 \rightarrow \text{N}_2\text{O} + \text{OH}]$	
<i>d</i>	$2[\text{HNNO}_2 + \text{OH} \rightarrow 2\text{NO} + \text{H}_2\text{O}]$	
<i>e</i>	$\text{HNNO}_2 + \text{NO} \rightarrow \text{NO}_2 + \text{HNNO}$	
<i>f</i>	$\text{HNNO} + \text{OH} \rightarrow \text{N}_2\text{O} + \text{H}_2\text{O}$	
<i>g</i>	$3[\text{NH}_3 + \text{OH} \rightarrow \text{H}_2\text{O} + \text{NH}_2]$	
<i>h</i>	$3[\text{NH}_2 + \text{NO} \rightarrow \text{N}_2 + \text{H}_2\text{O}]$	
<i>i</i> <sup>2</sup>	$9\text{ADN} \rightarrow 6\text{NH}_3 + 7\text{N}_2\text{O} + 10\text{NO}_2 + 9\text{H}_2\text{O} + 3\text{N}_2$	-49
<i>j</i> <sup>3</sup>	$12\text{ADN} \rightarrow 9\text{NH}_3 + 10\text{N}_2\text{O} + 10\text{NO}_2 + 9\text{H}_2\text{O} + 3\text{N}_2 + 3\text{HNO}_3$	-14
<i>k</i>	$4\text{NH}_3 + 4\text{NO}_2 \rightarrow 3\text{N}_2 + 2\text{NO} + 6\text{H}_2\text{O}$	-309
<i>l</i> <sup>4</sup>	$12\text{ADN} \rightarrow 5\text{NH}_3 + 10\text{N}_2\text{O} + 6\text{NO}_2 + 15\text{H}_2\text{O} + 2\text{NO} + 6\text{N}_2 + 3\text{HNO}_3$	-323
<i>m</i> <sup>5</sup>	$2\text{NH}_3 + 2\text{HNO}_3 \rightarrow 2\text{NH}_4\text{NO}_3$ (aerosol)	
<i>n</i> <sup>6</sup>	$12\text{ADN} \rightarrow 3\text{NH}_3 + 10\text{N}_2\text{O} + 6\text{NO}_2 + 15\text{H}_2\text{O} + 2\text{NO} + 6\text{N}_2 + \text{HNO}_3 + 2\text{NH}_4\text{NO}_3$	-323

<sup>1</sup> Assumes  $\Delta H_f$  (ADN) = -35 kcal/mol, and  $\Delta H_f$  [ $\text{HNO}_3(\text{g})$ ] is -33 kcal/mol.

<sup>2</sup> Sum of *a-h*.

<sup>3</sup> Sum of Branches A & B.

<sup>4</sup> Sum of reactions *j* + *k*.

<sup>5</sup> Occurs in gas phase away from surface so reaction *m* is not included in  $\Delta H$ .

<sup>6</sup> Sum of *l* and *m* gives the approximate gas phase stoichiometry at the end of the exotherm (Fig. 3).

first detected products are mostly  $\text{HNO}_3$ ,  $\text{NH}_3$ , and  $\text{N}_2\text{O}$  in roughly similar amounts. Minor quantities of  $\text{NO}_2$ , AN, and  $\text{H}_2\text{O}$  are also present in the initial spectrum. Note that the relative percentage of composition based on 100% of the detected gases is given in Fig. 3. This type of plot enables the behavior of the earliest gas products to be observed even though their concentrations are relatively low compared to later times, and the decomposition process is rapid. Following complete decomposition at 2.5 sec, the IR spectra reveal the approximate product ratios of  $12\text{N}_2\text{O}:6\text{NO}_2:3\text{AN}:2\text{NH}_3:\text{HNO}_3:\text{NO}$ . Gas-product ratios have also been obtained on a laser-pyrolyzed sample of ADN by the use of a quartz microprobe mass spectrometer [26] and are comparable to those obtained by IR spectroscopy. By mass spectrometry, the quantities of  $\text{H}_2\text{O}$  and  $\text{N}_2$  are found to be similar to  $\text{N}_2\text{O}$  and  $\text{NO}_2$ , respectively. The consistency of the IR and mass spectral data under rapid pyrolysis conditions gives confidence that the approximate concentration ratios of the gas products leaving the surface reaction zone of ADN at ignition/combustion conditions are now known. The task is to develop a reaction scheme that gives these approximate gas product ratios the sequence of appearance and high exothermicity in the early stage.

The formation of  $\text{HNO}_3$ ,  $\text{NH}_3$ , and  $\text{N}_2\text{O}$  in comparable amounts at the beginning suggests the presence of Branch A in Scheme II. This mildly endothermic reaction may have a role during slow decomposition at lower temperatures. It appears to be a minor branch during rapid heating, especially because it does not account for the major heat release that is experimentally observed. The slight excess of  $\text{HNO}_3$  compared to  $\text{NH}_3$  is consistent with reactions 6a, b, which occur to a small extent as well.

Branch B of Scheme II is proposed to dominate under rapid thermolysis conditions. Reaction *a* of Branch B is dissociation of ADN to produce  $\text{NH}_3$  and  $\text{HN}(\text{NO}_2)_2$ .  $\text{HN}(\text{NO}_2)_2$  is not detected and probably homolyzes in the condensed phase at high temperature by reaction *b* to  $\text{NO}_2$  and  $\text{HNNO}_2$ . Reactions *a* and *b* are endothermic. Because relatively large quantities of  $\text{NH}_3$  and  $\text{NO}_2$  occur early in

Branch B, much heat can be generated by reaction *k* in the gas phase near the surface or even as part of the heterogeneous gas-liquid zone at the surface. The high exothermicity is evident in the large control voltage deflection at 2.3 sec, and provides the energy to complete the decomposition process very rapidly. Some of the  $\text{NH}_3$  and  $\text{NO}_2$  remains unreacted because it escapes to the cooler region of the atmosphere. The fact that the surface temperatures of AN and ADN are similar implies that the heat released by reaction *k* occurs mostly in the gas phase near the surface and that the temperature of the gas phase must rise very rapidly as the products leave the surface. Reactions *c-h* are plausible subsequent steps for decomposition of  $\text{HNNO}_2$ , but they are not determined by T-jump/FTIR spectroscopy. They are simply proposed as reasonable sources of stable products in the quantities detected. The net reaction *i* of Branch B is mildly exothermic. Combining Branches A and B yields the exothermic reaction *j*. Adding some gas-phase recombination of  $\text{NH}_3$  and  $\text{HNO}_3$  (reaction *m*) to account for the observed AN solid aerosol yields reaction *n*, whose stoichiometry approximates the experimentally observed gas product ratios observed at 2.5 sec in Fig. 3.

Reaction *n* is not a perfect description of the experimentally observed gas product ratios from rapid decomposition of ADN. It contains more  $\text{H}_2\text{O}$ ,  $\text{NH}_3$ , and  $\text{NO}$  and less  $\text{N}_2\text{O}$  than is experimentally found. However, some variances would not be surprising considering the difficulty of precise measurements under these conditions. The agreement can be improved somewhat by allowing for variations in the products of reaction *k*. The amount of  $\text{NO}$  can be reduced and the amount of  $\text{N}_2\text{O}$  raised by noting the findings of Bedford and Thomas [24] indicating that reaction *k* can also occur partly with the stoichiometry of reaction 8.

As with AN, reaction *m* occurs in the cooler gas phase away from the surface and, therefore, does not contribute to the surface heat balance. Therefore, this reaction was not included in the net heat of reaction *n*. Reaction *m* contributes to the white smoke that is observed when ADN is rapidly decomposed in a cool atmosphere. It would not occur with a

flame present because the  $\text{NH}_3$  and  $\text{HNO}_3$  would react before recombining.

### COMPARISON OF AN AND ADN DECOMPOSITION

The rapid decomposition process of AN is clearly endothermic at pressures up to at least 30 atm. At higher pressure an exothermic component appears late in the decomposition process and brings the overall decomposition process closer to thermoneutrality. The exotherm is accompanied by a drop in the amount of  $\text{NH}_3$  and  $\text{NO}_2$  that appear in the gas phase. Although the reaction of  $\text{NH}_3$  and  $\text{NO}_2$  appears to be responsible for this exotherm, the amount of  $\text{NH}_3$  and  $\text{NO}_2$  is smaller for AN than for ADN and so much less heat is generated.

In contrast, the rapid decomposition process of ADN is strongly exothermic early in the reaction scheme. This behavior is consistent with the ease of formation of a large amount of  $\text{NH}_3$  and  $\text{NO}_2$  in the early decomposition steps. Because the reaction of  $\text{NH}_3$  and  $\text{NO}_2$  can dominate early and produces a large amount of heat, the overall decomposition and gasification process is driven at a much high rate for ADN than AN. Therefore, for both AN and ADN the reaction of  $\text{NH}_3$  with  $\text{NO}_2$  is implicated as the main source of heat when the pure material is decomposed at high temperature. For AN this reaction only becomes important under confinement, such as by the application of high pressure.

*We are grateful to the Air Force Office of Scientific Research for support of this work on AFOSR-89-0521. T.B.B. wishes to thank M.C. Lin, T. Litzinger, D. McMillen, and C. Melius for helpful discussions and data exchange on ADN.*

### REFERENCES

1. Federoff, B. T. *Encyclopedia of Explosives and Related Items*. Picatinny Arsenal, Dover, NJ, 1960, Vol. I, A311-379.
2. Medard, L. A. *Accidental Explosions* Wiley, New York, 1989, Vol. II, pp. 545-592.
3. Brower, K. R., Odley, J. C., and Tewari, M. J. *Phys. Chem.* 93:4029-4033 (1989).
4. Rosser, W. A., Inami, S. H., and Wise, H. J. *Phys. Chem.* 67:1753-1757 (1963).
5. Koper, J. H., Jansen, O. G., and van den Berg, P. J. *Explosivstoffe* 8:181-183 (1970).
6. Patil, D. G., Jain, S. R., and Brill, T. B. *Prop. Explos. Pyrotech.* 17:99-105 (1992).
7. Russell, T. P., and Brill, T. B. *Combust. Flame* 76:393-401 (1989).
8. Anderson, W. H., Bills, K. W., Mishuck, E., Moe, G., and Schultz, R. D. *Combust. Flame* 3:301-317 (1957).
9. Beckstead, M. W. *Twenty Sixth JANNAF Combustion Mtg.* CPIA Publ. 529, Vol. 4:255-268 (1989).
10. Bottaro, J. C., Schmidt, R. J., Pennwell, P. E., and Ross, D. S. *World Intellectual Property Organization* WO 91/19669 and WO 91/19670.
11. Determined in a bomb calorimeter under 25 atm  $\text{O}_2$ . Mark Swett, NWC, personal communication (1992).
12. Brill, T. B., Brush, P. J., James, K. J., Shepherd, J. E., and Pfeiffer, K. J. *Appl. Spectrosc.* 46:900-911 (1992).
13. Brill, T. B. *Prog. Energy Combust. Sci.* 18:91-116 (1992).
14. Feick, G. and Hainer, R. M., *J. Am. Chem. Soc.* 76:5860-5863 (1954).
15. Monroe, C. E. *Chem. Met. Eng.* 26:535-542 (1922).
16. Brewster, M. Q., Sheridan, T. A., and Ishihara, A. J. *Propuls. Power* in press.
17. Whittaker, A. G. and Barham, D. C. *J. Phys. Chem.* 68:196-199 (1964).
18. Falk, R., and Pease, R. N. *J. Am. Chem. Soc.* 76:4746-4747 (1954).
19. Shah, M. S., and Oza, T. M. *J. Chem. Soc.* 725-736 (1932).
20. Friedman, L., Bigeleisen, J. *J. Chem. Phys.* 18:1325-1331 (1950).
21. Saunders, L. H. *J. Chem. Soc.* 121:698-711 (1922).
22. Kaiser, R. *Angew. Chem.* 48:149-150 (1935).
23. Rosser, W. A., and Wise, H. J. *J. Chem. Phys.* 25:1078-1079 (1956).
24. Bedford, G., and Thomas, J. H. *J. Chem. Soc., Farad. Trans. I* 2168-2170 (1972).
25. Chaiken, R. F. *Combust. Flame* 3:285-300 (1959).
26. Fetherolf, B. L., and Litzinger, T. A., Penn State Univ., personal communication (1992).
27. Baulch, D. L., Cox, R. A., Hampson, R. F., Kerr, J. A., Troe, J., and Watson, R. T. *J. Phys. Chem. Ref. Data* 13:1259-1380 (1984).

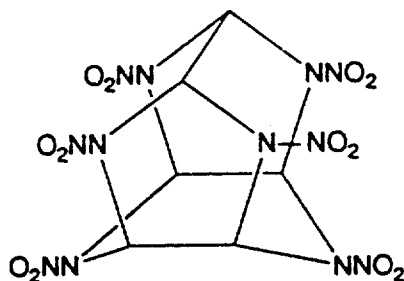
*Received 14 May 1992; revised 27 August 1992*

## Thermal Decomposition of Energetic Materials 59. Characterization of the Residue of Hexanitrohexaazaisowurtzitane

D. G. PATIL and T. B. BRILL\*

*Department of Chemistry, University of Delaware, Newark, DE 19716*

The polycyclic nitramine,  $\beta$ -hexanitrohexaazaisowurtzitane (HNIW), decomposes exothermically above 195°C, liberating large amounts of  $\text{NO}_2$  and NO and lesser amounts of CO,  $\text{CO}_2$ , HCN, HNCO, and  $\text{N}_2\text{O}$  [1]. A dark-colored residue remains.



The infrared spectrum of the residue formed at 220°C was found to contain broad absorbances characteristic of a complex mixture of CO, NO, CN, and CC single and double bonds and CH modes [1]. The residue of HNIW remaining after many hours at 205°C was 17% of the original sample weight and had an elemental composition of  $\text{C}_6\text{H}_5\text{N}_5\text{O}_2$  [2]. Little else has been reported.

The residue forms and burns during combustion of HNIW [3]. Therefore, the residue plays a role in the surface reaction zone of burning HNIW, and its decomposition characteristics are of interest. In this note, characterization and decomposition of the residue formed at various temperatures above 240°C are determined by using T-jump/FTIR spectroscopy.

T-jump/FTIR spectroscopy [4] enables a 200- $\mu\text{g}$  film of HNIW to be heated on a Pt

filament at 2000°C/s to a chosen constant temperature under 1 atm Ar. The IR spectra of the gaseous products are recorded in near real-time at 10 scans/s. The final temperature of the filament was 240°–320°C in 10°C intervals. This temperature was held for 3 s after the decomposition exotherm. The filament was then immediately cooled and the cell purged for 5 min with Ar to remove all decomposition gases. The residue remaining on the filament was then reheated in Ar at 2000°C/s to 700°C for 10 s. During this time the gaseous products from the decomposition of the residue were monitored. It was determined separately that 700°C was the temperature necessary to decompose the residue completely. A very small amount of residue remained at 650°C.

Figure 1 shows the relative concentrations of the IR active gaseous products 1 s after the first decomposition products from the residue are detected. The temperatures shown are those at which the original HNIW samples were decomposed (240°–320°C). The only IR active products detected are HNCO, HCN,  $\text{CO}_2$ , and (for decomposition of HNIW below 285°C)  $\text{NO}_2$ . The absolute IR absorbance of HNCO is unknown. A scaling factor of 1.5 was used for the 2280- $\text{cm}^{-1}$  stretching mode. This value is the average of the same mode of the isoelectronic  $\text{CO}_2$  molecule and  $\text{N}_2\text{O}$  [5]. Since the elements of HNIW are equally represented in HNCO, the absorbance value of HNCO is not a factor in determining the elemental composition of the residue.

The presence of gaseous  $\text{NO}_2$  in Fig. 1 indicates that some of the  $-\text{NO}_2$  functional groups are retained by the residue up to 285°C. Somewhat more  $\text{CO}_2$  is formed at lower tempera-

\* Corresponding author.

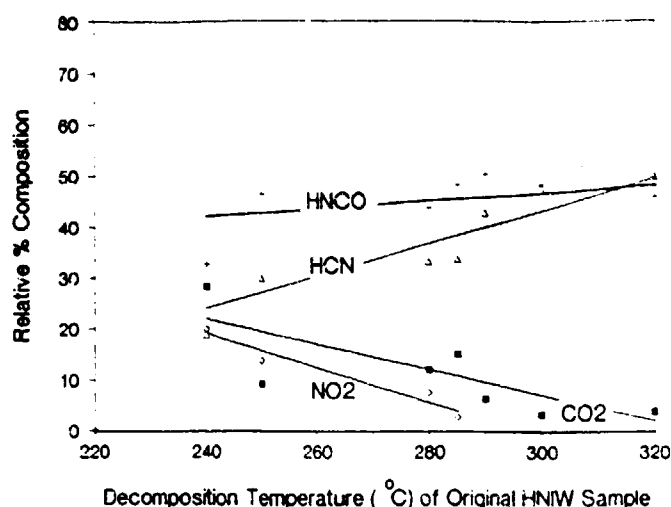
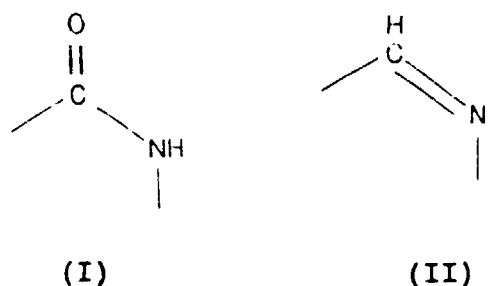


Fig. 1. The relative concentrations of the gas products detected 1 s after thermolysis occurs of residues of HNIW at 700°C under 1 atm Ar. The temperature shown are the original decomposition temperatures of the HNIW samples.

ture than at higher temperature, perhaps because the residual  $-\text{NO}_2$  groups can form  $\text{NO}_2$  and oxidize carbon. HNCO and HCN are the dominant decomposition products of the residue. HNCO can be produced by decomposition of the amide unit (I) [6, 7] and HCN can form from polyazine units (II) [8]. Cyclic azines, such as melon, are known to be thermally

stable up to at least 700°C [9, 10]. The high concentrations of HNCO and HCN along with the IR spectrum of the residue [1] indicate a high percentage of amide and azine linkages in the residue.

Figure 2 shows the elemental composition of the residues formed at each temperature based on the absorbance value of each gaseous product scaled by its absolute absorbance [5]. Above 285°C, when all of the  $\text{NO}_2$  groups have been eliminated, the elemental composition of the residue is relatively independent of the decomposition temperature of the original, rapidly heated HNIW sample and averages to about  $\text{C}_4\text{H}_4\text{N}_4\text{O}_2$ .



We are grateful to the Air Force Office of Scientific Research, Aerospace Sciences, for support of this work on AFOSR-89-0521.

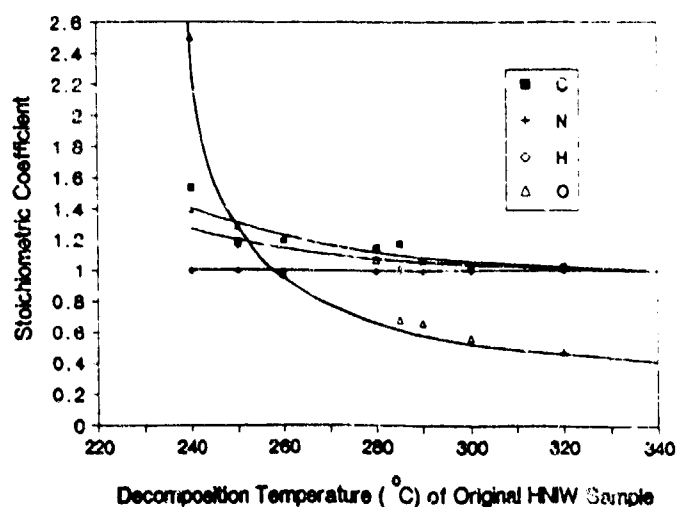


Fig. 2. The stoichiometric coefficients for C, H, N, and O of the residue of HNIW samples based on the gas products present after 1 s. The temperatures shown are the decomposition temperatures of the original HNIW sample in 1 atm Ar.



## REFERENCES

1. Patil, D. G., and Brill, T. B., *Combust. Flame* 87:145-151 (1991).
2. Krautle, K., Twenty-seventh JANNAF Combustion Meeting, CPIA Publ., 557, 1990, Vol. II, pp. 269-284.
3. Parr, T. P., NAWC, personal communication, 1992.
4. Brill, T. B., Brush, P. J., James, K. J., Shepherd, J. E., and Pfeiffer, K. J., *Appl. Spectrosc.* 46:900-911 (1992).
5. Brill, T. B., *Prog. Ener. Combust. Sci.* 18:91-116 (1992).
6. Palopoli, S. E., and Brill, T. B., *Combust. Flame* 87:45-60 (1991).
7. Oyumi, Y., and Brill, T. B., *Prop. Explos. Pyrotech.* 13:69-73 (1988).
8. Gao, A., Oyumi, Y., and Brill, T. B., *Combust. Flame* 83:345-352 (1991).
9. Finkelshtein, A. I., and Spiridonova, N. V., *J. Org. Chem. (Russ.)*, 1:602-604 (1965).
10. Stoner, C. E., Jr., and Brill, T. B., *Combust. Flame*, 83:302-308 (1991).

Received 29 June 1992; revised 20 October 1992

# Thermal Decomposition of Energetic Materials 63. Surface Reaction Zone Chemistry of Simulated Burning 1,3,5,5-Tetranitrohexahydropyrimidine (DNNC or TNDA) Compared to RDX

T. B. BRILL\* and D. G. PATIL

*Department of Chemistry, University of Delaware, Newark, DE 19716, U.S.A*

J. DUTERQUE and G. LENGELLÉ

*ONERA, B.P. No. 72, F. 92322 Châtillon Cedex, France*

The oxidizers 1,3,5,5-tetranitrohexahydropyrimidine (DNNC or TNDA) and RDX are found to have similar burn rates in a strand burner operating at 20–250 atm. These strand burner data extrapolate well to the regression rates obtained from high-rate weight-loss measurements by SMATCH/FTIR spectroscopy on films of DNNC and RDX of about 45  $\mu\text{m}$  thickness. This observation supports the use of rapid pyrolysis of films coupled with spectral diagnostics to determine chemical details about the surface reaction zone of burning DNNC and RDX. By using T-jump/FTIR spectroscopy, the gas product concentrations from DNNC rapidly decomposing at 220°–300°C reveal that DNNC and RDX thermolyze by different routes. Decomposition reactions that form NO are especially important for DNNC, but this does not affect the primary flame zone. The primary flame zone of both DNNC and RDX appears to be dominated by the reaction of  $\text{CH}_2\text{O}$  and  $\text{NO}_2$ , which contributes to the similarity of their burn rates.

## INTRODUCTION

During combustion of solid rocket propellants, thermal decomposition of the ingredients occurs in a thin heterogeneous reaction layer at the surface. Chemical description of this layer is needed to develop models of combustion that include the burning surface because the product gases play an important role in the flame structure [1]. Unfortunately, the flame interferes with determination of the surface reaction mechanisms because the decomposition products react further very close to the surface.

An alternative approach to learning about the surface reaction layer is to simulate the burning surface with a film of material in which quasi-isothermal decomposition is induced by rapidly heating to a high constant temperature. This objective is achieved with T-jump/FTIR spectroscopy in which a film-like quantity of material is ramp-heated on a Pt ribbon fila-

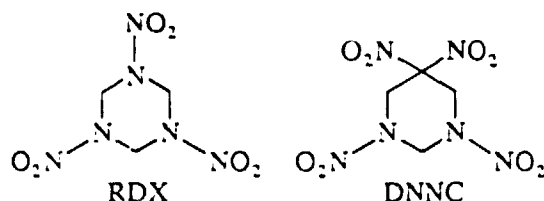
ment at 2000°C/s to a chosen constant temperature [2]. The decomposition products evolve into a cool nonreactive (Ar) atmosphere and are detected by rapid-scan FTIR spectroscopy. The gas products form the first stage of the flame zone if a steady flame is present. Simultaneously, the endothermic and exothermic responses of the sample are reflected in the control voltage of the filament. Details about the decomposition mechanism of the bulk material can be extracted from these data [3–5], and can be used to understand more about the burning surface.

Although T-jump/FTIR spectroscopy is intended to simulate surface decomposition for an instant during steady-state combustion, the validity of such an approach is best established by the second fast thermolysis technique, SMATCH/FTIR spectroscopy [6–9]. SMATCH/FTIR permits measurement of the rate of mass loss of the film during rapid heating at 1 atm. If the regression rate calculated from these data extrapolates to the burn rate of a bulk sample at higher pressure, then the decomposition mechanisms of the film and

\* Corresponding author.

the surface of the bulk sample are expected to be similar.

Of particular interest in this article is the fact that the burn rates of hexahydro-1,3,5-trinitro-s-triazine (RDX) and 1,3,5,5-tetranitro-hexahydropyrimidine (DNNC or TNDA, but hereafter referred to as DNNC) turn out to be nearly the same, whereas rather different decomposition gases were previously found [10]. New details about the rapid decomposition mechanism of RDX [11] and HMX [4] have recently been obtained from T-jump/FTIR spectroscopy. This technique is especially helpful because the sequence of formation of the gas products can be seen simultaneously with the overall balance of heat flow to and from the sample. A reexamination of DNNC by T-jump FTIR spectroscopy is in order, especially because of interest in DNNC as an oxidizer in minimum smoke propellant formulations. Moreover, the two types of energetic sites in DNNC make its decomposition mechanism potentially more complicated and intriguing than RDX.



## EXPERIMENTAL SECTION

DNNC [12-14] used for thermal decomposition studies was provided by SRI International, Menlo Park, CA. Burn rate measurements were made at ONERA on DNNC supplied by SNPE, Le Bouchet, France [15].

For burn rate measurements, rectangular blocks (15 × 5 × 5 mm) were formed by pressing under 13 metric tons/cm<sup>2</sup> to a density of 1.68-1.72 g/cm<sup>3</sup> for DNNC and 1.76-1.79 g/cm<sup>3</sup> for RDX. The sample was ignited by an electric wire in a strand burner under an N<sub>2</sub> pressure set as desired in the 20-250-atm range. The combustion time was determined by a photodiode signal.

The SMATCH/FTIR technique and data reduction methods have been described else-

where [6-9]. Briefly, films of DNNC (45 μm thickness) and RDX (40 μm) having about 900 μg mass were coated onto the stainless-steel end-tip of the quartz vibration element by repeatedly dipping the tube into an acetone solution and evaporating the acetone. The rate of weight loss during heating at 250°C/s was determined (Fig. 1). A thermocouple spot-welded to the metal end-tip provided a real-time temperature measurement. The initial 50% weight loss by DNNC and RDX was fit by the polynomial equation 1, with the coefficients given in Table 1:

$$1 - \alpha = \sum_{i=0}^3 a_i t^i \quad (1)$$

This polynomial and its first derivative yield  $1 - \alpha$ , and  $d\alpha/dt$ , respectively, for use in Eq. 2, where  $\alpha$  is the fraction of the sample decomposed [7-9]. Equation 2 was found to be linear with  $n = 2$  and, by use of the temperature at 25% weight loss, was

$$\ln \left[ \frac{d\alpha}{dt} \frac{1}{(1 - \alpha)^n} \right] = \ln A - \frac{E_a}{RT} \quad (2)$$

solved for the prefactor  $A$  and the global activation energy  $E_a$ . The resultant values are given in Table 1 and apply only to the pressure and temperature conditions of the SMATCH/FTIR experiment. The regression rate of the film,  $\dot{r}$ , was calculated by a modified

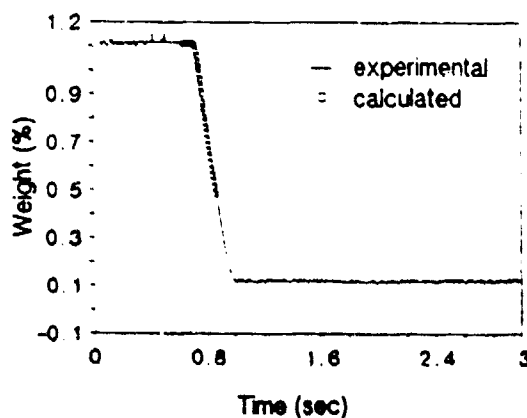


Fig. 1. The weight loss curve measured by SMATCH/FTIR spectroscopy on a 45-μm-thick film of DNNC heated at about 250°C/s under 1 atm Ar. The polynomial fit is shown.

TABLE I  
SMATCH/FTIR Data for DNNC and RDX

Compound	Polynomial Coefficients				Calculated Values		
	$a_0$	$a_1$	$a_2$	$a_3$	$E_a^a$	$\log A^b$	$r^c$
DNNC	0.6395	0.9605	2.3914	-4.4379	42.9	25.4	0.027
RDX	1.833	0.4929	-2.4250	0.8553	29.0	13.64	0.038

<sup>a</sup> kcal/mol.

<sup>b</sup> s<sup>-1</sup>.

<sup>c</sup> cm/s.

version of the pyrolysis law,

$$\dot{r} = A^{1/2} h e^{-E_a/2RT}, \quad (3)$$

where  $h$  is the film thickness given above. Equation 3 is valid if  $h$  is approximately the thickness of the surface reaction zone during combustion at 1 atm. Because  $A$  and  $E_a$  frequently are compensating, this equation yields values of  $\dot{r}$  that are similar to those determined by other equations [7-9].

Equation 3 is a specialized version of Eq. 4, which gives the generalized relationship between  $\dot{r}$  and Arrhenius parameters obtained from thermal decomposition data [1, 7-9, 11]:

$$\dot{r} = \left[ \frac{d_p RT_s}{E_a(-\ln Y_{p,s}) \left( 1 - \frac{T_0}{T_s} - \frac{Q_r}{2CT_s} \right) + \frac{Q_r}{CT_s}} \right]^{1/2} A^{1/2} e^{-E_a/2RT} \quad (4)$$

where  $T_s$  is the surface temperature,  $T_0$  is the initial temperature,  $d_p$  is the thermal diffusivity,  $C$  is the heat capacity,  $Q_r$  is the heat of reaction, and  $Y_{p,s}$  is the amount of nitramine reacting. Equation 4 has been used successfully to describe combustion of inert binders and HMX [1]. To reduce Eq. 4 to Eq. 3, the terms containing  $T_0$  and  $Q_r$  were assumed to be small or compensating. By doing so, the bracketed term in Eq. 4 is approximately the heat conduction length or reaction zone thickness,  $h$ .

SMATCH/FTIR spectroscopy induces sample decomposition along a temperature ramp. The gas products detected, therefore, come from reactions at somewhat different temperatures. This tends to complicate the description of the decomposition mechanism. Mechanistic details are obtained more clearly by decomposing a thin layer of sample quasi-isothermally

following rapid heating to a chosen relative constant temperature. These conditions are created by T-jump/FTIR spectroscopy [2] in which about 200  $\mu$ g of polycrystalline DNNC is thinly spread on a Pt ribbon filament. The filament is housed in a gastight IR cell containing 2.5 atm Ar. Sublimation of DNNC was greatly reduced by using this superatmospheric pressure of Ar. The Pt filament was resistively heated at 2000°C/s to a set temperature and held at that temperature for the duration of decomposition. DNNC initially melts to a thin film. It then decomposes releasing gas products into the cool, nonreactive Ar atmosphere where

they are quenched. The beam of a Nicolet 20SXB rapid-scan FTIR spectrometer focused about 3 mm above the Pt filament recorded an interferogram of the gas products every 200 ms. The endothermic and exothermic events of the sample are detected by monitoring the control voltage of the filament. A difference voltage was obtained by subtracting the control voltage without sample present from the control voltage with sample present. A downward deflection thus corresponds to a net heat release by the sample. By triggering the spectrometer and Pt heater circuit simultaneously, the thermal response of the sample and the IR spectra are correlated in time. Heat transfer limitations make it essentially impossible for the filament and sample to track one another as reactions occur, so the temperatures given in this paper are filament values based on calibration with melting point standards [2].

lease by the sample. By triggering the spectrometer and Pt heater circuit simultaneously, the thermal response of the sample and the IR spectra are correlated in time. Heat transfer limitations make it essentially impossible for the filament and sample to track one another as reactions occur, so the temperatures given in this paper are filament values based on calibration with melting point standards [2].

The IR absorbance of each product was converted to the apparent concentration by multiplying the intensity of a well-resolved vibrational mode by a factor [3] derived from the absolute absorbance. The rate of growth of concentration is obtained in this way throughout the decomposition process. The gas product profiles were smoothed to eliminate fluctuations caused by turbulence and the mirage effect in the gas layer above the filament resulting from intense heat release at the exotherm. The mirage effect redirects the IR beam causing all of the absorbances to decrease for about 0.5 s. IR inactive products are expected to have low concentration and are not included in the quantitation procedure. The  $2280\text{ cm}^{-1}$  mode of HNCO, for which no absolute IR absorbance value is available, was chosen to have a relative absorbance factor of 1.5 based on 1.0 for the isoelectronic  $\text{CO}_2$  molecule and 2.0 for  $\text{N}_2\text{O}$  [3].

### BURN RATE MEASUREMENTS

Linear burn rate data in the 20–250 atm range for pressed samples of DNNC and RDX are shown in Fig. 2. These burn rates are represented by Eqs. 5 and 6

$$\dot{r} = 0.027P^{0.37} \quad (\text{DNNC}), \quad (5)$$

$$\dot{r} = 0.04P^{0.3} \quad (\text{RDX}). \quad (6)$$

Extrapolation of the burn rates to 1 atm shows close intersection with the regression rates of 40–50- $\mu\text{m}$ -thick films of DNNC and RDX that are calculated from SMATCH/FTIR spectroscopy. This connection gives confidence in the use of fast thermolysis of thin layer-like samples at pressures below 20 atm to unravel the surface reaction products that are produced during combustion up to at least 250 atm. It is also significant that the decomposi-

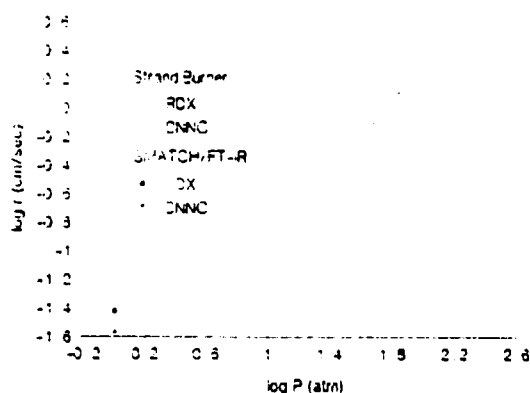


Fig. 2. Linear burn rates of DNNC and RDX measured in an  $\text{N}_2$  atmosphere by a strand burner and extrapolated to the regression rate calculated from SMATCH/FTIR data for a 45- $\mu\text{m}$ -thick film.

tion products of DNNC are found to have little temperature dependence in the 220°–300°C range (*vide infra*). This finding suggests that the decomposition mechanism of bulk DNNC is relatively insensitive to surface temperatures in this range. The final gas product ratios measured by SMATCH/FTIR spectroscopy are similar to those by T-jump/FTIR spectroscopy, but T-jump/FTIR permits the sequence of formation to be determined.

### GAS PRODUCTS AND EXPECTED FLAME STRUCTURE

Previously reported fast thermolysis data on DNNC obtained by ramp heating of a nichrome filament at 145°C/s reveal that  $\text{NO}_2(\text{g})$  dominates initially, but that  $\text{NO}(\text{g})$  grows to be the major product after several seconds [10]. Description of the decomposition mechanism by this method and by SMATCH/FTIR is potentially complicated by the fact that the reaction occurs along a temperature ramp. The deuterium isotope effect of the decomposition rate indicates that C–H bond dissociation in the condensed phase is rate controlling up to the 197°C limit of study [18]. Molecular conformational differences appear to play no role in the decomposition of RDX and DNNC because the interconversion barriers are low [19].

DNNC melts at 152°C and decomposes above 188°C according to DSC [18]. The surface temperature of DNNC during combustion will be much higher than 188°C, but has not been

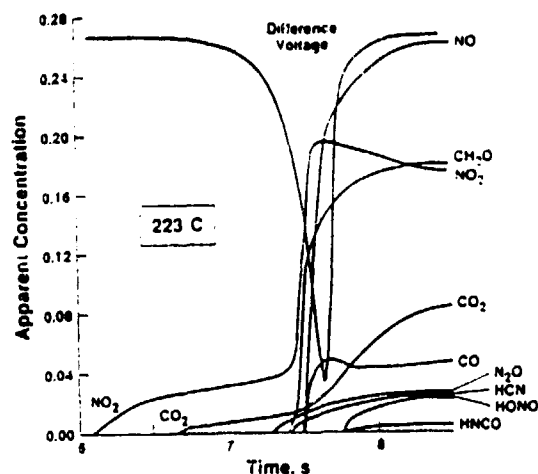


Fig. 3. The sequential appearance and change of concentration of the IR active gas products from DNNC heated at 2000°C/s to 223°C under 2.5 atm of Ar. The concentrations were obtained by scaling the IR absorbances according to the absolute IR intensity of the mode. The difference voltage trace of the Pt filament shows that the heterogeneous condensed phase chemistry becomes strongly exothermic after 7 s.

determined. A temperature of 300°C in the heterogeneous surface reaction zone is reasonable based on the fact that the surface temperature of RDX burning at 1–20 atm is about 100°–150°C above the normal decomposition temperature [20]. Therefore, DNNC was T-jumped to the 220°–300°C range and rapid-scan FTIR spectroscopy was used to determine the gas products generated by heterogeneous decomposition representative of the burning surface.

In Fig. 3 the growth in concentration of each gas product from DNNC heated at 2000°C/s to 223°C is shown along with the difference control voltage trace reflecting the energy release pattern of the condensed phase. Not shown is the endotherm that is completed after 1 s. The data at 223°C were chosen because the major details are clearly revealed. The postreaction product concentrations at 223°C are found to be the same as those up to the 300°C limit of study, indicating that the overall decomposition mechanism has little temperature dependence in the 220°–300°C range. A notable difference is the larger amount of NO<sub>2</sub> and CO<sub>2</sub> detected before the exotherm at 223°C compared to higher temperatures. For example, at 250°C only a trace

of NO<sub>2</sub> and CO<sub>2</sub> are detected 0.5 s before the exotherm. The most logical explanation for this difference is simply that the reaction rates at higher temperature exceed the spectral detection rate.

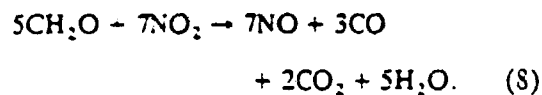
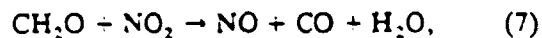
The detection of NO<sub>2</sub> as the initial gas product is good evidence that N–NO<sub>2</sub> and/or C–NO<sub>2</sub> homolysis initiates the decomposition of DNNC. Endothermicity associated with bond scission is offset by non-gas-producing rearrangements in the condensed phase because the control voltage trace indicates thermoneutrality. Overall exothermicity begins as CO<sub>2</sub> forms. The detection of CO<sub>2</sub> before the other redox products may result in part from its large IR absorptivity compared to other gases. However, any decomposition mechanism of DNNC needs to account for early formation of CO<sub>2</sub>.

The second major stage of decomposition of DNNC is strongly exothermic and begins at 7–7.5 s in Fig. 3. The NO, NO<sub>2</sub>, CH<sub>2</sub>O, and CO<sub>2</sub> concentrations rise sharply while CO, HCN, and N<sub>2</sub>O form in lesser amounts. Many reactions occur during this stage and will be discussed in the following section. The products are similar to those reported in an earlier study using steep ramp heating [10], except that no CH<sub>2</sub>O was reported. We can attribute the absence of CH<sub>2</sub>O only to an oversight in the previous data reduction.

A third stage of the reaction scheme involves the formation of a small amount of HONO and HNCO after most of the DNNC has reacted and the local temperature is the highest. HONO may form as a result of scavenging of H· by NO<sub>2</sub> [21]. H· becomes more available in the highly exothermic stage of decomposition. HNCO may originate from the decomposition of a small amount of residue that forms during decomposition at 223°C. In fact, the final gas product mixture in Fig. 1 has a higher oxygen content than DNNC, implying that a C, H, N-rich residue remains on the filament. A small amount of dark-brown film is indeed observable and can be completely removed in an Ar atmosphere only by heating to 700°C or higher. HNCO and HCN are the dominant gas products formed by this residue. On this basis HNCO may be formed by decomposition of the residue, as is the case for RDX and HMX [22]. Oxidation of HCN by NO<sub>2</sub> at

high temperature is also a source of HNCO [23]. If DNNC is decomposed at temperatures above 240°C, the C, N, O, and H composition of the gas products more closely matches the formula of DNNC. This suggests that the amount of nonvolatile residue depends on the decomposition temperature, that is, the lower the temperature and longer the reaction time, the greater the tendency to form a relatively thermally stable, nonvolatile residue. It is doubtful that this residue forms at the surface temperature of burning DNNC.

As is the case for RDX [11] and HMX [4], the decomposition process of DNNC (Fig. 3) becomes strongly exothermic at the time that NO and CO become major products. This suggests that the highly exothermic reactions 7 and 8 may be occurring. However, the fact that much more NO than CO is liberated by DNNC implies that sources of NO exist other than reactions 7 and 8:



It is also noteworthy that, in contrast to RDX and HMX,  $\text{CH}_2\text{O}$  and  $\text{NO}_2$  continue to be generated in the exotherm and remain in high concentration in the cool Ar atmosphere after the decomposition is complete. This observation has implications for the flame structure of DNNC. The primary flame of DNNC is expected to be dominated by reactions 7 and 8, which release a large amount of heat close to the surface and influence the surface regression (burn) rate. The primary flame zone of RDX and HMX also appears to be dominated by the heat of reaction 7 or 8 [11]. Therefore, it is not surprising that the burn rates of RDX and DNNC shown in Fig. 2 are quite similar. Unlike RDX and HMX, DNNC also generated a large amount of NO in the decomposition process. NO reduction is relatively slow in the temperature range of the primary flame [20], and so NO would be expected to pass through the primary flame and become the dominant oxidizing agent of the secondary flame. In fact, the similarity of the burn rates of RDX and

DNNC, coupled with the high concentration of NO entering the primary flame of DNNC and the lower concentration of NO entering the primary flame of RDX, is strong evidence that NO reactions are unimportant in the primary flame zone of nitramine propellants.

#### THE DECOMPOSITION MECHANISM OF DNNC

Despite the fact that the primary flame zone chemistry of DNNC, RDX and HMX is driven by similar reactants (reactions 7 and 8), the decomposition mechanism of bulk DNNC is significantly different from RDX and HMX. An obvious major reason is that competition between reactions of the C- $\text{NO}_2$  and N- $\text{NO}_2$  groups affects the subsequent reaction pathways. For bulk RDX and HMX, the early reaction steps form  $\text{NO}_2$  and  $\text{N}_2\text{O}$  and leave less volatile secondary products to decompose later and produce the  $\text{CH}_2\text{O}$  and HCN fuels [4, 11]. In keeping with the  $(\text{CH}_2\text{NNO}_2)_n$  ( $n = 3, 4$ ) formulae of RDX and HMX, the quantities of  $\text{NO}_2$  and  $\text{N}_2\text{O}$  closely resemble HCN and  $\text{CH}_2\text{O}$ , respectively, before the exothermic reactions 7 and 8 take over [4, 11]. On the other hand, Fig. 3 shows that DNNC liberates only a small amount of  $\text{N}_2\text{O}$  and HCN, but a large amount of  $\text{NO}_2$  and  $\text{CH}_2\text{O}$ . These differences suggest some plausible decomposition pathways for DNNC.

The fact that  $\text{NO}_2$  is the initially detected gas product from DNNC is good evidence that C- $\text{NO}_2$  and/or N- $\text{NO}_2$  homolysis initiates the process. C- $\text{NO}_2$  and N- $\text{NO}_2$  have about the same bond energy in the related molecule, TNAAZ [24], but, in general, the C- $\text{NO}_2$  bond is thought to be slightly weaker than an N- $\text{NO}_2$  bond [25]. Consequently, mechanisms that begin with C- $\text{NO}_2$  homolysis and produce the gas products shown in Fig. 3 are considered here. Another set of reactions could be written beginning with N- $\text{NO}_2$  homolysis. Even with this constraint, many possible secondary decomposition reactions emerge. Unfortunately, the reaction intermediates are necessarily speculative because each can decompose in several ways and could also engage in bimolecular chemistry at each step. Bimolecular chemistry has an important role in the decomposi-

tion of energetic materials, especially at higher pressure [26].

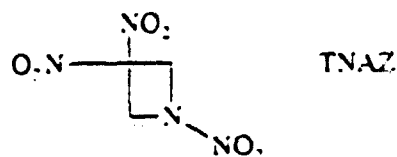
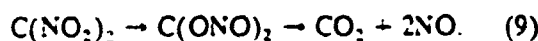


Figure 4 gives three of many reasonable reaction steps that can follow C-NO<sub>2</sub> homolysis. In routes I and III, the N or O atom of NO<sub>2</sub> could react bimolecularly at the carbon radical site leading to facile formation of NO and preparing the carbon atom to form CO<sub>2</sub>. Previously, double isomerization and decomposition of the C(NO<sub>2</sub>)<sub>2</sub> unit by reaction 9 was proposed [10] to account for the large amount of CO<sub>2</sub> and NO that is generated by gem-dinitro groups [10, 27]:



However, there is no evidence of reaction 9 in the unimolecular gas-phase decomposition of TNAZ [28]. On the other hand, in bulk material, the bimolecular stepwise reaction of NO<sub>2</sub> and the residual molecule (routes I and III), which is a variation on reaction 9, remains a plausible route to CO<sub>2</sub> and NO. Isomerization of the -NO<sub>2</sub> groups of gem-dinitroalkanes and scission of the -NO bond to a carbonyl and NO(g) has been proposed to account for the products of thermal decomposition [29]. Recently, pyrolysis of C(NO<sub>2</sub>)<sub>2</sub> above 250°C was observed to produce NO<sub>2</sub> and NO [30]. The resulting intermediate was proposed to be a

carbonyl that decomposed to CO and CO<sub>2</sub>. The absence of N<sub>2</sub> and O<sub>2</sub> was further evidence of a carbonyl of the type proposed in Fig. 4 [30].

The large amount of NO produced by DNNC suggests that other facile routes to NO must be present in the decomposition fragments. In route II, two NO molecules are indicated as products of a primary nitramine radical. This branch is proposed based on the loss of N<sub>2</sub>O<sub>2</sub> during unimolecular decomposition of TNAZ [28]. It has not been determined whether evolution of the N<sub>2</sub>O<sub>2</sub> unit leading to 2NO is unique to a nitroazetidine radical or whether it is characteristic of the RNNO<sub>2</sub> group in general.

Further decomposition of the intermediates of routes I-III in Fig. 4 would be expected to liberate CH<sub>2</sub>O, H<sub>2</sub>O, NO<sub>2</sub> and HCN as well. Bimolecular recombination reactions could generate a nonvolatile residue. The experimentally observed minimal temperature dependence of the concentrations of the major gas products may result from the fact that the multiple reaction pathways compete in forming each gas. When this occurs the numerous elementary steps in any particular reaction channel become disguised, if, as is the case here, only final gas products can be detected.

*T. Brill is grateful to the Air Force Office of Scientific Research, Aerospace Sciences, for support of this work on AFOSR-89-0521. The work at ONERA was carried out under a contract from DRET (Ministry of Defense).*

## REFERENCES

1. Lengfeld, G., Duterque, J., Godon, J. C., and Tribert, J., *J. Propuls. Power*, in press.
2. Brill, T. B., Brush, P. J., James, K. J., Shepherd, J. E., and Pfeiffer, K. J., *Appl. Spectrosc.* 46 900-911 (1992).
3. Brill, T. B., *Prog. Ener. Combust. Sci.* 18 91-116 (1992).
4. Brill, T. B., and Brush, P. J., *Philos. Trans. R. Soc. (Land.) A* 339 377-385 (1992).
5. Brill, T. B., Brush, P. J., and Patel, D. G., *Combust. Flame* 92 175-186 (1993).
6. Timbira, M. D., Chen, J. K., and Brill, T. B., *Appl. Spectrosc.* 44 701-706 (1990).
7. Chen, J. K., and Brill, T. B., *Combust. Flame* 85 475-488 (1991).
8. Chen, J. K., and Brill, T. B., *Combust. Flame* 87 157-168 (1991).

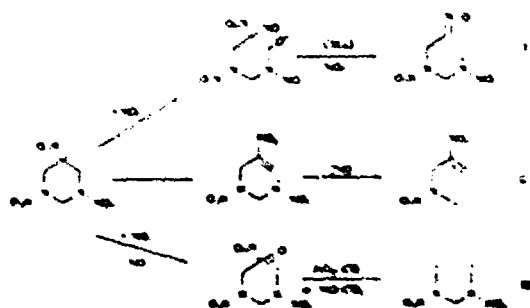


Fig. 4. Three of many plausible reaction routes of DNNC following C-NO<sub>2</sub> homolysis. Routes I and III involve bimolecular reaction of NO<sub>2</sub> and the resultant radical. Route II is a possible major source of NO.



9. Chen, J. K., and Brill, T. B., *Combust. Flame* 87:217-232 (1991).
10. Oyumi, Y., and Brill, T. B., *Combust. Flame* 62:215-231 (1985).
11. Brill, T. B., Brush, P. J., Paul, D. G., and Chen, J. K., *Twenty-Fourth Symposium (International) on Combustion*, The Combustion Institute, Pittsburgh, 1992, pp. 1907-1914.
12. Levins, D. L., Bedford, C. D., and Coon, C. L., *US Patent* 4,346,222 (24 Aug. 1982).
13. Cichra, D. A., and Adolph, H. G., *J. Org. Chem.* 47:2474-2476 (1982).
14. Shackelford, S. A., *J. Label. Cpts. Radiopharm.* 29:1197-1206 (1991).
15. Boileau, J., Piteau, M., and Jacob, G., *Prop. Explos. Pyrotech.* 15:38-40 (1990).
16. Langellé, G., *ALCh J.* 8:1989-1966 (1970).
17. Williams, F. A., *ALCh J.* 14:1328-1330 (1973).
18. Shackelford, S. A., and Goldman, J. F., *Twenty-Second ICT International Jahresagung*, Karlsruhe, Germany, 1991, pp. 14-1 to 14-14.
19. Oyumi, Y., Brill, T. B., Rheingold, A. L., and Haller, T. M., *J. Phys. Chem.* 89:4317-4324 (1985).
20. Melius, C. F., in *Chemistry and Physics of Energetic Materials* (S. Bylusu, Ed.), Kluwer, Boston, 1990, Vol. 309, p. 69.
21. Brill, T. B., and Oyumi, Y., *J. Phys. Chem.* 90:6848-6853 (1986).
22. Palopoli, S. F., and Brill, T. B., *Combust. Flame* 87:45-60 (1991).
23. Lin, M. C., Workshop on Fundamental Physics and Chemistry of Combustion, Initiation, and Detonation of Energetic Materials, Los Alamos National Laboratory, March, 1992.
24. Politzer, P., personal communication, 1992.
25. Batt, L., in *The Chemistry of Functional Groups* (S. Patai, Ed.), Wiley, New York, 1982, Suppl. F, Part 1, p. 417.
26. Oyumi, Y., and Brill, T. B., *Combust. Flame* 68:209-216 (1987).
27. Oyumi, Y., and Brill, T. B., *Combust. Flame* 65:103-111 (1986).
28. Anex, D. S., Allman, J. C., and Lee, Y. T., in *Chemistry of Energetic Materials* (G. A. Olah and D. R. Squires, Eds.), Academic, San Diego, CA, 1991, pp. 27-54.
29. Tormell, K., and Ryhage, R., *Arzu Kemi* 23:525-536 (1965).
30. Bock, H., and Zanathy, L., *Angew. Chem.* 31:900-902 (1992).

Received 21 January 1993; revised 7 June 1993